Design of a High Specific Power Electric Machine for Turboelectric Propulsion

by

Aidan Patrick Dowdle

B.S., Georgia Institute of Technology (2015)
S.M., Massachusetts Institute of Technology (2017)

Submitted to the Department of Electrical Engineering and Computer Science
in partial fulfillment of the requirements for the degree of

Doctor of Philosophy in Computer Science and Engineering

at the

MASSACHUSETTS INSTITUTE OF TECHNOLOGY

May 2022

Author .....
Department of Electrical Engineering and Computer Science
May 13, 2022

Certified by .....
Zoltán S. Spakovszky
Professor of Aeronautics and Astronautics
Thesis Supervisor

Accepted by .....
Leslie A. Kolodziejski
Professor of Electrical Engineering and Computer Science
Chair, Department Committee on Graduate Students

Design of a High Specific Power Electric Machine for Turboelectric Propulsion

by

Aidan Patrick Dowdle

Submitted to the Department of Electrical Engineering and Computer Science
on May 13, 2022, in partial fulfillment of the
requirements for the degree of
Doctor of Philosophy in Computer Science and Engineering

Abstract

The benefits of turboelectric propulsion for aviation, in which a gas generator core electrically drives motor-powered propulsors, are limited by the mass and losses of the electric components introduced into the drivetrain. These propulsion systems are predicted to result in a 15% fuel savings provided that megawatt-class electrical machines (EMs) and power electronics (PEs) are available with power-to-mass ratios exceeding 13 kW/kg and 16 kW/kg, respectively.

This thesis proposes an integrated prime mover concept enabled by the material choices and cooling technology available today. In this concept, an outer rotor, tooth-and-slot Halbach array is integrated with the low pressure compressor of a low fan pressure ratio aeroengine. The specific power of the integrated compressor generator is estimated to be 14.8 kW/kg, exceeding the NASA 2030 goal for aviation applications of 13 kW/kg for a standalone electric machine for aviation applications.

Relative to a standalone, optimized electrical machine, co-optimization of the EM, PEs, thermal management system, and turbomachine rim suggests a 38% increase in system specific power.

Based on these findings and supported by 2D and 3D finite element analysis, a 19.7 kW/kg, megawatt-class, air-cooled tooth-and-slot Halbach array electrical machine demonstrator is conceived. A detailed design study together with risk mitigation experiments of key components are carried out, setting the stage for megawatt-class, high power density, and high efficiency electrical machines for aerospace applications.

Thesis Supervisor: Zoltán S. Spakovszky
Title: Professor of Aeronautics and Astronautics

To my mom,

in loving memory.

Acknowledgments

I would like to express my sincere gratitude to my advisor, Professor Zoltán Spakovszky, for his guidance and support during my graduate studies. I am thankful for the weekly meetings and the frequent feedback on my research over the last several years. I have learned an incredible amount under his supervision regarding both project management and research that will serve me for years to come.

Professor Jeffrey Lang has been an immense help during my Ph.D. with the many meetings and discussions involving different aspects of the electric machine and electromagnetics. The 6.014 course material that he taught me was invaluable for this project. In addition, Professor James L. Kirtley Jr. played a critical role in estimating the Halbach array performance and in sanity checking all aspects of the design. I am thankful for all of his guidance on this project.

In addition to my committee, I would like to thank Professor Greitzer for his mentorship and helpful feedback during the weekly meetings. I very much appreciate your support with the fellowship my first few years as both an S.M. and Ph.D. student.

I owe an enormous thanks to my dad for inspiring me to pursue a Ph.D., for the helpful discussions regarding my research, and for his constant support. I would also like to acknowledge the rest of my family - Brendan, Betsy, Viktor, Melissa, Liam, Maeve, Olivia, and John for their love and support. I cannot thank Danielle enough for her continuous love and support throughout all of my research and writing.

This research involved many people to whom I owe my gratitude. I would like to thank Yuankang Chen for his enormous support and impressive work on structural, thermal, and even electrical engineering aspects of this project. I enjoyed the many productive debates regarding the physics of the machine, as well as the late nights

spent processing and discussing the co-optimization results. It is exciting to see this design take physical form after all of these years.

Mr. Marc Amato of Innova-logic has played a critical role as both my mentor and a collaborator on this project. Thank you for your hard work on manufacturing the electric machine in this thesis, the exciting discussions on upcoming electric machine technology, and for helping me with all things related to vendors and procurement. I thank Mohammad Qasim for always being willing to help out with the electric machine analysis as well as his excellent work on the electronics. Mr. David Otten has played a key role with all things electronic and I appreciate all the helpful feedback and close collaboration. Dr. Stephen Umans has been a constant source of advice on this project. I am thankful for his mentorship as well as his enthusiasm for my research. I would also like to thank Professor Perreault, Professor Cordero, David, Charlotte, and Henry for their hard work on this project and helpful insights. I would like to recognize the incredible amount of work from Pam, Jennie, and Robin and thank them for always ensuring that procurement runs smoothly.

I would like to thank Alex, Andras, Jonas, Vaishnavi, Geoff, Laurens, and Joe from the GTL, amongst others, for leaving me with great memories. I am lucky to have met such a passionate group of engineers, and I will miss the technical discussions as well as social hours. Lastly, I would like to thank my friends Adam, Sherman, Jordan, Matt B., Matt S., Will, and Misha for their support and great times.

Funding for this work was provided by Mitsubishi Heavy Industries, Ltd. I thank Iida-san, Sasaki-san, and Ezumi-san for their support and valuable insights on this project.

Contents

List of Figures

List of Tables

Chapter 1

Introduction

1.1 Background

Advancements in battery, power electronics, and electric generator/motor technology have renewed interest in electric propulsion for the potential improvement of aircraft performance. Specifically, electric propulsion is viewed as having the potential to enable short take-off and landing, reduce fuel burn, produce less noise, and cut back on emissions for aircraft. These performance benefits could be realizable through boundary layer ingestion (BLI) and distributed propulsion (DP), both of which electric propulsion facilitates [7]. In addition, new degrees of freedom in airframe design may be enabled if the gas generator core and fan are mechanically decoupled.

Due to the relatively low energy-to-mass ratio of batteries compared to jet fuel, it is likely that larger aircraft will still require gas generator cores as the prime mover in their propulsion systems. To electrify these aircraft, a generator can extract power from the core and electrically drive motor-powered propulsors. This type of drivetrain is known as a turboelectric (TE) propulsion system and is shown in Fig. 1 below [8].

For these types of drivetrains, the potential benefits of BLI and DP must be considered against the weight and inefficiencies added by the electrical distribution components. In their STARC-ABL concept, NASA has estimated that re-optimizing a single aisle aircraft with a TE propulsion system results in a 15% fuel savings [1]. This estimated benefit, however, assumes that the electric machines have a power-

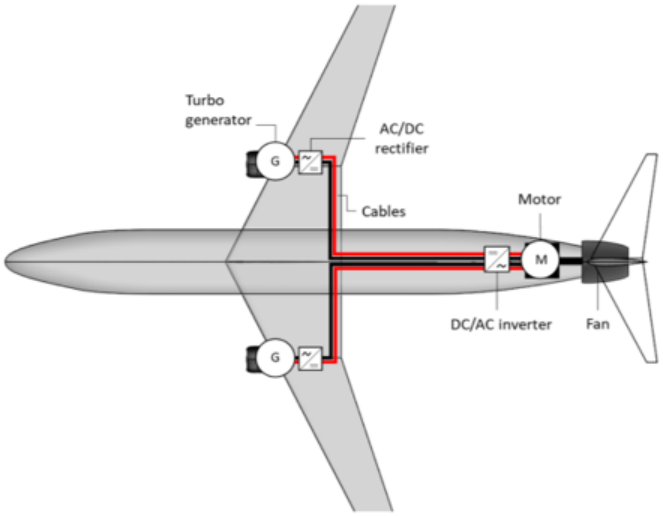

Figure 1-1: An example turboelectric propulsion system has two turbogenerators on the wings powering a rear BLI fan via electric power transmission [1].

to-mass ratio, or specific power (SP), of 13 kW/kg, and the power electronics have a SP of 16 kW/kg. However, a survey of the SPs of existing high-performance electric machines [2], shown in Fig. 1-2, shows that electric machine SP currently does not meet these targets with the peak at 8.5 kW/kg in the low kW range.

In a turboelectric propulsion system, power electronics such as AC-to-AC converters enable the generator and motor to operate at different speeds, provide torque and speed control, and can reduce the harmonics in the electrical transmission system. However, for fixed rated power, the power electronics can be just as heavy as the electric machines. NASA has established a year 2030 target of 15 kW/kg for a single AC-to-DC or DC-to-AC converter, or 7.5 kW/kg for an AC-to-AC converter [9].

Figure 1-3 shows the specific power for AC-to-AC converters. Typical multi-megawatt motor drives found in commercial applications today are for marine propulsion applications and their specific powers are in the 2-3 kW/kg range [10]. However, most prototypes and drives are either converters (DC-to-AC conversion) or inverters (AC-to-DC conversion), so their approximate AC-to-AC converter performance is estimated by dividing their specific power by two. An inverter prototype at 12 kVA/kg, based on silicon carbide transistor technology, has been demonstrated at the megawatt level [11]. The University of Nottingham has developed a Si-based, three

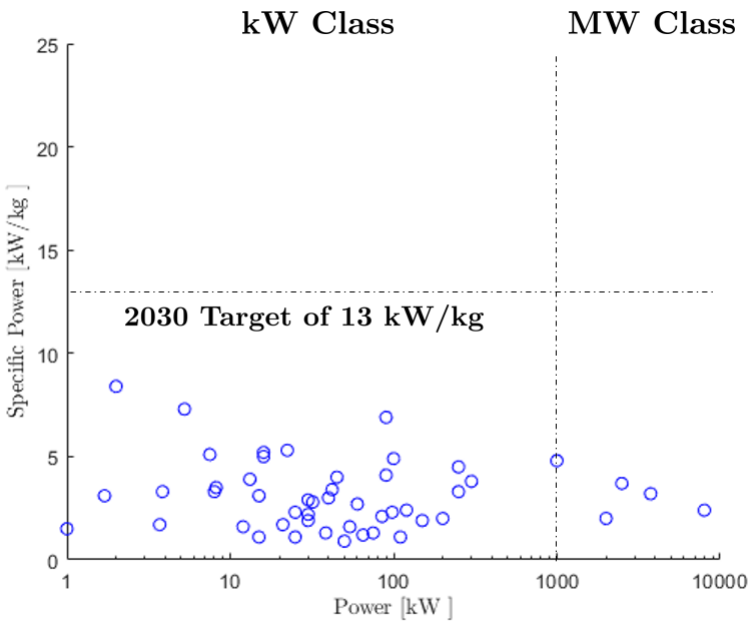

Figure 1-2: A survey of EM SPs from Ref. [2] found that the peak SP today of 8.5 kW/kg is below the NASA target of 13 kW/kg.

level neutral-point-clamped prototype that is projected to have 16.6 kW/kg specific power [12]. This design exceeds the NASA 2030 target of 7.5 kW/kg [9]. Other GaN, SiC, and cryogenically cooled Si designs have been proposed that will exceed 7.5 kW/kg [13].

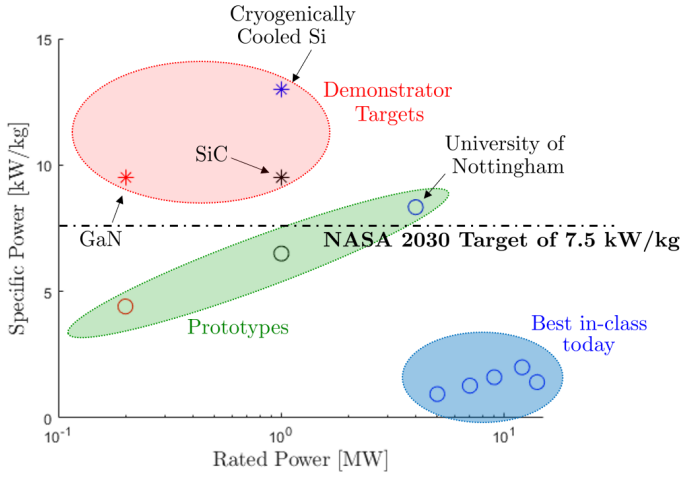

Figure 1-3: Surveyed power electronics peak at approximately 12 kVA/kg per inverter, or around 6 kVA/kg for an AC-to-AC converter.

1.2 Challenges in Obtaining High Specific Power Electric Machines

Two trends can be observed in the electric machine survey in Fig. 1-2 adapted from Ref. [2]. First, there is a wide range of specific powers for the surveyed machines. This may be attributed to the designs having different application requirements. For example, some of the surveyed motors may prioritize efficiency over mass. In addition, it is unclear which components of the electric machine, such as the thermal management system (TMS), are accounted for in the quoted specific power value. Second, the maximum attainable SP appears to decrease with rated power level, with the highest demonstrated megawatt-class electric machine at 5 kW/kg.

The scaling laws for a simplified electric machine highlight some of the fundamental challenges with designing megawatt-class, high SP electric machines. The rotor of the electric machine is modeled as a cylinder of radius r and axial length ℓ. The average electromagnetic torque can then be expressed as the product of the average electromagnetic shear stress in the airgap, $\bar{\tau}$, the surface area of the cylinder, and the

moment arm (i.e., airgap radius):

$$T = \bar{\tau}\,(2\pi r\ell)\,(r) \tag{1.1}$$

The specific power of the electric machine is then approximated by dividing the mechanical power by the volume of the rotor

$$\frac{P}{V} = \frac{\bar{\tau} 2\pi r^2 \ell \Omega}{\pi r^2 \ell} \tag{1.2}$$

where $U = \Omega r$ is the tip speed. Equation 1.2 can be recast in terms of the design parameters of electromagnetic shear stress, aspect ratio, tip speed, and rated power:

$$\begin{aligned}
\left(\frac{P}{V}\right)^2 &= \frac{(\bar{\tau})^2\, 4\pi^2 r^4 \ell^2 \Omega^2}{\pi^2 r^4 \ell^2} \\
&= \frac{(\bar{\tau})^2\, 4\pi^2 r^4 \ell^2 \Omega^2}{\pi^2 r^4 \ell^2} \cdot \frac{2\bar{\tau}\Omega}{2\bar{\tau}\Omega} \\
&= \frac{8\pi\,(\bar{\tau})^3\, r^3\,(\ell/r)\,\Omega^3}{2\bar{\tau}\pi r^2 \ell \Omega} \\
&= \frac{8\pi\,(\bar{\tau})^3\,(\ell/r)\,U^3}{P} \\
\frac{P}{V} &= 2\,(\bar{\tau})^{3/2} \sqrt{\frac{2\pi\,(\ell/r)\,U^3}{P}}
\end{aligned} \tag{1.3}$$

Equation 1.3 suggests that to maximize electric machine specific power, the electromagnetic shear stress, length-to-tip radius aspect ratio, and tip speed should be maximized. However, the achievable electromagnetic shear stress, $\bar{\tau}$, is limited by saturation of the magnetic core and the maximum temperature rating of electric machine components such as the stator winding insulation, both of which are material properties. The aspect ratio, ℓ/r, is limited by rotordynamics and thermal managment. With regards to thermal management, it is difficult to remove heat from longer machines for air-cooled designs. Lastly, the tip speed, U, is limited by the structural integrity of the rotor. High tip speeds increase the stress in the rotor during operation and may cause it to fail. In addition, this increases the thermal load on the TMS due to increased windage loss.

Assuming that these parameters are maximized to their physical limits in an optimized design, *specific power is inversely proportional to the square root of rated power.* This means it is fundamentally challenging to design high power, high specific power electric machines. In addition, while this scaling law informs how to design a high SP EM, it does not reflect how the thermal management system and power electronics are impacted by these design decisions.

1.3 Technology Enablers

The technology enablers for high specific power electric machines and their application to turboelectric propulsion are divided into two sections:

1. technologies and design methodologies that fundamentally improve the standalone electric machine specific power, and

2. integrated electric machine drive concepts that improve the overall propulsion system specific power.

Both avenues for specific power reduction are considered and discussed in the following subsections. In particular, the stator processing to minimize core loss is a key technology enabler for a high specific power, air-cooled electric machine. This topic is introduced below and discussed in more detail in Chapter 5.

1.3.1 Electric Machine

In Section 1.2, the rotor is assumed to be a solid, cylindrical block of magnetic core material. However, magnetically, the rotor only needs to be sized large enough to carry the magnetic flux, and a toroid can be used in place of a solid rotor to save material. The hoop stress also needs to be considered with this design. A high pole count electric machine design can further reduce the rotor back iron thickness. However, the trade-off is that electrical frequency is increased, which in turn increases electric machine losses and possibly penalizes the power electronics.

Thin stator laminations may be used to reduce the eddy current loss from the rotating magnetic field. The material with the lowest core loss that is available today is iron cobalt vanadium [14]. The thinnest available laminations of iron cobalt vanadium today are 4 mil or 0.1016 mm thick, which can be difficult to handle since the material is mechanically weak after an anneal that maximizes magnetic performance. In addition, the core loss can increase due to trauma imparted on the cut edge during the lamination processing [15]. Iron cobalt vanadium is typically processed via stamping or laser cutting. However, photochemical etching is predicted to minimize the cut edge effect and reduce core loss [16].

Additionally, if a Halbach array of permanent magnets is used, magnetic flux on the rotor back iron side is cancelled and the stator back iron can be entirely eliminated [17]. In a Halbach array, azimuthal facing magnets are added between the radial facing magnets to cancel the flux on one side of the array and reinforce it on the other, which has the additional benefit of increasing the strength of the magnet array [17].

Next, to maximize tip speed, a sleeve made from a high strength material (e.g., titanium) can be used to retain the permanent magnets. If the rotor is on the inside, this greatly increases the airgap of the electric machine and worsens performance. Instead, the rotor can be placed on the outside of the electric machine such that the rim does not impact the airgap. To produce the required electromagnetic shear stress, permanent magnets can be used in lieu of electromagnets since they can produce similar flux densities at lower losses.

Most high power electric machines use some form of liquid cooling. These cooling systems tend to be heavy and, for an aircraft, the heat must ultimately be dumped into an air stream. Instead, an aggressive, air-cooling only scheme may be used to push a large mass flow of air through the air gap and stator. The trade-off is that such an air-cooling system may require large amounts of input power and requires careful estimation of the electric machine losses and pressure drops across air flow paths.

1.3.2 Integrated Prime Mover Concept

Several conceptual designs targeted at improving electric machine (EM) or power electronics (PE) SP individually are in progress and are discussed in Section 1.4 below. However, an approach proposed in this thesis is to physically integrate and co-optimize the EM, PE, turbomachinery, and thermal management system (TMS) to achieve greater TE system specific powers, and thus fuel burn reduction. The hypothesis is that the system-level optimization of the physically integrated subsystems (i.e., EM, PE, TMS, and turbomachine) improves the performance of TE propulsion systems over optimizing any component individually. The integrated design may be a key enabler for building TE-based aircraft with reduced fuel consumption.

Aside from optimizing the total TE system specific power, such physical integration may eliminate large components such as mechanical gearboxes, oil cooling systems, and the generator/motor casing. Moreover, air from the gas path of the turbine may be used to cool the electric machine. The rotor of the electric machine may contain compressor or turbine blades to eliminate the windage loss that normally occurs at the rotor surface.

1.4 Related Work

Currently, there is interest from both government agencies and industry in the development of light weight, efficient electromechanical conversion devices for aviation. One example is NASA, which recently proposed the STARC-ABL turboelectric (TE) concept and is building the NEAT testbed for MW electronics testing [1].

1.4.1 Megawatt Demonstrators

To date, a megawatt (MW) class turboelectric drive that is sufficiently light for electrification of aviation has not been demonstrated. Although MW class electric machines are operational in both terrestrial power plants and marine electric propulsion systems, maximizing electric machine efficiency is prioritized over minimizing mass and

volume in these applications. In addition, these machines are designed for a 50/60 Hz electrical frequency, whereas aircraft already operate at 400 Hz [36] and a turbo-electric propulsion system could conceivably be designed for even greater frequencies.

Several projects focused on high specific power, megawatt-class demonstrators are in development. A research group led by Professor Kiruba Haran at the University of Illinois Urbana-Champaign (UIUC) is developing a one megawatt, slotless, Halbach array motor targeting a SP of 13.0 kW/kg [18]. This SP includes the mass of the EM heat sink. In addition, the motor uses a self-pumped air cooling system. In their most recent publications, UIUC confirmed the stator has been manufactured and tested, but their Halbach array rotor is incomplete because it was received with misoriented magnets [18]. A surface permanent magnet rotor was built in its place for preliminary testing [18].

At the University of Wisconsin-Madison (UW), a research group led by Professor Thomas Jahns is developing a 23.7 kW/kg, liquid-cooled, inner rotor surface PM machine that will operate at one megawatt of power [19]. The SP of the EM does not include the liquid cooling system. Since the machine spins at the high rotational speed of 20,000 rpm, the magnets on the inner rotor will be retained with a carbon fiber sleeve. UW is planning to test a 250 kW prototype prior to building the 1 MW design.

Another surveyed megawatt project is the Lightweight Innovative Generator for Future Air Transporation (LIFT) project led by PI Professor Chris Gerada at the University of Nottingham [20]. The objective of this project is to demonstrate a four megawatt generator with a specific power of 20 kW/kg. This design is an inner rotor, tooth-and-slot stator electric machine that is liquid cooled. Specifically, oil channels are inserted in the slot sections to pump coolant and the end windings are cooled by oil jet impingement [12]. A glass-fiber sleeve isolates the coolant in the stator from the rotor [12].

In addition to these three published EMs, General Electric (GE) stated in a 2017 white paper that they have demonstrated a one megawatt motor at 98% efficiency [21]. However, additional details on this design have not been found in published

literature.

1.4.2 Integrated Prime Mover Concepts

The concept of integrating the electric machine with the gas generator core has been explored in the "oil-free gas turbine engine" concept [22]. One example of electric machine and turbomachine integration is the AlliedSignal Under-Armor APU demonstrator [22]. In this design, the generator/motor was integrated onto the turbomachine spool between the compressor and turbine and successfully demonstrated in the Abrams M1A1 tank.

Other ideas have been proposed in patents. For example, one concept proposes installing permanent magnets into the tips of the fan blades and electromagnets in the case [23]. In another concept, the turbomachine shaft is replaced entirely with electric machines for torque transfer [24]. Counter rotating rotor stages can replace the turbomachine stator rows, which improves power transfer, reduces the number of turbomachine blade rows, and therefore increases specific power. Neither the detailed design nor demonstration of these concepts is found in literature.

Several integrated prime mover concepts specifically intended for turboelectric propulsion systems have been published. One such concept is a University of Illinois Urbana-Champaign concept in which an inner rotor permanent magnet synchronous machine is integrated with a propellor for a small passenger aircraft [25]. In this design concept, the overall propellor and electric machine subsystem is optimized, but the two components are not physically integrated. A concept design in which the electric machine and propellor are integrated is proposed in Ref. [26].

1.5 Thesis Objectives and Contributions

The first part of this thesis is the conceptual design of an integrated prime mover (IPM) in which an electric machine is embedded into a turbomachine, similar to the concepts discussed in Section 1.4.2. This IPM differs from the surveyed designs in that the electric machine is not retrofitted into an existing turbomachine engine.

Instead, the turbomachine engine is re-designed to optimize the overall specific power of the IPM system. The **first objective of this thesis** is to evaluate feasibility of this integrated design by re-optimizing a baseline low fan pressure ratio engine for integration. The **second objective of this thesis**, accomplished in parallel, is to maximize the overall IPM system specific power. Due to the absence of published IPM designs for comparison, this specific power is compared against the NASA targets for turboelectric propulsion [9].

The second part of this thesis is the conceptual and detailed design of a megawatt-class technical demonstrator. The **third objective of this thesis** is to identify a megawatt demonstrator design point for a technical demonstration. This is accomplished via a novel co-optimization methodolody which maximizes system-level specific power. The **fourth and final objective of this thesis** is to take this integrated design through a detailed design phase. This detailed design will ultimately be used in a technical demonstration to verify the predicted performance. This technical demonstration will test the

1. aggressive air-cooling of an integrated, high specific power electric machine;
2. structural integrity and rotordynamics of the turbomachine-integrated, high speed Halbach array rotor;
3. low-loss tooth-and-slot stator; and
4. integrated, high specific power electronics.

The contributions and key learnings of this thesis are the following:

- A novel integrated prime mover concept is feasible with the materials and technology available today. In this concept, an outer rotor, tooth-and-slot Halbach array is integrated with the low pressure compressor of a low fan pressure ratio engine. The integrated compressor generator module is predicted to have a specific power of 14.8 kW/kg, which exceeds the NASA 2030 target of 13 kW/kg for a standalone electric machine.

- Co-optimization of the electric machine, power electronics, thermal management system, and turbomachine rim results in a 38% greater predicted system specific power than optimizing for a standalone electric machine. Therefore, there is a substantial benefit for turboelectric propulsion applications from optimizing the system-level performance of the various subsystems.

- Lastly, a novel 19.7 kW/kg, air-cooled tooth-and-slot Halbach array machine design is proposed for the first time for a technical demonstration. This predicted performance is supported by 2D and 3D finite element analysis. The detailed design of the machine is complete, and initial bench tests have verified subsystem performance.

The work in this thesis involved many collaborators. Any contributions from collaborators will be explicitly stated beforehand. More broadly, Yuankang Chen lead the research effort on the mechanical and thermal subsystems and helped with the electromagnetic models for Chapter 2 [27]. Mohammad Qasim and Mr. David Otten are developing the power electronics for the demonstrator [28]. David Gonzalez Cuadrado developed the coolant flow system and superstructures of the demonstrator. Professor James Kirtley Jr. created the Halbach array model used in Chapters 3 and 4 and Appendix C. Mr. Marc Amato of Innova-Logic lead the manufacturing of the demonstrator and provided the photos in Chapter 5 where indicated. Lastly, Henry Andersen assisted with the stator field model in Chapter 4.

1.6 Key Differentiators

The megawatt demonstrator in this thesis differs from other machines discussed in Section 1.4 in several ways:

1. it is a co-optimized design of an electrical machine, thermal management system, turbomachine rim, and power electronics;

2. the demonstrator utilizes a combination of a slotted stator and an outer rotor

Halbach array design which is predicted to have the highest SP of surveyed PM motor types;

3. it employs a physically integrated architecture which minimizes power electronic lead lengths and air cooling flow paths;

4. the high specific power electric machine is enabled via an air-cooled, outer rotor, turbo-integrated configuration; and

5. single phase, full bridge power electronics are integrated into the design.

In comparison to the published University of Illinois Urbana-Champaign (UIUC), University of Wisconsin (UW), and University of Nottingham electric machine designs, the design in this thesis differs in its combination of geometry, topology, and design rotational speed. While the thesis, UIUC, and UW electric machines are all designed for one megawatt, the University of Nottingham electric machine is actually designed for four megawatts. The details of each design are summarized in Table 1.1. Unlike the UW and University of Nottingham designs, the design in this thesis uses an outer rotor geometry to facilitate integration with turbomachinery. This outer rotor design helps secure the magnets in place at high speed operation. In addition, while the UIUC also uses an outer rotor geometry, the design of this thesis differs in that it has a tooth-and-slot stator. Both the outer rotor and tooth-and-slot design decisions are based on a trade space study comparing different design options. In this project, it was concluded that the tooth-and-slot Halbach array combination conceptually offers the highest SP compared to surface PM and slotless architectures for outer rotor geometries. In addition, the MIT EM design differs from UW, UIUC, and University of Nottingham in that it has a lower rotational speed. Relative to the UW and UIUC designs, the design in this thesis likely has a relatively lower speed because the design assumes a core loss safety factor of two, which is discussed in further detail in Chapter 4. The full bridge power electronics topology is predicted to have a standalone specific power of 37.8 kW/kg based on mass buildup models and early prototypes [29].

Table 1.1: Each demonstrator electric machine design optimized to different geometries, topologies, and design parameters.

	Thesis Design	**University of Wisconsin 2019 [30], [19]**	**UIUC 2018-2019 [18], [31]**	**University of Nottingham 2021 [32]**
Electric Machine Type	Radial PM Synchronous Machine	Radial PM SM	Radial PM SM	Radial PM SM
Geometry	Outer Rotor	Inner Rotor	Outer Rotor	Inner Rotor
Rotor Type	Four Block Halbach Array	Surface Mount	Six Block Halbach Array	Four Block Halbach Array
Stator Type	Tooth-and-Slot	Tooth-and-Slot	Slotless	Tooth-and-Slot
Cooling Technique	Air-cooled	Liquid-cooled	Self pumped air-cooled	Liquid-cooled
Rated Power [MW]	1	1	1	4
Estimated Demonstrator SP [kW/kg]	12.8	7.5	7.2	6.6
Electric Machine SP [kW/kg]	19.7	23.7	13.0	17.5
Angular Speed [rpm]	12,500	20,000	15,000	15,000
Shear Stress [kPa, psi]	35, 5.0	51, 7.4	23, 3.3	104, 15
Slot Current Density [Apk/mm^2]	13.3	28.3	10.3	38.9
Number of Pole Pairs [-]	10	6	10	4
Electrical Frequency [Hz]	2083.3	2000	2500	1000
Switching Frequency [kHz]	80	20	-	15
Ripple Frequency [kHz]	160	-	-	-

1.7 Thesis Organization

Chapter 2 details the integrated prime mover study. Trade-offs between different architectures and EM types are discussed, and a conceptual design is presented at the end. Next, Chapter 3 builds on the framework from Chapter 2 to identify a candidate design for a one megawatt demonstrator. The details of the candidate one megawatt demonstrator design are worked out in Chapter 4. Bench tests to characterize the subsystem performance of the demonstrator are discussed in Chapter 5. Finally, Chapter 6 summarizes the work of this thesis and discusses directions for future work.

Chapter 2

Integrated Prime Mover Study

2.1 Introduction

An integrated prime mover (IPM) is defined as an electric machine that shares a rotor, cooling system, and support structures with a turbomachine. The potential benefit of an IPM is improved turboelectric system specific power (SP). Different IPMs may be conceptualized based on various combinations of electric machine types and locations for integration within a turbomachine. In this chapter, a trade space analysis is performed and used to select a single IPM architecture to take through a conceptual design in Chapter 3.

The objective of this trade space analysis is to find an IPM with maximum specific power that can be cooled on the basis of a heat flux metric. This analysis features four different IPM architectures which are selected based on scaling laws and published electric machine surveys. The outcome of this study is that the most promising IPM architecture is a permanent magnet synchronous motor placed radially internal to a compressor.

The first two sections of this chapter discuss how the broad IPM design space is reduced to just a few of the IPM architectures with stronger potential. First, the possibilities for IPM architectures are discussed in Section 2.2. Candidate EM topologies and geometries are defined which may be feasible for turbomachine integration. Then, in Section 2.3, scaling laws based on first principles are derived to show that plac-

ing the EM either radially internal or axially to the turbomachine results in greater system specific power. Second, based on the maximum tip speeds of existing electric machines, only the permanent magnet synchronous machine and solid rotor induction machine are considered eligible for the IPM concept. Therefore the design space is reduced to just four candidate architectures. These candidate machines are carried through a trade space analysis in Section 2.4. The results of the trade space analysis and selection of a single architecture for a conceptual design are discussed in Section 2.5.

2.2 Integrated Prime Mover Architectures

Various IPM architectures are eligible for a more detailed study due to the numerous combinations of

1. EM geometries,

2. locations for integration within a turbomachine, and

3. electric machine (EM) topologies.

For example, a permanent magnet synchronous electric machine could be integrated within the low pressure compressor, or a variable reluctance electric machine might be integrated axially onto the high pressure turbine.

In this section, the first two items, EM geometries and locations for integration, are discussed. Three IPM architectures are identified by considering common geometries of EMs and how they might fit within the turbomachine. Section 2.2.1 provides a survey of the more common geometries. Next, the different locations for integration within a turbomachine are discussed in Section 2.2.2. Due to low maximum operating temperatures for electric machines, the low pressure compressor is identified as the most likely location for EM integration. Finally, three concepts are defined for further exploration in Section 2.2.3.

2.2.1 EM Geometry Considerations

The typical outer rotor, inner rotor, and axial electric machine configurations are considered for the IPM. These three configurations are common in their cylindrical structure; however, they differ in their magnetic flux paths as well as the relative locations of the EM rotor and stator as depicted in Fig. 2-1 for permanent magnet synchronous machines. These EM geometries also exist for other machine types such as induction machines.

In an outer rotor configuration, the magnetic flux path is radial and the rotor is located radially exterior to the stator. This arrangement is shown in Fig. 2-1a. The inner rotor configuration in Fig. 2-1b also has a radial flux path, but the rotor is interior to the stator. Lastly, in an axial configuration, shown in Fig. 2-1c, the rotor and stator are parallel to each other and the magnetic flux path is in the axial direction.

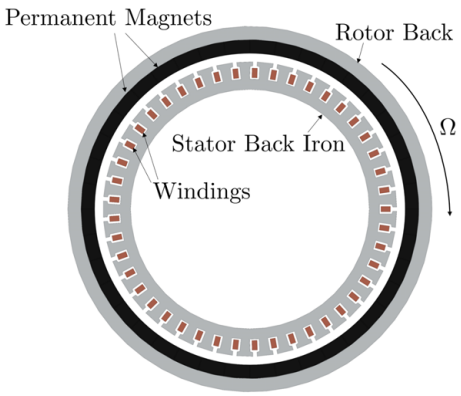

(a) 2D cross-section of the outer rotor geometry.

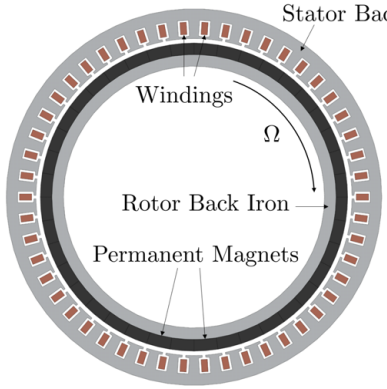

(b) 2D cross-section of the inner rotor geometry.

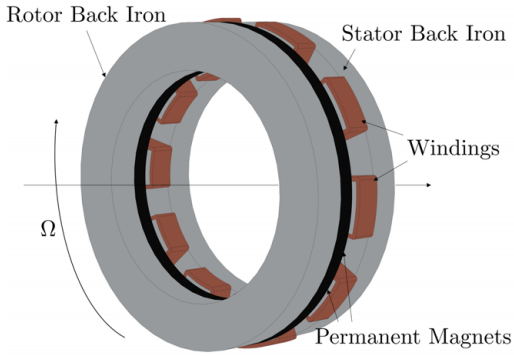

(c) 45 degree angle view of the axial rotor geometry.

Figure 2-1: Drawings of the inner rotor, outer rotor, and axial machine types show the different stator and rotor configurations.

2.2.2 Locations for Integration Within Turbomachine

For an IPM which generates power, the turbomachine compressor, spool, and turbine are all rotating components which might be suitable for integration with the rotor of the electric machine. However, the low radius of the spool limits the EM tip speed and, as will be shown in Section 2.3, a low tip speed limits the achievable IPM specific power. The spool is therefore eliminated as a location for integration, which leaves the compressor and turbine for the IPM architecture.

A first consideration for integrating an EM with either a compressor or turbine is the environmental temperatures for these components. A standard compressor inlet temperature is 15°C at sea level and the outlet can reach temperatures on the order of 300°C depending on the compressor pressure ratio. The turbines, on the other

hand, have typical inlet temperatures of about 1600°C.

The maximum operating temperatures of current electric machine materials are comparatively low. Typical winding insulations only operate up to 200°C and magnet adhesives are generally limited to 260°C [33]. Therefore, short of using exotic, unconventional materials that are expensive and difficult to work with, electric machines are generally limited to around 200°C environments.

With this EM temperature limitation, the turbine is a challenging location for integration due to its gas temperatures greatly exceeding 200°C. The gas temperatures of the compressor, however, are comparable to the temperature limits of the EM. However, since the outlet temperatures can reach as high as 300°C, special attention is required to the thermal design to insulate critical electric machine components from the hot gas temperatures. In addition, since the inlet gas temperature of a compressor is low, it may be feasible to bleed air from the compressor to cool the electric machine. This concept of bleeding air for EM cooling purposes could potentially eliminate the mass and complexity of a liquid cooling system and it is considered in further detail in Chapter 3.

2.2.3 IPM Architecture Concepts

Based on the gas path and rotor geometry, three integrated stage designs are conceptualized: the radial external, radial internal, and axial designs. In each of these configurations, the EM is integrated with at least one stage of a low pressure compressor. In the *radial external* architecture, shown in Fig. 2-2, an inner rotor electric machine is placed outside of an axial flow turbomachine. The blades are mounted on the rim of the EM and protrude radially inward where the air flows between the rotor and turbomachine stator. The downside to this configuration, which will be discussed further in Section 2.3, is that the tip speed of the turbomachine blades is limited which reduces the turbomachine specific power.

In a *radial internal* architecture, an outer rotor electric machine is placed interior to an axial flow turbomachine. Similar to the inner rotor geometry, the turbomachine blades are mounted on the EM rim but protrude radially outward in this case. This

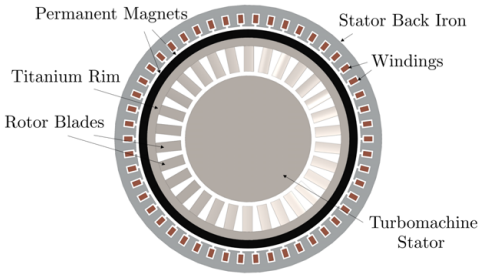

(a) 2D cross-section of the radial external architecture.

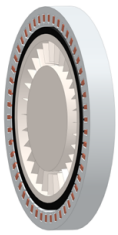

(b) Isolateral view of radial external architecture.

Figure 2-2: In the radial external architecture, the turbomachine is placed radially inside the electric machine.

configuration is shown in Fig. 2-3.

Lastly, in the *axial* architecture, an axial EM rotor is combined with the web and disk of the turbomachine rotor as shown in Fig. 2-4. The blades again protrude radially outward from the rim in this case.

In the next section, these three geometries are compared and further details of the EM are discussed to generate four IPM concepts that can be carried through a trade space analysis.

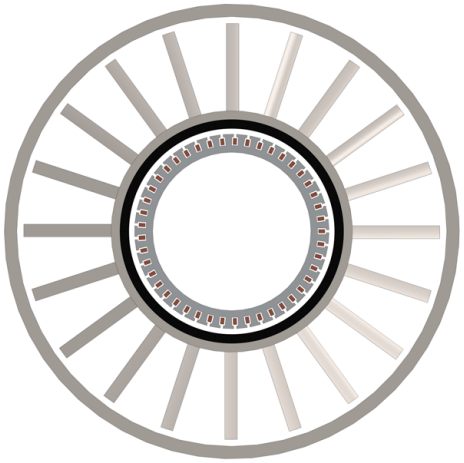

(a) 2D cross-section of the radial internal architecture.

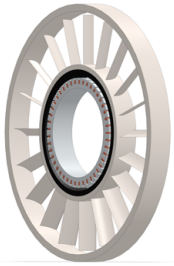

(b) Isometric view of radial internal architecture.

Figure 2-3: In the radial internal architecture, the turbomachine is placed radially outside of the electric machine.

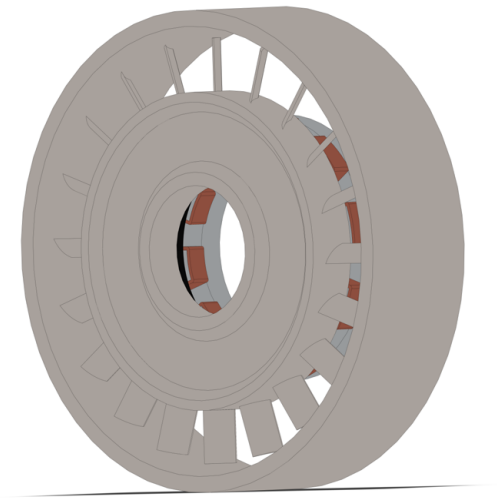

(a) 2D cross-section of the axial architecture.

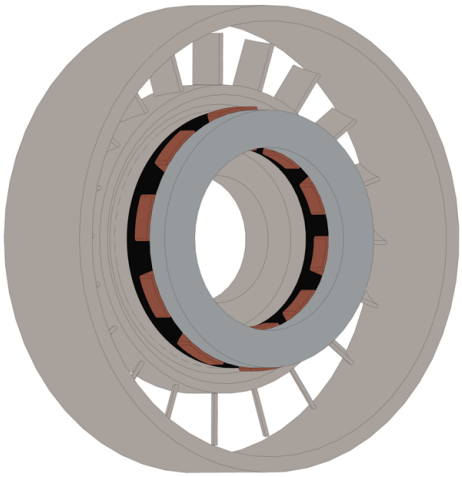

(b) Isolateral view of axial architecture.

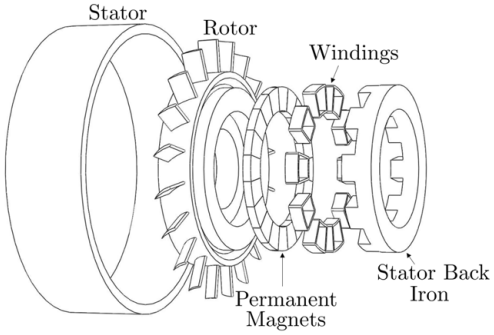

(c) Exploded view of the axial architecture.

Figure 2-4: In the axial architecture, an axial electric machine is integrated into the rotor disc.

2.3 IPM Architecture Down-Selection

In Section 2.2, three IPM architectures are defined based on possible EM geometries and locations for integration within the turbomachine. Further details of the electric machine implementation, such as using permanent magnets versus electromagnets, are considered in this section. This broadens the design space to include 15 combinations of EM types and IPM architectures. The design space is narrowed to just four designs on the basis of simple scaling laws for electric machines and turbomachines. In Sections 2.4 and 2.5, these designs are taken through a trade space analysis to select just one design to take through a conceptual design stage.

2.3.1 Scaling Laws

First, scaling laws based on first principles are derived for the turbomachine blades. Second, scaling laws are derived for the electric machine. These scaling laws reveal two important parameters for the scaling of both turbomachine and EM specific power: tip radius, r_t, and mechanical rotational speed, Ω. The separate scaling laws are integrated to obtain scaling laws for the integrated stage concepts.

Turbomachinery Scaling Laws

The turbomachinery scaling laws were originally derived by colleague Yuankang Chen [27] and are briefly summarized here. Only the turbomachine rotors and stators are considered in these scaling laws. Other components, such as the rotor bore or web, affect specific power, but are not considered here because they are included in the support structure.

From the first law of thermodynamics, the turbomachine rotor power is the product of the mass flow through the rotor and the change in stagnation enthalpy. Assuming uniform air flow through a turbomachine rotor with tip radius r_t and hub radius r_h, the mass flow is the product of the density of air, ρ_a, annulus area, and flow velocity, c_x:

$$\dot{m} = \rho_a \pi (r_t^2 - r_h^2) c_x = \rho_a \pi r_t^2 (1 - {\chi_{\text{TM}}}^2) c_x \tag{2.1}$$

where $\chi_{\text{TM}} = r_h / r_t$ is the rotor hub-to-tip radius ratio. Next, the change in stagnation enthalpy and the flow velocity are expressed in terms of common nondimensional turbomachine design parameters known as the work coefficient, ψ, and flow coefficent, ϕ. These coefficients are defined as

$$\begin{aligned} \Delta h_t &= \psi U_m^2 \\ c_x &= \phi U_m \end{aligned} \tag{2.2}$$

where U_m is the tip speed at the mean blade radius, $(r_t + r_h)/2$. The work and flow coefficients are unitless. The stagnation enthalpy, Δh_t, has units of J/kg or m^2/s^2, which is the same as tip speed squared. Similarly, the flow velocity, c_x, has units of m/s, which is the same as tip speed. Combining Eqn. 2.1 and Eqn. 2.2 with the first law of thermodynamics, the rotor power is expressed as a function of tip radius, angular speed, and other turbomachine design parameters:

$$\begin{aligned} P_{\text{turbo}} &= \dot{m} \Delta h_t \\ &= \rho_a \pi r_t^2 (1 - {\chi_{\text{TM}}}^2) c_x \psi U_m^2 \\ &= \rho_a \pi r_t^2 (1 - {\chi_{\text{TM}}}^2) \phi \psi U_m^3 \\ &= \rho_a \pi r_t^2 (1 - {\chi_{\text{TM}}}^2) \phi \psi r_t^3 \left(1 + r_h/r_t\right)^3 \Omega^3 \\ &= \psi \phi \rho_a \pi (1 - {\chi_{\text{TM}}}^2) \frac{\left(1 + \chi_{\text{TM}}\right)^3}{8} r_t^5 \Omega^3 \end{aligned} \tag{2.3}$$

Next, assuming t_b is the average blade thickness and s is the blade pitch, the blade volume, V_{blades}, is approximated as a fraction of the total flow volume,

$$V_{\text{blades}} = \frac{t_b}{s} \left(\pi r_t^2 \left(1 - \chi_{\text{TM}}^2 \right) \ell \right) \tag{2.4}$$

Then, the mass of the turbomachine rotor and stator blades is simply the product of the mass density of the blades, $\rho_{m,blades}$, and the blade volume V_{blades}:

$$m_{\text{turbo}} = \rho_{m,blades} \frac{t_b}{s} \pi (1 - {\chi_{\text{TM}}}^2) \frac{\ell}{r_t} r_t^3 \tag{2.5}$$

The specific power of the turbomachine Ξ_{turbo} is turbomachine power divided by mass:

$$\Xi_{\text{turbo}} = \frac{P_{\text{turbo}}}{m_{\text{turbo}}} = \psi\phi \frac{\rho_a}{\rho_{m,blades}} \frac{(1 + \chi_{\text{TM}})^3}{8 \frac{t_b}{s} \frac{\ell}{r_t}} r_t^2 \Omega^3 \tag{2.6}$$

Therefore, the turbomachine SP increases with tip radius squared and angular speed cubed.

2.3.2 Electric Machine Scaling Laws

Two scaling laws are presented in this subsection: one for radial flux machines, and one for axial flux machines. The radial flux scaling laws cover both outer rotor and inner rotor machines.

Radial Flux Machines

For both inner and outer rotor electric machines, the torque on an electric machine rotor can be expressed as the product of the average electromagnetic shear stress, $\bar{\tau}$, the area of the electromagnetic air gap, $2\pi r_t \ell$, and the tip radius of the rotor which is defined as the airgap radius:

$$T = \bar{\tau} \left(2\pi r_t \ell\right) r_t. \tag{2.7}$$

The mechanical power of the electric machine is then

$$P_{\text{em,radial}} = T\Omega = \bar{\tau}(2\pi r_t l) r_t \Omega = 2\pi \bar{\tau} \left(\frac{l}{r_t}\right) r_t^3 \Omega \tag{2.8}$$

In this simplified EM scaling law, only the masses of the ferromagnetic rotor and stator back irons are considered. Other components such as EM windings or magnets are ignored for now since they are specific to the EM topology and do not scale in as simple of a manner. The rotor back iron of the electric machine must be sufficiently

thick to guide the magnetic flux of half of a pole. The magnetic flux in the back iron of thickness t_{rbi} is

$$\phi_{\text{rbi}} = B_{\text{rbi}} t_{\text{rbi}} \ell \tag{2.9}$$

Similarly, assuming the magnetic flux density is sinusoidal with the azimuth angle, the flux from a pole is

$$\phi_{\text{pole}} = B_{\text{ag}} \frac{2 r_t \ell}{N_p} \tag{2.10}$$

where N_p is the number of rotor poles. The necessary back iron thickness is therefore solved via Eqn. 2.9 and Eqn. 2.10:

$$t_{\text{rbi}} = \frac{B_{\text{ag}}}{B_{\text{rbi}}} \frac{2 r_t}{N_p} \tag{2.11}$$

The thickness of the stator back iron, t_{sbi}, is similarly

$$t_{\text{sbi}} = \frac{B_{\text{ag}}}{B_{\text{sbi}}} \frac{2 r_t}{N_p}. \tag{2.12}$$

The rotor and stator thicknesses can be minimized by sizing them such that their flux densities, B_{rbi} and B_{sbi}, are close to the saturation levels of their materials, B_{sat}. For a high performance ferromagnetic material such as iron cobalt, the saturation flux density is close to 2.1 T. As evident from Eqns. 2.11 and 2.12, increasing the number of poles reduces the back iron thickness and hence mass. However, this model does not capture the fact that this also increases the electrical frequency and magnet-to-magnet flux leakage. Increasing electrical frequency increases core loss, proximity and skin effect losses in the windings, and permanent magnet losses, if applicable. Therefore there is a trade-off between mass and efficiency when choosing the number of poles in practice.

Assuming the total component thickness is much smaller than the tip radius, the electric machine volume is approximated as an annular cylinder with mean radius r_t, length ℓ, and thickness $(t_{\text{rbi}} + t_{\text{sbi}})$. The mass is simply this volume times the mass

density of the ferromagnetic material, as shown in Eqn. 2.13.

$$\begin{aligned} m_{\text{em,radial}} &= \rho_{m,em} 2\pi r_t \ell \left(t_{\text{rbi}} + t_{\text{sbi}}\right) \\ &= \rho_{m,em} 8\pi r_t^2 \ell \left(\frac{B_{\text{ag}}}{B_{\text{sat}} N_{\text{p}}}\right) \end{aligned} \tag{2.13}$$

Combing Eqns. 2.8 and 2.13, the specific power of the electric machine, Ξ_{em}, is then:

$$\Xi_{\text{em,radial}} = \frac{P_{\text{em,radial}}}{m_{\text{em,radial}}} = \frac{\bar{\tau}\Omega}{4\rho_{m,em}\left(\frac{B_{\text{ag}}}{B_{\text{sat}} N_{\text{p}}}\right)} \tag{2.14}$$

Similar to the turbomachine rotor blades, the radial flux electirc machine SP scales proportional to speed. However, unlike the turbomachine, this SP is independent of tip radius.

Axial Flux Machines

The scaling law for an axial flux EM is derived in a similar manner to that of a radial flux EM. Due to the different flux path, the shear stress interface has a different area than that of a radial machine and the total moment is calculated by integrating the shear stress over this area

$$\begin{aligned} T &= \int_0^{2\pi} \int_{r_i}^{r_o} \bar{\tau} r \left(r dr d\theta\right) \\ &= 2\pi\bar{\tau}\left[\frac{r_o^3}{3} - \frac{r_i^3}{3}\right] \end{aligned} \tag{2.15}$$

The average shear stress used for the torque in Eqn. 2.15 is the average in both the azimuthal and radial directions. The power is simply the torque times rotational speed:

$$P_{\text{em,axial}} = \bar{\tau}\frac{2\pi}{3}(r_o^3 - r_i^3)\Omega \tag{2.16}$$

The thickness of the rotor back iron is again set by equating the flux carried in the back iron with the flux from half a pole:

$$t_{\text{rbi}} = \frac{B_{\text{ag}}}{B_{\text{rbi}}}\frac{\pi\left(r_o + r_i\right)}{N_p} \tag{2.17}$$

and

$$t_{\text{sbi}} = \frac{B_{\text{ag}}}{B_{\text{sbi}}} \frac{\pi \left(r_o + r_i\right)}{N_p} \tag{2.18}$$

where a sinusoidal flux density in the airgap is again assumed. If both the back irons are sized for saturation, or $B_{\text{sbi}} = B_{\text{rbi}} = B_{\text{sat}}$, then the electric machine mass is calculated as an annular cylinder of back iron with inner and outer radii, r_i and r_o, respectively, and length $(t_{\text{rbi}} + t_{\text{sbi}})$:

$$\begin{aligned} m_{\text{em,axial}} &= \rho_{m,em} \pi (r_o^2 - r_i^2)(t_{\text{rbi}} + t_{\text{sbi}}) \\ &= \rho_{m,em} \pi (r_o^2 - r_i^2) \left(r_o + r_i\right) \left(\frac{B_{\text{ag}}}{N_{\text{p}} B_{\text{sat}}}\right) \end{aligned} \tag{2.19}$$

Combining Eqns. 2.16 and 2.19 The specific power of the electric machine $\Xi_{\text{em,axial}}$ is then:

$$\begin{aligned} \Xi_{\text{em,axial}} &= \frac{P_{\text{em,axial}}}{m_{\text{em,axial}}} \\ &= \frac{1}{3} \frac{r_o^2 + r_o r_i + r_i^2}{r_o^2 + 2 r_o r_i + r_i^2} \frac{1}{\frac{B_{\text{ag}}}{N_{\text{p}} B_{\text{sbi}}}} \bar{\tau} \Omega \\ &= \frac{1}{3} \frac{\chi_{\text{em}}^2 + \chi_{\text{em}} + 1}{\chi_{\text{em}}^2 + 2 \chi_{\text{em}} + 1} \frac{1}{\frac{B_{\text{ag}}}{N_{\text{p}} B_{\text{sat}}}} \bar{\tau} \Omega \end{aligned} \tag{2.20}$$

where $\chi_{\text{em}} = \frac{r_o}{r_i}$. In the limiting case where $r_o = r_i$, then Eqn. 2.19 collapses to Eqn. 2.14. In all practical cases, χ_{em} will be greater than one. Therefore, if all other parameters are held constant, the axial electric machine SP will be lower than that of the radial EM.

2.3.3 Integrated Architecture Scaling

The specific power scaling of the different integrated architectures is derived by combining the scaling of the turbomachinery and electric machines derived above. The total specific power for the integrated architecture is

$$\Xi_{\text{IPM}} = \frac{P_{\text{IPM}}}{m_{\text{em}} + m_{\text{turbo}}} \tag{2.21}$$

This total SP can be expressed in terms of the individual EM and TM SPs as shown in Eqn. 2.22 below. Therefore, maximization of the total integrated prime mover specific power is equivalent to minimization of each of the electric machine and turbomachine SPs.

$$\Xi_{\text{IPM}} = \frac{1}{\Xi_{\text{em}}^{-1} + \Xi_{\text{turbo}}^{-1}} \tag{2.22}$$

Radial Internal and External

The specific power of both the radial internal is derived by combining Eqns. 2.6, 2.14, and 2.22:

$$\Xi_{\text{radial}} = \Omega \left[\frac{\bar{\tau}\Omega}{4\rho_{m,em}\left(\frac{B_{\text{ag}}}{B_{\text{sat}}N_{\text{p}}}\right)} + \frac{1}{\psi\phi}\frac{\rho_{m,blades}}{\rho_a}\frac{8\frac{t_b}{s}\frac{l}{r_t}}{(1+\chi_{\text{TM}})^3}\frac{1}{U_t^2} \right]^{-1} \tag{2.23}$$

Since the radial EM scaling law is independent of whether the EM rotor is on the inside or outside, the radial external architecture has an identical form. The SP of both radial architectures scale linearly with rotational speed. Assuming identical electric machine designs, the two radial architectures will differ in the turbomachine SP. Specifically, the achievable tip speed, U_t, is different.

Axial

The axial IPM specific power is derived by combining Eqns. 2.6, 2.20, and 2.22. Like the radial IPM architectures, the axial IPM SP increases linearly with rotational speed. The specific power of the axial machine is similar except that the electric machine scaling differs from that of the radial architectures.

$$\Xi_{\text{axial}} = \Omega \left[\frac{1}{3}\frac{\chi_{\text{em}}^2 + \chi_{\text{em}} + 1}{\chi_{\text{em}}^2 + 2\chi_{\text{em}} + 1}\frac{\bar{\tau}}{\frac{B_{\text{ag}}}{B_{\text{spi}}N_{\text{p}}}} + \frac{1}{\psi\phi}\frac{\rho_{m,blades}}{\rho_a}\frac{8\frac{t_b}{s}\frac{l}{r_t}}{(1+\chi_{\text{TM}})^3}\frac{1}{U_t^2} \right]^{-1} \tag{2.24}$$

These architectures do not yet consider the type of electric machine that will be integrated with the turbomachinery. The next section reviews different EM topologies

feasible for aerospace applications. Pros and cons of each topology are evaluated to down-select to the topologies that merit further study for the IPM design.

2.3.4 EM Topologies for Integration

Figure 2-5, adapted from Ref. [3], shows various EM configurations that are potentially suitable for aerospace applications and that were initially considered for the IPM. This list is not exhaustive, but summarizes the more common EM topologies that could be used in aerospace applications.

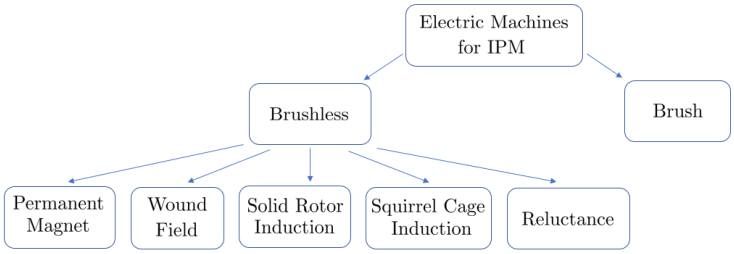

Figure 2-5: Various EM topologies were considered prior to beginning the detailed trade analysis [3].

The EM topologies are first separated into two categories: brushless and brush machines. In brush machines, electricity is conducted from a stationary carbon contact (i.e., brush) on the stator to rotating slip rings attached to the rotor. The issue with brushes is that they degrade fast and spark [34]. During World War II, the rapid deterioration of the brush lead to failure of the DC generators in high-altitude bombers, which in part motivated the development of the brushless motors [34]. Therefore, for an aerospace application - where machine life is critical and sparking is unacceptable - these brush-type machines are excluded from further consideration.

The brushless category consists of a variety of machines: wound field, permanent magnet, squirrel cage induction, solid rotor induction, and reluctance machines. Both the wound field and permanent magnet machines are synchronous machines. The difference between the two is that wound field machines have electromagnets on both the stator and rotor, whereas permanent magnet machines have PMs on either the

stator or rotor, with the latter being far more common. Most reluctance machines are operated to be synchronous via power electronics.

Both the squirrel cage and solid rotor induction machines are asynchronous machines in which the rotor leads or lags the stator depending on whether the machine is operating as a generator or motor, respectively. The coated, solid rotor induction machine, in which a solid copper layer surrounds ferromagnetic material, offers both relatively high efficiency and high tip speed [6].

There are therefore six EM types that were considered for the IPM: wound field synchronous, reluctance, solid rotor induction, squirrel cage induction, and permanent magnet synchronous machines. The following subsections describe the pros, cons, and feasibility of these different machines for the IPM architecture.

Wound Field Synchronous Machine

Wound-field synchronous machines (WFSMs) are used extensively as starter generators in commercial aircraft such as the Boeing 777, Boeing 787, Airbus 340, and Airbus 380 [35]. In a WFSM, separate electromagnets are used on the rotor and stator to generate magnetic fields at synchronous speed. Although WFSMs have simple control, fail-safe operation, and a precedent for application in aerospace, the electromagnet in the WFSM rotor generates comparatively high loss to permanent magnets in a PMSM machine. Therefore, the WFSM cannot compete with PM motors on the basis of efficiency or specific power except perhaps at very high power levels where the cost of PMs may become prohibitive. In addition, at high power levels, the losses in the field winding are relatively small due to the larger WFSM size and the electromagnets can produce higher flux densities than permanent magnets.

To achieve brushless excitation on the rotor side, one solution is to place a rotating diode rectifier on the WFSM rotor shaft [36]. This rotating diode rectifier limits the maximum speed, adds mass to the WFSM system, and therefore limits the maximum SP of the WFSM. Other solutions for exciting the WFSM, such as using a separate permanent magnet synchronous generator, likewise limit the maximum achievable SP of the WFSM due to the heavy mass of this generator.

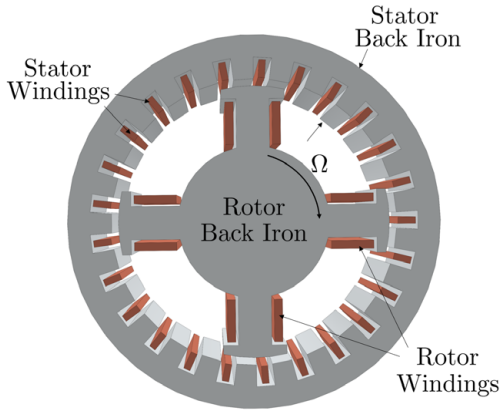

(a) 2D cross-section of a wound field synchronous machine.

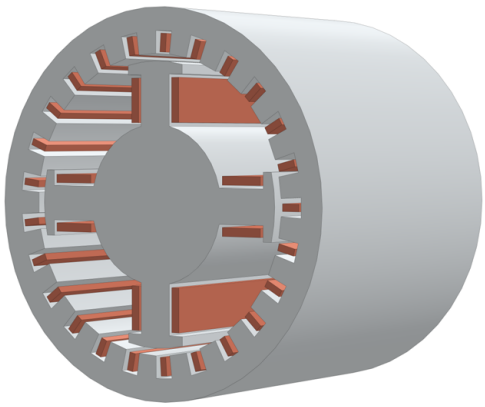

(b) Isolateral view of the WFSM.

Figure 2-6: In a wound field synchronous machine, both the rotor and stator have windings. The rotor must be excited with a separate component not shown here.

Reluctance Machine

Reluctance machines have been used as starter generators in military aircraft such as the Lockheed Martin F-22 [37] in the early 2000s. An attractive feature of the reluctance machine is its simple construction: both the stator and rotor are made entirely of ferromagnetic material, with an electromagnet wound only on the stator side. Construction of these reluctance machines are therefore cheap. In addition, this simple structure allows the reluctance machine rotor to operate at high temperatures.

Due to non-sinusoidal waveforms, reluctance machines require more complicated power electronics than the other EM types. In addition, the salient pole structure of the reluctance machine poses several disadvantages. These salient poles generate increased windage loss and also mechanically limit the maximum tip speed of the reluctance machine due to stress concentration in these poles. Reluctance machines also tend to have low efficiencies compared to solid rotor induction and permanent magnet machines.

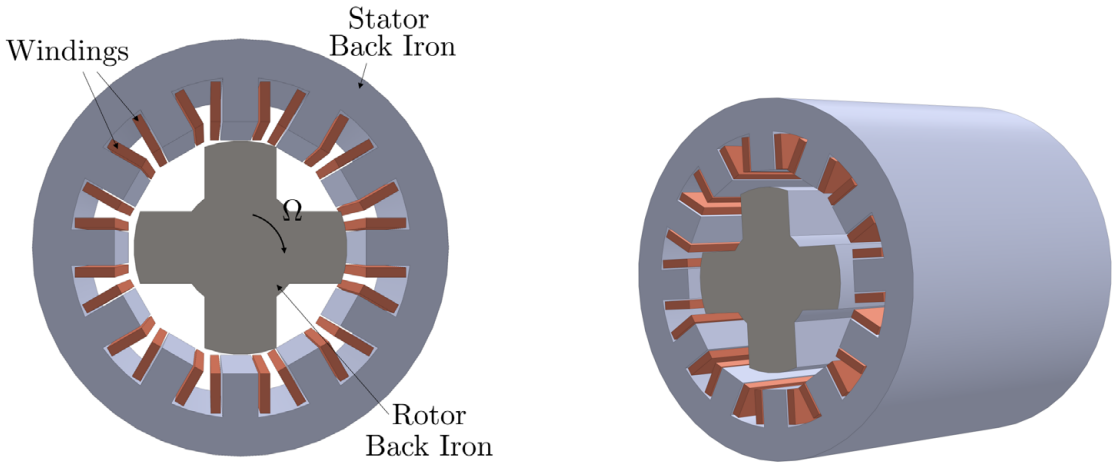

(a) 2D cross-section of a variable reluctance machine.

(b) Isolateral view of the variable reluctance machine.

Figure 2-7: In a variable reluctance machine, only the stator has windings. Torque is generated due to the saliency (non-uniformity) of its rotor structure.

Induction Machines

In an induction machine, the stator windings generate a magnetic field which induces currents in the rotor. The rotor currents in turn establish a magnetic field which interacts with the stator field to generate torque. Two types of induction machines are the squirrel cage induction machine and solid rotor induction machine. In a squirrel cage induction machine, conductive material is embedded into grooves in the ferromagnetic rotor or stator and connected at the axial ends of the machine via conductive rings. In a solid rotor induction machine, the rotor is a solid cylinder of ferromagnetic material which may be coated with a conductive material such as copper. Although just having this ferromagnetic rotor is sufficient to generate torque, a thin conductive shell may be added for improved performance [6].

Due to its simple cylindrical rotor structure consisting of just ferromagnetic and conducting material, the solid rotor induction machine offers some of the greatest EM tip speeds at high power. Induction machines can be operated over a much wider range of speeds than permanent magnet machines at high efficiency. However, PM machines reach higher peak efficiencies due to lower rotor losses. The higher efficiency of the PM machine may be important in an aerospace application where the majority

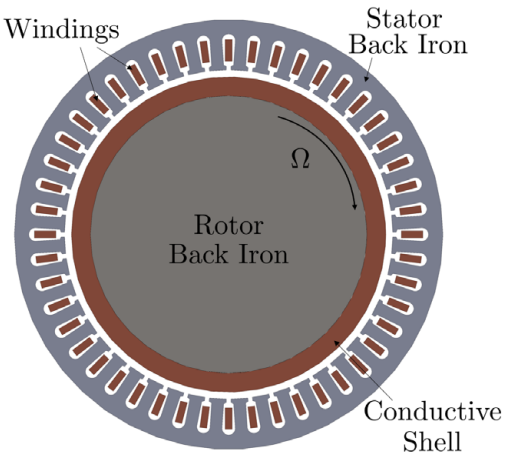

(a) 2D cross-section of a solid rotor induction machine.

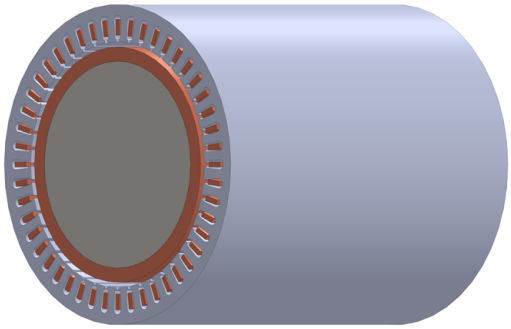

(b) Isolateral view of the solid rotor induction machine.

Figure 2-8: In the solid rotor induction machine, the stator has windings and the rotor consists of a solid conductive shell surrounding the rotor back iron.

of the mission is at cruise. In addition, the solid rotor induction machine efficiency limits its maximum achievable specific power.

Permanent Magnet Machine

The components and layout of a permanent magnet machine were shown previously in Figs. 2-1. For fixed volume, permanent magnets generate comparatively large magnetic fields to those of electromagnets. Although the PMs are subject to losses due to eddy currents from the slots modulating the stator magnetic field, these losses are manageable via careful airgap sizing and slot design. The result is that PM machines are typically more efficient and power dense than the other machine types.

One drawback to permanent magnet machines is that the permanent magnets have a maximum operating temperature beyond which the PMs experience irreversible demagnetization. In addition, the PMs have a temperature limit (the Curie temperature) at which point they are fully demagnetized. This demagnetization is irreversible in that once the temperature is reduced, the magnetization does not return. Second, the PMs are typically secured to the rotor via an adhesive. This adhesive can limit the achievable tip speeds in PM machines. Sleeves made out of conductive materials

such as Titanium or fibers such as carbon or glass may be used to secure the magnets, but these add mass and possibly eddy current losses. In an inner rotor configuration, these sleeves could also expand the air gap, reducing torque. Lastly, unlike electromagnets, PMs are not controllable, which can lead to safety issues because the induced voltage at the power electronics terminals is non-zero.

2.3.5 EM Topology Summary

At a high-level, the benefits and drawbacks of the different EM types are summarized in Table 2.1.

Table 2.1: Comparison of candidate EM topologies.

Machine Type	Benefits	Drawbacks
Wound-field synchronous machines	• Proven EM technology in aerospace applications	• Additional exciter machine required • Ohmic losses generated from rotor winding
Reluctance machines	• Ease of manufacture • No winding on rotor reduces total Ohmic loss	• Poor efficiency due to nonsinusoidal waveforms • Complex power electronics control
Induction machine	• High tip speeds obtainable • Wide speed range operation	• Low power factor and efficiency compared to PM machines • Performance is load dependent which is not ideal for a generator
Permanent magnet machines	• High efficiency	• Risk of irreversible demagnetization • Risk of damaging power electronics during short circuit • Risk of fire in event of insulation failure

2.3.6 IPM Down-Selection

Turbomachine tip speeds in modern jet engines reach up to 450 m/s at takeoff [38]. However, a survey of electric machines found that maximum reported EM rotor tip speeds reach between 200 to 400 m/s depending on EM rotor type (e.g., permanent magnet, induction, etc.) [6]. These maximum reported tip speeds are used to down select to the most promising IPM architectures.

Table 2.2: Highest surveyed tip speeds of different electric machine types summarized from Ref. [6].

Machine Type	**Tip Speed** (m/s)
Solid Rotor Induction Machine	400
Surface Permanent Magnet Machine	300
Solid Caged Induction Machine	236
Switched Reluctance Machine	210

The derived EM scaling laws and surveyed EMs do not indicate a difference in specific power between the inner rotor and outer rotor EM designs. However, the placement of the turbomachine compressor on the inside or outside of the electric machine will affect the turbomachine SP based on the scaling from Section 2.3.1. Specifically, the compressor tip speed is limited to below its optimized tip speed of 450 m/s in a turbofan if it is to be placed interior to the electric machine.

For example, based on the maximum tip speeds from Ref. [6], an IPM with a solid rotor induction machine external to the compressor will limit its tip speed to a maximum of 400 m/s. Since the turbomachine specific power scales with tip speed squared, this is a projected $1-(400\,m/s)^2\,/\,(450\,m/s)^2 = 21\%$ reduction in its SP. For permanent magnet machines with a maximum reported tip speed of 300 m/s, this tip speed mismatch would result in a projected 66% reduction. A 72.5% turbomachine compressor SP reduction is projected for a squirrel cage induction machine with a maximum reported tip speed of 236 m/s. Lastly, for the reluctance machine with a maximum reported tip speed of 210 m/s, this would result in an 80% reduction in the turbomachine compressor SP. These estimates may be optimistic since they assume the tip speeds for standalone electric machines are still achievable when the rotors

are loaded with compressor blades.

Since the electric machine tip speed limit is anticipated to penalize the turbomachine specific power by 21% even with a high speed, coated solid rotor induction machine, the radial external IPM architecture is excluded from a more detailed study. Even if the electric machine is placed internal to the compressor, the squirrel cage induction and reluctance machine tip speeds are sufficiently low such that they are expected to limit the turbomachine compressor blade tip speeds and thus its specific power. Although a 250 kW switched reluctance machine developed by GE Corporate Research & Development was used as an integrated starter generator for a more electric aircraft intiative, this reluctance machine is estimated to only reach 185 m/s tip speed based on the 6.25 inch rotor diameter and 22,224 rpm rotational speeds reported in Ref. [39] and Ref. [40], respectively.

Therefore, only the coated, solid rotor induction and surface permanent magnet machines are considered in the trade study of this chapter due to their higher tip speeds. If the IPM optimizes to a sub-300 m/s tip speed, the squirrel cage and switch reluctance machines could be viable.

2.3.7 Summary of IPM Architecture Selection

Ultimately, two EM topologies were selected for the IPM design space exploration as having the most potential from a specific power point-of-view: the solid rotor induction and permanent magnet machines. Of the three different IPM geometries, the radial external architecture SP was eliminated due to the maximum EM tip speed limiting the compressor or fan tip speed and resulting in a low IPM specific power. Therefore, only four architectures were selected for a more detailed study:

1. radial internal solid-rotor induction,
2. radial internal permanent magnet,
3. axial solid-rotor induction, and
4. axial permanent magnet architecture.

In the next section, more detailed models for each of these architectures are used in a trade space exploration. A single architecture with the most promise is selected in Section 2.5.

2.4 Design Space Exploration

With four integrated prime mover architectures selected for a more detailed analysis, a framework was developed to assess the feasibility and performance of each. This framework focuses on the EM design only to identify a single IPM architecture for a more detailed design in Chapter 3. The framework, models, and parameters were developed in collaboration with colleague Yuankang Chen [27]. The presented results are unique to this thesis.

2.4.1 Framework

Based on a set of material and design parameters described in the following subsections, this framework first sizes the electric machine by calculating the maximum EM shear stress that can be produced at each tip radius. This calculation accounts for the magnetomotive force (MMF) drop across the steel. The machine design therefore closes at the tip radius where the both shear stresses match. The framework then calculates the mass of the different electric machine components (windings, steel, and magnets), and the ohmic, core, and windage losses. Lastly, these losses in the rotor and stator are used to generate the output of the framework: **specific power** and **heat flux**. The outcome of this design space exploration is a comparison of the magnitudes and trends of SP and heat flux for the four candidate architectures. In the next subsections, the models, performance metrics, material assumptions, and input parameters of the framework are discussed.

Models

The detailed sizing and loss models for all four machine types are presented in Appendix A. At a high level, the EMs are sized by expanding the electromagnetic shear

stress as the product of the air gap flux density from the rotor and the stator surface current density. This approach is based on that from Ref. [41]. From the Maxwell stress tensor [41], the average electromagnetic shear stress in the air gap, $\bar{\tau}$, is expressed as the product of the magnitudes of the air gap flux density, B_s, and the stator surface current density, K_s:

$$\bar{\tau} = \frac{B_s K_s}{2}. \tag{2.25}$$

The air gap flux density is produced on the rotor side either by induced currents in the conductive shell or permanent magnets, depending on machine type. The surface current density, on the other hand, is produced on the stator side. The currents in the slot windings are approximated as an equivalent current sheet at the air gap interface whose magnitude depends on the current density of the windings. This equivalence is expressed as

$$K_s = (1 - f_{\text{tooth}}) J_m t_{\text{tooth}}, \tag{2.26}$$

where f_{tooth} is the fraction of a pole occupied by the stator tooth, J_m is the slot current density, and t_{tooth} is the stator tooth thickness, and approximately the winding thickness. To maximize electromagnetic shear stress, this surface current density is assumed to be the minimum of two limits: the tooth tip magnetic saturation limit, $K_{s,sat}$, which varies between machine type, and a spatial limit, $K_{s,sp}$, due to the maximum winding thickness possible. The parameter $K_{s,sp}$ varies depending on magnetic flux direction.

The permanent magnet machine is sized by considering the remanent flux density of the PMs and sizing them to produce the desired shear stress while taking into account MMF drops across the teeth and back iron. The induction machine is sized similarly, except the air gap flux is generated by the induced currents in the rotor and has a different form. The details of both sizing models are available in Appendix A.

Performance Metrics

As mentioned previously, the specific power is defined as output power divided by machine mass:

$$\Xi_{\text{em}} = \frac{P_{\text{em}}}{m_{\text{em}}} \tag{2.27}$$

where m_{em} is the EM mass. For the induction machine, this mass consists of the stator back iron, stator teeth stator windings, conductive shell on the rotor, and the rotor back iron. For the PM machine, this mass consists of the stator back iron, stator teeth, stator windings, rotor permanent magnets, and rotor back iron. Since the specific power uses output power as opposed to input power, machines with low mass but high losses are also penalized since they need to be rated for greater input powers.

Without a thermal model to estimate hotspot temperatures in the IPMs, the thermal feasibility of the different architectures is unknown. Instead, heat flux is used as a surrogate for a hotspot temperature model. A large heat flux represents a machine that is challenging to cool[1]. Therefore, the two performance metrics of the design space exploration framework in this chapter are specific power and heat flux.

The heat flux metric was developed by colleague Yuankang Chen and is estimated by considering the losses in the EM and dividing by the available cooling surface area. The total machine heat flux is the lost power divided by total cooling surface area A:

$$\frac{P_{loss}}{A} = U_t \frac{G_E}{A/2\pi r_t^2}(1-\eta)\bar{\tau} \tag{2.28}$$

Equation 2.28 indicates that the heat flux scales linearly with tip speed, electromagnetic shear stress, machine geometry, and inefficiency. Since specific power also scales linearly with tip speed and shear stress, these variables trade specific power and cooling requirements. The machine geometry is ultimately limited by rotordynamics and thermal constraints, with shorter machines presenting rotordynamic challenges and longer machines limiting heat extraction from the center of the machine. Lastly

[1]The actual hotspot temperatures are considered in Chapter 3 for the selected architecture.

$A/2\pi r_t^2$ is the fraction of the EM surface area utilized for cooling. As expected, the heat flux decreases when a greater fraction of the EM surface area is available for cooling.

Material Assumptions

In this trade space analysis, the electric machines are assumed to use commercial materials available today. The windings and, in the case of the solid rotor induction machine, the conductive shell are both assumed to be made of copper. For both the permanent magnet and induction machines, the stator and rotor back irons are assumed to be made of an iron cobalt material (e.g., Hiperco 50) which offers high saturation flux density and low core loss - two desirable properties for high specific power EMs. Lastly, the permanent magnets for the permanent magnet synchronous machine case are made from neodymium-iron-boron (NdFeB) due to their high remanent flux density. If the temperatures in the IPM are unsuitable for NdFeB, then Samarium Cobalt (SmCo) permanent magnets may be a viable alternative. This alternative is considered in Chapter 3. The SmCo magnets offer a higher Curie temperature, but have slightly lower remanent flux density, greater cost, and rely on cobalt which is a strategic metal. The material parameters for the framework are summarized in Table 2.3.

Table 2.3: Summary of material properties.

Material Parameter	**Assumed Value**
Stator Winding Resistivity	$1.68 \cdot 10^{-8}\ \Omega \cdot m$
Stator Winding Mass Density	8940 kg/m^3
Copper Rotor Shell Resistivity	$1.68 \cdot 10^{-8}\ \Omega \cdot m$
Copper Rotor Shell Mass Density	8940 kg/m^3
Rotor Shell Magnetic Permeability	1
Ferromagnetic Core Mass Density	8110 kg/m^3
Ferromagnetic Core Saturation Flux Density	2.4 T
Ferromagnetic Core Magnetic Relative Permeability	18
Permanent Magnet Mass Density	7400 kg/m^3
Permanent Magnet Remanent Flux Density	1.2 T

Design Parameter Assumptions

To simplify the design space for these initial trade studies, a few design parameters that might be free in a detailed design are fixed. These are summarized in Table 2.4 below. The rated power is fixed to 2.5 MW for the results presented in this section because 2.5 MW may be representative of the power of a compressor stage for a small business jet. However, the results from the trade space analysis, discussed in Section 2.5, were found to be consistent at one MW and five MW as well.

Table 2.4: Summary of design parameter assumptions.

Design Parameter	**Assumed Value**
Rated Power	2.5 MW
Stator Tooth Fraction	0.5
Slot Fill Factor	0.5

The stator tooth fraction trades the space available in the stator for windings with the space for the stator teeth composed of ferromagnetic material. A large value leaves no space for conductors and a small value saturates the teeth, which leads to greater core loss and reduced torque. A value of 0.5 is selected for the trade studies based on the optimized permanent magnet machine design from Ref. [17]. This parameter is freed in Chapter 3, but similarly optimizes to about 0.5 which suggests

this is a reasonable value for the trade analysis.

The slot fill factor is the ratio of the winding volume to the total slot volume. A high fill factor is equivalent to having a stator slot composed almost entirely of copper. Realistically, this parameter is less than one because the winding insulation and space between Litz winding strands take up space in the slot. This parameter affects the efficiency of the machines since it modifies the winding resistance and thus the Ohmic losses. A value of 0.7 is the upper end of achievable slot copper fill factors for rectangular Litz bundles as presented in Ref. [42]. A value of 0.5 is used in these trade studies based on estimates received from winding manufacturers early in the design process.

2.4.2 Trade Studies

The input parameters to the assessment framework, their nominal values, and the range over which they are examined for the design trade study are presented in Table 2.5. The usage of these input parameters in the EM models may be found in the Appendix A. Nominal values were chosen as reasonable starting points for the sweeps.

Table 2.5: Design trade study: list of input parameters

	Units	**Nominal Value**	**Range Examined**
Tip Speed, U_t	m/s	300	200 - 400
Number of Poles, N_p	-	10	6 - 14
Slot Current Density, J_m	A/mm^2	10	5 - 12
Electric Machine Geometry, G_E	-	0.3	0.3 - 0.7
Air Gap Thickness / Tip Radius, g/r_t	-	0.01	0.01 - 0.015

A maximum tip speed of 400 m/s is selected based on the maximum surveyed EM tip speed from Ref. [6]. Although PM machines have been observed at 300 m/s, a lower bound of 200 m/s is selected in anticipation that other constraints such as rotordynamics could limit the realizable tip speed of multi-megawatt, integrated machines. The pole pair count is limited between 6 to 14 because this range covers

electrical frequencies up to 2000 Hz, the latter of which aligns with proposed high SP electric machines such as that from University of Illinois Urbana-Champaign in Ref. [18].

A survey from Ref. [2] shows which cooling techniques are typically used with different slot current densities and this is summarized in Table 2.6. These current densities are estimated as the total current carried through a slot divided by the total slot area (i.e., copper area plus insulation and potting areas). The liquid bathing method consists of placing the whole electric machine in dielectric liquids for cooling purposes [2]. In the indirect water or oil cooling methods, the lubricant extracts heat from the stator; however, in the direct liquid cooling method, coolant is in contact with the conductors [2]. Primarily the range of forced air is considered in these trade studies since the IPM will ideally be cooled by bleeding compressor air. However, the bottom end of the liquid cooling, current density range is also considered.

Table 2.6: Summary of cooling techniques versus slot current densities [2].

Slot Current Density [$\mathbf{A/mm^2}$]	**Cooling Technique**
5-12	Forced Air
10-15	Indirect Water Cooling
10-15	Indirect Oil Cooling
15-25	Liquid Bathed
15-30	Direct Liquid
> 28	Oil Spray

The electric machine geometry factor, G_E, differs based on whether the machine is in a radial flux or axial flux configuration. For radial flux machines, this geometry factor is the axial length-to-tip radius ratio, ℓ/r_t. For axial flux machines, this parameter is related to the tip radius-to-hub radius ratio and is derived from the heat flux form given in Eqn. 2.28. The exact form of the axial geometry parameter is given in 2.29 below. The lower range of this factor is 0.3 because the axial machine designs do not converge for lower values. The upper range is 0.7 to show the general trends of each machine type, although these values are not realistic.

$$G_E = \frac{(1 - \chi_{\text{em}}^{-3})}{3} \tag{2.29}$$

Lastly, a small air gap increases the risk of the rotor rubbing into the stator. In addition, for a permanent magnet machine, the magnets are exposed to larger asynchronous magnetic fields which increases the magnet eddy current losses. Typical air gap thickness values surveyed are between 0.625 mm for a smaller, lower speed magnet machine [17] to 2 mm for a proposed one megawatt design [18]. For this trade space analysis, it is assumed that the air gap will roughly be proportional to the tip radius since larger machines will likely have greater moments of inertia and require greater clearances. An air gap thickness-to-tip radius ratio of 0.01 to 0.015 is surveyed which corresponds to air gap thicknesses from approximately 1.5 mm to 4 mm.

Tip Speed Scaling

Figure 2-9 shows that the EM specific power scales approximately linearly with tip speed for all EM types. Therefore, it is desirable to push the tip speed as high as structurally possible. This is expected since EM specific power scales with the square root of tip speed cubed. The slope of the axial induction machine in Fig. 2-9 changes at 250 m/s because the stator surface current density is at the saturation limit discussed in Section 2.4.1 for speeds less than 250 m/s, and is unconstrained saturation-wise or spatially for tip speeds greater than 250 m/s. For all tip speeds under consideration, the radial induction machine offers the highest specific power, but it also has the greatest heat flux and will therefore be the most challenging to cool in practice. The second highest performing EM type is the radial PM machine which also has the second highest heat flux. Lastly, both axial machines have the lowest SP but also have much lower heat fluxes as can be seen in Fig. 2-9b.

The slot current density of the axial flux machines can be adjusted to achieve comparable heat fluxes to those of the radial flux machines. When this is performed, the axial flux machines do have comparable specific powers to those of the radial flux machines, but require approximately triple the slot current density. The assumption in this study is that the slot current densities in Table 2.6 are reflective of the cooling techniques required for both axial and radial flux motors. The slot current density

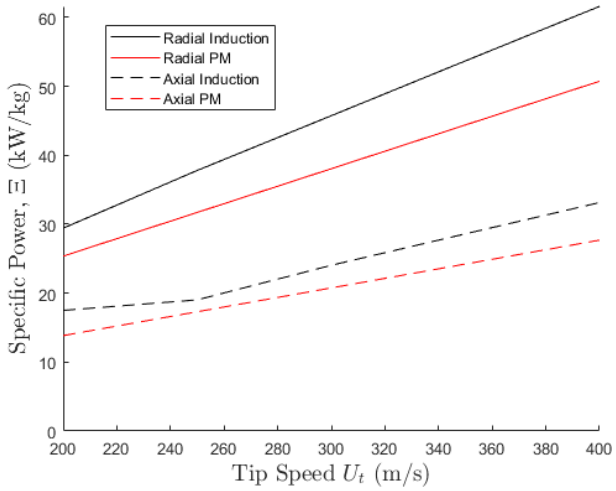

(a) Specific power vs. tip speed.

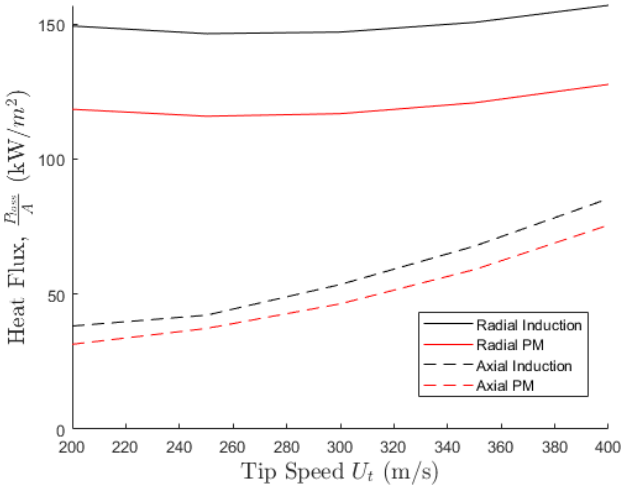

(b) Heat flux vs. tip speed.

Figure 2-9: Tip speed sweeps.

assumption is explored for one architecture in more detail in Chapter 3 for an air cooled, radial flux, tooth-and-slot Halbach array architecture.

The radial induction machine offers approximately 18% greater SP than the radial PM for all tip speeds, but at 30% greater heat flux. The radial induction machine has 3-5 times the heat flux of the axial variants, but 80% greater SP. Therefore the selection of EM architecture is a trade between SP and heat flux, or cooling feasibility. As mentioned in Section 2.4.1, the specific power accounts for efficiency since it uses output power which is lower with greater losses.

Slot Current Density Scaling

The electromagnetic shear stress scales linearly with slot current density as shown via Eqns. 2.25 and 2.26. Therefore increasing slot current density improves EM specific power, but it also increases the cooling requirements of the machine due to increased Ohmic losses.

Figure 2-10a shows the specific power scaling of each of the four machine types with slot current density. Similar to the tip speed scaling study, the radial induction EM has the greatest SP, followed by the radial PM and finally the two axial machines. The axial induction slot again changes due to the surface current density no longer being constrained due to tooth saturation. The SP has a particularly strong scaling with slot current density. This is expected from the simple electric machine SP scaling in Section 2.3.2, which showed that SP scales linearly with electromagnetic shear stress, which in turn scales linearly with slot current density. Therefore a doubling of the slot current density doubles the SP. However, this quadruples the losses for radial machines whose losses are primarily Ohmic. Similar to the tip speed study, the higher SP machine types also have the greater heat fluxes.

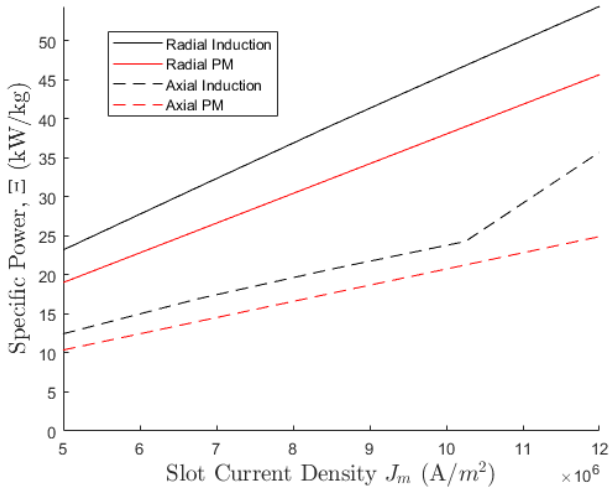

(a) SP vs. slot current density.

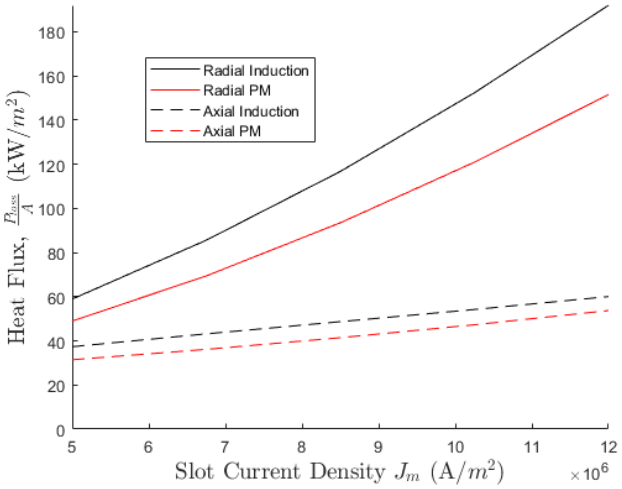

(b) Heat Flux vs. slot current density.

Figure 2-10: Slot current density sweeps.

EM Geometry Scaling

When scaling the electric machine geometry factors which are proportional to heat flux, the radial induction machine still offers the greatest SP with the trade-off of having the greatest heat flux as shown in Fig. 2-11. Unlike those two studies, the axial machines pass the radial PM architecture in SP for high geometric factors while still having lower heat fluxes.

For an axial machine, a large geometry factor, G_E, corresponds to a large tip radius-to-hub radius ratio. Increasing the tip radius-to-hub radius ratio increases

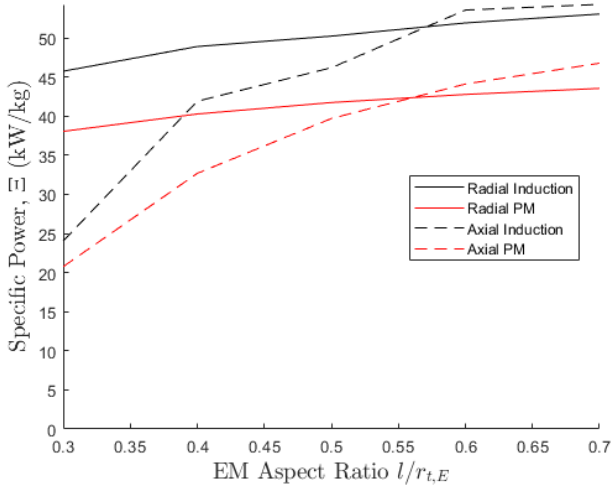

(a) SP vs. EM geometry.

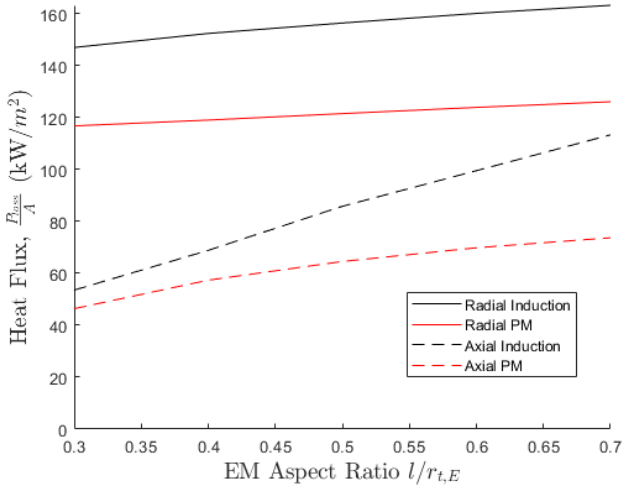

(b) Heat Flux vs. EM geometry.

Figure 2-11: EM geometry sweeps.

the thickness of the IPM rotor which presents structural challenges. In addition, this increases the axial length of the machine because the back iron thicknesses are proportional to the tip radius-to-hub radius ratio. From a practical point-of-view, it is undesirable to design an axial IPM with large aspect ratios because stacking the integrated prime movers in close axial promixity, which is done in conventional turbomachine compressors, would be impossible without increasing the axial length of the turbomachine blades. Similar to the other two studies, the radial induction machine has 20-25% greater SP than the radial PM machine for 30-40% greater heat

flux even across all aspect ratios. The change in slopes is due to the surface current density being constrained due to saturation or due to the stator slots reaching their height limit (i.e., there is no room to grow the slots further radially inwards).

Pole Pair Scaling

The ranking of machines with respect to specific power do not change with increasing the number of pole pairs as shown in Fig. 2-12. However, the axial machines do approach those of the radial PM machine at higher pole pair counts. The specific power increases across all machine types because the back iron thicknesses decreases with greater pole pair numbers. This trend is expected from Eqns. 2.14 and 2.20.

Counter-intuitively, the heat flux of the radial machines actually decreases for increasing pole pair counts. Although the core loss increases with a greater number of pole pairs for all machine types due to increasing electrical frequency, the core volume is also decreasing since less magnetic flux needs to be passed through the rotor and stator back irons. This decreasing volume effect is enough to result in a net reduction in heat flux for the radial flux machines. This is not true for the axial machines, where the heat flux increases with pole pair count. The radial machine heat flux trend could be reversed if the core loss model, which is based on manufacturer data, is inapplicable to machines that operate at the IPM conditions. Regardless, Fig. 2-12 shows that it is desirable to maximize pole pair count. This is studied in more detail in Chapter 3.

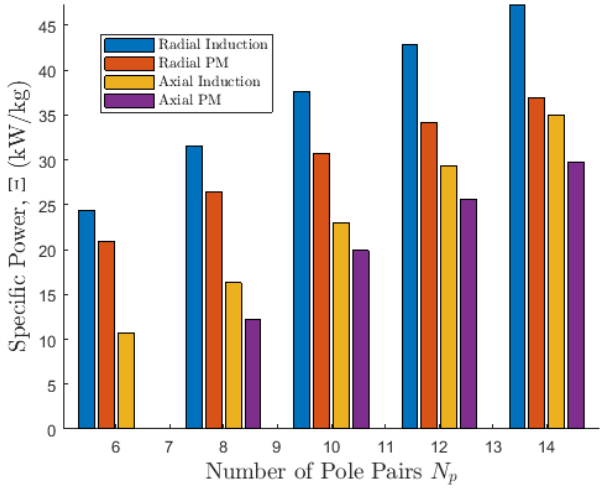

(a) SP vs. number of pole pairs.

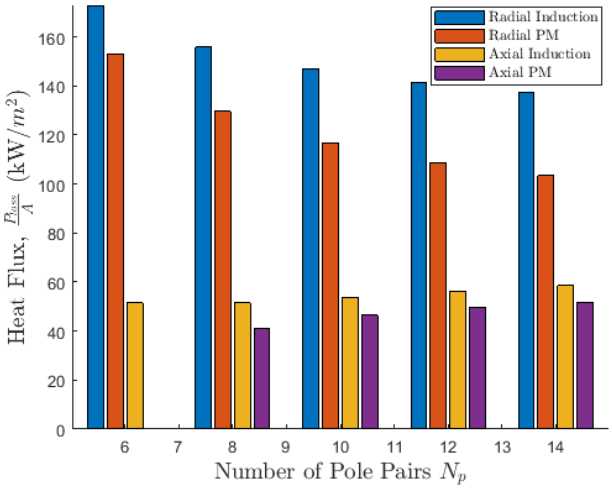

(b) Heat Flux vs. number of pole pairs.

Figure 2-12: EM pole pair sweeps.

Air Gap Thickness Scaling

Since the tip radius differs for all machine types at the nominal point, the air gap-to-tip radius value for each machine will result in a different air gap thickness. For example, an air gap-to-tip radius value of 0.01 corresponds to an air gap thickness of 2.7 mm for the axial PM machine, but just 1.5mm for the radial induction machine. Overall, air gap thicknesses ranged from approximately 1.5 mm to 4.5 mm in these sweeps. Figure 2-13 shows that the machine specific powers and heat fluxes are relatively insensitive to the air gap thickness.

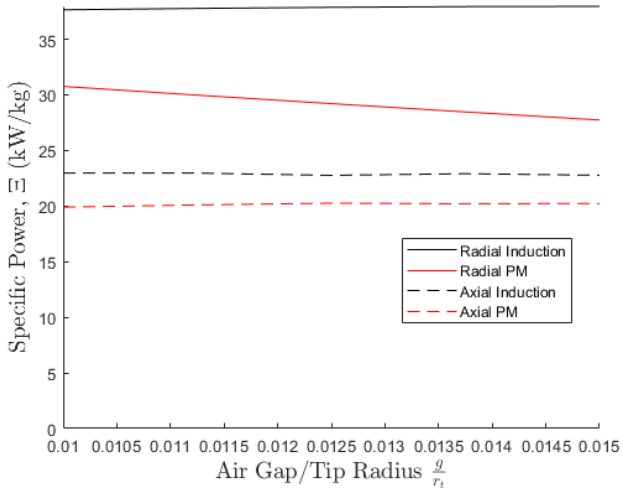

(a) SP vs. air gap thickness-to-tip radius ratio.

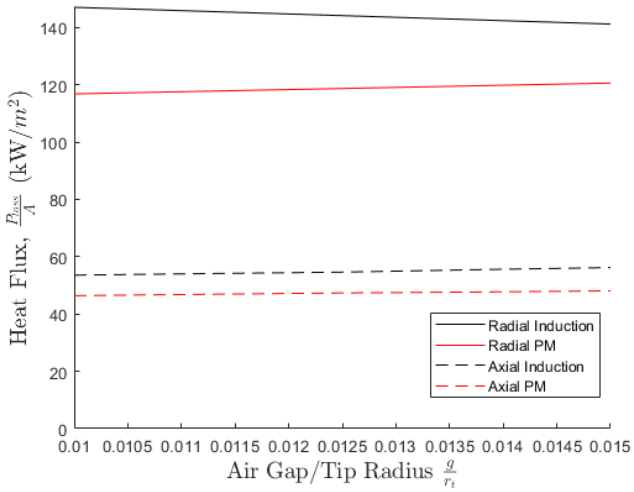

(b) Heat Flux vs. air gap thickness-to-tip radius ratio.

Figure 2-13: Air gap thickness-to-tip radius ratio sweeps.

The results are insensitive to air gap thickness because (1) coarse models are used to estimate the leakage flux of the machine, and (2) the air gap is small relative to the back iron, copper shell, and permanent magnet thicknesses and therefore has negligible impact on mass. However, air gap thickness is considered further in later chapters since it has a major effect on permanent magnet losses, stator flux densities, rotordynamics, and heat transfer which is not captured here.

2.4.3 Trade Study Results

The following trends are observed from the trade studies:

- With the exception of air gap thickness, the electric machine SP increases with increasing tip speed, pole pair count, slot current density, and the electric machine geometry factor. Heat flux behaves similarly with the exception of tip speed, in which case the heat flux is approximately constant for the radial induction and radial PM machines. Therefore, is it desirable to push slot current density, tip speed, pole pair count, and the radial or axial geometric factor to their technological limits.

- For all swept parameters, the radial induction machine offers the greatest SP but also has the greatest heat flux. Radial PM machines have the second greatest SP and heat flux except at high geometric factors, where the axial induction and PM machines surpass it in SP, but with lower heat flux.

- Compared to PM machines, induction machines have 18-25% greater SP, but at 30-40% greater heat flux. The induction machine will always be less efficient than a comparable PM machine as the gap flux for the PM machine is produced without loss in the magnets, but at the cost of resistive loss in the rotor windings for the induction machine.

- Axial flux electric machines have up to 50% lower specific power and heat flux than the radial PM and induction machines, but with 65-80% lower heat fluxes. The lower specific power for axial machines is a result of the reduced effective slot current density due to the trapezoidal shaped slot cross sections, and as such is inherent to the axial flux architecture.

- All electric machine designs around the nominal design points for this trade space analysis are insensitive to air gap thickness due to comparatively large magnet, copper shell, winding, and back iron thicknesses. Air gaps from 1.5 to 4 mm thicknesses appear feasible with the trade space analysis models, but

analysis of its impact on permanent magnet losses, rotordynamics, cooling, and stator flux densities remains.

2.5 Summary of Key Results

The results of the design space exploration are summarized in the design matrix in Table 2.7. The maximum observed EM tip speeds from Ref. [6] are used to select a subset of architectures for the trade study. The reluctance and squirrel cage induction electirc machines are not considered in the trade studies because they operate at approximately half the tip speed of modern turbomachinery, and turbomachine specific power scales proportional to tip speed squared. In addition, the radial external IPM architecture is ruled out since the electric machine will always limit the turbomachine tip speed and hence achievable specific power.

The results of the design trade study show that both axial flux machines have approximately 50% lower specific power than comparable radial machines as a result of their reduced winding area near the rotor hub. However, these machines also have about 25% of the heat flux of the radial machines. With regards to the radial flux machines, the radial induction machine has 30%-40% greater heat flux than its PM counterpart due to the resistive losses generated in the rotor conductive shell, but it also offers 18-25% greater SP. Therefore the decision between axial, radial PM, and radial induction machines is a trade-off between SP and heat flux. The nominal values of the input parameters used in the design trade study are representative of current technology, which suggests that an IPM may be feasible with the materials and technology available today.

Without a model to estimate hotspot temperatures in the EM, a large heat flux at this stage represents the risk of an inability to cool the machine. The radial induction machine is high SP, but high risk. The radial flux PM machine offers medium specific power at medium risk. Lastly, both axial machines offer low SP with low risk. Although the radial flux induction machine losses might not seem significantly greater than those of the radial PM machine, the induction losses occur

Table 2.7: Summary of key results.

Machine Type	**Integration Architecture**		
	Radial Internal	Radial External	Axial
Reluctance	Limits TM tip speed	Limits TM tip speed	Limits TM tip speed
Induction	High tip speed and SP, but high heat flux	Limits TM tip speed	Low SP, but low heat flux
Permanent Magnet	Medium tip speed and SP, with medium heat flux	Limits TM tip speed	Low SP, but low heat flux

primarily in the rotor shell and the rotor is more difficult to extract heat from than the stator. This difficulty arises because one side of the rotor is the compressor gas which, depending on location, is equal to or hotter than the coolant air in the EM. Therefore heat can only be extracted by forcing air through the small airgap. On the other hand, both sides of the stator plus the end windings are available for forced air cooling.

At this stage of the IPM design, the radial flux PM is deemed to be an acceptable option to proceed with for a conceptual IPM design since it offers reasonably high specific power, but it is not as challenging to cool as the radial induction machine. In the event that there is sufficient margin on the hotspot temperatures of the radial PM machine, it might be worthwhile to return and look at the solid rotor induction machine in more detail to achieve greater overall IPM SP. If the radial PM machine were to be thermally infeasible, the axial variants have far lower heat fluxes and would potentially be feasible. Chapter 3 focuses on the conceptual design and analysis of the radial internal PM IPM.

Chapter 3

Integrated Prime Mover Conceptual Design

In Chapter 2, various integrated prime mover architectures were studied and the most promising one with respect to specific power and heat flux was identified. Specifically, the internal radial architecture with a permanent magnet electric machine offers a balance between high performance and medium risk and it was selected to carry through to a conceptual design. The specific permanent magnet machine type used in the Chapter 2 studies was the common surface permanent magnet, tooth-and-slot stator architecture. However, other permanent magnet configurations are possible and are considered in this chapter to potentially improve the performance of the IPM. For example, the permanent magnets can be magnetized in either the radial or azimuthal direction, or the teeth in the stator can be eliminated such as in the design in Ref. [18].

This chapter consists of an additional trade space analysis followed by the conceptual design of the IPM. While only the electric machine was evaluated in Chapter 2, this chapter considers the thermal management system design and performance as well. The trade space analysis in this chapter is used to decide between liquid versus air-cooling as well as to select a specific permanent magnet (PM) electric machine type for the conceptual IPM design.

Four different types of permanent magnet electric machines are introduced in

Section 3.1. Reduced order models for these four types are incorporated into the framework from Chapter 2 and are discussed in Section 3.3. In addition, reduced order models for the structural and thermal subsystems of the integrated prime mover are developed in this section. These models are used in a trade space analysis in Section 3.5 to identify the performance trends of the four PM machine types. The tooth-and-slot, Halbach array electric machine is selected on the basis of specific power to use in the conceptual IPM design.

In Section 3.6, a baseline low fan pressure ratio, turbofan engine is redesigned and optimized for integration with an electric machine. The framework is again updated to include models for the low pressure compressor, spool, and turbine. The constraints of each of these components are considered in conjunction with those of the electric machine and thermal management system. The output of this updated framework is a first-of-its-kind integrated prime mover conceptual design which meets power, aerodynamic, structural, thermal, and electromagnetic requirements. The electromagnetic performance is simulated using 2D finite element analysis and is found to match that of the reduced order model to within 15%. This chapter addresses objective one and two defined in Chapter 1.

3.1 Outer Rotor Permanent Magnet EM Types

For the outer rotor permanent magnet electric machine, four different machine architectures are considered based on combinations of permanent magnet arrangements and stator architectures. The rotor architectures under consideration are the surface permanent magnet array and Halbach array. For the stator, both tooth-and-slot and slotless architectures are candidates for the IPM design. The details of these architectures and discussed in the following subsections.

3.1.1 Rotor Types

Two degrees of freedom in designing permanent magnet rotors are the directions of magnetization and the usage and placement of ferromagnetic material referred to as

rotor back iron. The surface permanent magnet is a common magnet arrangement used in high power density motors such as the MIT electric vehicle motor in Ref. [17] and the high torque-density Cheetah motor in Ref. [43]. The Halbach array has been proposed for more recent high power density motor designs such as the University of Illinois Urbana-Champaign motor [18] and the University of Nottingham motor [20] because it can eliminate the need for a rotor back iron and generates larger magnetic fields. The details of these arrangements are shown and discussed below.

Surface Permanent Magnet

In the surface permanent magnet topology for radial flux machines, the direction of magnetization for each magnet alternates radially inward and outward as shown in Fig. 3-1a for a single pole pair. This particular topology is common since it is simple to manufacture and assemble. Due to this alternating magnetization pattern, the magnetic flux density in the air gap is approximately a square wave. When surrounded by air, the magnetic fields form the pattern shown in Fig. 3-1b. However, it is common to use a ferromagnetic material on the outside of the magnet array to increase the magnitude of the fundamental compononet of magnetic flux density on the air gap side, which in turn increases machine torque.

Figure 3-2a shows the placement of the rotor back iron radially outward of the magnet array. The downside to adding this rotor back iron is that it adds mass to

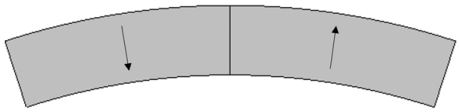

(a) Directions of magnetization are radially inward or outward.

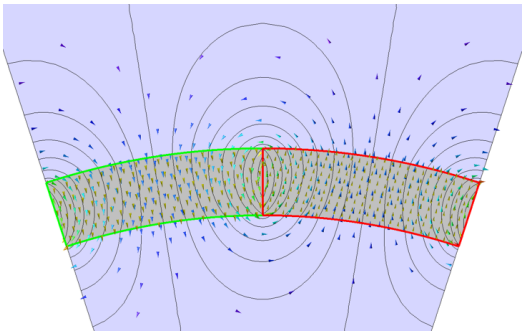

(b) Flux lines and vectors of SPM topology without back iron.

Figure 3-1: In the surface PM topology, the permanent magnets are magnetized either radially inward or outward.

the electric machine. However, the back iron may be kept relatively thin if it is sized to operate at the saturation flux density limit of the back iron material. The back iron is sized in this manner in the trade space analysis of Chapter 2. In addition, increasing the number of pole pairs can also decrease the back iron thickness, but at the cost of increasing electrical frequency and hence core losses.

A 2-D electromagnetic finite element analysis (FEA) is used to simulate the relative performance of the surface permanent magnets with and without back irons. In Fig. 3-3a, the magnetic flux density is extracted from the 2-D FEA software at 2 mm radially internal to the permanent magnet array. This flux density was extracted for both the back iron and non-back iron arrays. Figure 3-3b shows that the flux density magnitude more closely approximates a square wave and has increased amplitude relative to the case without back iron.

Next, a fast fourier transform is used to extract the fundamental component of the magnetic flux density. For this particular example, the fundamental component of the flux density is increased by 50% due to the addition of the back iron as shown in Fig. 3-4. In addition, the third and higher order harmonics, which contribute to losses in the machine, are approximately the same as those of the surface permanent magnet without back iron.

Since the surface permanent magnet topology with the rotor back iron produces a greater fundamental flux density component with similar harmonics, this rotor type

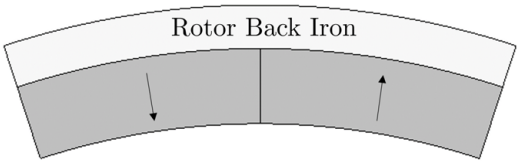

(a) Ferromagnetic material may be added to one side of the PM array.

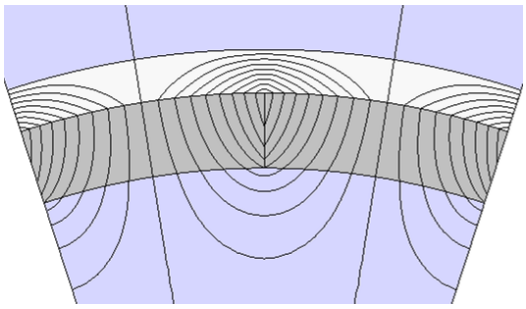

(b) Flux lines are now confined to the rotor back iron.

Figure 3-2: A rotor back iron is commonly used with the surface permanent magnet topology to increase the air gap flux density and machine torque.

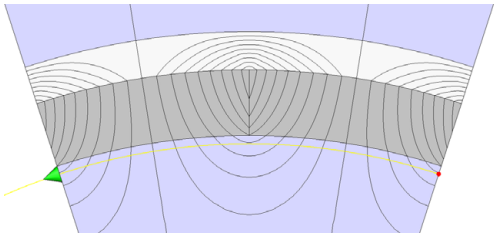

(a) B-field measured 2 mm from PM surface for comparison.

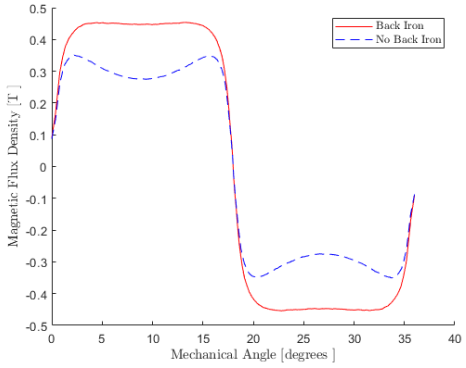

(b) Flux lines and vectors of SPM topology without back iron.

Figure 3-3: The addition of a rotor back iron increases the magnitude of the flux density on the air gap side of the machine.

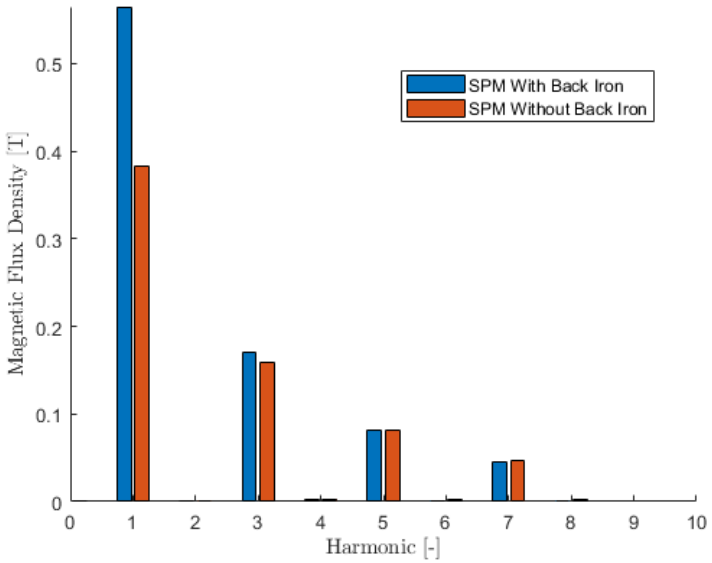

Figure 3-4: The fundamental of the air gap flux density is increased with the addition of a rotor back iron.

is considered for comparison with the Halbach array which is discussed next.

Halbach Array

The Halbach array is an alternative permanent magnet arrangement in which the directions of magnetization alternate between a radial and azimuthal direction as shown in Fig. 3-5a for a single pole. A possible benefit of this arrangement is that the magnetic flux density is reinforced on the air gap side of the array and canceled out on the other. Although Fig. 3-5a shows four directions of magnetization, it is possible to use a greater amount of directions to obtain a larger fundamental field component and increased cancellation. In an ideal Halbach array with perfectly sinusoidal directions of magnetization, the amplitude of the fundamental component of the field is increased by $\sqrt{2}$ [44].

The cancellation of the external magnetic field can be seen in Fig. 3-5b, although the cancellation is not perfect. The downsides to the Halbach array are that (1) it is difficult to assemble, and (2) the force between adjacent magnets is such that it could pull the magnets away from the rotor rim during operation.

Although the cancellation of the flux density on the radially outward side is not perfect, the addition of a ferromagnetic rotor back iron provides negligible benefit to the Halbach array topology. This is seen in Fig. 3-6 where the B-field is again extracted 2 mm from the airgap side of the magnet surface. In addition, the magnetic flux density is more sinusoidal than that of the surface PM topology (see Fig. 3-7), the latter of which closely resembles a square wave. Since the electric machine torque is primarily due to the fundamental component of the B-field, the Halbach array can

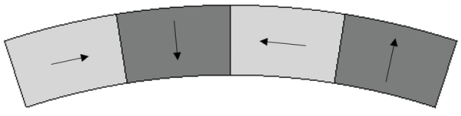

(a) Azimuthal magnets are inserted between radial magnets.

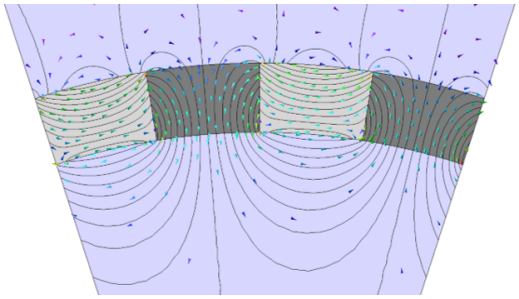

(b) Flux lines and vectors of Halbach array topology without back iron.

Figure 3-5: In the halbach array topology.

generate greater torque than a surface permanent magnet machine for fixed magnet volume. In Ref. [17], the author found that the Halbach array produces greater torque than an equivalent volume of a surface permanent magnet array except when the magnet volume is low (i.e., a few kilograms) and thin.

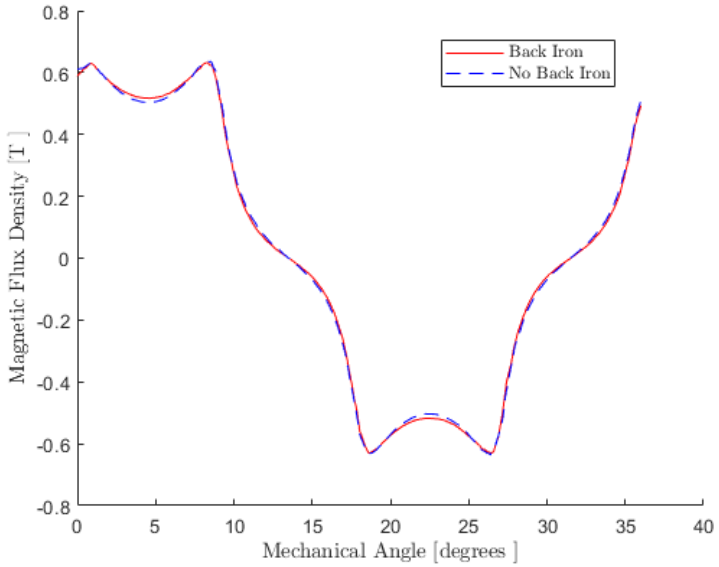

Figure 3-6: The addition of a rotor back iron has negligible effect on the flux density of the reinforced side.

Comparison of Rotor Topologies

Compared to the surface permanent magnet array, the Halbach array does not require a rotor back iron and it produces a greater fundamental magnetic flux density component which results in greater torque. However, as discussed previously, the downside is its increased assembly complexity and risk of adhesive failure during operation.

A comparison of the harmonics from a 2D FEA simulation for the surface permanent magnet and Halbach array is shown in Fig. 3-7. For this particular example, the Halbach array produces a 5% greater fundamental flux density component than the surface permanent magnet array with a rotor back iron.

The Halbach array eliminates the third harmonic from the surface PM array; however, its fifth and ninth harmonics are greater in magnitude compared to those

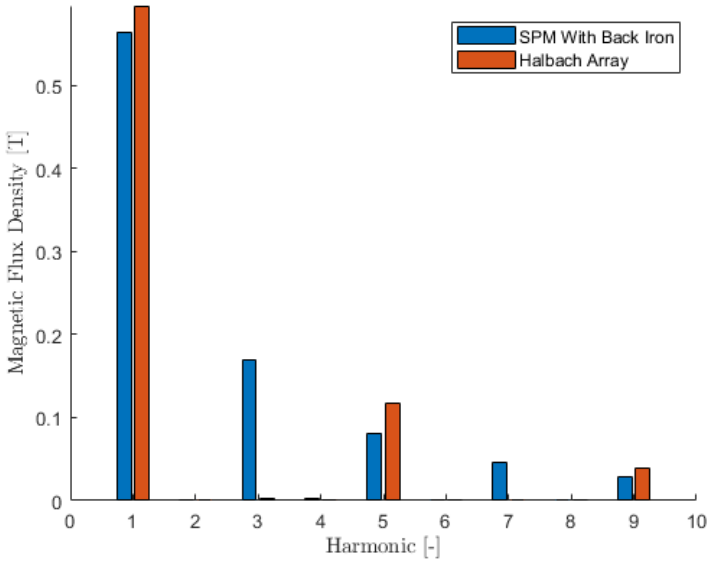

Figure 3-7: The Halbach array increases the fundamental component of the flux density while eliminating the third and seventh harmonics.

of the surface PM array. Depending on the stator geometry, these higher order harmonics may increase losses and torque ripple.

Both the surface permanent magnet array with a rotor back iron and the Halbach array without back iron are considered in the trade space analysis for this chapter. The Halbach array is anticipated to perform better, but it represents an increased risk with respect to assembly.

3.1.2 Stator Types

Two common types of stators considered in the trade space analysis are tooth-and-slot and slotless stators. Their structure and general pros and cons are discussed in the following subsections.

Tooth-and-Slot

The tooth and slot stator is a common configuration where windings wrap around teeth made from ferromagnetic material. In addition to providing a reference for locating the windings, the teeth reduce the amount of air in the magnetic circuit

between the rotor and stator, which helps increase the air gap magnetic flux density and hence the torque. An example of the tooth-and-slot geometry is shown in Fig. 3-8.

The tooth-and-slot stator is a common stator geometry that has been successfully used in a variety of machines such as the high torque density Cheetah motor [43] and the MIT electric vehicle motor [17]. One downside to the tooth-and-slot stator is that the teeth occupy space that could be used to place more windings, which reduces copper losses. In addition, the stator teeth can saturate if sufficient magnetic flux is created from the permanent magnets and stator windings. This saturation limits the theoretical maximum shear stress of tooth-and-slot machines.

In Ref. [41], the theoretical shear stress limit is derived to be equal to $B_{\text{sat}}^2/(16\mu_0)$, where B_{sat} is the saturation flux density of the ferromagnetic material and μ_0 is the permeability of free space. For iron cobalt, which offers the highest available saturation flux density today of 2.36 T, this theoretical shear stress limit is 277 kPa. In practice, tooth-and-slot machines do not reach this limit yet due to cooling constraints.

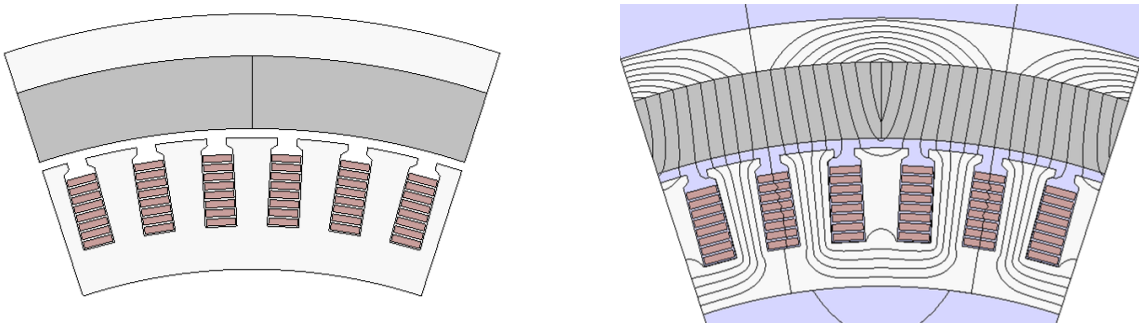

(a) Example cross-section of the tooth-and-slot stator with an outer rotor, surface permanent magnet array.

(b) Magnetic flux density is concentrated in a path from the magnets through the air gap, stator teeth and stator back iron.

Figure 3-8: Single pole for a tooth-and-slot, surface permanent magnet topology.

Slotless

The stator teeth are eliminated in a slotless configuration. This teethth elimination allows greater winding volume compared to an equivalently sized tooth-and-slot stator. However, the winding material (e.g., copper) acts magnetically similar to air, so slotless machines have large effective air gaps and lower air gap flux densities than their tooth-and-slot correspondents. An additional benefit of the slotless configuration is that the electromagnetic shear stress is not limited by the magnetic saturation of the teeth. Instead, it is limited by the ability to cool the machine. An example of the slotless stator configuration and the flux lines with a permanent magnet array are shown in Fig. 3-9. The conductors are shown as rectangular blocks, but in practice could be implemented as transposed litz bundles to minimize eddy current and proximity effect losses.

In addition to having a large effective air gap, a challenge with slotless machines is attaching the windings to the machine given the lack of stator teeth to hold them in place. Due to a lack of reference points on the stator back iron, locating the windings can be difficult. A consequence may be an uneven space distribution between the windings and stator as found in Ref. [31].

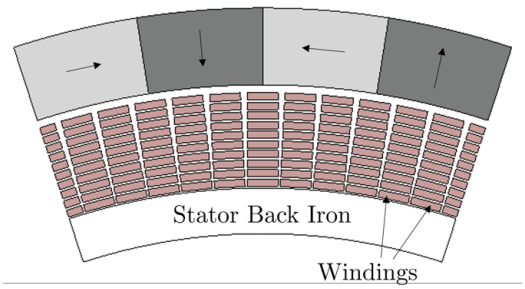

(a) The teeth are removed and instead only windings separate the magnets and stator back iron.

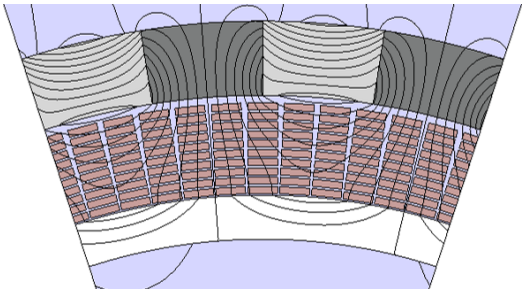

(b) Flux lines must pass across both the air gap and all the windings to reach the stator back iron.

Figure 3-9: Slotless halbach array.

3.1.3 Summary of PM Electric Machine Types

With two rotor and two stator configurations under consideration, four permanent magnet electric machine topologies are implemented for the trade space analysis. These are the

1. tooth-and-slot surface PM,
2. tooth-and-slot Halbach array,
3. slotless surface PM, and
4. slotless Halbach array.

These are all considered in their outer rotor configuration for the radial internal IPM architecture. The following subsections briefly describe these configurations.

3.2 Permanent Magnet Machine Assessment Framework

With four PM EM topologies to consider, the framework from Chapter 2 was updated with models of each type. In the trade studies of Chapter 2, only the EM design was considered and heat flux was used as a surrogate for cooling feasibility. This chapter utilizes an expanded framework that captures thermal constraints on the electric machine via hotspot temperature estimation. In addition, the structural integrity of the turbomachine is considered. This framework does yet not consider the actual turbomachine performance, which is instead reserved for Section 3.6 during the integrated prime mover conceptual design.

3.2.1 Framework Objectives

Each of the electric machine, thermal management system, and turbomachinery rim components impose constraints on the feasibility of an IPM design. To manage these constraints, the framework from Chapter 2 is expanded to include additional models.

In addition, the sizing approach is different and is described in Section 3.2.2. The objective of this framework is to maximize the overall system specific power which accounts for the electric machine, thermal management, and turbomachine subsystems. The numerator of this specific power metric is the input power to the electric machine, $P_{\text{in,em}}$ minus the sum of the electric machine losses, $P_{\text{losses,em}}$, and power required to drive the thermal management system pump, $P_{\text{pump,tms}}$. This quantity is divided by the total mass of the electric machine, m_{em}, thermal management system, m_{tms}, and turbomachine rim, m_{rim}. This specific power metric is shown in Eqn. 3.1 below. This specific power metric therefore includes the performance impact of using either an air cooling or liquid cooling system.

$$\Xi_{\text{PM}} = \frac{P_{\text{in,em}} - P_{\text{losses,em}} - P_{\text{pump,tms}}}{m_{\text{em}} + m_{\text{tms}} + m_{\text{rim}}} \tag{3.1}$$

The framework objective is to identify the highest specific power, permanent magnet systems across different power levels and input parameters. The results inform the selection of a single permanent magnet architecture to use in the integrated prime mover conceptual design.

3.2.2 Approach

A multidimensional grid search is used to estimate the highest specific power permanent magnet systems. Multiple input parameters are swept over fixed ranges to determine the optimum machine with respect to system specific power. However, unlike Chapter 2, all input parameters are free as opposed to some being fixed to nominal values. Structurally and thermally feasible machines for each combination of inputs are stored in software structures. Once the sweep is complete, the machine with the highest specific power is extracted from the structures. The swept input parameters are

- shear stress,
- rotational speed

- length-to-tip radius aspect ratio,
- slot current density,
- number of poles, and
- air gap thickness.

Although Section 2.5 concluded that the electric machine specific power was insensitive to air gap thickness, the performance of the added thermal management system will depend on this parameter. Cooling air flows through the air gap, so a larger air gap thickness allows greater mass flows, which in turn may reduce the hotspot temperature.

A flow diagram of the permanent magnet machine design and assessment framework is presented in Fig. 3-10. The framework begins with a calculation of the maximum possible rotor thickness as detailed in Section 3.3.1. This rotor thickness limits the possible thickness of the magnets, the rotor back iron, and the turbomachine rim that retains them both. This rotor thickness constraint is passed to the electric machine sizing loop. The size of the electric machine windings and magnets are swept until they are of a thickness that can theoretically meet the input shear stress requirement. A combination of magnet and winding thicknesses produce the target shear stress may not exist without exceeding the allowable rotor thickness. In this case, the design point is deemed infeasible and a new combination of inputs is tested.

If a combination of magnet and winding thicknesses can produce the target shear stress, then the geometry, mass and losses of the electric machine are estimated. The geometry and losses are passed to the thermal management system design module. In this module, a 2D temperature distribution calculation is used to estimate the hotspot temperatures of the EM. The temperatures in both the air-cooling case and liquid-cooling case are calculated. In addition, an estimate of the corresponding thermal management system mass and its power requirement are calculated to factor into the system specific power.

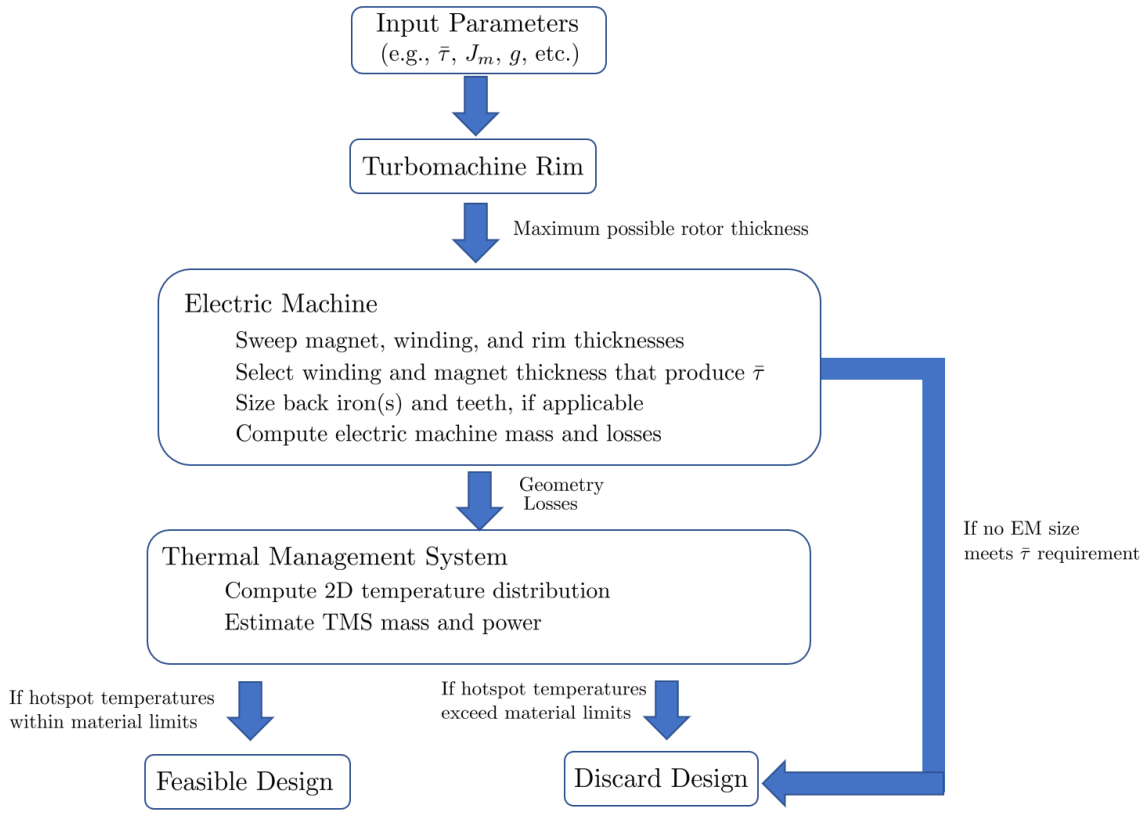

Figure 3-10: A high specific power machine is found via multidimensional grid search using the sizing modules shown in the above block diagram.

As a final step, the maximum operating temperature of the various electric machine materials is used to filter out infeasible designs. For example, the winding hotspot temperature cannot exceed 180°C based on the temperature limit for typical winding insulations.

The output of this framework is a six dimensional structure containing all feasible designs and their associated performance. Two important scaling parameters from the scaling laws discussed in Chapter 2 are the electromagnetic shear stress and mechanical speed. The six-dimensional space can be collapsed and viewed in terms of these two parameters as shown in Fig. 3-11. In this case, the highest specific power machines at each shear stress and rotational speed are displayed. A clear boundary shows the shear stresses and rotational speeds where no electric machine designs are feasible.

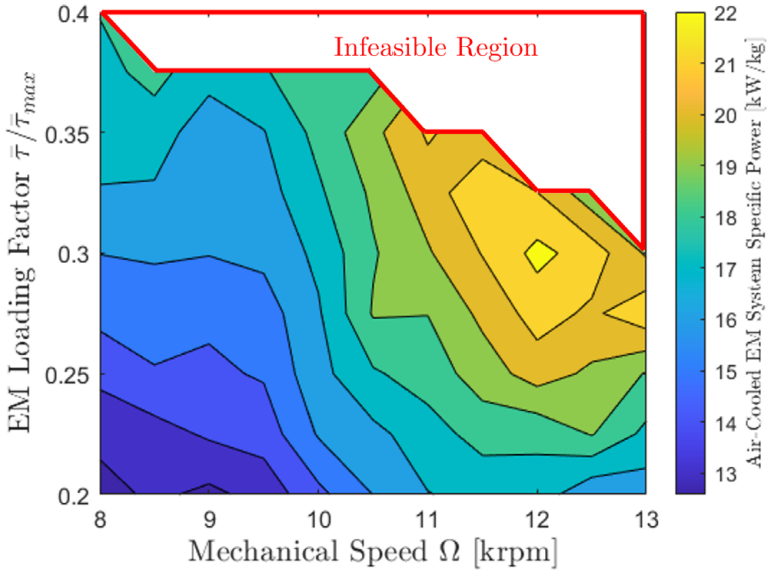

Figure 3-11: Example of framework output.

3.3 Reduced Order Models

Reduced order models, which are simple scaling laws in this thesis, were developed and implemented for each of the integrated prime move subsystems. These various reduced order models and their coupling are described in this section.

3.3.1 Turbomachine and Electric Machine Rotor

The turbomachine sizing model was designed by colleague Yuankang Chen in Ref. [27] and is briefly summarized here. For an outer rotor electric machine, the magnets and rotor back iron are contained by the turbomachine rim such that it bears the entire load of the rotor. The turbomachine rim is sized via a force balance. The centrifugal stress from the magnets, rotor back iron, and the rim itself are equal to the yield stress of the titanium rim, σ_y, with some safety factor, SF. Using a thin shell hoop stress model, the turbomachine is sized as

$$\frac{\sigma_Y}{SF} t_{rim} = \rho_{\mathrm{EM,rotor}} r_{\mathrm{EM,rotor}}^2 \Omega^2 t_{EM,rotor} + \rho_{rim} r_{rim}^2 \Omega^2 t_{rim} \tag{3.2}$$

where ρ_{rim}, r_{rim}, t_{rim}, and Ω are the rim mass density, rim mean radius, rim thickness,

and rotational speed, respectively. Similarly, $\rho_{\text{EM,rotor}}$, $r_{\text{EM,rotor}}$, and $t_{\text{EM,rotor}}$ are the average mass density, mean radius, and total thickness of the electric machine rotor elements, respectively. As shown in Fig. 3-10, an electric machine design is infeasible if a value of rim thickness that satisfies Eqn. 3.2 does not exist.

3.3.2 Electric Machine Mass and Performance

Four models were implemented for each of the rotor and stator combinations from Section 3.1. The models are briefly described here.

Tooth-and-Slot Surface Permanent Magnet and Halbach Array

The tooth-and-slot, surface permanent magnet model is the same as that of Chapter 2, where the sizing is based on Eqn. 2.25 [41]:

$$\bar{\tau} = \frac{B_s K_s}{2} \tag{3.3}$$

The winding and magnet thicknesses are swept such that they produce the target shear stress. The rotor and stator back irons are sized as discussed in Chapter 2. One addition to the framework is that the permanent magnet performance is adjusted based on assumptions on their operating temperature. Specifically, the remanent flux density of the permanent magnets is modeled to decrease linearly with temperature:

$$B_{\text{rem}} = B_{\text{rem, 20°C}} \left(1 - \alpha_m \left(T_{\text{mag}} - 20°C\right)/100\right) \tag{3.4}$$

where $B_{\text{rem, 20°C}}$ is the magnet remanent flux at 20°C, T_{mag} is the magnet temperature, and α_m is the temperature coefficient of the magnet material.

In addition, some details of the windings are now considered because the winding insulation impacts the hotspot temperatures of the machine. It is assumed that the electric machine is driving a load and can be modeled as an ideal, three-phase current source. The peak current, I, is calculated based on the electric generator geometry,

slot current density, and number of turns:

$$I = \frac{J_m A_{\text{slot}}}{N_{\text{turns}}} \tag{3.5}$$

where J_m is the peak slot current density, A_{slot} is the area of a stator slot, and N_{turns} is the number of winding turns. The per-phase voltage, V, is approximated as

$$V = P/\left(3I\right) \tag{3.6}$$

The area of a single turn (i.e., a bundle of Litz strands) is

$$A_{\text{wire}} = \frac{K_u A_{\text{slot}}}{N_{\text{turns}}} \tag{3.7}$$

and the radius of the turn is $r_{\text{wire}} = \sqrt{A_{\text{wire}}/\pi}$. The corresponding litz bundle diameter, $2r_{\text{wire}}$, is used to set the slot width. Next, the number of Litz wire strands is calculated to approximate the amount of insulation in the slot, which impacts the effective slot thermal resistance. An initial litz strand size of US American Wire Gauge (AWG) 28, which has a radius of $r_{\text{str}} = 0.1605\,\text{mm}$, was assumed based on discussions with the winding vendor and an anticipated machine electrical frequency in the low kilohertz range. A bundle packing factor of 0.91 is assumed based on the ideal hexagonal packing factor, and the total number of strands is thus

$$n_{\text{str}} = 0.91 \frac{A_{\text{wire}}}{\pi r_{\text{strand}}^2} \tag{3.8}$$

The necessary dielectric thickness for each Litz wire strand, t_{di}, is sized from the maximum electric field in a cylindrical dielectric:

$$t_{\text{di}} = r_{\text{str}} \left(e^{\left(\frac{V}{r_{\text{str}} E_{\text{max}}}\right)} - 1 \right) \tag{3.9}$$

where E_{max} is the maximum dielectric strength – a material property. For Kapton MT 100 insulation, the dielectric strength is $2.16 \cdot 10^8\,\text{V/m}$. A safety factor of 10 is used

such that the effective dielectric strength used in the calculations is $2.16 \cdot 10^7\,\mathrm{V/m}$.

Tooth-and-Slot Halbach Array For the electric machine trade studies, the tooth-and-slot Halbach array electromagnetic model is the same as the tooth-and-slot surface permanent magnet model, but it is assumed that the rotor back iron is eliminated during the turbomachinery rim sizing and mass calculation. The basis for this assumption is that (1) for the magnet thicknesses expected in these machines, the Halbach array will produce at least as much magnetic flux in the airgap as an equivalent surface PM machine as shown in Ref. [17] and (2) the azimuthal magnets cancel the flux on the outside of the electric machine as shown in Section 3.1, which eliminates the need for the rotor back iron. Finite element analysis is ultimately used to obtain a higher fidelity assessment of the output torque and verify these assumptions. A detailed 2-D analytic model for the tooth-and-slot Halbach array that estimates the increased flux density is used in Chapter 4.

Slotless Surface PM and Halbach Array

The slotless surface PM and Halbach array electric machine performances are estimated using the model from Chapter 2 of Ref. [17], which is not repeated here for brevity. To summarize, this model is a two-dimensional analysis of the magnetic flux distribution based on the magnetic scalar potential. This analysis superimposes the flux density solutions from both the radial-facing and azimuthal-facing permanent magnets. The torque is computed through integrating the product of the radial component of the total air gap flux density and the armature current density over the winding volume. Lastly, similar to the tooth-and-slot model, the winding thickness and magnet thickness are varied until the desired shear stress, $\bar{\tau} = T/\left(2\pi r_{\mathrm{ag}}^2 \ell\right)$, is produced.

3.3.3 Electric Machine Losses

In this framework, the Ohmic, core (i.e., stator eddy current and hysteresis), windage, and rotor losses are estimated and passed to the thermal management model to

estimate the winding and magnet hotspot temperatures of the electric machine. The loss models are described below.

Ohmic Losses

The Ohmic losses include those from both the fundamental as well as those from the proximity and eddy current effects. The resistance value used in these calculations is adjusted for the winding temperature.

Core Losses

The stator eddy and hysteresis losses per unit mass, $P_{\text{core}}/m_{\text{core}}$, are estimated using the classic Bertotti loss separation model [45]:

$$\frac{P_{\text{core}}}{m_{\text{core}}} = P_h + P_c + P_e \tag{3.10}$$

$$= K_h f B^{\alpha} + K_c f^2 B^2 + K_e f^{1.5} B^{1.5} \tag{3.11}$$

where P_h, P_c and P_e are hysteresis, classic eddy current, and additional current loss, respectively, and K_h, K_c, and K_e are their coefficients. These coefficients are derived from manufacturer data. The variable B is the peak B-field.

The stator is assumed to be designed such that the ferromagnetic material is saturated to minimize the back iron thickness. Therefore, the peak B-field used in Eqn. 3.10, which is the B variable, is assumed to be 2.36 T throughout the stator. This value is reduced in Chapter 4 to closer to 2.2 T since the stator is designed to be limited primarily to the knee of the B-H curve. In addition, in these sweeps, the core loss is computed directly from the manufacturer data. However, this core loss is doubled in Chapter 4 and Chapter 5 for safety margin, which accounts for effects such as flux concentration in the actual machine.

Windage Losses

The windage loss model was developed by colleague Yuankang Chen [27]. These losses are estimated on the outer and inner rotor surfaces with empirical correlations

for surface skin coefficients and have the form

$$\dot{W}_{windage} = \pi C_d \rho_a r^4 \Omega^2 \ell \tag{3.12}$$

where ρ_a is the air density, r is the surface radius, ℓ is the machine length, and C_d is an empirical skin friction coefficient.

Rotor Losses

The eddy current losses in the permanent magnets and rotor back iron are functions of multiple design variables such as the air gap thickness, slot current density, and pole pair count, amongst others. As a rough approximation, a constant power loss per unit mass is assumed for each of the permanent magnet and rotor core losses based on electromagnetic FEA assessments of several output designs from the framework. The permanent magnet lossses are studied in more detail in Chapters 4 and 5.

3.3.4 Thermal Management

For these studies, the electric machine stator can either be (1) entirely air cooled, or (2) a combination of air-cooled and oil-cooled. In both cases, the stator is cooled via a pump that drives air through both the air gap and through a heat sink on the inside of the inner diameter of the stator. This heat sink is constructed of aluminum, has four millimeter thick fins, and one millimeter thick walls. The liquid cooling case utilizes the same air cooling scheme but also includes the addition of oil cooling to heat sinks attached on the end turns of the machine. Free-air convection is assumed on the outside of the rotor.

As mentioned in Section 3.2, an electric machine is deemed thermally feasible if the hotspot temperatures in the machine are below the maximum operating temperatures of the components. Colleague Yuankang Chen developed a 2D thermal resistance network to estimate hotspot temperatures in the machine [27]. The thermal resistance of the windings is calculated using a homogenized slot approximation. The convective heat transfer coefficients are estimated using Nusselt number correlations.

For an air cooling system, the mass comprises the aluminum heat sink in the stator inner diameter. For the oil cooling system, the thermal management system mass also accounts for the oil cooling heat rejection system. This sizing is based on existing aircraft oil cooling system components from the work of Ref. [46], except the gear and bearing heat loads are replaced by the end turn heat sinks. Lastly, the thermal management system power requirement is the pump power required to restore the coolant exit total pressure to inlet total pressure as derived by colleague Yuankang Chen [27].

3.4 Permanent Magnet Machine Performance Sweeps

Using the framework from Section 3.2 and reduced order models from Section 3.3, the various PM configurations are compared on the basis of system specific power. The following subsections detail the material assumptions, design parameter assumptions, and the parameter sweep ranges.

3.4.1 Material Assumptions

Similar to Chapter 2, currently available materials are assumed in the trade studies. Some new additions are the rotor sleeve, which is composed of Ti-6Al-4V alloy for its high strength-to-weight ratio. In addition, electrical insulation and winding potting are considered since they impact the thermal conductivity of the slot. The insulation is Kapton-MT and the potting is Cooltherm SC-324. Lastly, the heat sink is assumed to be composed of aluminum 7075 due to its low mass density and high thermal conductivity. The various materials used for the trade space analysis are summarized in Table 3.1.

Table 3.1: Summary of material assumptions.

Component	**Material**
Stator	Hiperco-50
Permanent Magnets	Samarium Cobalt
Rotor Sleeve	Ti-6Al-4V Alloy
Conductor	Copper
Electrical Insulation	Kapton-MT
Winding Potting	Cooltherm SC-324
Heat sink	Aluminum 7075

3.4.2 Design Parameter Assumptions

Several design parameters are assumed to simplify the trade space and these are summarized in Table 3.2. Similar to Chapter 2, the slot copper fill factor is fixed to a value of 0.5. In addition, the electric machine is assumed to have one slot per pole per phase based on the design from Ref. [17] since there is no obvious benefit at this level of analysis to using a fractional number of slots per pole per phase. This same assumption was used for the analysis in Chapter 2.

The winding hotspot temperature is limited to 180°C which is the limit for the IEC 60085 standard, class H insulation [47]. Although insulations rated for 200°C, 220°C, and 250°C exist, they are more expensive and difficult to work with. Since the permanent magnet adhesives for attachment to the rotor operate a maximum temperature of approximately 260°C [33], the magnets are limited to 200°C to provide margin. The assumptions on the cooling system were chosen by Yuankang Chen [27]. Lastly, a safety factor of two is assumed for the turbomachine rim.

Table 3.2: Summary of design parameter assumptions.

Design Parameter	**Assumed Value**
Slot copper fill factor	0.5
Slots per pole	3
Winding temperature limit	180°C
Winding operating temperature	180°C
Magnet temperature limit	200°C
Magnet operating temperature	200°C
Air pressure and temperature	$101kPa, 300K$ (Sea level)
Air cooling inlet Mach number	0.3
Pump isentropic efficiency	91%
Structural safety factor	2

3.4.3 Swept Parameter Ranges

The performance of the four machine types are estimated at 100 kW, 500 kW, 1 MW, and 3.6 MW. The kilowatt-range power levels may be representative of a short range aircraft, whereas the megawatt-class ones could be applicable to single- or twin-aisle aircraft. In addition, for each of the four machine types, both air-cooled and liquid-cooled machines are optimized. This leaves thirty-two combinations for comparison. At each combination of machine type, cooling system type, and power level, six parameters are swept: rotational speed, electromagnetic shear stress, electric machine aspect ratio, slot current density, number of poles, and air gap thickness. Although Chapter 2 concluded that the machine performance is insensitive to air gap thickness, this parameter is now important due to the air cooling. Nominal ranges of these parameters are given in Table 3.3 below. Due to the long runtime for testing all possible permutations, some of these ranges were narrowed and refined after viewing where the optimum might exist from a coarse sweep.

Table 3.3: Swept parameter ranges

	Units	**Range Examined**
Rotational Speed, Ω	rpm	6,000-30,000
Shear Stress, $\bar{\tau}$	kPa	0.025-0.4
Electric machine aspect ratio (length divided by tip radius), ℓ/r_t	-	0.1-3
Slot current density, J_m	A/mm^2	7.5-40
Number of Poles, N_p	-	4 - 56
Air gap thickness, g	mm	0.1 - 4

3.5 Trade Space Analysis

As discussed in Chapter 1, the specific power of the electric machine is expected to decrease with increasing rated power. Specifically, the power per unit volume, P/V, for an idealized electric machine scales as

$$\frac{P}{V} = 2\bar{\tau}^{3/2}\sqrt{\frac{2\pi\,(\ell/r)\,U^3}{P}} \tag{3.13}$$

where $\bar{\tau}$ is the electromagnetic shear stress, ℓ/r is the length-tip radius aspect ratio, and U is tip speed. These parameters are limited by material properties, cooling technologies, and rotordynamics. Although Chapter 2 studied the impact of these parameters on machine performance, the parameter ranges were largely based on surveyed data as opposed to any physics-based constraints. With the additions of the structural and thermal management system models in this chapter, the shear stress, length-to-tip radius aspect ratio, and tip speed limits are dictated by the physics-based models. This trade space analysis does not encapsulate all limiting factors such as the rotor dynamics of the machine, but many of these additional details are considered in the following chapters.

3.5.1 Rated Power Trends

The following subsections show how the overall integrated prime mover system specific power scales with rated power. Although the electric machine in isolation is expected to scale roughly per Eqn. 3.13, this scaling does not consider that the optimal shear

stress, aspect ratio, and tip speed are also functions of rated power. In addition, this scaling does not consider the thermal management system.

Air-Cooled Machines

Figure 3-12 shows the maximum module specific power versus rated power for air cooled machines. In this figure, both tooth-and-slot (TaS) and slotless machines are compared. Each of the four architectures are optimized at the power levels of 100 kW, 500 kW, 1 MW and 3.6 MW. As expected from Eqn. 3.13, specific power for all machines decreases with increasing rated power. However, the optimal air gap thickness, slot current density, pole pair count, and length-to-tip ratio also change with rated power levels as constrained by the structural and thermal models. Therefore the EM system specific power is found to scale closer to rated power to the negative one-fourth power. Therefore, the specific power does not decrease with increasing rated power as fast as Eqn. 3.13 suggests.

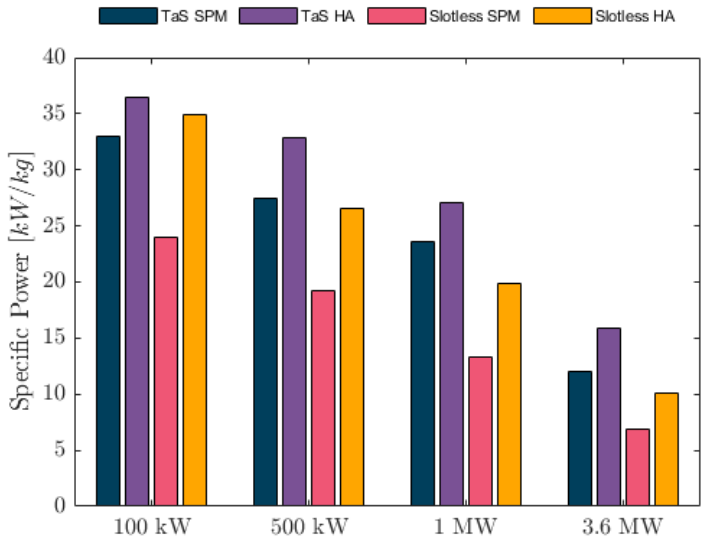

Figure 3-12: Module specific power falls with rated power for air cooled machines.

A key finding from this study is that the system specific power of tooth and slot architectures is consistently greater than that of the slotless machines. In addition, the system specific power of the Halbach array architectures is greater than that of

surface PM counterparts. This performance difference is due strictly to the rotor back iron elimination. For an air-cooled system, the tooth-and-slot Halbach array machine has the greatest specific power across all rated power levels.

For air-cooling machines, the efficiency generally increases as rated power increases. An exception is from 1 MW to 3.6 MW, where the efficiency nominally remains the same. All machine efficiencies optimize to between 95% to 98%. The following trends[1] are observed for the input parameters and electrical frequency:

- the optimal rotational speed decreases with increasing rated power;
- the optimal length-to-tip radius ratio increases with increasing rated power;
- the optimal slot current density decreases with increasing rated power;
- the optimal electrical frequency decreases with increasing rated power level; and
- the optimal air gap thickness increases with rated power level.

Unlike Chapter 2, the airgap is important in this study for cooling and its optimal thickness increases with rated power to provide more flow-through area for the cooling air. This optimal airgap increases approximately linearly with rated power and the optimized values are given in Table 3.4. Three constraints are not captured in this analysis which could limit the achievable air gap in practice.

First, a small air gap places the permanent magnets close to the asynchronous magnetic fields created by the stator windings. This could generate large eddy currents in the magnets and result in an unacceptable magnet hotspot temperature. While finite element analysis was used to estimate the permanent magnet losses for a few designs, this method was not used to cover all electric machine designs. The permanent magnet loss scaling is explored in Chapters 4 and 5. A second constraint not captured here is the rotor dynamics. For a smaller air gap thickness, it may be difficult to maintain clearance between the electric machine rotor and stator. This rotor dynamic constraint was studied in more detail by colleague Yuankang Chen [27].

[1] An 'optimal' parameter refers to the parameter value corresponding to the system design with maximized system specific power.

Lastly, thermal expansion of the stator could also render these air gap thicknesses infeasible.

Table 3.4: Optimal air gap thicknesses for all machine types.

Air Gap Thickness				
	100 kW	**500 kW**	**1 MW**	**3.6 MW**
Tooth-and-Slot SPM	0.15 mm	0.5 mm	1 mm	3.5 mm
Tooth-and-Slot HA	0.25 mm	0.4 mm	1	3.5 mm
Slotless SPM	0.3 mm	0.4 mm	0.5 mm	2.5 mm
Slotless HA	0.3 mm	0.4 mm	0.5 mm	2.5 mm

As mentioned, both the optimal rotational speed and slot current density decrease with increasing rated power level. These trends are shown in Fig. 3-13. The optimal rotational speed for the one megawatt slotless Halbach array machine is 15,500 rpm which is nearly identical to the 15,000 rpm used in the slotless University of Illinois Urbana-Champaign design [18].

In addition, the peak slot current densities optimize to as high as 35 A/mm^2 for the 100 kilowatt machines. This suggests that the slot current density range of 5-12 A/mm^2 for air-cooling, which was used in Chapter 2, may not be applicable to all power levels. However, further analysis and experimentation is necessary to confirm this. Similar to the air gap thickness, the length-to-tip radius aspect ratio increases approximately linearly with rated power. The optimal aspect ratios are shown in Table 3.5.

Table 3.5: Optimal length-to-tip radius aspect ratios for all machine types.

Length-to-Tip Radius Ratio				
	100 kW	**500 kW**	**1 MW**	**3.6 MW**
Tooth-and-Slot SPM	0.25	0.5	1	2
Tooth-and-Slot HA	0.2	0.425	0.5	2
Slotless SPM	0.5	1	1.5	2.75
Slotless HA	0.4	1	1.5	2.5

Lastly, the optimal electrical frequencies are shown in Table 3.6. All electrical frequencies optimize to values greater than one kilohertz. Electric machines for terrestrial power grids in the United States operate at 60 Hz, and the military standard

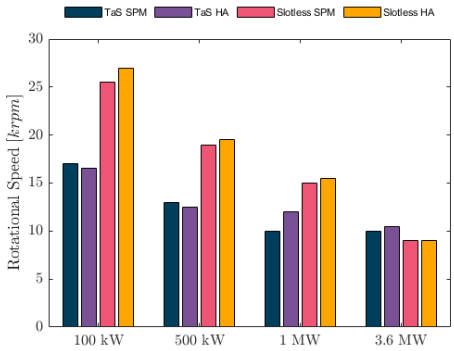

(a) Optimal rotational speed versus power level.

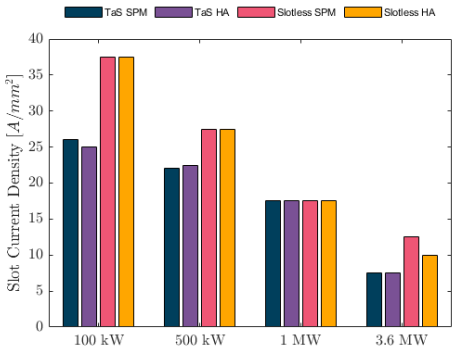

(b) Optimal slot current density versus power level.

Figure 3-13: Both optimal rotational speed and slot current density decrease with rated power level.

for aircraft power systems is 400 Hz [48]. This suggests that these high specific power machines have to be designed for a new, less explored frequency regime. In this study, frequency-dependent variables such as the electric machine core loss were extrapolated to these multiple kiloherz frequencies. However, experiments are necessary to validate the extrapolations.

Table 3.6: Optimal electrical frequency.

Electrical Frequency				
	100 kW	**500 kW**	**1 MW**	**3.6 MW**
Tooth-and-Slot SPM	5.1 kHz	3.9 kHz	3 kHz	1.67 kHz
Tooth-and-Slot HA	4.95 kHz	3.75 kHz	2.8 kHz	1.75 kHz
Slotless SPM	4.25 kHz	3.8 kHz	2.5 kHz	1.2 kHz
Slotless HA	5.4 kHz	3.9 kHz	2.58 kHz	1.35 kHz

Liquid-Cooled Machines

Similar to the air-cooled machines, the specific power of liquid-cooled electric machine systems decreases with rated power as shown in Fig. 3-14. At 100 kW and 500 kW, the liquid cooled machines are inferior to air-cooled machines with respect to specific power. However, at one megawatt they break even, and at 3.6 megawatts they slightly surpass that of air-cooled machines. For an integrated prime mover architecture, the cooling air may be bled from the low pressure compressor. This eliminates the need

for an external liquid cooling system and it is considered in the conceptual design in Section 3.6

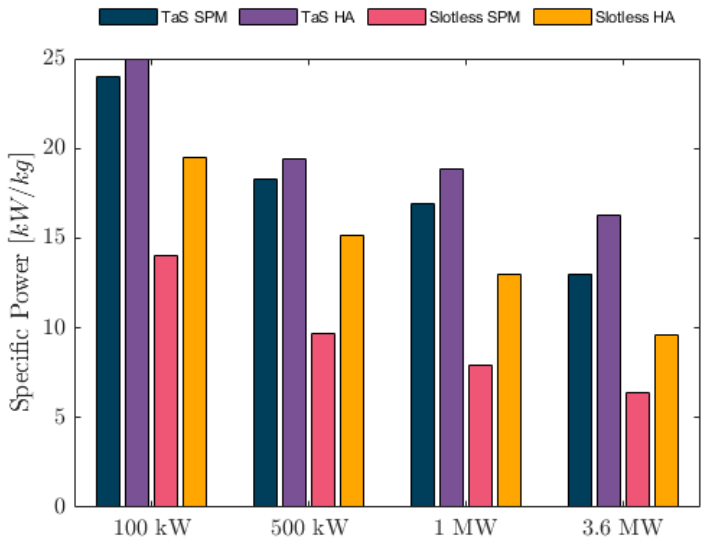

Figure 3-14: Similar to air-cooled machines, module specific power falls with rated power for liquid cooled machines.

3.5.2 Surface Permanent Magnet Versus Halbach Array

In this trade space analysis, the tooth-and-slot Halbach array simply eliminates the need for a rotor back iron. In practice, for thicker magnets, the Halbach array can produce greater magnetic flux at fixed volume as discussed in Section 3.1. Therefore the results in this section might understate the potential benefits of the Halbach array since they only show the performance impact of eliminating the rotor back iron. Nonetheless, the impact is significant. As shown in Figs. 3-12 and 3-14, the tooth-and-slot Halbach array offers anywhere from 9% to 75% greater performance over its surface PM counterpart. In addition, the slotless HA offers 8% to 56% greater specific power than slotless SPM. Therefore, there is a strong benefit to choosing a Halbach array over a surface permanent magnet array for the integrated prime mover despite the increased complexity with assembling a Halbach array.

3.5.3 Tooth-and-Slot Versus Slotless

For both air-cooled and liquid-cooled systems, the tooth-and-slot machines consistently out-perform their slotless counterparts with regards to the metric of specific power. Although the slotless architecture eliminates the stator teeth, the larger effective airgap greatly reduces the achievable electromagnetic shear stress. This can be seen in the comparison of shear stresses Table 3.7. However, the slotless machines typically meet the power requirement via higher rotational speeds than the tooth-and-slot machines. The exception is in the multi-megawatt range, where the speeds are comparable.

Table 3.7: Optimal speeds and shear stresses for tooth-and-slot and slotless Halbach array machines.

Power Level	**Rotational Speed**		**Shear Stress**	
	Tooth-and-Slot	**Slotless**	**Tooth-and-Slot**	**Slotless**
Air-Cooled				
100 kW	16500 rpm	27000 rpm	76 kPa	41 kPa
500 kW	12500 rpm	19500 rpm	83 kPa	41 kPa
1 MW	12000 rpm	15000 rpm	83 kPa	41 kPa
3.6 MW	10500 rpm	9000 rpm	62 kPa	35 kPa
Liquid-Cooled				
100 kW	16500 rpm	24000 rpm	76 kPa	48 kPa
500 kW	11000 rpm	15000 rpm	55 kPa	55 kPa
1 MW	12000 rpm	12000 rpm	69 kPa	55 kPa
3.6 MW	10500 rpm	9000 rpm	62 kPa	42 kPa

3.5.4 Hotspot Temperature Limit

Increasing the hotspot temperature limit not only expands the design space to greater speeds and shear stresses, but also shifts the optimal design point. Figure 3-15 shows how the design space and optimum shift with increases in winding hotspot temperature. This example is for the air-cooled, one megawatt, tooth-and-slot Halbach array machine. At 180°C, the optimal electric machine has a shear stress of 83.1 kPa and a rotational speed of 12,000 rpm. The corresponding specific power is 22.3 kW/kg. If the hotspot temperature limit is increased to 200°C, which is equivalent to moving

to a higher insulation class, the new optimum shifts to 12,500 rpm and the system specific power is 23.5 kW/kg - a 5.3% increase. As expected, even more designs are possible with greater specific powers if an insulation rated for 240°C is used. Therefore the optimal system specific power, shear stress, and torque are sensitive to the allowable hotspot temperatures in the machine.

Although this example is for a one megawatt, tooth-and-slot Halbach array machine, similar results are observed for the other machine types and power levels. This result suggests that the optimal machine design will attempt to push the hotspot temperatures as close to the material limits as possible. Alternatively, the electric machine thermal constraint can be relaxed by reducing inlet coolant temperatures. For example, it will be easier to cool an electric machine in an aircraft at cruise than at ground level due to the reduced atmospheric temperature.

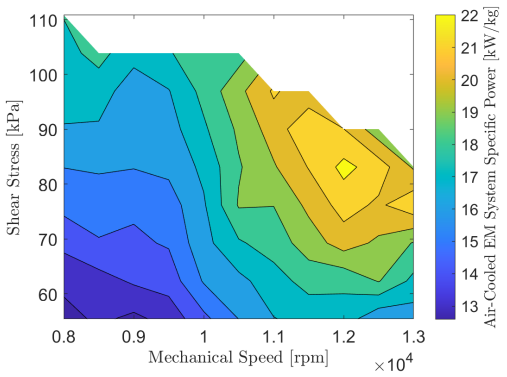

(a) Design space with 180°C temperature limit.

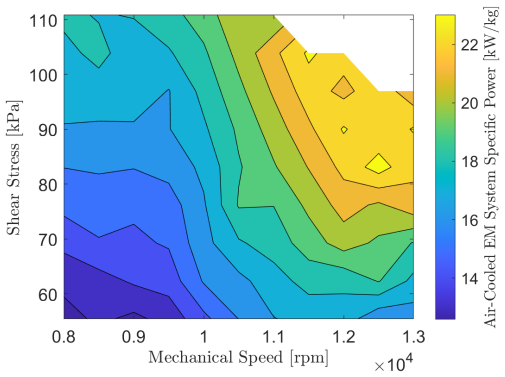

(b) Design space with 200°C temperature limit.

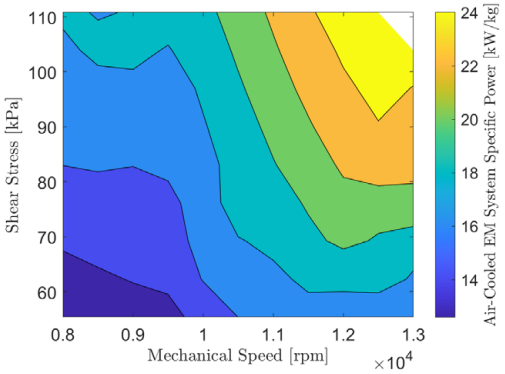

(c) Design space with 240°C temperature limit.

Figure 3-15: Increasing material temperature limit expands design space and improves maximum specific power.

3.6 Integrated Prime Mover Concept Design

The key result from the sweeps in Section 3.5 is the identification of the tooth-and-slot, Halbach array topology as having the highest performance with respect to system specific power across all studied power levels. This machine is structurally and thermally viable. While the previous section focused on the electric machine and thermal management system optimization, this section considers how the rest of the turbomachine (e.g., the compressor and turbine) might be re-designed and co-optimized with the electric machine. In this concept, the fan is removed. Instead, electric power is extracted from an electric machine that is integrated with the lower pressure compressor (LPC) of the engine. The LPC is a source of bleed air for cooling

the electric machine.

This section details the conceptual design of the integrated prime mover. First, the framework from Section 3.2 is modified such that an existing turbofan engine is optimized alongside the IPM. Second, a conceptual design of the IPM is detailed. This includes the system mass, losses, and geometry. Electromagnetic finite element analysis is used to compare the torque of the machine with the estimate from the reduced order model.

3.6.1 Integrated Prime Mover Design Approach

The conceptual IPM is designed by updating the framework from Section 3.2 to include a model of a candidate turbofan engine for integration. First, a low fan pressure ratio turbofan engine is selected as a baseline engine to be re-optimized. The max low pressure rotor speed is 12,680 rpm and the engine shaft power for turboelectric propulsion is estimated to be 3.6 MW. The engine cycle performance at cruise was estimated by colleague Yuankang Chen using a combination of publicly available information and the GasTurb software package [49]. Next, the fan on the low pressure spool is replaced with a low pressure compressor integrated with an electric generator. This integrated module is referred to as the integrated compressor generator. A sketch of this integrated prime mover configuration is shown in Fig. 3-16. The compressor and turbine geometry in Fig. 3-16 is not drawn to scale.

To maximize system specific power[2], mechanical speed is swept as an input parameter. Thermal, structural, and electromagnetic finite element analyses (FEA) are used to assess the reduced order models used in the sweeps. Finally, The rotordynamic stability of the machine was evaluated by colleague Yuankang Chen using a lumped parameter model [27].

[2]Specific power for the integrated prime mover is defined as output power of the electric machine divided by the total electric machine and compressor mass.

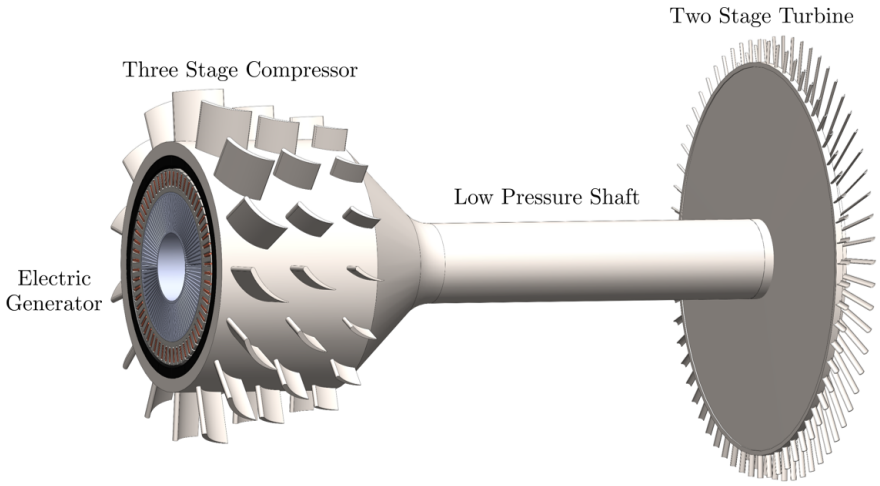

Figure 3-16: This concept sketch shows the overall layout of the integrated prime mover, but the compressor blades, shaft, and turbine blades are not drawn to scale.

3.6.2 Integrated Prime Mover Sizing and Performance

The low pressure spool consists of

1. the integrated compressor generator,
2. the low pressure shaft, and
3. the low pressure turbine.

The low pressure spool design is conducted by sweeping over a range of stage numbers, stage work coefficients, and stage flow coefficients to find a design which maximizes the integrated prime mover system specific power. A 1D meanline calculation approach is used for sizing the low pressure spool of the engine. In the 1D meanline approach, a single stream-line through the engine is used to represent the entire air flow. The electric machine, thermal management system, turbomachine rim, low pressure compressor blades, shaft, lower pressure turbine blades, dead rims, webs, and disks are all accounted for in the integrated prime mover system specific power.

The electric machine and its thermal management system sizing and performance use the models presented in Section 3.3. Their geometries must be consistent with those of the low pressure compressor (LPC). The LPC is designed to meet a pressure

ratio requirement as given in Table 3.8. Losses are estimated using a compressor loss model from Ref. [50]. The LPC blades and load-bearing rim are constructed together as a blisk, which is a component in which the blades and rim are fabricated as a single part. The load-bearing rim of the blisk is sized for both the electric machine rotor and LPC blade loads.

The lower pressure turbine (LPT) inlet conditions are calculated using the pumping characteristics of a generic low pressure ratio turbofan that were estimated from GasTurb [49].The LPT performance is estimated with meanline geometry and a Smith chart [51]. A Smith chart, published in Ref. [51], is used to estimate turbine efficiency as a function of work and flow coefficients. Specifically, the efficiency estimate is correlated to work and flow coefficients based on numerous measurements from turbine experiments. Lastly, for the sizing model, the LPT structural elements are sized to bear the centrifugal loads of the blades and rim.

The low pressure shaft segment connecting the integrated compressor-generator and LPT is assumed to be as long as the generic low pressure ratio turbofan core with an outer radius of 0.07m. The core length is estimated at 1.5m. The shaft thickness is then sized to bear the torsional load at takeoff.

3.6.3 Conceptual LP Spool Design: Sweep Input Parameters

The list of input parameters for the conceptual LP spool design was developed by Yuankang Chen [27] and is presented in Table 3.8. The definition of these parameters can be found in turbomachine textbooks such as Ref. [52] and Ref. [38]. The compressor is constructed from annealed, grade five titanium Ti-6Al-4V. The turbine and shaft are constructed from Inconel 718.

Table 3.8: Input Variables for Conceptual LP Spool Design Sweep

Design Parameter (units)	**Compressor**	**Turbine**
Pressure Ratio [-]	2.2	-
Physical Mass Flow [kg/s]	10.44	-
Target Isentropic Efficiency [-]	0.91	0.925
Structural Safety Factor, SF [-]	2	2
Material Mass Density, ρ_t [kg/m^3]	4430	8190
Material Yield Strength, σ_Y [MPa]	990	1124
Nondimensional Blade Tip Gap, $\frac{\tau}{r_t - r_h}$ [-]	0.01	-
Blade Aspect Ratio, $\frac{r_t - r_h}{c}$ [-]	0.8	4
Blade Solidity, $\frac{c}{s}$ [-]	1	-
Zweifel Coefficient [-]	-	1
Mean Blade Thickness to Chord Ratio, $\frac{t_b}{c}$ [-]	0.02	0.08
Disk Mean Radius to Blade Tip Radius Ratio, r_i/r_t [-]	-	0.1
Sweep Range for Work Coefficient [-]	0.2 to 0.4	1.2 to 2
Sweep Range for Flow Coefficient [-]	0.2 to 0.8	0.4 to 1.1
Sweep Range for Number of Stages [-]	3 to 4	2 to 4

3.6.4 Results

An integrated prime mover concept, based on an existing low fan pressure ratio engine and reduced order models, is found that is feasible and that maximizes system specific power. A representative picture of just the integrated compressor generator module is shown in Fig. 3-17. The compressor and turbine are not drawn to scale in Fig. 3-17. A sketch of the full low pressure spool was shown previously in Fig. 3-16.

The low pressure compressor has inlet guide vanes, which are not shown, and three stages. The optimal outer rotor, Halbach array electric machine for integration with the LPC has the specifications shown in Table 3.9 below. The integrated LPC is connected via a shaft to a two-stage low pressure turbine.

Since the electric machine design is conceptual at this stage, single copper blocks are shown in the slots to represent the conductors. The implementation of the windings, including the number of Litz strands and slot insulation, are discussed in the next chapters. The dimensions of the proposed electric machine design are summarized in Table 3.10 below.

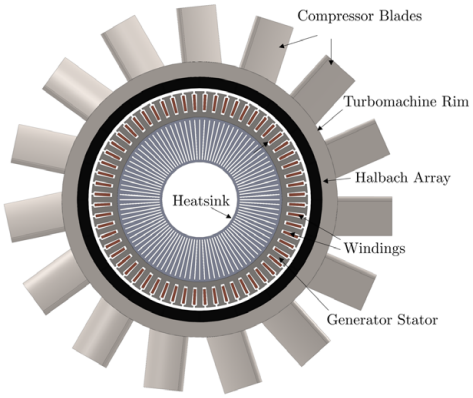

(a) Cross-sectional view of a sketch of the ICG shows its various turbomachine and electric machine components.

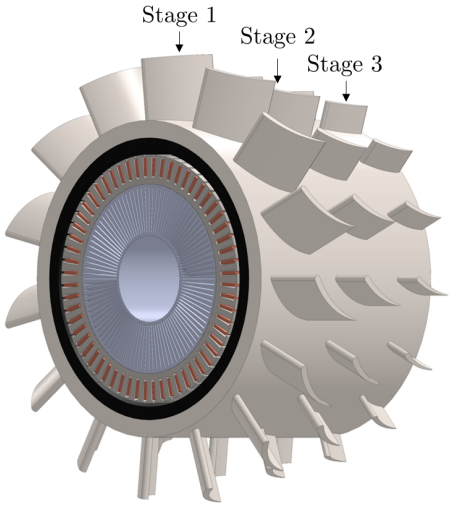

(b) Isometric view of a sketch of the ICG shows its three compressor stages.

Figure 3-17: Sketches of the conceptual integrated compressor generator module.

Specifications	**Value**
Shaft Power (P) [MW]	3.6
Mechanical Speed (Ω) [rpm]	10,000
Electromagnetic Loading $\bar{\tau}^*$ [-]	0.2
Electromagnetic Shear Stress $\bar{\tau}$ [kPa]	55.4
Torque (T) [Nm]	3,437
Number of Pole Pairs (n_{pr}) [-]	10
Number of Slots (n_{ps}) [-]	60
Slot Current Density (J_m) [A/mm^2]	10
Magnet Material	SmCo at 200 °C
Core Material	Hiperco-50 [75]
Winding Material	Copper at 180 °C

Table 3.9: Summary of electric machine design parameters.

Geometric Parameter	**Value [mm]**
Stator Inner Radius (r_{si})	131.4
Airgap Radius (r_{ag})	172.4
Magnet Inner Radius (r_{ri})	177.4
Magnet Outer Radius (r_{ro})	195.6
Rim Outer Radius (r_{rim})	219.9
Axial Length (ℓ)	332.2

Table 3.10: Summary of the electric machine dimensions

Low Pressure Compressor

The low pressure compressor, consisting of inlet guide vanes and three stages, has a total compression ratio of 2.20 and isentropic efficiency of 91.0%. The stage work coefficient, ψ, and flow coefficient, ϕ, defined in Chapter 2 are 0.295 and 0.650 respectively. The physical mass flow through the LPC is 10.44 kg/s. The dimensions of each LPC stage are listed in Table 3.11 below. These quantities were extracted and provided courtesy of colleague Yuankang Chen [27].

Dimension [Units]	**First Stage**	**Second Stage**	**Third Stage**
Blade Mean Radius r_m [m]	0.263	0.274	0.286
Hub-to-Tip Radius Ratio r_h/r_t [-]	0.717	0.792	0.849
Blade Axial Chord Length l_{c_x} [m]	0.0872	0.0639	0.0468
Blade Tip Speed U_t [m/s]	321	321	324

Table 3.11: LPC dimensions

Low Pressure Turbine

The integrated compressor-generator module is connected to a two-stage low pressure turbine. The turbine expansion ratio is 7.84 and its isentropic efficiency is 92.5%. The stage work coefficient and flow coefficient are 1.60 and 0.920, respectively, and the physical mass flow through the turbine is 10.60 kg/s. The dimensions of each LPT stage, provided courtesy of colleague Yuankang Chen [27], are listed in Table 3.12:

Dimension [Units]	**First Stage**	**Second Stage**
Blade Mean Radius r_m [m]	0.361	0.324
Hub-to-Tip Radius Ratio r_h/r_t [-]	0.877	0.661
Blade Axial Chord Length l_{c_x} [m]	0.0108	0.0303
Blade Tip Speed U_t [m/s]	402	408
Inner Rim Mean Radius r_i [m]	0.0384	0.0390
Inner Rim Thickness w_i [m]	0.0089	0.0176

Table 3.12: LPT dimensions

Mass and Loss Breakdowns

The proposed integrated compressor design achieves a specific power of 14.8 kW/kg and efficiency of 98.5%. This specific power at 3.6 MW is greather than that from the trade study in Section 3.5 because the electric machine was designed at cruise where the temperatures are lower. The framework estimates of component masses are shown in Table 3.13. The thermal management system is approximatley 14% of the total module mass.

Component	**Mass (kg)**
Stator Teeth	42.0
Stator Back Iron	21.5
Dielectric	3.30
Winding	21.9
End Winding	1.3
Magnet	59.4
Rim	48.1
Thermal Management System	33.2
Compressor Blades	6.6
Total	239.6

Table 3.13: Integrated compressor-generator component masses

The framework estimates for electric machine losses and thermal management system input power are summarized in Table 3.14. Despite the machine being designed for 10,000 rpm, the windage losses are quite low compared to the ohmic, core, and permanent magnet losses. The stator losses, or core plus ohmic losses, are at 30 kW compared to the 14.8 kW in the magnets. Therefore the majority of the heat will be dissipated in the stator.

Loss Source	**Loss (kW)**
Winding Ohmic Losses	14.4
Stator Core Losses	16.2
Airgap Windage Losses	2.3
Permanent Magnet Losses	14.8
Thermal Management System Power	7.4
Total Losses	55.1

Table 3.14: Integrated compressor-generator loss sources

Electromagnetic Performance

A 2-D transient electromagnetic finite element analysis (FEA) is used to assess the predicted performance of the analytic electromagnetic sizing and performance models. The FEA is performed with the Altair Flux^{TM} software [4]. The average torque computed over one period is 3,969 Nm, exceeding the target 3,437 Nm torque by 15.9%. Figure 3-18 shows that the magnetic flux is concentrated in the back iron and teeth, and that the tooth tips are saturated as designed. In addition, the azimuthal facing magnets cancel the magnetic flux on the outer surface of the machine, eliminating the need for a rotor back iron. The permanent magnet losses are assessed to be 16.3 kW, or 274 W/kg. This is within 10% of the 250 kW/kg value assumed by the framework and used in the thermal analysis.

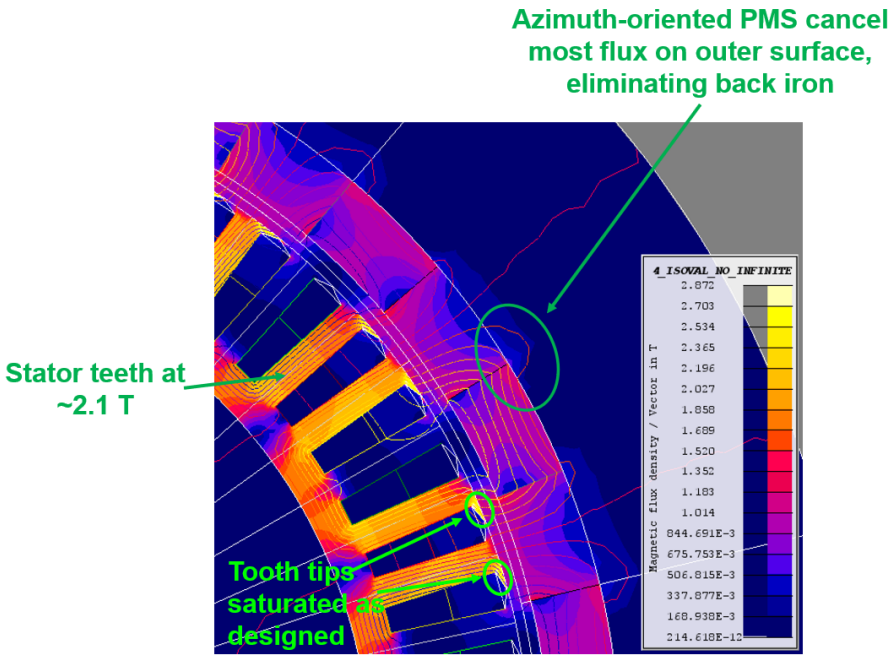

Figure 3-18: Electromagnetic finite element analysis of the electric machine shows the flux density of the stator teeth is limited to 2.1 T and that the flux is cancelled on the permanent magnet outer surface. This FEA was simulated using Altair Flux [4]

3.7 Summary of Key Results

In this chapter, four different permanent magnet electric machine types were considered for integration within the turbomachine. Specficially, the tooth-and slot surface permanent magnet, tooth-and-slot Halbach array, slotless surface permanent magnet, and slotless Halbach array were considered as potential machines for integration. Unlike Chapter 2, thermal and structural models were incorporated into the optimization framework as feasibility constraints. Reduced order models were developed for these four machines and a trade space analysis was conducted to compare architectures assuming the use of modern technology. Four different power levels representative of different application areas were surveyed. In addition, both liquid cooling and air cooling are compared. The key findings from the trade space analysis were the following:

- for all machine types, the specific power is inversely proportional to rated power;
- electric machine efficiency improves with increasing rated power;
- unlike Chapter 2, the optimal airgap is important for air cooling and its optimal thickness increases with rated power;
- the tooth-and-slot Halbach array has the highest performance with respect to system specific power across all power levels;
- with modern technology, tooth-and-slot stators offer greater specific power than those of slotless stators;
- similarly, Halbach array rotors offer greater specific power than those with surface permanent magnet rotors; and
- air-cooled electric machines offer competitive specific powers to liquid-cooled machines in the multi-megawatt power range when accounting for the mass and input power of the thermal management system.

In the second part of this chapter, the permanent magnet machine optimization framework was updated for integration within a turbomachine engine. Both the electric machine and low pressure spool of the engine were co-optimized to maximize the system level performance of an integrated prime mover concept. The first finding of this framework was that it is feasible to integrate a tooth-and-slot Halbach array machine into a jet engine at cruise conditions. The integrated compressor generator design has a specific power of 14.8 kW/kg. The design was evaluated in 2D finite element analysis and it was confirmed that it meets the torque requirement for the conceptual design.

Chapter 4

One Megawatt Demonstrator Trade Space Analysis

In Chapters 2 and 3, an integrated prime mover architecture is proposed and a combination of trade space analysis and finite element analysis is used to take the IPM through to a conceptual design. The key result is that an outer rotor, permanent magnet machine with a tooth-and-slot stator, Halbach array, and air cooling maximizes the specific power of the system. However, the promising performance of this architecture relies on modeling assumptions that may not be realizable in practice. Given the absence of electric machines in this design space, the next phase of this project is to take this topology through detailed design and ultimately a technical demonstration. The machine in question is rated at one megawatt, which is the power level required for turboelectric propulsion systems for regional aircraft [1]. Therefore this chapter focuses on the selection of key design decisions for a one megawatt demonstrator via a final set of trade space analyses. Chapter 5 then goes through the detailed design and some experiments. This chapter addresses objective three defined in Chapter 1.

In this chapter, the following design decisions are addressed:

- number of Halbach array directions of magnetization,
- selection of neodymium-iron-boron vs. samarium cobalt for the permanent magnet material,

- the use of end turn cooling,
- selection of Litz wire gauge, and
- degree of skewing the stator.

Sensitivity studies are performed on the design parameters of the electric machine. For the first time, the chapter introduces the power electronics necessary for a turbo-electric drive. In addition, an iterative design approach is used in which key learnings from the design phase are incorporated back into the framework to assess the impact on the electric machine design point.

4.1 Demonstrator

4.1.1 Configuration

A back-to-back configuration, shown in Fig. 4-1, will be used to characterize the integrated demonstrator performance. In this configuration, one copy of the electric machine operates as a generator and powers the other copy which is operating as a motor. The two copies are coupled via a shaft such that the motor is providing power back into the generator. Thus, only the losses of the system need to be provided by an external source. Assuming 92% efficiency, only 160 kW of power are required to operate two integrated demonstrators, as opposed to 1 MW for a standalone one. This power is available in the Gas Turbine Lab test cell.

The electric machine will not have turbomachine blades on the outer diameter because they only generate windage loss in the proposed demonstrator configuration, but the design could be integrated with compressor blades in future iterations to test the IPM concept from Chapter 3. Each electric machine is connected to thirty sets of full bridge converters. The power electronics utilize low loss, high voltage silicon carbide transistors as switches.

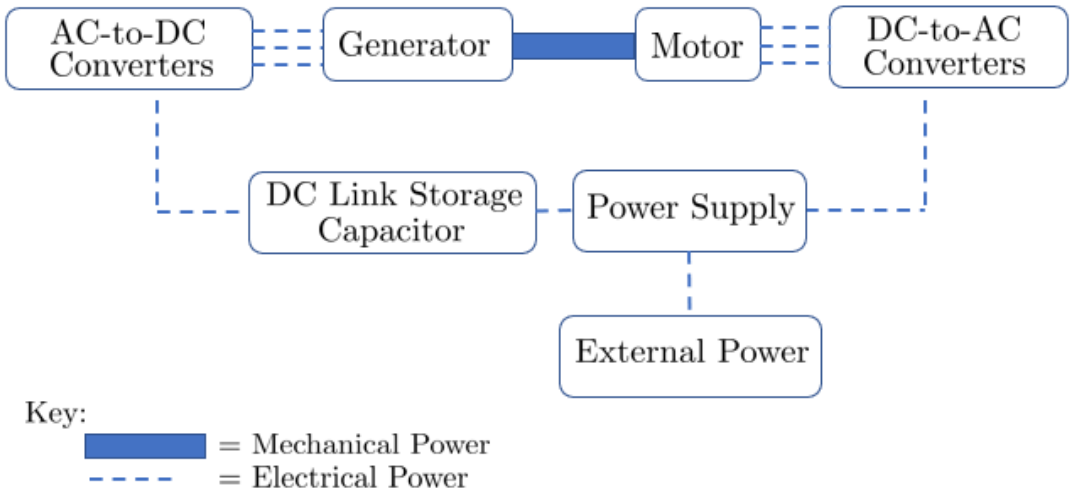

Figure 4-1: In the demonstrator configuration, a motor and generator are connected back-to-back such that only the losses need to be provided by an external power source.

4.1.2 Objectives

The objective of the demonstrator is to prove the feasibility of the high specific power, tooth-and-slot Halbach array design via a one megawatt technology demonstration. The demonstrator seeks to showcase four critical enabling technologies:

1. air-cooling of an integrated, high power density electric machine,
2. structural integrity and rotordynamics of the high-speed Halbach array rotor,
3. low-loss performance of the stator architecture, and
4. integrated, high specific power electronic drives.

The mass of each component of the demonstrator will be measured such that the specific powers of each subsystem can be compared to their predicted specific powers. In addition, the efficiency of the power electronics and electric machines will be measured for comparison against their predicted efficiencies. The technical demonstration will be considered successful if the overall demonstrator meets its efficiency and specific power targets, discussed in Chapter 5, at one megawatt of rated power.

In addition to measuring the specific power and efficiency, other parameters of interest on the electric machine side are the torque, torque ripple, open circuit voltage, terminal voltage, resistance, inductance, and hotspot temperatures. These values will be compared against the analytic and finite element analysis predictions to identify where the machine performance deviates from the models in practice. This information could be incorporated back into the co-optimization approach for any future iterations.

4.2 Co-optimization

The optimization framework in this chapter derives from the trade space analysis framework in the prior chapters. However, the framework is now updated to include the power electronics design. The thermal management system is then designed for cooling both the electric machine and the power electronics. In addition, design decisions on the power electronics, such as transistor switching frequency, affects the performance of the electric machine and vice versa. The objective of the framework in this chapter is to maximize system specific power which accounts for the electric machine, power electronics, turbomachine rim, and thermal management system. This system-level optimization is referred to as co-optimization.

4.2.1 Approach

Figure 4-2 shows how the co-optimization framework functions at a high level. This is similar to the block diagram for the trade space analysis framework in Chapter 3, except that it now includes the power electronics. The power electronics module includes mass, available cooling area, and loss models. The mass and losses both factor into the specific power metric. The power electronics cooling area and losses are used for the thermal management system design.

An iterative approach was used to arrive at an initial design point for a detailed design. These iterations have included a non-advocate review (NAR), several rounds of co-optimization, and ultimately a preliminary design review (PDR) where the

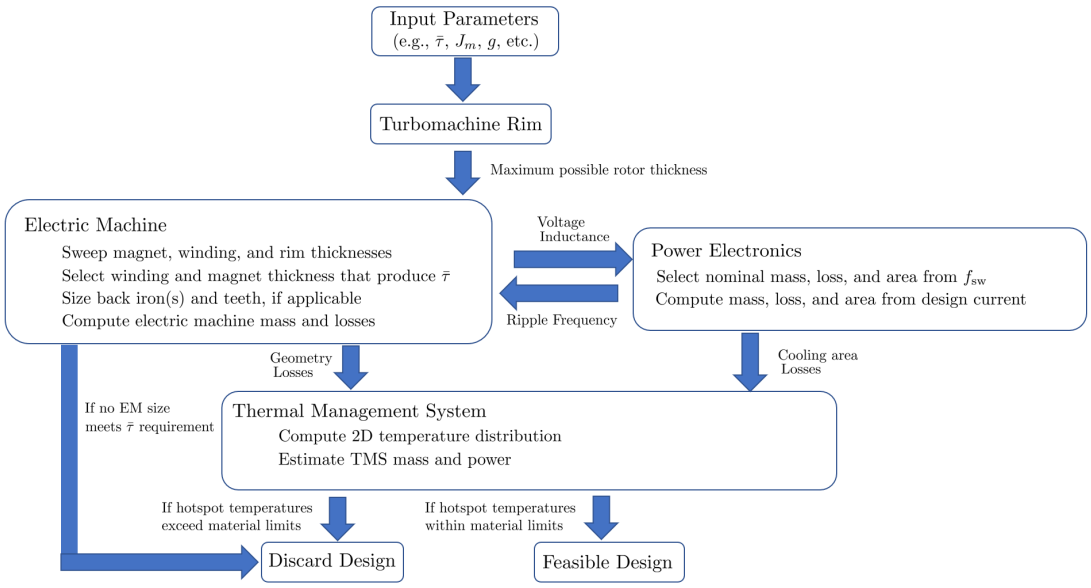

Figure 4-2: The framework from Chapter 3 is updated to include the power electronics.

design was nominally frozen. As the project moved from non-advocate review (NAR) to preliminary design review (PDR), new findings such as measured core loss data were continuously incorporated into the co-optimization framework in the form of new models and data to understand their impact on the optimal design point. Figure 4-3 summarizes the major model changes that were included from NAR to PDR.

As the co-optimization framework was updated to include the new findings from Fig. 4-3, the optimum demonstrator, and hence its specific power, changed as well. Figure 4-4 shows specifically how the electric machine specific power changed with each iteration as a consequence of the updates shown in Fig. 4-3. The University of Illinois Urbana-Champaign, University of Wisconsin, and University of Nottingham motor conceptual designs, and NASA 2030 specific power target for electric machines are shown for comparison.

Several models were added and changes were made to the framework from Chapter 3. These additions are described in the next section.

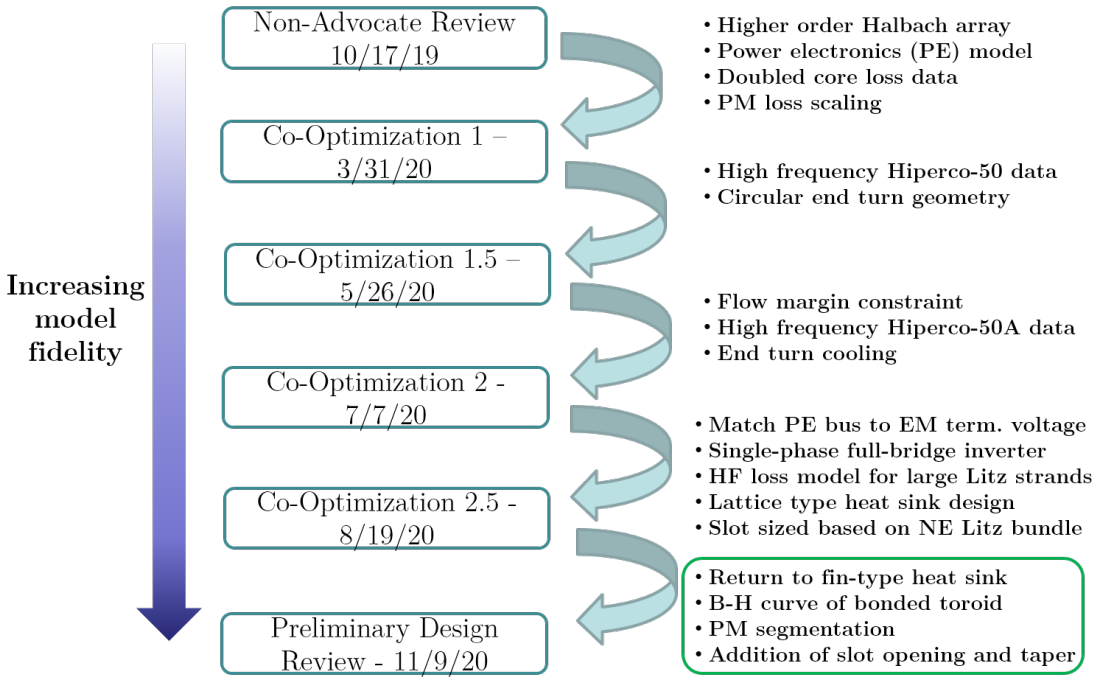

Figure 4-3: Each design iteration incorporated additional models or data to increase fidelity.

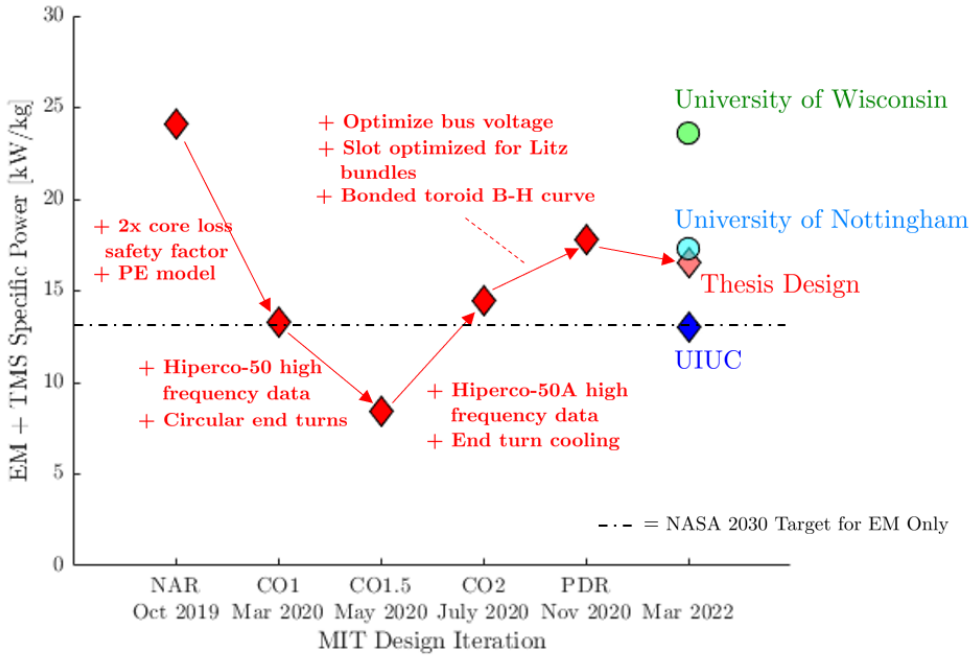

Figure 4-4: Specific power first decreases from NAR to CO1, but continually increases after CO1 with additional thermal modeling.

4.3 Optimization Framework Updates

The optimization framework used in this chapter includes the following new models and changes:

- higher order Halbach array magnetic flux density model,
- power electronics mass, area, and loss models,
- high frequency electric machine loss models,
- doubling of the manufacturer core loss,
- Litz wire and slot insulation model, and
- permanent magnet loss model.

Descriptions of these models are provided in the following subsections.

4.3.1 Higher Order Halbach Array Model

Whereas the slotted Halbach array model in Chapter 3 only considered the elimination of the turbomachine rim, an improved Halbach array model is incorporated into the framework in this chapter. This model is based on a derivation provided by Professor James L. Kirtley Jr. at MIT, where the permanent magnets of the Halbach array are represented with 'Chu' magnetic charges [53] and/or Amperican current densities depending on the direction of magnetization [54]. The new model is capable of estimating the increased airgap flux density and torque generated by the Halbach array, as well as the torque ripple. The details of the model are provided in Appendix C with permission of Professor Kirtley.

4.3.2 Power Electronics Models

The power electronics mass and loss models were developed by colleague Mohammad Qasim [29]. Both three phase and full bridge inverters were considered at the beginning of the demonstrator design as discussed in Ref. [28]. Three phase inverters are

a common way of driving electric machines. An example of a three phase inverter is shown in Fig. 4-5. The switches shown in the circuit diagram of Fig. 4-5 are silicon carbide MOSFETs.

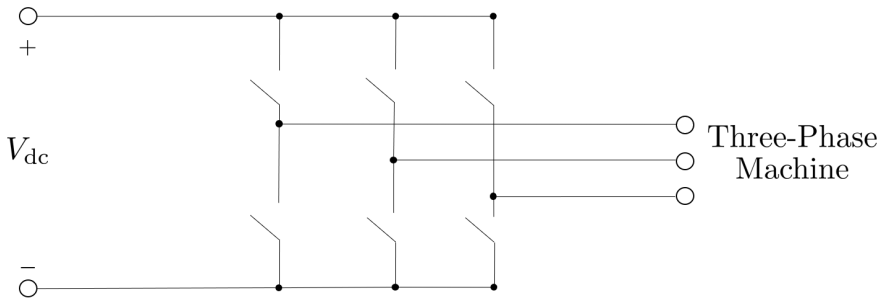

Figure 4-5: Circuit representation of a three-phase inverter.

However, since the electric machine for the demonstrator is in a new design regime (i.e., high power, high speed, and low inductance), single phase, full bridge inverters were also considered for the motor drive. In a comparison study between three phase and full bridge inverter circuits, it was concluded that individual, full bridge circuits for each phase are desireable for high-speed, low-inductance machines [28].

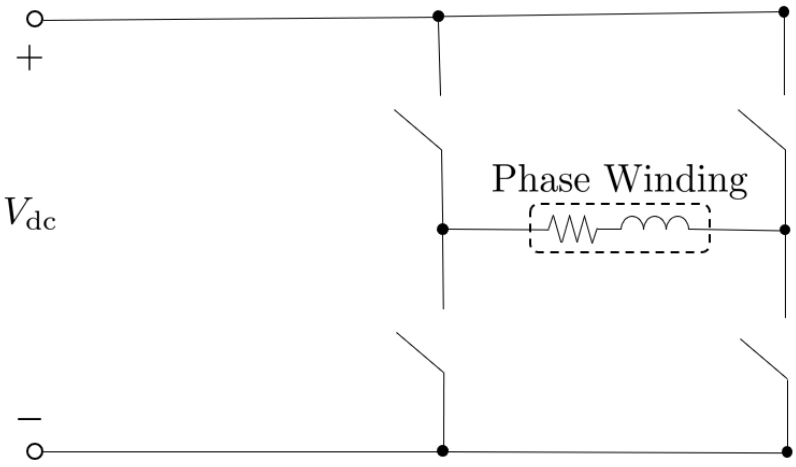

Figure 4-6: Circuit representation of a full bridge inverter.

The power electronics constrain the electric machine design in that they have a maximum operating voltage depending on the transistor type. For the full bridge

circuits for the demonstrator, silicon carbide MOSFETs were used. The electric machine terminal voltage is constrained such that it does not exceed the MOSFET device limit. This constraint was added to the co-optimization loop.

The switching of the power electronics transistors generate a high frequency ripple that create additional losses in the electric machine, which increases the hotspot temperatures of the machine. These high frequency losses are described in the next subsection.

4.3.3 High Frequency Electric Machine Losses

The transistors in the power electronics switch such that a higher frequency ripple current is generated. Thus, the current in the electric machine consists of the drive current at the fundamental frequency plus this ripple current. While the loss models for the fundamental frequency were established in previous chapters, the losses due to the ripple current were not. Therefore two new loss models for the electric machine were developed:

1. high frequency AC winding loss, and

2. high frequency core loss.

The high frequency AC winding loss model was implemented by Mohammad Qasim and it is based on work from Xi Nan and C. R. Sullivan in Refs. [55] and [56]. The high frequency core loss model was implemented by creating a reluctance circuit to estimate the resistance of the laminations.

4.3.4 Detailed Winding Geometry

Although Chapter 3 considered some aspects of the windings such as the winding insulation, the number of turns were fixed at two since there were no voltage or current requirements. However, with the addition of the power electronics, the number of turns in a slot is now an important design parameter. Specifically, additional turns will increase the voltage.

To maximize the amount of copper in a rectangular slot, rectangular Litz bundles such as that of Fig. 4-7 or from Ref. [67] were considered in the design. This particular bundle consists of 19 Litz strands of US American Wire Gauge (AWG) 24, which corresponds to a 0.511 mm diameter for each strand. The bundle in Fig. 4-7 only has two rows of strands - one with nine and the other with ten strands. However, it is feasible to use other strand counts or wire gauges at the tradeoff of achieving a different fill factor. The details of the windings were considered in this design phase.

Figure 4-7: Photo of a 19 strand Litz bundle that was ultimately selected for the final machine.

4.3.5 Permanent Magnet Loss Model

In Chapter 3, the permanent magnet loss was modeled as a simple, constant power loss per unit mass. This value was based on finite element analysis of several design points. In this chapter, the framework is updated to include more detailed permanent magnet scaling that captures the dependence on design parameters such as slot current density, angular speed, and pole pair count.

A model for estimating the losses due to modulation of the permanent magnet flux density from the slot openings is derived in Ref. [57]. This loss component was simulated in 3D finite element analysis and was found to be on the order of 150 W for the demonstrator design point, which is small relative to the kilowatts of loss generated from the winding spatial harmonics. For the co-optimization model, this loss component is assumed to be negligible compared to the spatial harmonics of the

windings. However, this loss component can be on the order of kilowatts if large slot openings are used so this assumption is checked in finite element analysis. For example, for the PDR design point, the permanent losses increase from 1.5 kW to 10.4 kW if the slots are completely open.

Permanent Magnet Eddy Currents

For tooth-and-slot permanent magnet machines, the eddy currents in the permanent magnets are generated by (1) the modulation of the Halbach array magnetic field from the slot openings [57], (2) the space harmonics from the stator windings, and (3) the time harmonics from the power electronics switching. A simplified model, shown in Fig. 4-8, helps explain the source of the eddy current loss. In this model, a radial, time-varying magnetic field, B_r, is passing through a magnet segment spanning from an initial angle, ϕ_i, to a final angle, ϕ_f, with thickness t_{mag}. The magnet segment is assumed to be sufficiently thin such that B_r does not vary radially, but does vary azimuthally.

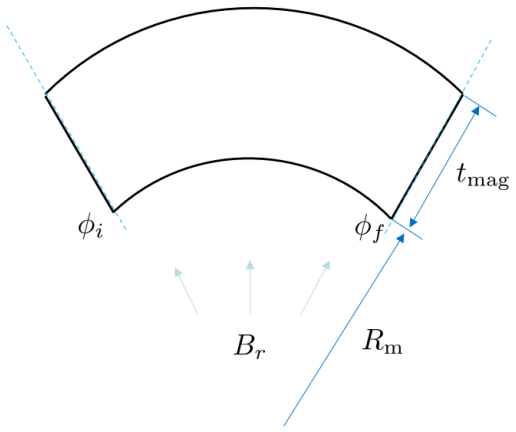

Figure 4-8: The magnetic flux density at the stator surface becomes more sinusoidal with increasing number of magnetization directions.

From Faraday's law,

$$\nabla \times E = -\frac{\partial B_r}{\partial t}\hat{r} \tag{4.1}$$

then, expanding the left-hand side of Eqn. 4.1 and considering the radial component,

$$\frac{1}{r}\frac{\partial E_z}{\partial \phi} - \frac{\partial E_\phi}{\partial z} = -\frac{\partial B_r}{\partial t} \tag{4.2}$$

In this simplified model, the magnet is assumed to be axially long such that there is negligible variation of the azimuthal electric field in the axial direction, or $\frac{\partial E_\phi}{\partial z} = 0$. For a smaller magnet, the eddy current turns at the front and back of the permanent magnet such that this term could contribute to the loss. This contribution is computed in 3D finite element analysis. For this simple model, the electric field in the axial direction, as a function of the azimuthal angle, ϕ, is solved via the integral:

$$E_z(\phi) = -\int_{\phi_i}^{\phi} \frac{\partial B_r(\phi)}{\partial t} R_m d\phi \tag{4.3}$$

where R_m is used as the radius under the radially thin magnet assumption. The eddy currents in the permanent magnet circulate such that there is zero net current:

$$t_{\text{mag}} \int_{\phi_i}^{\phi_f} \sigma E_z(\phi) R_m d\phi = 0 \tag{4.4}$$

or, equivalently, the average value of the E-field is zero. If $B_r(\phi, t)$ is known, the E-field can be solved by Eqn. 4.3 and Eqn. 4.4. Lastly, the power dissipated in the permanent magnet segment is

$$P(t) = \ell t_{\text{mag}} \int_{\phi_i}^{\phi_f} \sigma E_z(\phi, t)^2 R_m d\phi \tag{4.5}$$

The primary challenge in estimating these losses in closed form is deriving an expression for $B_r(\phi, t)$, and subsequently $E_z(\phi, t)$ via Eqns. 4.3-4.4.

The following subsection describes the losses due to the winding spatial harmonics. The losses due to the time harmonics from the power electronics switching are simulated in 3D FEA in Chapter 5.

Stator Spatial Harmonics

The fundamental component of the magnetic field from the stator is synchronous to that of the rotor, so this fundamental component does not generate permanent magnet losses. However, for a tooth-and-slot stator, the stator magnetic field concentrates at the slot openings, which appear closer to a square wave then a sinusoid. The effect is that higher order harmonics are generated, which create asynchronous fields in the permanent magnet frame of reference. Therefore, the $\frac{\partial B_r}{\partial t}$ term in Eqn. 4.1 is non-zero and eddy currents are generated.

For a one slot per pole per phase configuration with three phases, the equivalent surface current from the three slots is approximately

$$\begin{aligned} K(\theta_m, t) = & \frac{I_{\text{pk}}}{w_{\text{so}}} \sum_{n=1,3,5,\cdots} K_n \sin(np\theta_m) \cos(\omega_e t) + \\ & K_n \sin(np(\theta_m - 2\pi/3)) \cos(\omega_e t - 2\pi/3) + \\ & K_n \sin(np(\theta_m + 2\pi/3)) \cos(\omega_e t + 2\pi/3) \end{aligned} \tag{4.6}$$

where $I_{\text{pk}} = J_{\text{pk}} A_{\text{slot}}$ is the peak current in a turn and w_{so} is the slot opening width. The Fourier series coefficients, provided courtesy of colleague Henry Andersen, are

$$K_n = \frac{2}{n\pi} \left[\cos\left(\frac{n\pi}{2} - np \frac{w_{\text{so}}}{2R_{\text{ag}}} \right) - \cos\left(\frac{n\pi}{2} + np \frac{w_{\text{so}}}{2R_{\text{ag}}} \right) \right] \tag{4.7}$$

Equation 4.6 can be simplified to

$$K(\theta_m, t) = \frac{3}{2} \frac{I}{w_{\text{slot}}} \left[\sum_{n=1,7,\cdots} K_n \sin(np\theta_m - \omega_e t) + \sum_{n=5,11,\cdots} K_n \sin(np\theta_m + \omega_e t) \right] \tag{4.8}$$

From the rotor frame of reference, the 7th, 13th, etc. harmonics appear to be traveling in the same direction as the rotor. However, the 5th, 11th, 17th, etc. are traveling in the opposite. Considering angle $\theta_m = \Omega t$ and $p\Omega = \omega_e$, Eqn. 4.8 can be rewritten as

$$K(t) = \frac{3}{2} \frac{I}{w_{\text{slot}}} \left[\sum_{n=1,7,13,\cdots} K_n \sin((n-1)\omega_e t) + \sum_{n=5,11,17,\cdots} K_n \sin((n+1)\omega_e t) \right] \tag{4.9}$$

which is lastly equivalent to

$$K\left(\theta_m\right) = \frac{3}{2}\frac{I}{w_{\text{slot}}}\left[\sum_{n=0,6,12,\cdots}\left(K_{n-1}+K_{n+1}\right)\sin\left(n\omega_e t\right)\right] \tag{4.10}$$

The scalar potential solution to Laplace's equation in cylindrical coordinates has the general form

$$\psi = \sum_{n}^{\infty}\left(A_n\sin\left(np\theta_m\right)+B_n\cos\left(np\theta_m\right)\right)\left(C_n r^{np}+D_n r^{-np}\right) \tag{4.11}$$

where n is the harmonic number, p is the number of pole pairs, and A_n, B_n, C_n and D_n are scalars that can vary with harmonic number [58].

Since there is no ferromagnetic material outside the Halbach array, the potential decays to zero as $r \to \infty$ which is compatible with the r^{-np} solutions. In addition, if $K\left(\theta_m\right)$ is used as a boundary condition at the stator surface and the ferromagnetic stator is assumed to be infinitely permeable (i.e., ψ vanishes at the stator surface), then the scalar potential solution will contain the $\cos\left(np\theta_m\right)$ terms. Therefore, the scalar potential in the airgap has the form

$$\psi_{\text{ag}} = \sum_{n}^{\infty} D_n r^{-np}\cos\left(np\theta_m-\omega_e t\right)+E_n r^{-np}\cos\left(np\theta_m+\omega_e t\right) \tag{4.12}$$

Lastly, taking $H=-\nabla\psi$ and setting it equal to 4.10 at $r=R_{\text{ag}}$, the coefficients D_n and E_n are solved as

$$D_n = -\frac{3}{2}\frac{I_{\text{pk}}}{w_{\text{so}}}\frac{K_n}{npR_{\text{ag}}^{-np-1}}, \qquad n=1,7,13,\cdots \tag{4.13}$$

$$E_n = -\frac{3}{2}\frac{I_{\text{pk}}}{w_{\text{so}}}\frac{K_n}{npR_{\text{ag}}^{-np-1}}, \qquad n=5,11,17,\cdots \tag{4.14}$$

The radial H-field is therefore

$$H_r = -\left[\sum_{n=1,7,\cdots} D_n \left(np\right) r^{-np-1} \sin\left(np\phi - \omega_e t\right) + \sum_{n=5,11,\cdots} E_n \left(np\right) r^{-np-1} \sin\left(np\phi + \omega_e t\right) \right] \tag{4.15}$$

or substituting Eqn. 4.13 into Eqn. 4.15

$$H_r = \frac{3}{2}\frac{I_{\text{pk}}}{w_{\text{so}}}\left[\sum_{n=1,7,13,\cdots} K_n \left(\frac{r}{R_{\text{ag}}}\right)^{-np-1} \sin\left(np\phi - \omega_e t\right) + \sum_{n=5,11,17,\cdots} K_n \left(\frac{r}{R_{\text{ag}}}\right)^{-np-1} \sin\left(np\phi + \omega_e t\right) \right] \tag{4.16}$$

In the rotor frame of reference, the radial H-field is the sum of radially decaying $6n$ harmonics:

$$H_r = \frac{3}{2}\frac{I_{\text{pk}}}{w_{\text{so}}}\left[\sum_{n=0,6,\cdots} \left(K_{n-1} \left(\frac{r}{R_{\text{ag}}}\right)^{-(n-1)p-1} \cdots + K_{n+1} \left(\frac{r}{R_{\text{ag}}}\right)^{-(n+1)p-1} \right) \sin\left(n\omega_e t\right)\right] \tag{4.17}$$

and the radial B-field, B_r, is equal to $\mu_0 H_r$. If the time derivative of Eqn. 4.17 is taken, then $\frac{\partial B_r}{\partial t}$ is notably proportional to slot current density from the I_{pk} term and electrical frequency from the sine term. The permanent magnet losses are therefore expected to scale with slot current density and electrical frequency squared per Eqn. 4.5.

Comparison With 2D Finite Element Analysis

The scaling from the prior subsection was checked and informed with the use of 2D finite element analysis (FEA). In this 2D FEA setup, a three phase current source is driving an electric machine as a motor. The rotor is fixed to rotate at a constant speed corresponding to the design speed. The time-varying magnetic fields were extracted

throughout the permanent magnets and the eddy current loss, as computed by the 2D FEA software, was collected.

An example rotor, shown in Fig. 4-9, was discretized into many segments radially to extracted the B-field. Specifically, the time-varying field was extracted along each radial arc at a fixed angle in the rotor frame of reference. In this particular example, the electric machine was driven at 2 kHz fundamental.

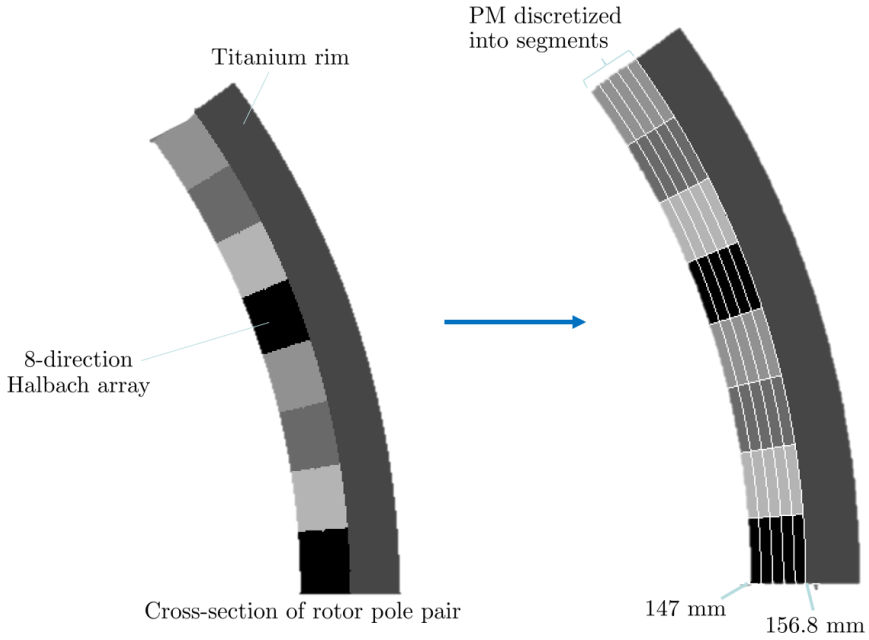

Figure 4-9: The time-varying magnetic flux density was extracted at different radii for an example in 2D finite element analysis.

Figure 4-10 shows the derivative of the time-varying B-field within the permanent magnets at different radii. All of the signals are periodic as expected from Eqn. 4.17. However, the magnetic flux density becomes more sinusoidal towards the back of the permanent magnet which suggests that the higher order harmonics have decayed.

A fast fourier transform on the waveform from Fig. 4-10 shows the spectrum of the time-varying magnetic flux density. The spectrum shows the 6n harmonics at 12 kHz, 24 kHz, etc. Since the fundamental is 2 kHz, these 6n harmonics match that predicted from Eqn. 4.8.

The peak magnitudes of the harmonics are plotted versus radii in Fig. 4-12. When plotted this way, the harmonics clearly decay with radius as expected from Eqn. 4.17.

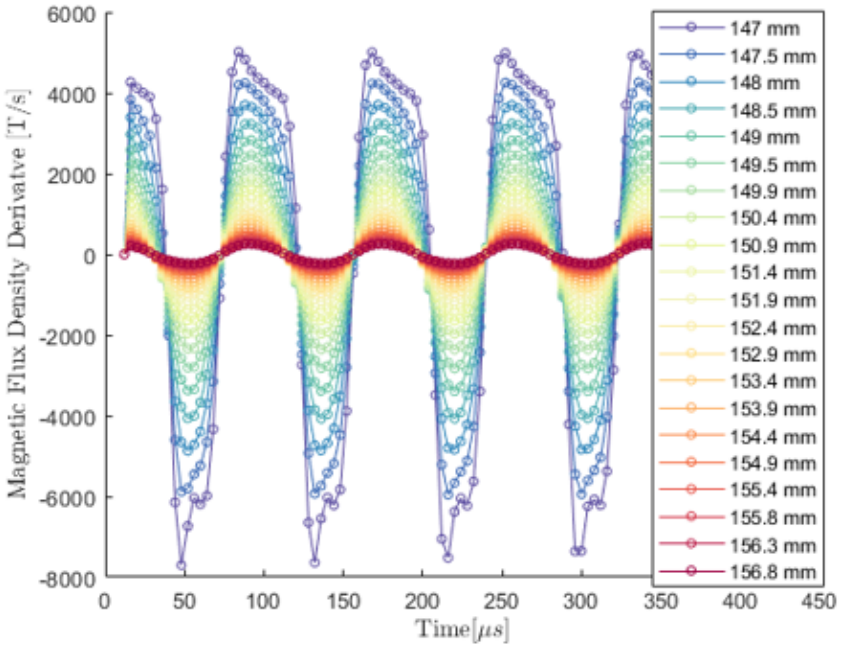

Figure 4-10: The time-varying magnetic flux density more closely approximate a pure sinusoid towards the back of the permanent magnet.

For the 10 pole machine in this example, the first harmonic ($n = 6$) is expected to be the sum of an $r^{-5(10)-1}$ and $r^{-7(10)-1}$ term. A curve fit, shown with the blue squares in Fig. 4-12, shows the FEA data matches this trend. The power dissipated in this magnet is then proportional to the area under the curve, or

$$P_{loss,PM} \propto \int_{R_{\text{ag}}+g}^{R_{\text{ag}}+g+t_{\text{mag}}} \left[C \left(\frac{r}{R_{\text{ag}}} \right)^{-51} + D \left(\frac{r}{R_{\text{ag}}} \right)^{-71} \right]^2 dr \tag{4.18}$$

The scaling law is finally derived by considering what happens when, for example, the airgap thickness is changed. Figure 4-13 shows how the integration window for the permanent magnet loss shifts when the air gap is increased from 2mm to 4mm. In this particular example, the higher order harmonics are negligible.

In general for a machine with p pole pairs, and only considering the first harmonic term, the permanent magnet losses are proportional to the magnet radius, air gap thickness, and geometry as

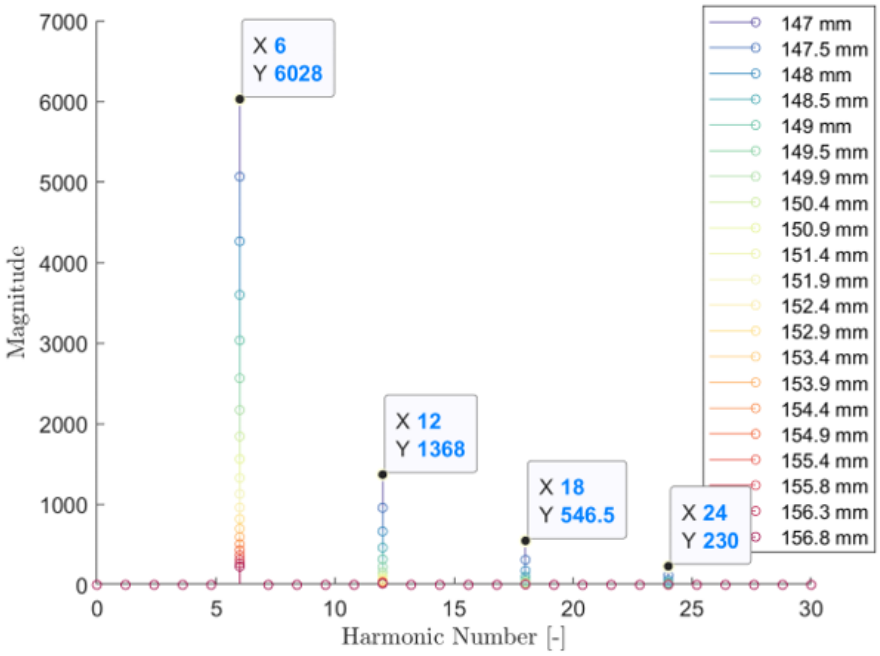

Figure 4-11: The spectrum of the dB_r/dt signals shows the $6n$ harmonics of the signals relative to the fundamental at 2 kHz.

$$P_{loss,PM} \propto \int_{R_{\text{ag}}+g}^{R_{\text{ag}}+g+t_{\text{mag}}} \left[C \left(\frac{r}{R_{\text{ag}}} \right)^{-5p-1} + D \left(\frac{r}{R_{\text{ag}}} \right)^{-7p-1} \right]^2 dr \tag{4.19}$$

For higher pole pair count machines, the $\frac{r}{R_{\text{ag}}}^{-5p-1}$ term does not decay as fast as the $\frac{r}{R_{\text{ag}}}^{-7p-1}$, so the latter can be neglected as an approximation. Then, starting from a nominal power loss, P_{nom}, air gap thickness, g_{nom}, and magnet thickness t_{nom}, the permanent magnet losses at a new design point are scaled by

$$f\left(R_m, g, p, t_{\text{mag}}\right) = \frac{\int_{R_{\text{ag}}+g}^{R_{\text{ag}}+g+t_{\text{mag}}} \left[C \left(\frac{r}{R_{\text{ag}}} \right)^{-5p-1} + D \left(\frac{r}{R_{\text{ag}}} \right)^{-7p-1} \right]^2 dr}{\int_{R_{\text{ag}}^{nom}+g^{\text{nom}}}^{R_{\text{ag}}^{nom}+g^{\text{nom}}+t_{\text{mag}}^{nom}} \left[C \left(\frac{r}{R_{\text{ag}}^{nom}} \right)^{-5p^{nom}-1} + D \left(\frac{r}{R_{\text{ag}}^{nom}} \right)^{-7p^{nom}-1} \right]^2 dr} \tag{4.20}$$

This scaling provides the last information needed to derive the PM scaling formulation in the co-optimizer.

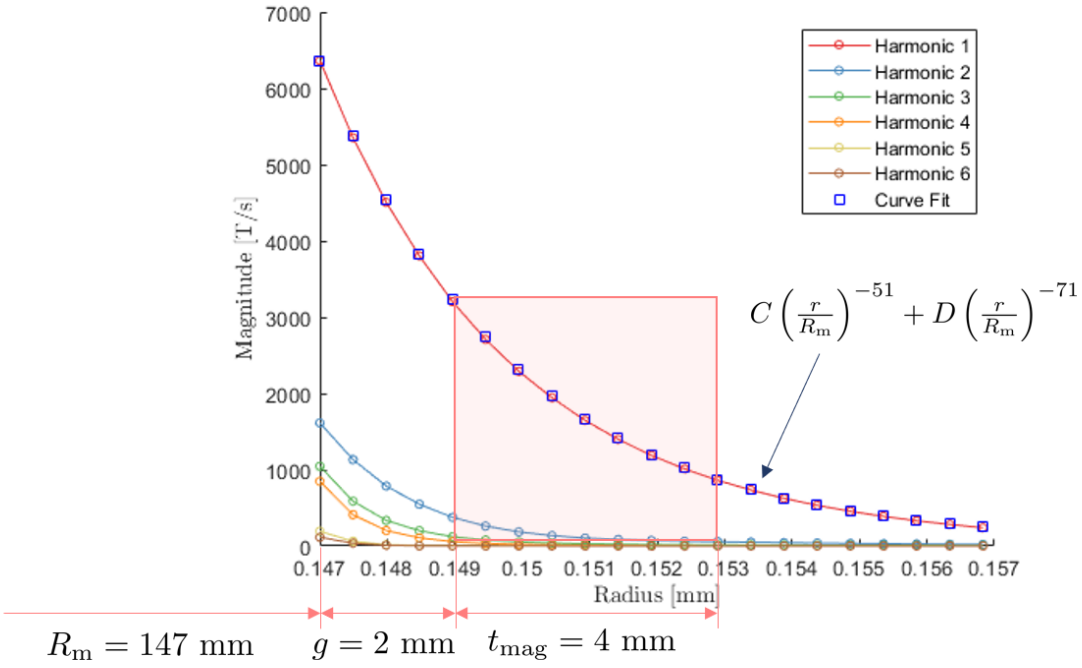

Figure 4-12: The magnetic flux density at the stator surface becomes more sinusoidal with increasing number of magnetization directions.

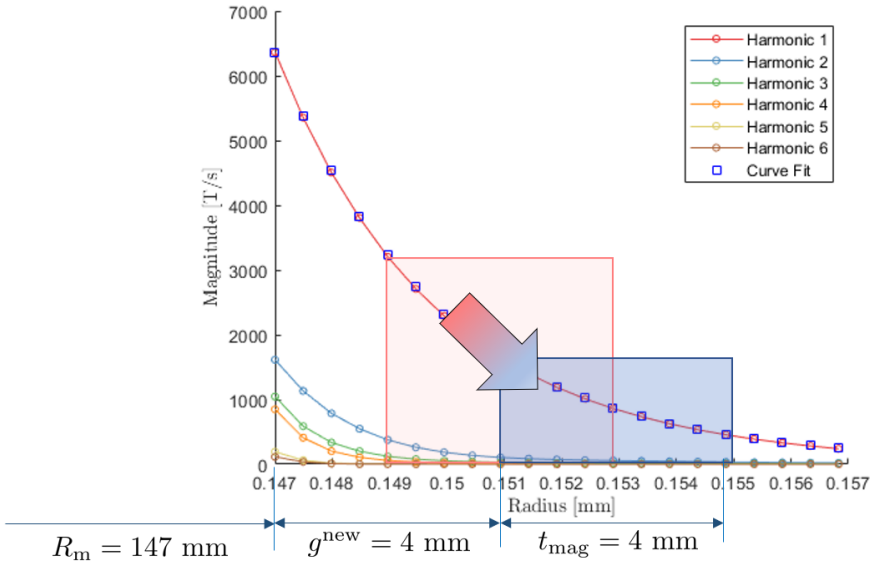

Figure 4-13: The magnetic flux density at the stator surface becomes more sinusoidal with increasing number of magnetization directions.

Scaling Formulation

The permanent magnet loss scaling formulation is based on using 2D FEA data from a nominal design point, whose variables are denoted with subscript *nom*, and then using the scaling discussed in the last two subsections to estimate the loss at a new design point. From Eqn. 4.5, the ratio of these losses is

$$\frac{P_{\mathrm{PM}}}{P_{\mathrm{nom}}} = \left(\frac{\sigma}{\sigma_{\mathrm{nom}}}\right)\left(\frac{\ell}{\ell_{\mathrm{nom}}}\right)\left(\frac{t_{\mathrm{mag}}}{t_{\mathrm{mag,nom}}}\right)\frac{\int_{\phi_{i,nom}}^{\phi_{f,nom}} E_{\mathrm{z,nom}}\left(\phi\right)^2 R_{m,nom} d\phi}{\int_{\phi_i}^{\phi_f} E_z\left(\phi\right)^2 R_m d\phi} \tag{4.21}$$

Specifically, the permanent magnet loss scales as

$$P_{\mathrm{PM}} = P_{\mathrm{PM,nom}}\left(\frac{\sigma}{\sigma_{\mathrm{nom}}}\right)\left(\frac{\ell}{\ell_{\mathrm{nom}}}\right)\left(\frac{\omega_e}{\omega_{\mathrm{e,nom}}}\right)^2\left(\frac{t_{\mathrm{winding}}}{t_{\mathrm{winding,nom}}}\right)^2\left(\frac{J}{J_{\mathrm{nom}}}\right)^2 f\left(r_{\mathrm{ag}}, p, t_{\mathrm{mag}}, g\right) \tag{4.22}$$

where $f\left(r_{\mathrm{ag}}, p, t_{\mathrm{mag}}, g\right)$ corresponds to the form of Eqn. 4.20. The J and t_{winding} terms appear under an assumption of constant $w_{\mathrm{slot}}/w_{\mathrm{so}}$. In addition, only the first harmonic term was considered in this scaling, but higher order harmonics can be incorporated to improve accuracy.

This permanent magnet loss scaling was tested using 2D FEA by varying different design parameters that appear in Eqn. 4.22 and comparing the permanent magnet loss. Figure 4-14 shows the loss scaling with slot current density, air gap thickness, pole pair count, and rotational speed. For this particular study, the nominal slot current density was 13 A/mm^2, nominal rotational speed was 12,000 rpm, nominal pole pair count was 10, and nominal air gap thickness was 2mm. The largest observed difference was for the air gap thickness scaling, which was found to be approximately 30%. For the co-optimizer, permanent magnet losses were therefore extracted at all swept air gap thicknesses and used as nominal losses to improve the scaling accuracy.

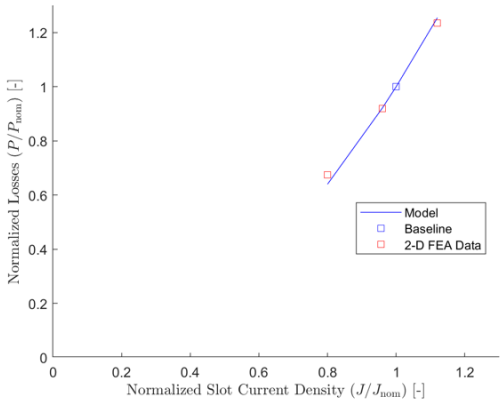

(a) PM loss scaling with slot current density.

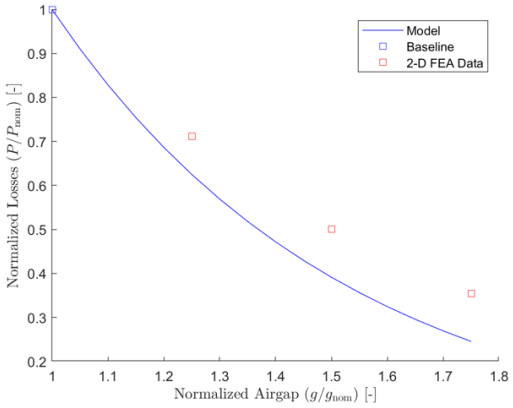

(b) PM loss scaling with air gap thickness.

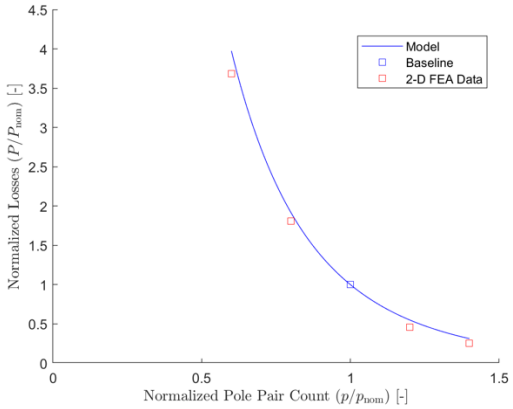

(c) PM loss scaling with pole pair count.

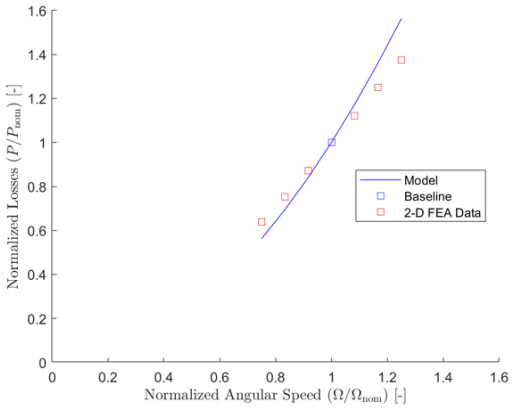

(d) PM loss scaling with rotational speed.

Figure 4-14: PM loss scaling.

4.4 Design Decisions

The updated models from Section 4.3 were used to inform many demonstrator design decisions from the non advocate review up to the preliminary design review. The following subsections describe the steps towards making these decisions and the outcomes.

4.4.1 Torque Ripple Reduction Technique

An electric machine designed for integration with a turbomachine will ideally produce constant torque without ripple. The torque ripple is undesirable because it can lead to mechanical issues such as bearing wear as well as noise [59]. A traditional method

for reducing the torque ripple is to skew either the rotor or the stator [58]. This method involves staggering the laminations or rotor magnets in the axial direction of the machine. A second method discovered during this design phase is to use more directions of magnetization in the Halbach array. Both options are discussed in the following subsubsections. Ultimately, the machine is not skewed and instead a four-directional Halbach array is used.

Stator Skew

One method for reducing the torque ripple of an electric machine is to skew the stator [58]. Skewing means to stack each lamination of the electric machine at an angle compared to the previous lamination. The interaction between the stator and rotor fields will average out across the lamination stack, which eliminates the cogging and ripple torque. There are two downsides to skewing the stator. First, features such as keyways for the internal heatsink will be staggered and would require either a complicated heatsink design or custom laminations throughout the stack to keep the heatsink in place. Second, the length of the winding in the slot is increased, which increases Ohmic losses [58]. An example of a skewed stator is shown in Fig. 4-15.

(a) Isolateral view of skewed stator.

(b) Side view of skewed stator.

Figure 4-15: The laminations in a skewed stator are stacked at angular offsets such that the full machine appears twisted.

To evaluate the impact of skewing the stator, the skewing factor derived by Professor Kirtley in Ref. [60] was used. The skew factor, $k_{\sigma n}$, is defined as

$$k_{\sigma n} = \frac{\sin\left(n\frac{\sigma}{2}\right)}{n\frac{\sigma}{2}} \tag{4.23}$$

where σ is the skew angle and n is the harmonic number. The impact of the skew on an example two block Halbach array machine similar in design to the final demonstrator machine, assuming sinusoidal input currents, is shown in Fig. 4-16. The skew factor and torque harmonics were considered for every odd harmonic from $n = 1$ to $n = 181$.

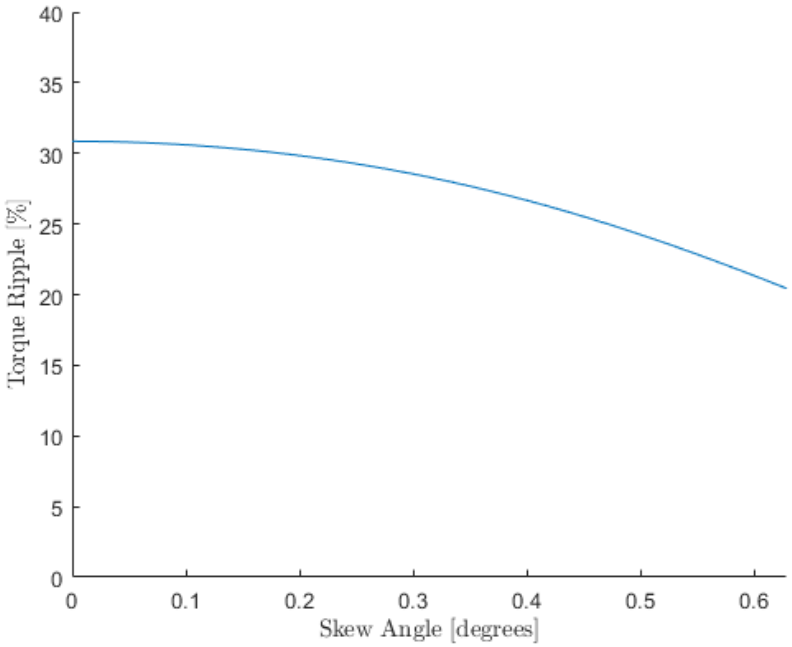

Figure 4-16: Increasing the skew angle of the stator further reduces the torque ripple.

The torque ripple values corresponding to Fig. 4-16 are summarized in Table 4.1. Even with a large skew angle of 36°, the torque ripple is still 133 Nm which is 20% of the average torque. Larger skew angles could be pursued for further reduction, but would also increase the winding loss and manufacturing complexity. Instead, as will be shown in the next subsection, a higher order Halbach array can reduce the torque ripple.

Table 4.1: Torque ripple decreases with increasing skew angle.

Skew Angle [degrees]	**Torque Ripple [Nm]**
0	204.6
9	200.3
18	186.9
27	164.2
36	133.3

Higher Order Halbach Array

A Halbach array reduces the torque ripple from a surface permanent magnet array because it does not produce as many higher order harmonics as a surface permanent magnet array. Although the conventional Halbach array has just four directions of magnetization, it is feasible to add even more directions of magnetization to further reduce torque ripple as shown in Fig. 4-17. However, these higher order Halbach arrays are more complicated to manufacture and add both cost and lead time.

Figure 4-18 shows how additional directions of magnetization in the Halbach array result in a more sinusoidal magnetic flux density. The flux densities in this example are taken at the surface of a stator that is three millimeters from the magnet arrays. Otherwise, the magnet thickness is the same at 10.30 millimeters.

The harmonic content of each type of magnet array is shown in Table 4.2. For this particular design, the swap from surface permanent magnet to the Halbach array increases the fundamental component by 40%. An additional 10% increase is feaible by moving from a two segment array to a six segment array, at increased assembly

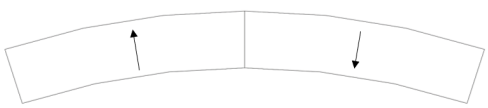

(a) Surface permanent magnet array.

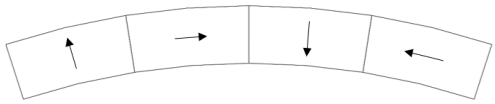

(b) 2 block Halbach array.

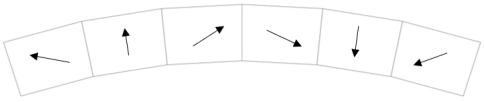

(c) 3 block Halbach array.

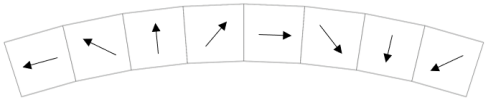

(d) 4 block Halbach array.

Figure 4-17: Higher order Halbach arrays have an increasing amount of directions of magnetization to produce a more sinsusoidal magnetic flux density.

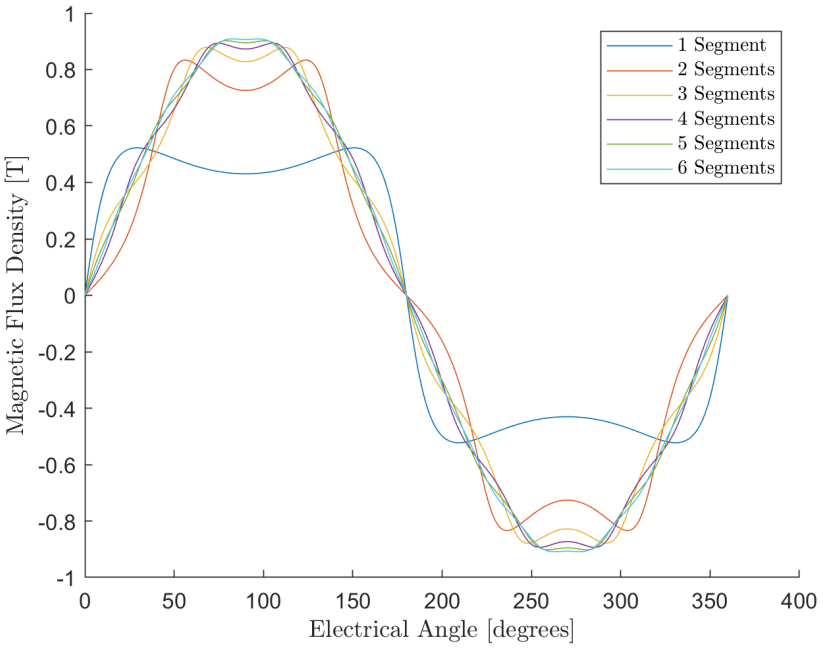

Figure 4-18: The magnetic flux density at the stator surface becomes more sinusoidal with increasing number of magnetization directions.

complexity, cost, and lead time.

While the PDR design did not have a specific torque ripple requirement, the four block Halbach array was selected for PDR design based on both the sub 1% ripple and discussions on cost and lead time with the magnet manufacturer.

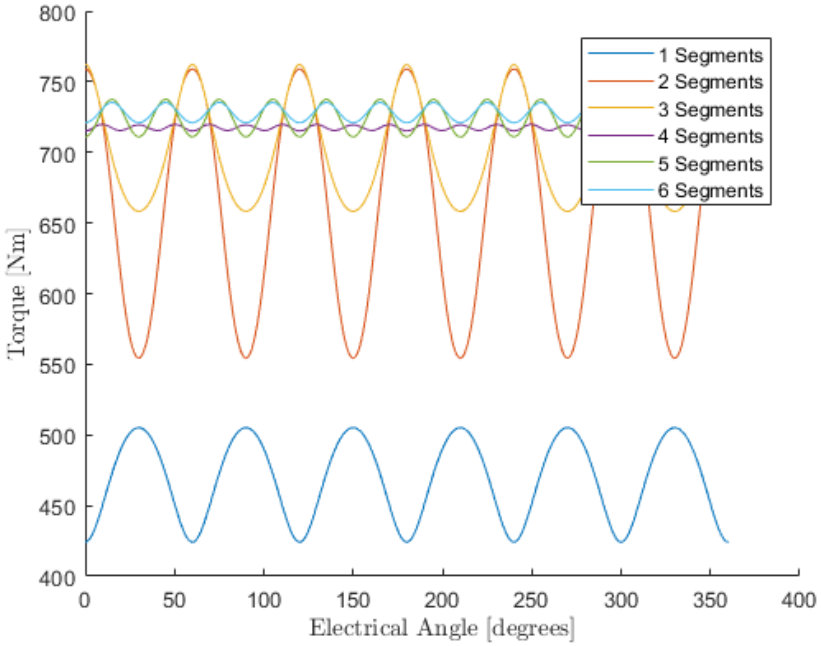

Figure 4-19: Torque ripple is substantially reduced with 4 directions of magnetization onwards.

Table 4.2: The fundamental component of the flux density increases with increasing number of Halbach array segments.

Harmonic Number	**1 Segment**	**2 Segments**	**3 Segments**	**4 Segments**	**5 Segments**	**6 Segments**
1	0.59	0.83	0.88	0.90	0.91	0.92
2	0.22	0	0	0	0	0
3	0.09	-0.13	0	0	0	0
4	0.04	-0	0.06	0	0	0
5	0.02	0.03	0	-0.03	0	0
6	0.01	0	0	0	0.02	0
7	0.01	-0.01	0.01	0	0	-0.01
8	0.03	0	0	0	0	0
9	0.0018	0.0025	0	0.0027	0	0

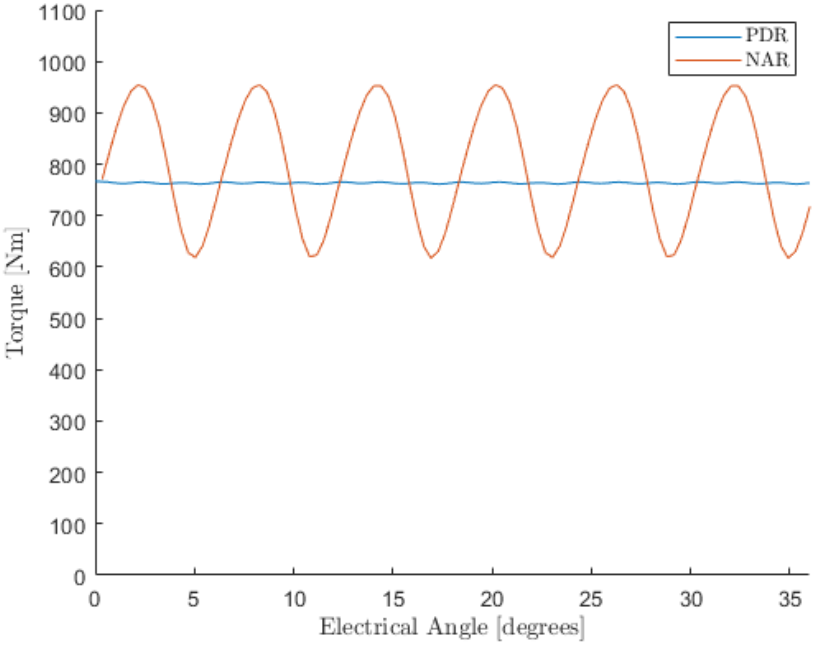

Figure 4-20: The use of a Halbach array reduced the torque ripple from 25% for NAR to less than 1% for the PDR design without skew.

4.4.2 Slot Fill Factor

A common packing structure for litz bundles is a hexagonal packing structure as shown in Fig. 4-21. This structure results in a theoretical 91% fill factor assuming the strands are made entirely of copper. In practice, each strand has an outer insulation layer such that the fill factor is lower than 91%. This outer insulation layer is also shown in Fig. 4-21. The strand insulation thickness decreases with higher American wire gauge (AWG) or, equivalently, thinner litz strands. For example, the insulation thickness for AWG 30 strands is 0.7 mil, whereas for AWG 24 strands the thickness is 0.95 mil. These are thicker than what might be found in literature because the insulation has to withstand the bundle compaction process.

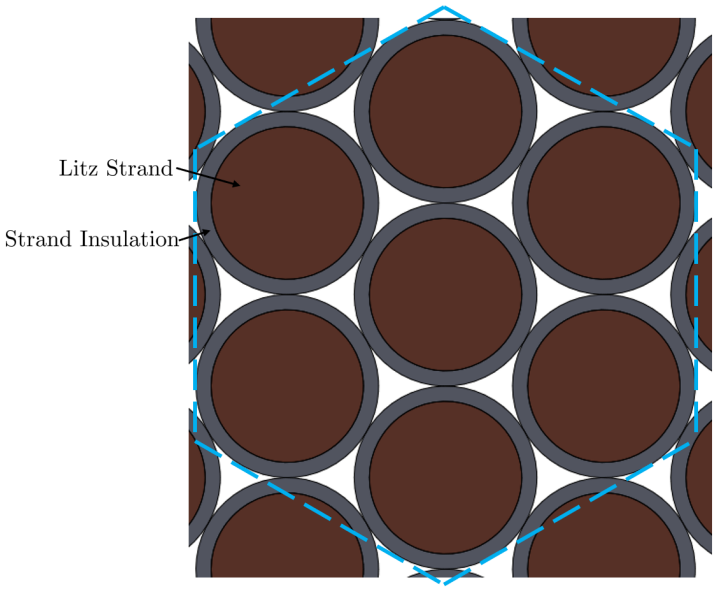

Figure 4-21: 2D cross-sectional area of the hexagonal packing structure as indicated with the light blue hexagon.

A litz bundle consists of multiple litz strands and typically have either a circular or rectangular form. In the rectangular case, the edges of the bundle will have empty space due to the circular form of the strands. The space along the edges for an example litz bundle is shown in Fig. 4-22. Due to this edge effect, the achievable packing factor is closer to around 80% for this example. The impact of this edge effect is ultimately a function of the bundle shape and dimensions.

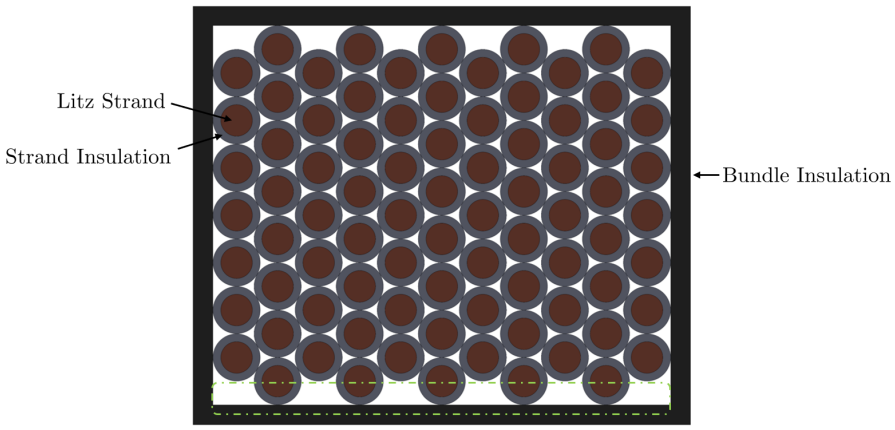

Figure 4-22: When the bundles are packed in a rectangular area, there are large gaps at the edges which minimize packing factor.

Lastly, thicker insulation is placed between the winding turns as well as around the edge of the slot to insulate against the larger turn voltages. A possible layout is shown in Fig. 4-23. These thick insulation layers reduce the available space in the slot for litz wire and therefore further reduces the achievable slot copper fill factor. These insulation layers are made of a material such as Nomex 410 [61] to prevent the bundles from shorting with the stator core. The ratio of slot liner area to total slot area will be a function of the slot dimension, number of turns, and insulation requirements which directly affects the slot liner thickness. Assuming 7 mil slot liner for the example design in Fig. 4-23, only 92% of the slot is left for the litz bundles.

The slot fill factor is expressible as the product of the fraction of the slot remaining after the slot liner, K_{sl}, the fraction of insulated strands to the bundle area, K_{bundle}, and the fraction of a strand that is actually copper, K_{strand}.

$$K_{\text{cu}} = K_{\text{sl}} K_{\text{bundle}} K_{\text{strand}} \tag{4.24}$$

For AWG 24 wires with 0.95 mil insulation thickness, the strand copper fraction, K_{strand}, is 0.84. Although the ideal bundle packing factor is 0.91 for hex, a more realistic number is on the order of 0.8 for K_{bundle}. Lastly, the slot liner factor, K_{sl}, for the example in Fig. 4-23 is 0.92. Using these values for Eqn. 4.24, a maximum slot

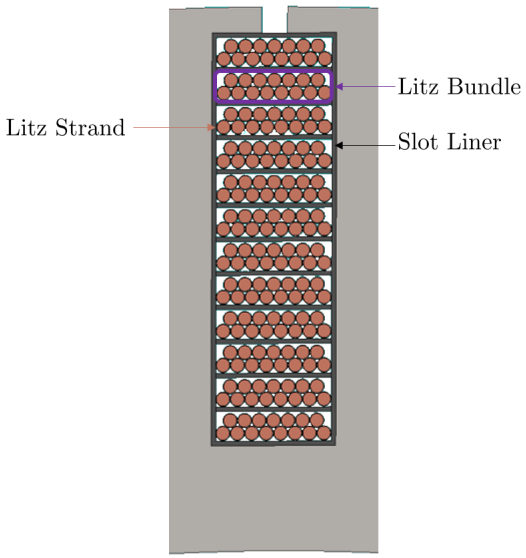

Figure 4-23: Cross-sectional view of a slot with the detailed Litz strands, strand insulation, and slot liner.

copper fill factor of 61.8% is achievable. During the sweeps, the slot copper fill factor optimizes closer to 50% because K_{bundle} is less than 0.8 for the two row rectangular litz bundles shown in Fig. 4-7.

Although the baseline sweep assumed 50% slot copper fill factor, the design space was reswept with 65% fill factor to examine the sensitivity of the optimum to this parameter. Figure 4-24 shows that the higher fill factor shifts the optimum design point to a greater speed. In addition, the demonstrator specific power increases by 6%.

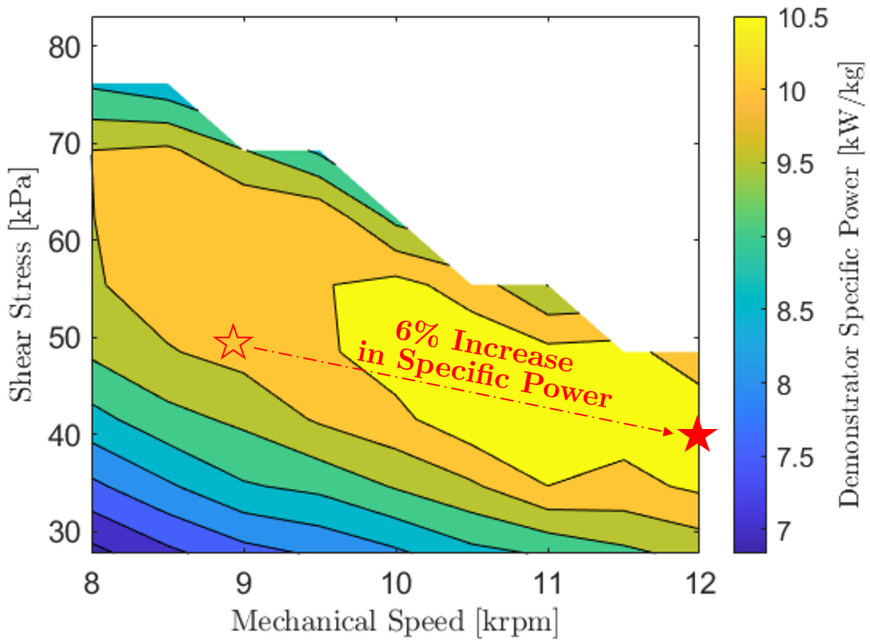

Figure 4-24: Slot copper fill factor of 0.65.

4.4.3 Litz Wire Gauge

A smaller Litz wire diameter reduces the proximity effect and skin effect losses in the windings. The skin effect is the tendency of AC current to concentrate towards the edges of a wire. Since the current is concentrated near the edges, the effective cross-sectional area of the strand is smaller and therefore the resistance and hence losses are greater.

When two conductors are nearby with an alternating current, the magnetic field generated by one will influence the current distribution in the other and vice versa. Similar to the skin effect, this reduces the effective cross-sectional area of the strand and therefore increases losses. This is known as the proximity effect.

The peak B-field in a slot is $B_{1\text{pk,AC}} = \mu_0 \frac{N_a I_{pk}}{w_s}$, where μ_0 is the vacuum permeability constant, N_a is the number of turns, I_{pk} is the peak current in a turn, and w_s is the width of the slot. The losses due to the litz wire depend on the distribution of the litz wire (i.e., number of rows and columns). As an approximation, the litz strands are assumed to be distributed uniformly and each litz strand occupies a region of dimensions d_{str} by d_{str}. If there are n_{rows} rows of strands and n_{cols} columns, then the

total area of the Litz strands is

$$n_{\text{rows}} n_{\text{cols}} d_{\text{str}}^2 = K_u h_s w_s \tag{4.25}$$

and

$$n_{\text{rows}} = \frac{\sqrt{K_u} h_s}{d_{\text{str}}} \tag{4.26}$$

$$n_{\text{cols}} = \frac{\sqrt{K_u} w_s}{d_{\text{str}}} \tag{4.27}$$

The power dissipation is derived based on Ref. [62]. Assuming the B-field passes through a strand in only one direction, the time-average power dissipated in a litz strand due to eddy currents is

$$P_{\text{ec,wire}} = \frac{\pi \ell \omega_e B_{\text{1pk,AC}}^2 \sigma_{20} d_{\text{str}}^4}{128} \tag{4.28}$$

The total AC losses accounting for all the strands, $P_{\text{AC,tot}}$, is therefore

$$P_{\text{AC,tot}} = n_{\text{rows}} n_{\text{cols}} P_{\text{ec,wire}} \tag{4.29}$$

$$= \frac{n_{\text{rows}} n_{\text{cols}} \pi \ell \omega_e B_{\text{1pk,AC}}^2 \sigma_{20} d_{\text{str}}^4}{128} \tag{4.30}$$

where $P_{\text{ec,wire}}$ is the AC loss per strand. Equation 4.29 shows that the total AC winding loss is linearly proportional to the axial length of the machine and electrical frequency which are swept parameters in the co-optimizer. The conductivity, $\sigma_2 0$, is a fixed material property. The peak B-field, $B_{\text{1pk,AC}}$, is a function of a slot current density and slot geometry which is also a swept parameter. Therefore the primary degree of freedom in modifying the AC winding loss is the selection of the litz strand diameter, which the loss scales with to the fourth power. For type 8, rectangular litz bundles, the manufacturer stated that AWG 24 is the smallest strands that they can make a bundle with. Any smaller strands will lead to the bundle losing its form. Smaller, circular litz bundles are feasible, but have much lower bundle packing factors. For earlier co-optimization design iterations, these circular bundles of AWG

30 strands resulted in copper fill factors on the order of 36%.

To determine if it was worth trying to find higher gauge rectangular litz bundles, the optimum design with AWG 24 was compared to a case where the AC losses are zero. Slot copper fill factor was held constant. This resulted in a 7% increase in demonstrator specific power. Given that the strand fill factor decreases with increasing gauge, this 7% may be optimistic and did not warrant pursuing higher gauge rectangular bundles.

4.4.4 NdFeB Versus Samarium Cobalt

In earlier iterations of the EM design, both neodymium-iron-boron (NdFeB) and samarium cobalt (SmCo) magnets were considered. While the NdFeB magnets are lighter than SmCo magnets and may be capable of producing greater torque, they are also more sensitive to temperature and at higher risk of demagnetization. In particular, the reversible temperature coefficient for NdFeB is four times greater than the coefficient for SmCo, as shown in Table 4.3. If the magnet temperature exceeds 70°C, SmCo has a greater remanent flux density. In addition, from the permanent magnet scaling from Eqn. 4.22, NdFeB magnets will have approximately twice the loss to that of SmCo, all else equivalent, due to their lower electrical resistivity.

Table 4.3: Although NdFeB permanent magnets have greater remanent flux densities and lower mass densities than SmCo does, they can only operate up to 220°C.

Parameter	**NdFeB [63]**	**SmCo [5]**
Remanent Flux Density at 20°C [T]	1.24	1.19
Mass Density [kg/m^3]	7500	8300
Maximum Operating Temperature [°C]	220	350
Resistivity [$\Omega \cdot \mu m$]	0.9	1.6
Reversible Temperature Coefficient [%/°C]	-0.12	-0.035

Optimal NdFeB and SmCo designs are shown in Table 4.4 after co-optimization sweeps using each material. The magnet performance is adjusted for 100°C based on

the magnet hotspot temperatures from prior design iterations. The actual magnet hotspot temperatures estimated from the framework are 99°C and 93°C for NdFeB and SmCo, respectively. Due to the larger permanent magnet loss from the NdFeB design, the SmCo based demonstrator has a 3% greater specific power. Due to enabling a greater demonstrator specific power and offering a higher maximum operating temperature, SmCo magnets were selected for the final demonstrator design.

Table 4.4: Summary of NdFeB vs. SmCo designs.

Parameter	**NdFeB**	**SmCo**
Demonstrator Module Specific Power $[kW/kg]$	9.62	9.94
Demonstrator Module Efficiency [%]	95.1	95.5
Shear Stress $[kPa]$	48.5	62.3
Rotational Speed $[rpm]$	9500	8000
Magnet Hotspot Temperature °C	99	93
Winding Hotspot Temperature °C	179	180
Slot Current Density $[A/mm^2]$	10	10.5
Aspect Ratio $[-]$	2.2	1.8
Active Length $[mm]$	261	224
Tip Radius $[mm]$	118	127
Pole Pair Number $[-]$	10	12
Fundamental Frequency $[kHz]$	1.583	16
Switching Frequency $[kHz]$	60	60
Air Gap Thickness $[mm]$	2.5	2.5
Magnet Thickness $[mm]$	12.9	13.8
Winding Thickness $[mm]$	18.4	20.5

4.4.5 Doubled Core Loss

As mentioned in Chapter 3, the core loss in the stator ferromagnetic material is based on a fit of the Steinmetz equation to manufacturer data. An example of the core loss data for four mil, Hiperco 50A is shown in Fig. 4-25.

In the real machine, the core loss can exceed that provided by the manufacturer by up to 100% [64]. For example, the flux densities in the machine will contain harmonics if the steel saturates. In addition, the cut edge of the laminations may have reduced permeability due to trauma during the laser cutting or stamping process, which can also increase core loss. While finite element analysis can estimate the harmonics,

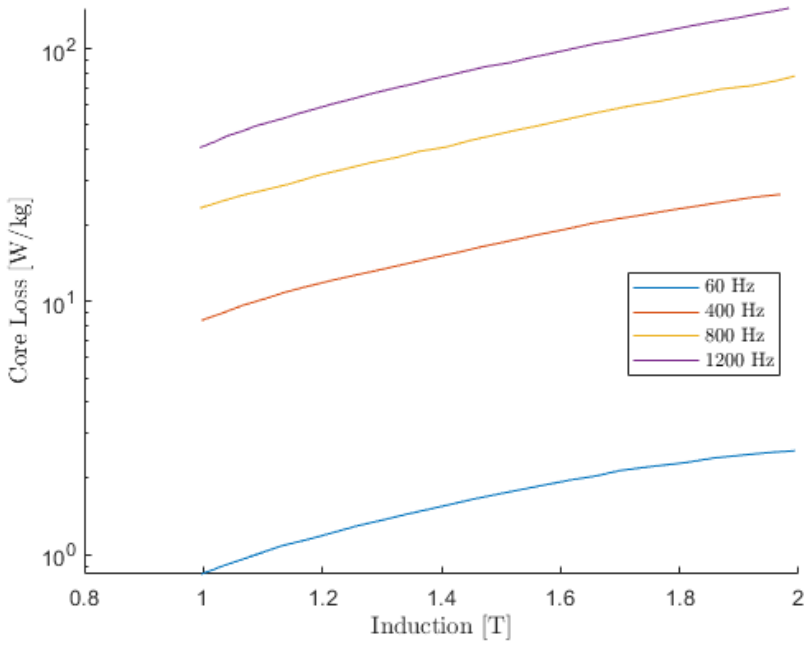

Figure 4-25: Manufacturer core loss for four mil Hiperco 50A after an annealing [75].

the other effects are more difficult to estimate before manufacturing and testing the machine. To account for this deviation, the core loss estimated from the Steinmetz equation, which is based on the manufacturer data, is doubled in the co-optimizer software. This doubling of the core loss has a significant effect on the demonstrator optimum. Shown in Fig. 4-26, if the safety factor of two is removed, the demonstrator specific power increases by 17% and optimizes to a greater rotational speed.

Due to the uncertainty in the core loss, the safety factor of two on the core loss was maintained throughout the rest of the machine design. Given that the machine will be aggressively air cooled, a major objective throughout the detailed design and manufacturing of the stator is to maintain low core loss. If the core loss is found to be closer to the manufacturer data, it would be possible to revisit the results of Fig. 4-26 and obtain up to 17% greater demonstrator specific power.

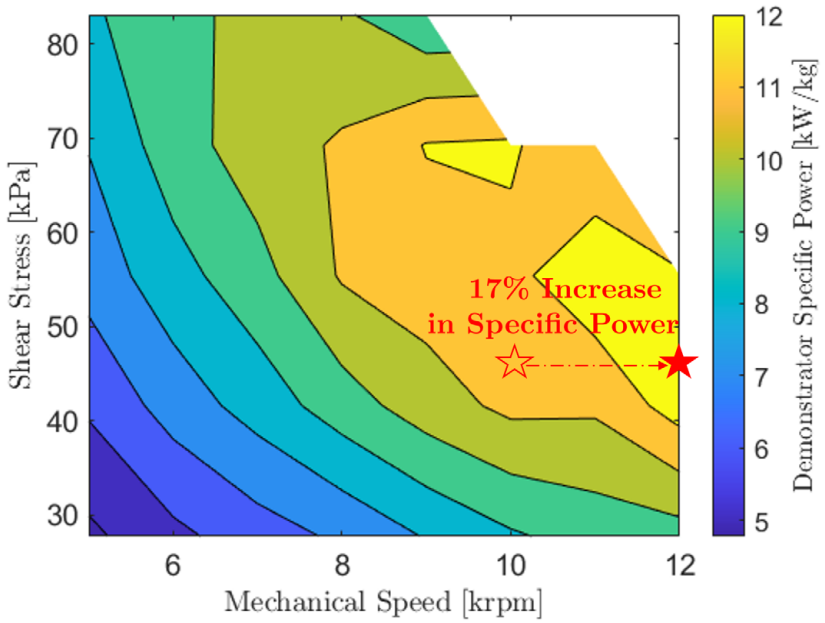

Figure 4-26: The demonstrator specific power increases by 17% if the core loss safety factor of two is removed.

4.4.6 End Turn Geometry

The end turns on the electric machine are the portions that extrude beyond the stator of the machine. The volume of these end turns typically comprise a small fraction of the overall winding volume and therefore have a minor impact on resistance, inductance, and winding losses. To attempt to capture as much of the electric machine design performance analytically as possible, an initial triangular end turn geometry based on Ref. [17] was assumed.

Initially, the end turns were assumed to have a negligible impact on electric machine performance since they would only add a small amount of Ohmic loss and therefore temperature rise. However, a mockup stator section showed that the end turns were actually circular rather than triangular. A circular end turn model was adopted into the model, and the winding hotspot temperature increased by approximately 18°C due to its longer length. At the time, the air cooling only extracted heat via the airgap and heat sink on the inner diameter of the machine. Heat from the end turns was conducted axially into the machine and pulled out via the airgap or heat

sink. This sensitivity of the winding hotspot temperature to the end turn geometry motivated the use of end turn air cooling.

Circular End Turns

A 3D mockup of the electric machine was created and it was found that the end turns are more circular rather than triangular for this particular machine. Therefore, the co-optimization model was updated to include circular end turns. An example of circular end turns is shown in Fig. 4-27.

The circular end turn model is similar to that for the MIT cheetah robot in Ref. [43]. The radius of this circular end turn, $r_{\text{et,circ}}$, is approximately half the distance from the exiting slot of the end turn to its returning slot, or

$$r_{\text{et,circ}} = \frac{\pi r_{\text{wind}}}{2p} \tag{4.31}$$

where r_{wind} is average radius of the windings (i.e., the center of the slot). In practice, the circular end turns do not immediately bend when coming out of the slot. Instead, it extrudes axially several millimeters which is captured with a variable $\ell_{\text{et,axialext}}$. Therefore the total circular end turn length is the sum of the axial extrusions and half the circumference of the circular bend:

$$\ell_{\text{et,circ}} = \pi^2 \frac{r_{\text{wind}}}{2p} + 2\ell_{\text{et,axialext}} \tag{4.32}$$

When the triangular end turn model was switched to a circular end turn model for an intermediate co-optimization design iteration (CO1.5), the end turn length increased by 36% which resulted in 12% greater I^2R loss in the machine. In addition, the longer end turn length increased the thermal resistance between the end turn and the cooling flow in the air gap and heat sink channels. These two effects resulted in a 30°C greater winding hotspot temperature, which exceeded the 180°C limit. This motivated the consideration of end turn cooling for the machine which is discussed next.

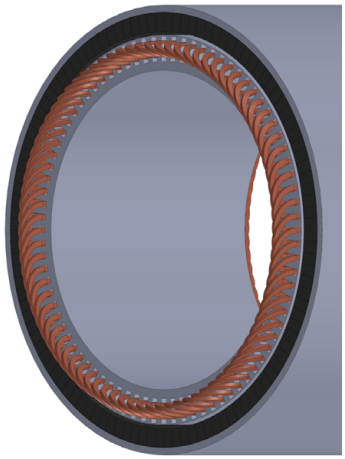

(a) Isolateral view of motor with circular end turns.

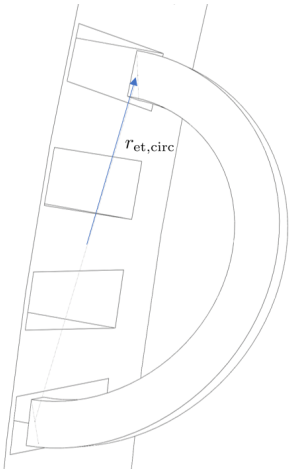

(b) Drawing of circular end turns.

Figure 4-27: Circular end turn geometry.

End Turn Cooling

Since it was discovered that the electric machine winding hotspot temperature is sensitive to the end turn geometry, it was decided to air-cool the end turns as well. Due to the complicated 3D geometry of the end turns, a 3D computational fluid dynamics simulation is necessary to evaluate the impact of air cooling the end turns. Prior to running this more complex simulation, an attempt to estimate the impact of end turn cooling was made by reducing the thermal resistance by a factor of ten. A co-optimization sweep was run and the results are shown in Fig. 4-28. The optimal demonstrator specific power increased by 16% due to the usage of end turn cooling. This large difference in specific power motivated a more detailed end turn cooling design which is discussed in Ref. [27].

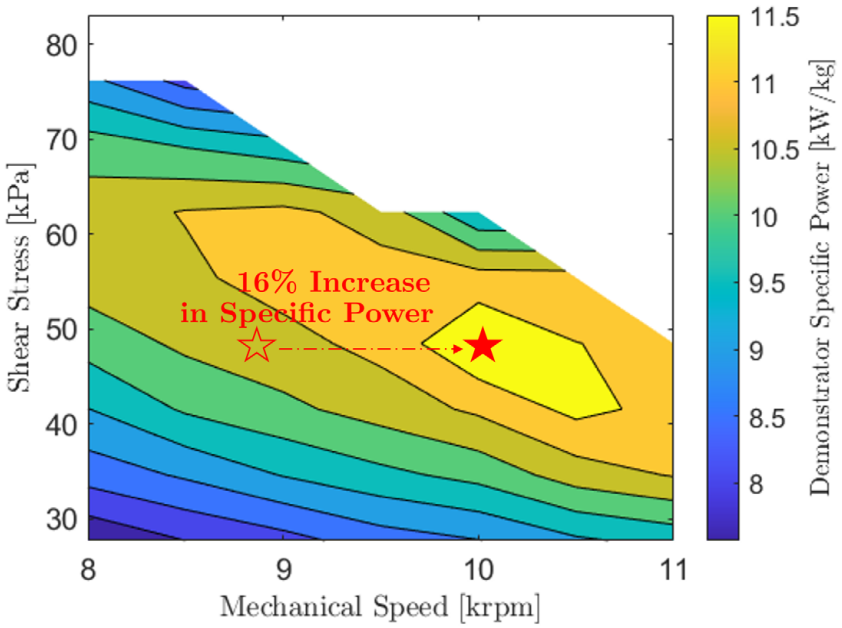

Figure 4-28: Thermal resistance value that is used in the co-optimizer is reduced by a factor of ten to simulate end turn cooling.

4.5 Demonstrator Design Point

To generate a final design point for a more detailed design, the following design parameters were swept:

Table 4.5: List of input parameters for design trade study.

	Units	**Range Examined**
Rotational speed	rpm	10000 - 13000
Shear stress	kPa	14:7:62
Length-to-tip radius ratio	-	1, 1.5, 1.75, 2, 2.25
Number of pole pairs	-	20, 24, 28, 32
Slot current density	Apk/mm^2	10:1/3:14
Air gap thickness	mm	2.5, 3, 3.5
Nondimensional magnet thickness	-	0.3, 0.4, 0.5
Switching frequency	kHz	20, 40, 60, 80

The specific power of the highest performance designs versus shear stress and rotational speed is shown in the contour plot in Fig. 4-29. The optimum rotational speed is at 12,500 rpm and electromagnetic shear stress is at 42 kPa. The shear stress of the PDR design is actually lower at 34 kPa because it had to be adjusted

to reduce the stator tooth magnetic flux density saturation. Although the design is at the edge of feasibility, several measures of conservatism were adopted in the co-optimization framework which are discussed in Section 4.5.3. If even these measures prove inadequate, the co-optimizer can be rerun with more conservative assumptions.

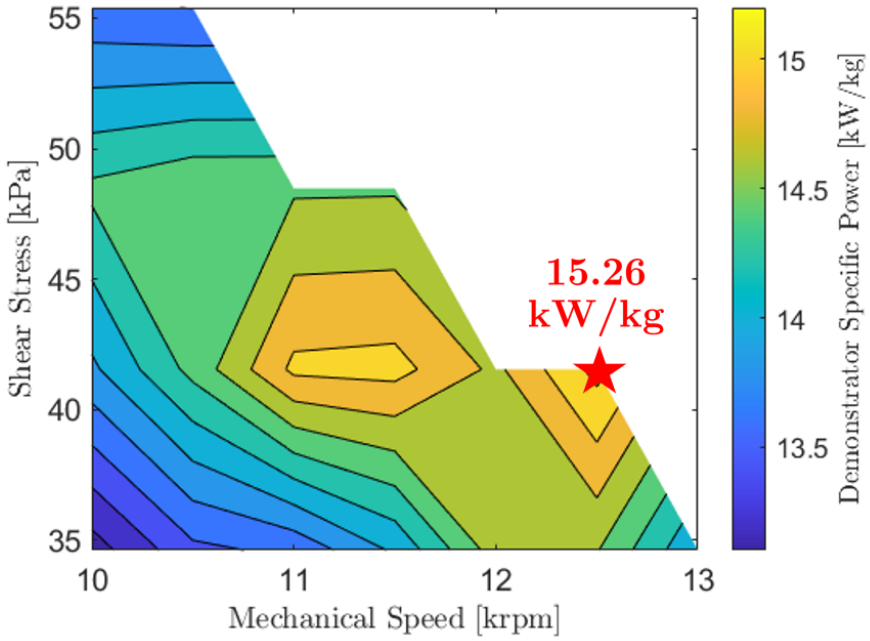

Figure 4-29: A contour plot shows a maximal SP demonstrator design at a rotational speed of 12,500 rpm and an electromagnetic shear stress of 42 kPa.

Of the explored design space, higher specific power electric machines may be feasible than that corresponding to the optimum demonstrator. Table 4.6 shows a comparison of optimizing for demonstrator system specific power, versus optimizing for standalone electric machine specific power. Optimizing for electric machine SP increases the electric machine SP by 18.7%. However, optimizing for the overall demonstrator system specific power results in a specific power increase of 38% with the trade off that the electric machine SP is lower.

To maximize the standalone electric machine specific power, the power electronics losses are minimized and the thermal management system power is maximized to increase the capacity for cooling the electric machine. Table 4.6 shows how the PE losses are halved but the PE mass increases four fold when moving from system-level optimization to EM optimization. In addition, the TMS power increases by

Table 4.6: Maximizing system specific power results in an estimated 38% greater system specific power than optimizing for just the standalone electric machine specific power.

	Objective Function	
Parameter	**Maximize System Specific Power**	**Maximize Electric Machine Specific Power**
Demonstrator Specific Power $[kW/kg]$	15.26	11.07
Demonstrator Efficiency [%]	93.99	93.72
Electric Machine Specific Power $[kW/kg]$	25.85	30.69
Electric Machine Mass $[kg]$	37.98	31.91
Electric Machine Losses $[kW]$	20.7	24.6
Power Electronics Mass $[kg]$	9.83	40.09
Power Electronics Losses $[kW]$	18.6	9.5
TMS Mass $[kg]$	13.77	12.70
TMS Power $[kW]$	21.5	29.7
Tip Radius $[mm]$	118.7	129.7
Axial Length $[mm]$	207.7	227.0
Shear Stress $[rpm]$	41.55	34.6
Rotational Speed $[rpm]$	12,500	11,500
Pole Pairs $[rpm]$	12	16
Electrical Frequency $[Hz]$	2500	3067
Core Loss $[W]$	6702	8364
Ohmic Loss $[W]$	6280	7586

approximately 8 kW.

These two effects allow the maximal SP electric machine to optimize to a greater number of poles, which reduces back iron thickness and improves electric machine SP. Although this increases electrical frequency and hence core loss, this is feasible with the increased TMS cooling capability. In addition, the optimized standalone machine is axially larger with a smaller airgap of 3 mm, greater current density of 13 A/mm^2, and both thinner magnets and stator teeth. In contrast, the EM that

maximizes system SP has an airgap of 3.5 mm and slot current density of 12 A/mm^2. Therefore, there is a system level benefit to co-optimization, but it may be feasible to construct higher specific power electric machines at the expense of heavier power electronics and greater input power to the thermal management system.

4.5.1 Finite Element Analysis

The demonstrator design point from Fig. 4-29 was simulated using 2D finite element analysis in the Altair Flux software [4] to obtain higher resolution estimates of the machine performance and to check the level of saturation in the stator. The design is considered over saturated if sections of the stator surpass the "knee" of the B-H curve of the ferromagnetic material as indicated in Fig. 4-30. This "knee" corresponds to about 2.1-2.2T for FeCoV material.

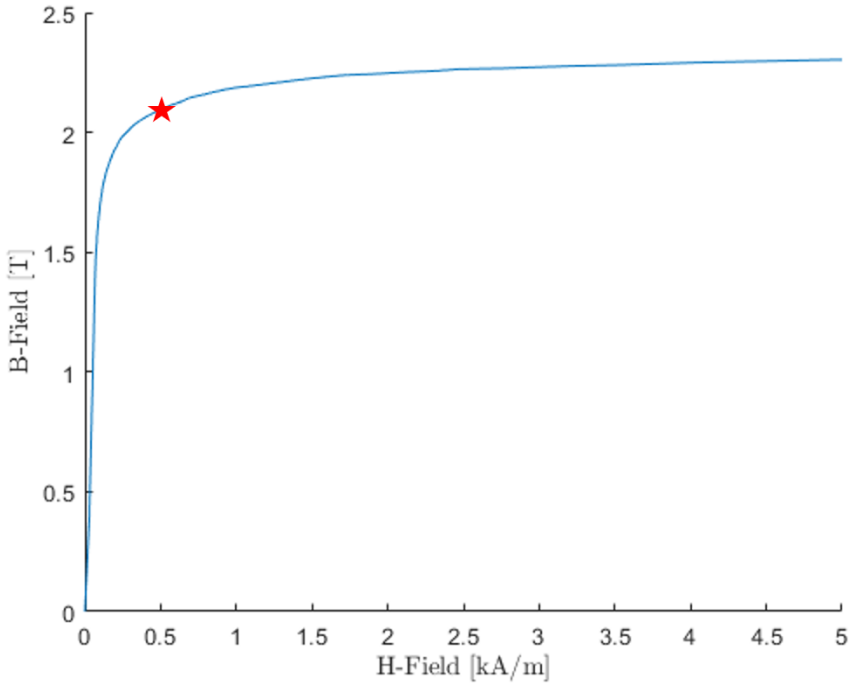

Figure 4-30: BH curve used in FEA corresponding to Hiperco 50.

From the 2D FEA, the torque of the machine was found to be below that estimated from the co-optimization framework. Figure 4-31 shows the electric machine torque with and without saturation. The case without saturation is simulated by setting the

relative permeability of the stator to a large value (i.e., 10,000). For the saturated case which uses the manufacturer material data, the average torque is just 661 Nm and the peak-to-peak torque ripple is 130 Nm, which is 19.7% of the average. Therefore the machine design needs to be modified to reduce saturation.

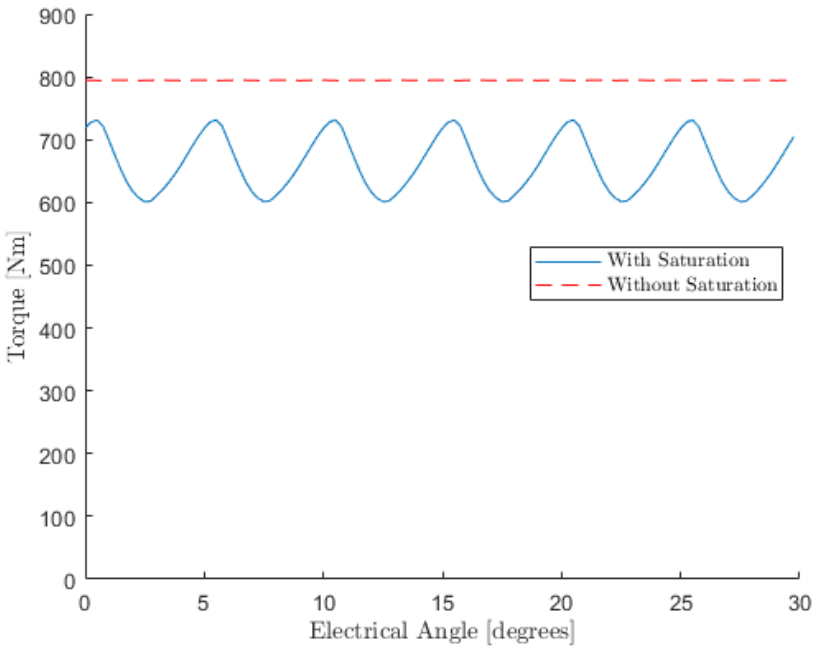

Figure 4-31: Large ripple found in first iteration of the PDR design due to saturation in the stator teeth.

The tooth tips, bottom of the stator teeth, and the stator back iron were found to be saturated past 2.2 T as shown in Fig. 4-32. The tooth tips can be modified with a taper to reduce the flux density magnitude as will be discussed in Chapter 5. The rotor back iron can also be extended radially inward to increase its cross-sectional area and hence reduce the flux density.

However, it is difficult to reduce the B-field at the bottom of the stator teeth. The slot section is sized specifically for the rectangular litz bundle from Section 4.3.4. The stator teeth therefore cannot simply be expanded wider because it reduces the available area for windings, which increases the I^2R losses. In turn, this increases the winding hotspot temperature which was already at the 180°C limit by design. Instead, the approach described in the following subsection is used to find a valid

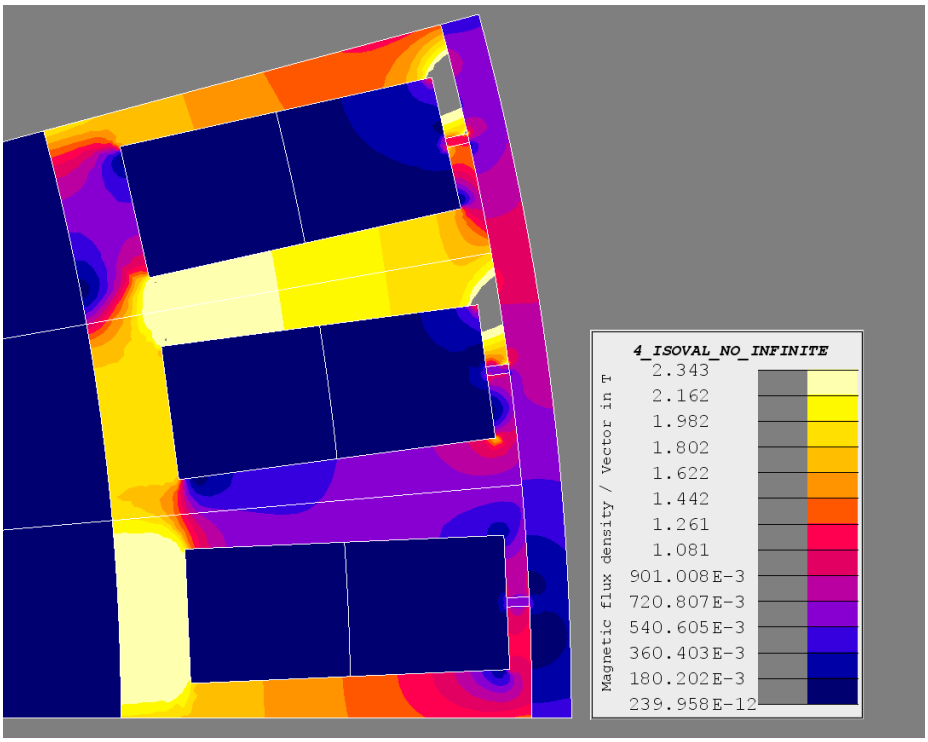

Figure 4-32: The tooth tips, bottom of the teeth, and stator back iron are saturated at 2.3 T - well beyond the knee of the B-H curve [4].

electric machine design without oversaturating the machine.

4.5.2 Design Modifications

The approach to finding an unsaturated electric machine design is the following. First, the winding hotspot temperature is reduced and the optimal design is extracted and simulated in 2D FEA. If the machine is still saturated, the number of pole pairs, rotational speed, slot current density, air gap, and magnet thickness are all parameters that can be tuned such that the teeth are no longer saturated. For some hotspot temperatures, this tuning is not possible since all variations in slot current density, air gap thickness, etc., still result in a winding hotspot temperature that exceeds the 180°C limit. The approach to finding a valid demonstrator design point is shown in Fig. 4-33.

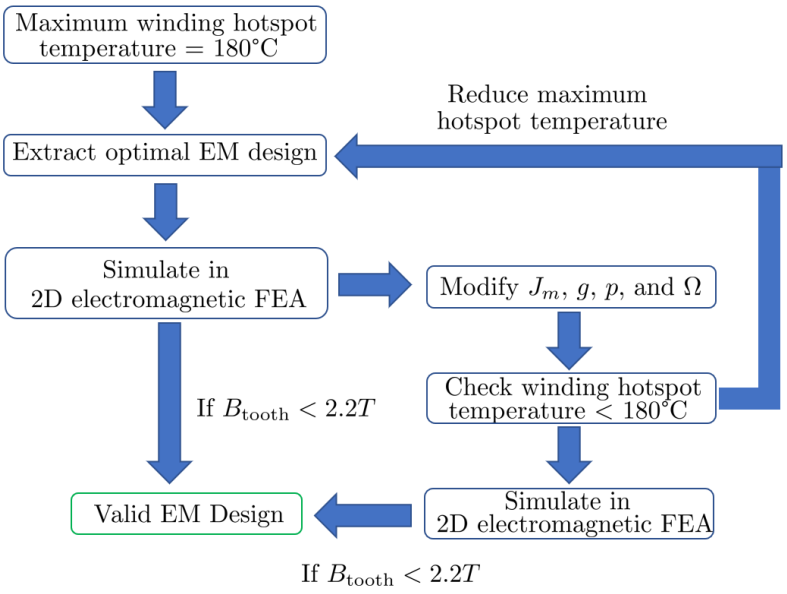

Figure 4-33: Block diagram showing the methodology for finding a valid demonstrator design.

A winding hotspot temperature of 173°C was found to provide sufficient margin to generate an electric machine without saturation. This provides 7°C of temperature margin to modify aspects of the design such as the slot width which will increase loss and hence winding temperature. Next, the electric machine was simulated in finite element analysis. After parametric analysis, the pole pair count was reduced from twelve to ten, and the speed was increased from 11,500 rpm to 12,500 rpm without

violating any structural, voltage, and thermal constraints. The magnetic flux density contours after these changes are shown in Fig. 4-34. The majority of the stator is below the knee of the B-H curve, with the two exceptions being the base of the stator tooth and the corner of the tooth tip. The flux density levels throughout the stator are discussed more in Chapter 5.

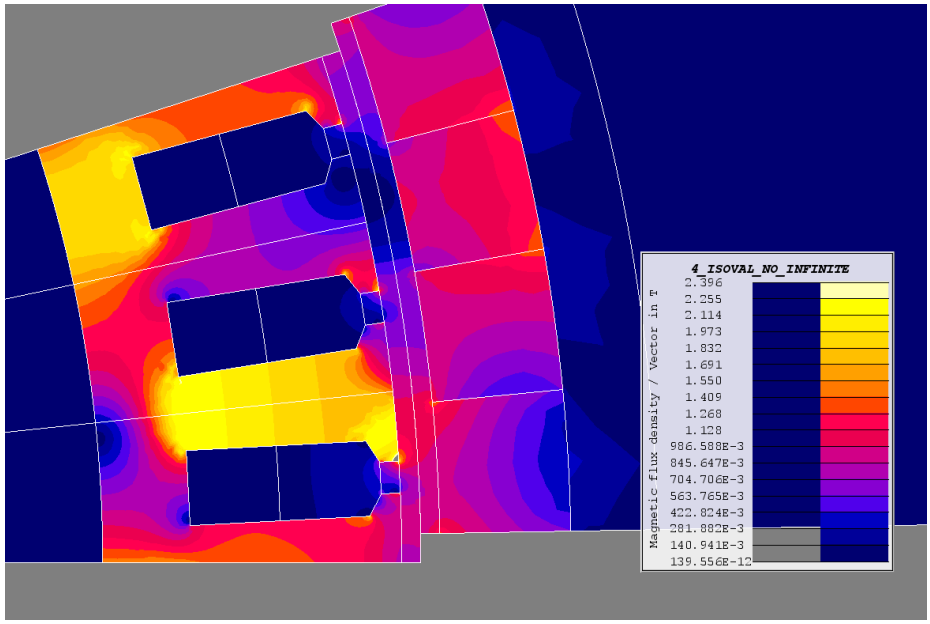

Figure 4-34: The saturation levels are reduced with the changes described above [4].

Lastly, the torque of the machine was checked in 2D FEA and is shown in Fig. 4-35. This machine produces the target 765 Nm of torque at 12,500 rpm to generate one megawatt of power. In addition, the peak-to-peak torque ripple is minimized to just 0.95% by the use of four directions of magnetization in the Halbach array. This design sets the basis for a more detailed design in Chapter 5. The 2D and 3D finite element analysis of other parameters, such as voltage, are the subject of the next chapter.

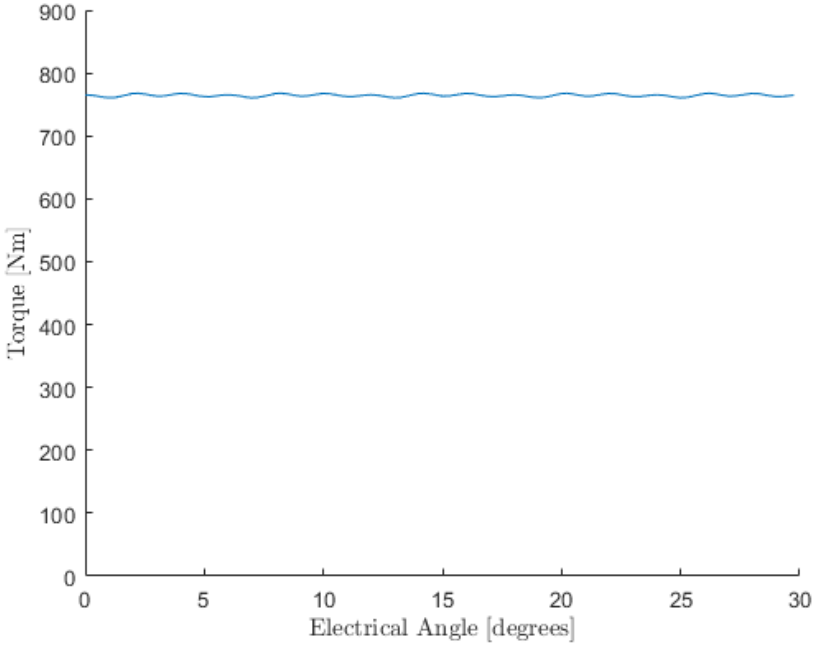

Figure 4-35: Torque waveform over one mechanical cycle for the PDR design extracted from Altair Flux [4].

4.5.3 Measure of Conservatism

The following measures of conservatism are assumed on the electromagnetics side:

- **Empirically-estimated core losses doubled:** the core losses measured on the toroid are doubled to try to account for harmonics, rotating B-fields, and other sources of loss in the full stator that are not accounted for in the toroid test.
- **Winding hotspot temperature margin:** although the co-optimizer filters designs with winding hotspot temperatures at 180°C, the actual winding insulation is rated up to 200°C to provide margin.
- **Flux densities throughout stator limited to knee of curve:** the flux densities in the stator are limited to the knee of the curve to try to keep the B-H curve in the linear regime. This is done due to the concern that the FEA may not properly capture the machine performance if the steel is pushed too far into saturation.

On the structural side, the titanium rim is sized such that the stresses in the rim are less than or equal to half the titanium yield stress [27]. Similarly, the bearing inner diameter must be large enough such that at least an additional 30% of the design cooling air mass flow can be passed in the event that additional cooling is required [27].

4.5.4 Demonstrator Specific Power Comparison

Due to the absence of publications on integrated electric machine (EM), power electronics (PE), and thermal management systems (TMS), hypothetical University of Illinois Urbana-Champaign (UIUC), University of Wisconsin (UW), and University of Nottingham demonstrators are considered as a baseline for comparison.

Both UIUC and University of Nottingham have published high SP EM and PE designs, whereas UW has only published an EM design. Thus, a hypothetical demonstrator system for UIUC could be the UIUC motor plus the UIUC conceptual, high SP GaN inverter at 19 kW/kg and 99% efficiency [65]. The University of Nottingham hypothetical demonstrator includes their four MW motor [32] as well as their 16.6 kW/kg, Si-based power electronics [12]. A hypothetical UW demonstrator might be the UW motor plus the 19 kW/kg, 99% efficient GE Silicon Carbide inverter [65]. Lastly, the UW and University of Nottingham electric machines are liquid cooled, so a TMS heat-to-mass ratio of 0.68 kW/kg, based on aircraft oil-cooling systems, is used to estimate the mass of these liquid cooling systems.

Table 4.7 shows a comparison of these hypothetical demonstrators. Since the specific powers of the other university electric machines are comparable to (or in some instances greater than) that of the thesis electric machine, the thesis overall demonstrator performance is predicted to be greater due to the comparably low power electronics and TMS mass and losses.

Table 4.7: Summary of thesis demonstrator performance versus other predicted, megawatt-class motor drive systems.

Thesis PDR 1 MW Design	12.8 kW/kg
UIUC 1 MW motor drive	7.5 kW/kg
UW + 19 kW/kg SiC 1 MW motor drive	7.2 kW/kg
University of Nottingham 4 MW motor drive	6.6 kW/kg

4.6 Summary of Results

An outer rotor, tooth-and-slot Halbach array concept design for a technical demonstration was created in this chapter. The objective of this demonstrator is to achieve predicted specific power and efficiencies, discussed in Chapter 5, at one megawatt of rated power. Three measures of conservatism were assumed on the electric machine side to mitigate risk. Specifically, the empirically-estimated core losses are doubled, the winding hotspot temperature is limited to 20°C below the insulation rating, and the flux densities throughout the stator are limited to 2.1 T or below. The electric machine is predicted to achieve a specific power of 18.4 kW/kg and efficiency of 97.8%.

The overall demonstrator system specific power was optimized via a novel co-optimization process that considers all subsystems (i.e., electric machine, power electronics, and thermal management system) simultaneously. From the co-optimizer results, a 19% greater specific power electric machine may be feasible at the cost of a 28% reduction to the overall demonstrator specific power.

Additional findings of this chapter include:

- a 18.4 kW/kg, tooth-and-slot Halbach array machine is feasible based on 2D electromagnetic finite element analysis, structural analysis, and thermal analysis,

- the permanent magnet eddy current losses in the electric machine can be modified by input design parameters,

- a higher order Halbach array can substantially reduce the torque ripple of a tooth-and-slot permanent magnet machine,

- air-cooling the end turns of the electric machine is critical for obtaining a high demonstrator specific power,
- rectangular litz bundles of US AWG 24 are state-of-the-art, and
- slot copper fill factors of approximately 50% are obtainable for high SP machines.

The electric machine design from Section 4.5.2 forms the basis for a detailed design phase which is the subject of Chapter 5.

Chapter 5

Detailed Design of Megawatt Demonstrator

In Chapter 4, a demonstrator design point was identified via a co-optimization approach for the electric machine, power electronics, and thermal management system. An initial 2D finite element analysis was performed to check magnetic flux density levels throughout the machine as well as torque and torque ripple. This chapter focuses on the detailed design of the electric machine.

First, an overview of the demonstrator subsystems is given in Section 5.1. A summary of the overall demonstrator, electric machine, power electronics, and thermal management system performance is given and compared against similar machines in development. Next, the key risks in the design and risk mitigation steps are described in Section 5.3. These risks are addressed in the detailed designs for the windings in Section 5.4, for the rotor in Section 5.5, and for the stator in Section 5.6. These sections include details on the manufacturing, additional analysis to support design decisions, and bench tests where applicable. To conclude this design phase, a preliminary controller design for the back-to-back electric machines is presented in Section 5.8. Lastly, the key findings of this design phase are summarized in Section 5.9. This chapter addresses objective four defined in Chapter 1.

5.1 Overview of Demonstrator Subsystems

As mentioned in Chapter 4, the technical demonstrator consists of a motor and generator connected back-to-back via a shaft. A cross-section of the back-to-back configuration, provided courtesy of colleague Yuankang Chen, is shown in Fig. 5-1. The motor and generator may have separate shafts connected at the center to a torque meter and possibly a brake in the final design; however, only a single shaft that connects the two machines is shown in Fig. 5-1.

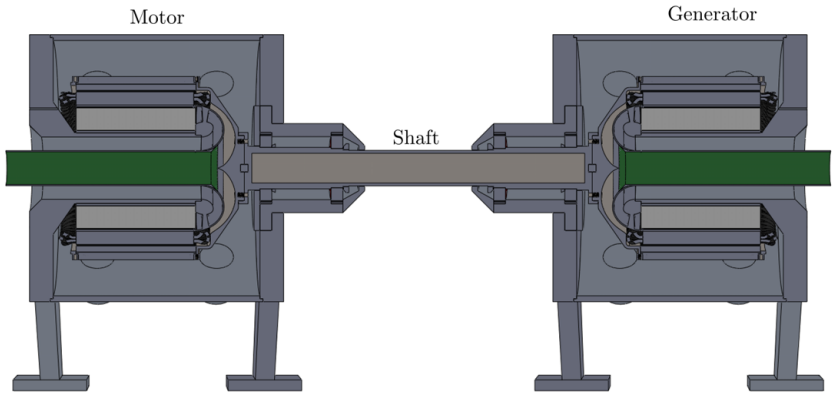

Figure 5-1: Full demonstrator layout provided courtesy of Yuankang Chen.

The layout for a single motor or generator is shown in Fig. 5-2. Each electric machine is mounted on its respective heat sink and is surrounded by a support structure. Cooling air flows through the center of the machine, indicated in the green in Fig. 5-2, turns into the the end windings, passes through the air gap, and ultimately exhausts through openings in the support structure casing. Just outside the center air flow passage is another cooling channel to pass air through the heat sink. This flow mixes with the air gap flow at the end turns.

Several key parameters of the demonstrator derived in Chapter 4 are summarized in Table 5.1 below. The following subsections will discuss each of the subsystems (e.g., electric machine or thermal management system) in further detail.

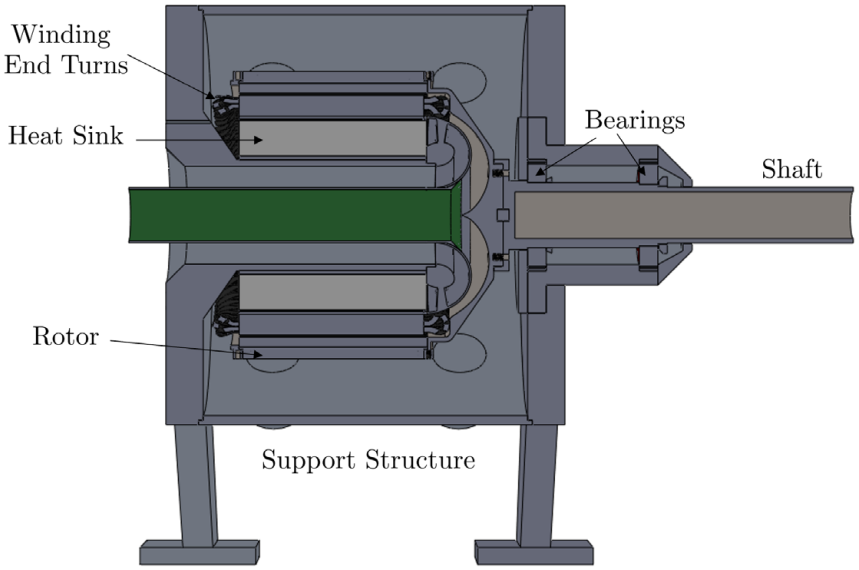

Figure 5-2: Single electric machine setup for the demonstrator.

Table 5.1: Summary of MIT demonstrator predicted performance.

Demonstrator SP (kW/kg)	12.8
Angular Speed (rpm)	12,500
Shear Stress (kPa, psi)	34.9, 5.0
Slot Current Density (Apk/mm^2)	13.3
Number of Pole Pairs (-)	10
Electrical Frequency (Hz)	2083.3
Switching Frequency (kHz)	80
Ripple Frequency (kHz)	160

5.1.1 Electric Machine

The electric machine for the demonstrator is the outer rotor, tooth-and-slot, Halbach array design shown in Fig. 5-3. The layout of the individual components is found in Fig. 5-3a. Litz bundles are used in the slots and a titanium retaining sleeve is used to support the permanent magnets. Rectangular copper blocks are shown in place of the litz bundles in Fig. 5-3.

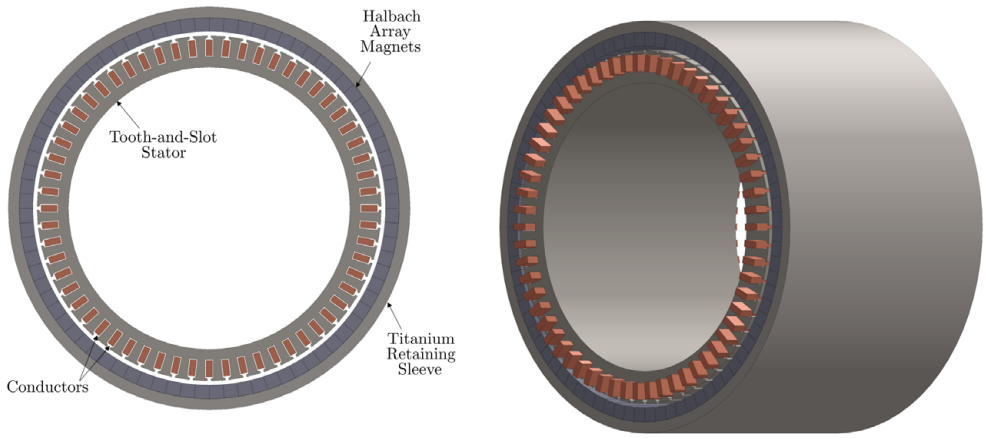

(a) Cross sectional area of the electric machine shows the outer rotor topology and tooth-and-slot stator.

(b) Isolateral view of the electric machine for PDR.

Figure 5-3: Electric machine layout for demonstrator.

5.1.2 Power Electronics

As mentioned in Chapter 4, the power electronics boards are single-phase, full-bridge converters. An overview of the proposed converters for the demonstrator, as designed by colleague Mohammad Qasim, is provided in Table. 5.2 [29]. The specific power of the total power electronics boards is predicted to be 37.9 kW/kg based on mass buildup models as well as prototypes [29].

Table 5.2: Summary of the power electronics predicted performance and parameters for the demonstrator.

Parameter	**Value**
Average switching frequency [kHz]	80
DC Bus Voltage[V]	720
SiC MOSFET voltage rating [V]	1200
Specific power[kW/kg]	37.9
Efficiency [-]	98.3%
Total weight [kg]	25.95

Thermal Management System

The winding and magnet hotspot temperatures are estimated at 177°C and 76°C which are below the material temperature limits. The thermal management system

performance and design parameters are summarized in Table 5.3. The power electronics heat sink mass is estimated using the heat-to-mass ratio of the electric machine heat sink. The compressor input power is estimated assuming an isentropic efficiency of 90%.

Table 5.3: Summary of thermal management predicted performance and parameters.

Thermal Management System Parameter	**Value**
Electric Machine Heat Sink Mass [kg]	6.21
Power Electronics Heat Sink Mass [kg]	9.61
Compressor Input Power [kW]	21.5
Winding Hotspot Temperature [$^{\circ}C$]	177
Magnet Hotspot Temperature [$^{\circ}C$]	76
Air Gap Mass Flow [kg/s]	0.285
Heat Sink Mass Flow [kg/s]	0.774
Rear End Turn Mass Flow [kg/s]	0.285
Total Mass Flow [kg/s]	1.344
Flow Margin [-]	0.3

5.1.3 Summary of Demonstrator Predicted Performance

A summary of the demonstrator and subsystem predicted performances and a comparison with those from public literature is given in Table 5.4. Overall, the concept design in this thesis is predicted to have the greatest overall system specific power at 11 kW/kg. Of the air-cooled designs, the electric machine design in this thesis is also predicted to have the greatest specific power.

With the power electronics, thermal management system, and demonstrator predicted performances summarized, the rest of the chapter will focus on the details of the electric machine design.

Table 5.4: Thesis motor drive is projected to have greatest overall system SP due to integration and co-optimization.

	Thesis Concept Design (Air cooled)	**UIUC (Air cooled)**	**University of Wisconsin (Liquid Cooled)**	**University of Nottingham (Liquid Cooled)**
Power Level [MW]	1	1	1	4
Demonstrator Specific Power [kW/kg]	11.0	7.2	7.5	6.6
Demonstrator Efficiency [%]	92.5	95.4	96.2	96.8
EM Specific Power [kW/kg]	19.7	13.0	23.7	17.3
EM Efficiency [%]	97.8	96.0	97.2	98.3
EM Shear Stress [kPa, psi]	35, 5.0	51, 7.4	23, 3.3	104, 15
PE Specific Power [kW/kg]	38.5	19.0	19.0	20.8
PE Efficiency [%]	98.2	99.0	99.0	98.5
TMS Mass [kg]	17.1	-	-	-
TMS Power Requirement [kW]	21.8	-	-	-

5.2 Electric Machine Design Details

This section details different aspects of the electric machine such as its mass, losses, and performance parameters. The details of the electric machine implementation are discussed in subsequent sections.

Electromagnetic analysis is used to confirm that the electric machine meets the demonstrator torque and power requirements. In addition, the EM circuit parameters

that are required for the PE design and the EM loss estimates are required for the thermal analysis. These quantities are estimated analytically and, when possible, in 2D or 3D electromagnetic FEA.

5.2.1 Finite Element Analysis Setup

The electric machine performance is simulated in the JMAG® FEA software [66] assuming constant rotor speed and using a current source drive. The EM is driven with a balanced three-phase current source composed of:

1. an excitation current at fundamental frequency (103.96 Apk, 2083 Hz), and
2. the PE ripple current due to pulse width modulation, which is approximated as a sinusoid with twice the inverter device switching frequency (2.86 Apk, 160 kHz).

For example, the total current for Phase A, $I_a(t)$, which contains both the fundamental and PWM ripple currents, is

$$I_a(t) = I_{\text{fund}} \sin(2\pi f_e t) + I_{\text{pwm}} \sin(2\pi f_{\text{ripple}} t) \tag{5.1}$$

where I_{fund} is the magnitude of the fundamental current, I_{pwm} is the magnitude of the ripple current, f_e is the fundamental frequency, and f_{ripple} is the ripple frequency (i.e., twice the switching frequency). The ripple current magnitude is estimated using an analytic model reported in Ref. [28]. The three-phase circuit setup is shown in Fig. 5-4. Although it does not change the FEA results, the full bridge circuits in the real machine will not have the common neutral shown in Fig. 5-4.

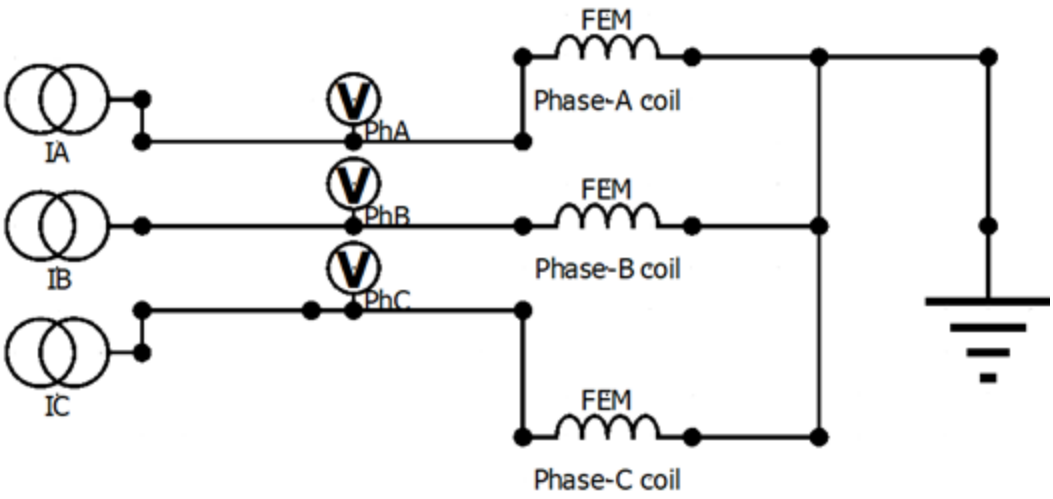

Figure 5-4: FEA circuit setup.

5.2.2 Torque and Torque Ripple

The torque and torque ripple were simulated in Chapter 4 and the results for the final design have not changed. Rotating at a constant 12,500 rpm and excited with the balanced three phase current source at fundamental frequency only, the simulated electric machine meets the average torque requirement of 763 Nm to output one MW of power. In addition, the peak-to-peak torque has a small ripple of 0.7% due to the use of a four block Halbach array. This design is not skewed.

5.2.3 Circuit Parameters

The primary circuit parameters required from the EM for the PE analysis are the open circuit voltage, terminal voltage, and inductance.

Open Circuit and Terminal Voltage

The open circuit and terminal voltage extracted from FEA are shown in Fig. 5-5. The terminal voltage is due to fundamental frequency excitation only. The peak terminal voltage is 692 V which is below the 800 V device limit.

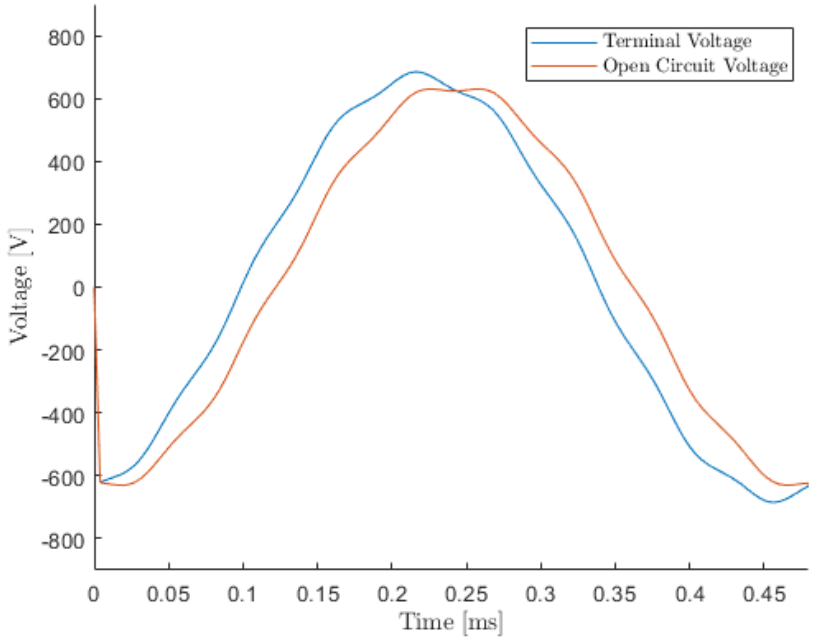

Figure 5-5: Open-circuit and terminal voltage.

Self Inductance

To estimate the self inductance, first a single phase is excited with a DC current equal to the peak rated current of the machine. The flux linkage for that phase is then extracted from the simulation, and the self inductance is $L_{\text{self}} = \lambda_a / I_{\text{a}}$. In FEA, the phase winding is assumed to be continuous through all twenty poles. However, for the design, ten circuit boards will be used to drive the electric machine. Therefore the FEA flux linkage must be divided by ten. For this stator, the flux linkage for phase A is $0.01506 Wb$ and the DC current is $103.96 A$. Therefore, the self inductance is found to be $L_{\text{self}} = 144.9 \mu H$.

Mutual Inductance

The mutual inductance is found by exciting one phase, measuring the flux linkage for another phase, and computing $L_{\text{mutual}} = \lambda_b / I_{\text{a}}$. For this stator, the flux linkage for phase A is $-0.00905 Wb$ and the DC current is $103.96 A$. Therefore, the mutual inductance is found to be $L_{\text{mutual}} = -8.7 \mu H$.

5.2.4 Peak Magnetic Flux Density

Magnetic flux density saturation in the stator steel generates higher order harmonics and hence additional losses. Thus, to avoid pushing the steel too far into saturation, the magnetic flux density throughout the machine is limited to approximately 2.2 T maximum, or close to the knee of the FeCoV alloy B-H curve. To confirm that the design satisfies this condition, the B-field versus time was extracted in FEA from three locations where the steel is observed to be most saturated. As shown in Fig. 5-6, point one is at the base of the stator, point two is in the tooth tip, and point three is in the stator back iron.

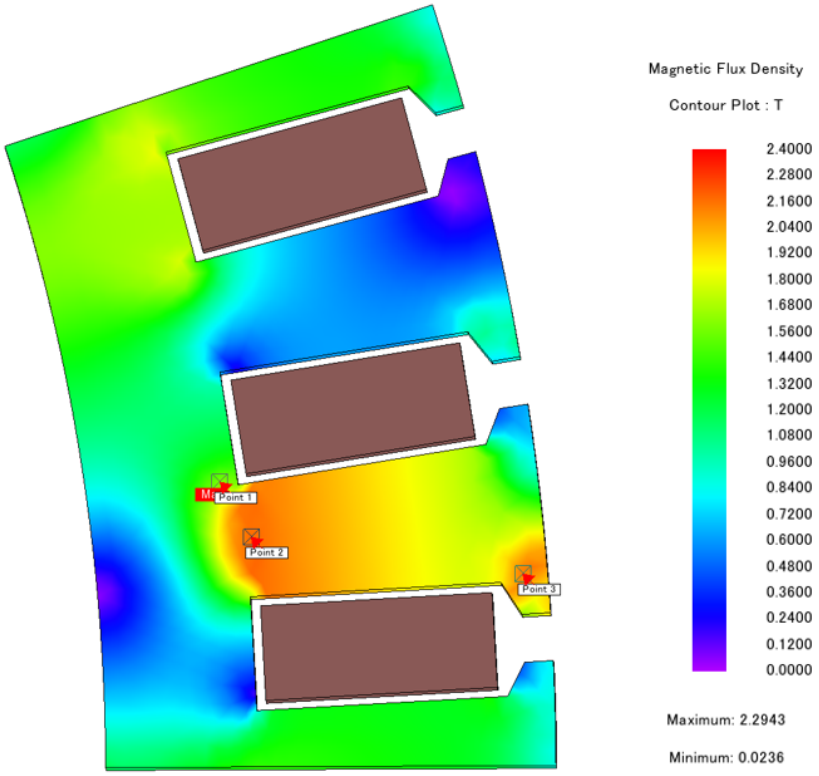

Figure 5-6: Three high flux density points were probed to verify that the stator is not over-saturated.

During steady state operation, the flux density peaks at 2.18 T in the bottom of the tooth. Although this is past the knee of the B-H curve as shown in Fig. 5-7, the relative permeability at this point is 400. This was verified to not be an issue for the design via FEA since this saturation is just localized to the base of the tooth and

corner of the tooth tip. The remainder of the machine is below the knee of the curve.

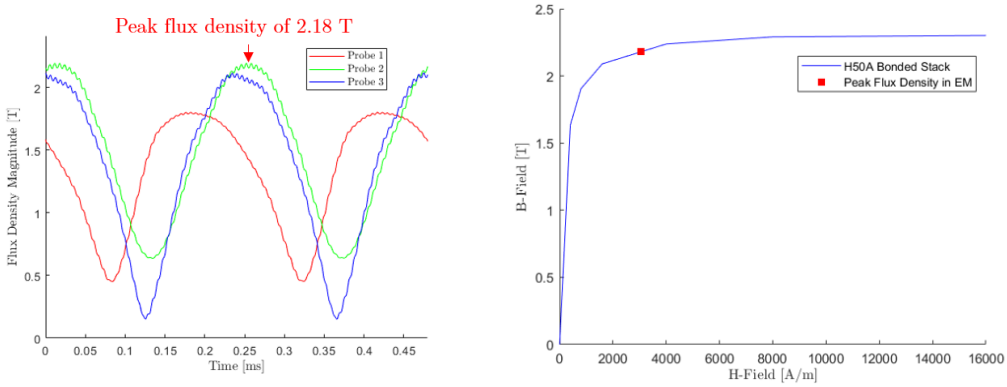

(a) Magnetic flux densities versus time at probed locations.

(b) Peak B-field slightly beyond knee of curve.

Figure 5-7: Peak B-field in stator is around 2.18 T.

5.2.5 Electric Machine Mass

The titanium turbomachine rim, the electric machine stator, permanent magnets, windings, and heat sink each contribute to the total mass of the machine. A breakdown of their contributions to the total mass is provided in Fig. 5-8.

The mass is distributed relatively evenly among the EM components, so simply substituting a lighter material alone is unlikely to provide a large specific power benefit. The material would need to provide additional benefits to mass density such as higher thermal conductivity or greater remanent flux density. For example, although NdFeB magnets increase remanent flux density and have a lower mass density than samarium cobalt, they are not worth using due to their lower maximum operating temperature.

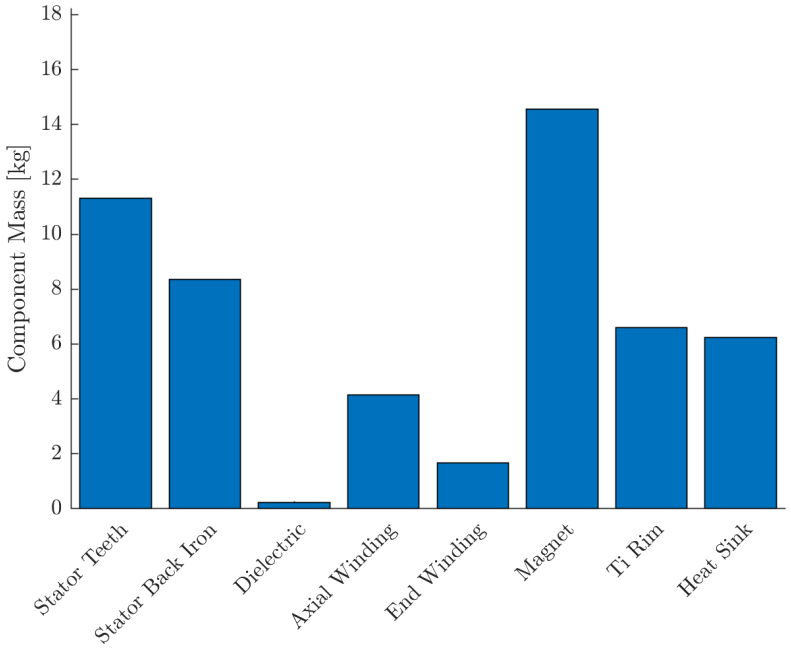

Figure 5-8: Breakdown of the electric machine mass.

5.2.6 Electric Machine Losses

FEA loss values are preferred to be used in thermal analysis when available because some effects (e.g., permanent magnet segmentation) were not captured analytically. Table 5.5 summarizes the loss components estimated analytically and in FEA. The core loss uses a safety factor of two (i.e., is doubled) as a measure of conservatism. Both the high frequency (HF) and fundamental eddy current and proximity effect losses used in the thermal analysis are greater than those in analytic and FEA to also be conservative. These loss values (1646 and 535 Watts, respectively) assume the eddy current and proximity effects are present in the end turns, which would not be true in practice since the magnetic fields rapidly decay beyond the axial end of the machine as found in Section 5.7.3.

For the PDR design, the core and Ohmic losses comprise the majority of the EM losses at 38% and 27%, respectively, as shown in Fig. 5-9. Although the permanent magnet losses are just 8% of the total after segmentation, they required careful attention because they are local to the magnet. These losses will increase the magnet

Table 5.5: Summary of electric machine losses.

Loss Component	Analytic	FEA	Thermal Analysis
Fundamental Ohmic Losses [W]	6342	-	6342
Eddy Current and Proximity Effect Losses due to Fundamental [W]	381	407	535
Core Losses due to Fundamental [W]	2 x 4410 = 8820	2 x 3630 = 7260	8820
Inner Windage [W]	1955	-	1955
Outer Windage [W]	2382	-	-
Permanent Magnet [W]	3450	1835	1835
High Frequency Eddy Current and Proximity Effect Losses [W]	1172	1135	1646
High Frequency Core Losses [W]	282	-	282

hotspot temperature and therefore increase the risk of demagnetization. The high frequency and windage represent a small, but not negligible, fraction of the total loss. The outer rotor windage losses exceed those in the airgap due to the strong dependence of windage loss on radius as well as the relatively large air gap for this electric machine design.

The following sections will discuss further details of the rotor, stator, and windings including their implementation and manufacturing.

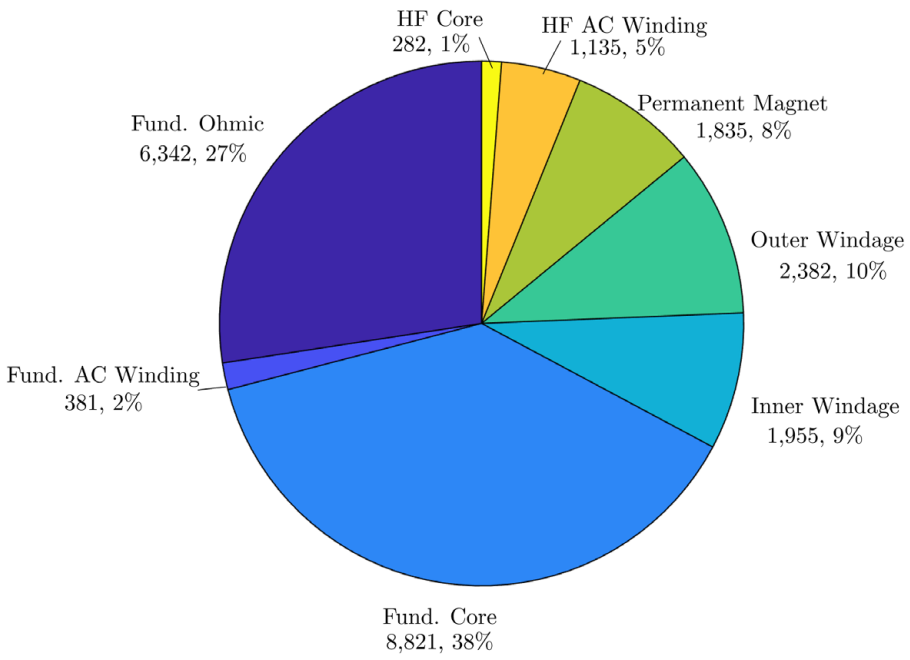

Figure 5-9: Breakdown of the electric machine loss.

5.2.7 Electric Machine Geometry

The geometry and dimensions of the electric machine used in the analysis of this chapter are shown in Fig. 5-10.

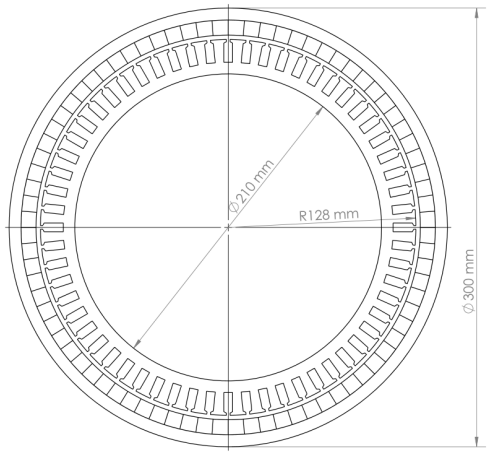

(a) Cross-sectional area of electric machine.

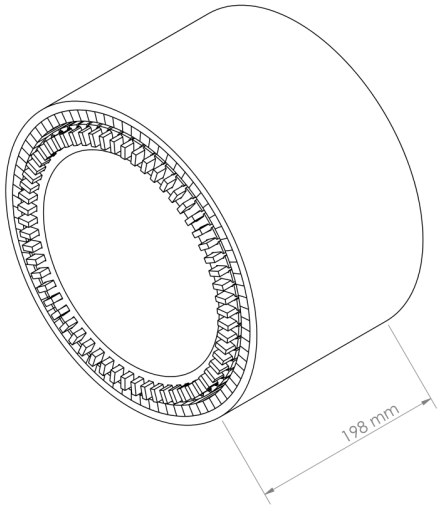

(b) Isolateral view of electric machine.

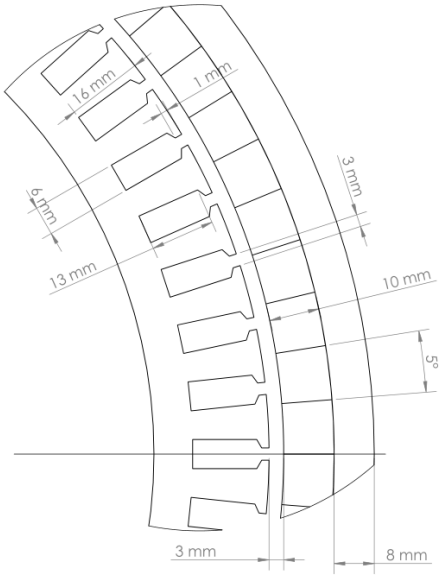

(c) Closeup of electric machine pole.

Figure 5-10: Dimensions of the electric machine geometry.

5.3 Risk Reduction

Various risks are identified for the demonstrator as a first of its kind machine. The risks are described at a high level here and are discussed in more detail throughout the rest of the chapter.

5.3.1 Winding Insulation

The insulation could break down between the litz bundles or the ground wall. Therefore, the insulation system is designed with a large safety margin between the dielectric strength and rated machine voltage. This insulation system is used in mockups of the final machine to confirm its feasibility.

5.3.2 Winding Pattern

The conceptual winding pattern assumed for the design may not be achievable in practice. To test this, a stator mockup was 3D printed and the actual windings for the final design were wound in the mockup by the vendor. There is an additional risk that the leads cannot be passed through the casing and seals of the final demonstrator while preventing cooling air leakage. This will be tested with additional mockups.

5.3.3 Permanent Magnet Loss

If the permanent magnet losses are too high, both the airgap cooling air and the magnet temperature will increase beyond current estimates. While the magnets can operate up to 350°C, there is an increased risk of demagnetization at higher temperatures. In addition, the hotter cooling flow could make it more challenging to cool the stator windings which are already designed around the 180°C limit.

To reduce this risk, the permanent magnet losses are simulated in 3D finite element analysis. In addition, the permanent magnets are axially segmented to reduce the eddy current loss. Lastly, 3D FEA is used to evaluate whether or not the magnets demagnetize under rated operating conditions.

5.3.4 Stator Lamination Insulation

A common technique for insulating FeCoV laminations is oxide coating. However, the thickness of the oxide layer is unknown prior to application which could result in a poor stacking factor and hence increased core loss. Therefore, alternate stator

insulations were considered and ultimately an industry standard process called C5 coating was selected for the demonstrator.

An unknown with the C5 coating is if the thin, 4 mil stator laminations can be used on the roller systems that apply the coating. Therefore, several laminations will be sent to the C5 coating vendor for test runs prior to coating the entire stack.

5.3.5 Core Loss

The stator core serves as the primary thermal conduction path for heat generated from both the stator core and the copper windings. As the core generates more heat, the winding temperature increases as well. Excessive winding temperature may deteriorate their insulation, resulting in short circuits and failure of the electric machine.

If the core losses are estimated incorrectly, the electric machine will have a lower efficiency than predicted at best. At worst, the excessive winding temperatures may deteriorate their insulation, resulting in short circuits and failure of the electric machine.

The factor of two deviation may be due to mechanical stress applied to the magnetic steel during manufacturing and operation. Figure 10 shows that the core losses for Hiperco-50 deviate by as much as 20% due to the tensile stress applied to the steel. To limit core losses, the exact fabrication of the demonstrator and the stresses applied to the stator will be analyzed. Manufacturing techniques such as laser cutting will be used to minimize stress.

5.3.6 Annealing

Impurities in the annealing furnace can contaminate the stator laminations and obstruct the etching process. In addition, there is a risk that the thin, 4 mil laminations can stick together during the annealing. A trial run will be initially conducted with a smaller test batch. If unsuccessful, the annealing protocols will need to be modified for a successful anneal.

5.3.7 Spin Pit Test

The magnetized permanent magnets could come loose during electric machine operation. Alternatively, the titanium rim could fail due to excessive hoop stress. Therefore a spin pit test, in which just the rotor will be spun to rated rotational speed, will be conducted prior to integration with the stator and ultimately demonstrator.

5.4 Winding Design Details

The windings were the first components of the electric machine whose design was finalized. In this section, the following aspects of the winding design are detailed:

1. the winding and slot layout,
2. the winding pattern to achieve ten turns,
3. a stator mockup bench test,
4. the end turn geometry, and
5. eddy current and proximity effect estimation via finite element analysis.

Items one and two cover the design and implementation of the windings and slot. Items three through five are used to mitigate the risk associated with the windings.

5.4.1 Slot Layout

As discussed in Chapter 4, rectangular, copper litz bundles consisting of two layers of US AWG 24 (0.511 mm diameter) strands will be used for the conductors in the electric machine. These bundles are manufactured by New England Wire Technologies (NEWT) in Lisbon, New Hampshire, and are referred to as Type 8 Litz bundles [67].

The slot design is similar to that of Chapter 4. Conceptually, the rectangular Litz bundle will stack on top of itself as it is wound through the stator, as shown in Fig. 5-11. The ten rectangular sections represent the ten turns of the machine. Each Litz bundle has 19 strands of AWG 24 copper strands that are transposed throughout the

slot. Between each turn is a 7 mil slot separator. In addition, the perimeter of the slot is lined with a 7 mil Nomex 410 slot liner to insulate the bundles from the stator. Both the space between the litz strands as well as the top of the slot will be potted to improve thermal heat transfer from the windings to the airgap and heat sink.

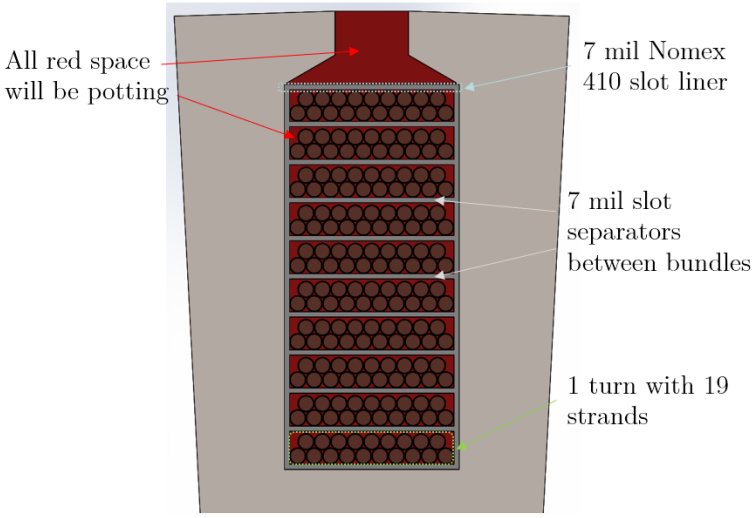

Figure 5-11: A cross-sectional area of a single stator slot shows how the 10 turns of the rectangular litz bundle stack on top of each other.

5.4.2 Winding Pattern

A unique winding pattern is used for this stator design due to the fact that one inverter per phase per pole pair, or thirty full bridge inverters will be used for the final electric machine. In Fig. 5-12, an overhead view of seven of the stator slots is used to show the winding pattern for a single phase. In this configuration, the winding wraps five times around three slots, which corresponds to one pole of a pole pair, before switching directions and wrapping five times around the next three slots. This winding therefore links the magnetic flux density from the pole pair ten times.

Figure 5-13 shows in dashed lines how the turns from the second and tenth inverters will appear in slots seven and one, respectively. Therefore, each slot will have ten turns total although in certain slots these will be split between two inverters.

Lastly, the winding pattern for the three phases of one inverter is shown in Fig.

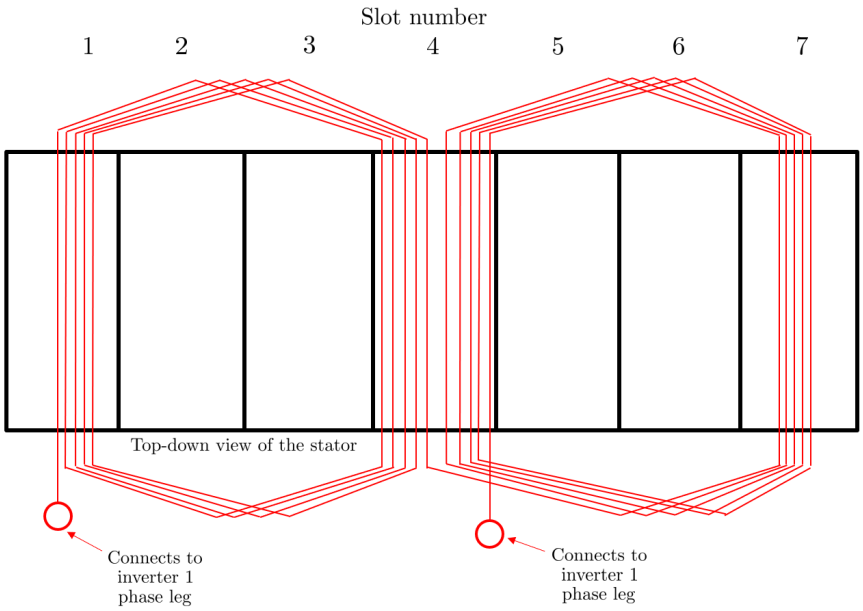

Figure 5-12: Winding pattern for a single phase of one inverter.

5-14.

To confirm the viability of this winding pattern, two mockups of different design iterations of the electric machine were created and are discussed in the next subsection.

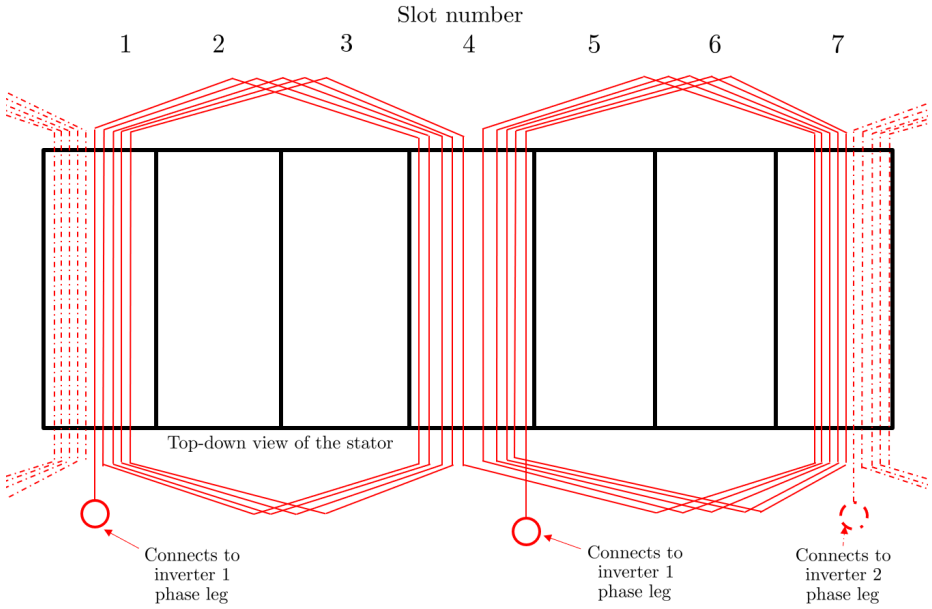

Figure 5-13: Two of the slots will contain five turns from the second and tenth inverters as well.

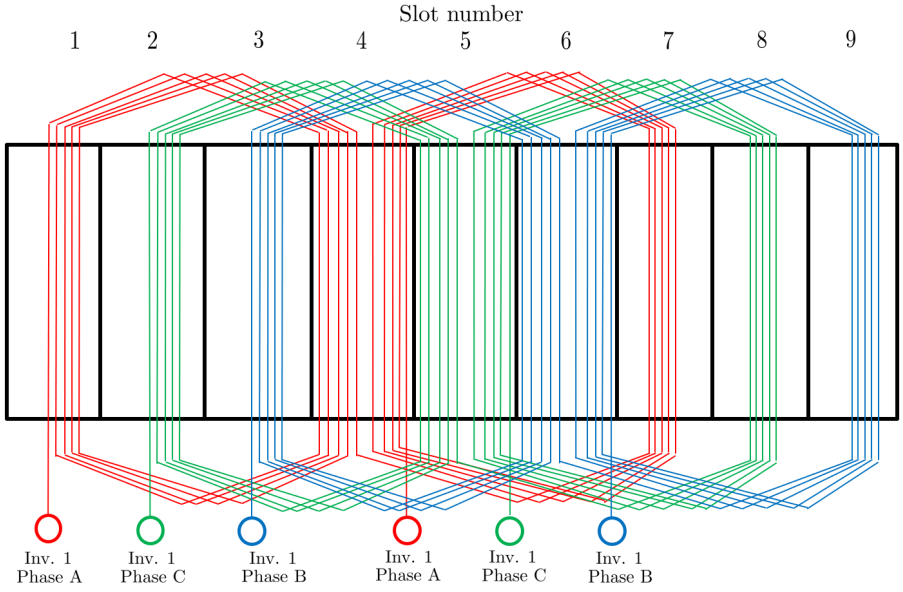

Figure 5-14: Winding pattern with all three phases of one inverter.

5.4.3 Stator Mockup

A 3D printed mockup was made of two of the stator design iterations to test the feasibility of the rectangular litz bundles and proposed winding pattern. The objectives of the 3D printed mockup tests were three-fold:

1. test if the conceptual winding pattern for the stator was feasible,
2. test if the rectangular litz bundles could be wound through the slots without losing stability, and
3. determine the 3D end turn geometry for thermal analysis.

The slot section also included the Nomex slot liner and slot separators to closely resemble the final stator build. A 3D printed stator was created for this mockup test as shown in Fig. 5-15. At the beginning of this test, the CO1 design had just been conceptualized. Therefore, the windings were tested on a printed CO1 stator which featured closed slots. However, this test is repeated for the PDR stator, which now has open slots through which the bundles could possibly be slid through during winding.

The 3D printed mockup test was a success. The winding pattern was achieved for eight slots which is slightly larger than a pole. The bundles maintained their shape. In addition, the end turns, shown in Fig. 5-16a, achieved the desired circular shape.

The 3D printed mockup test was repeated for the final PDR stator to verify the correct dimensions and to check the end turn geometry. Figure 5-17 shows different views of the mockup. For unknown reasons, the slot height in the mockup was shorter than that of the PDR design. Despite the reduced room for the bundles, the mockup was still successfully wound.

Figure 5-15: 3D printed stator is used for the mockup test. Figure provided courtesy of Mr. Marc Amato of Innova logic.

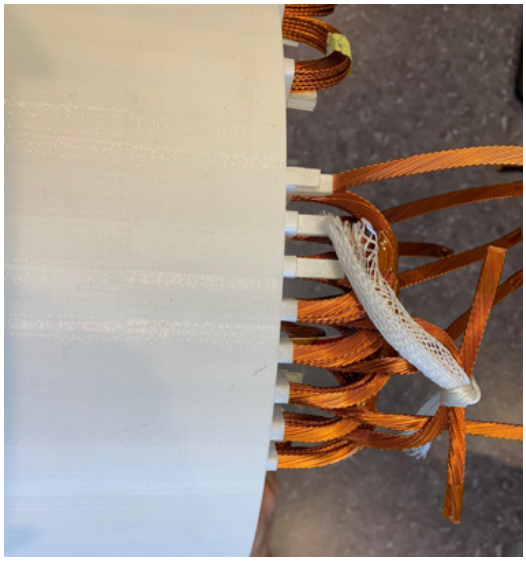

(a) Circular end turns from mockup test.

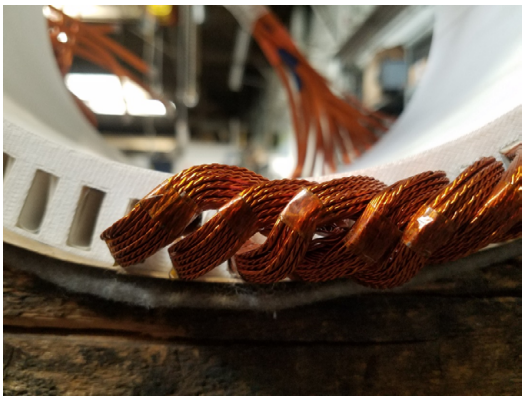

(b) CO1 stator with formed end turns.

Figure 5-16: Photos of 3D-printed CO1 mockup provided courtesy of Mr. Marc Amato of Innova Logic.

(a) Overhead view of the PDR mockup.

(b) PDR mockup endturns.

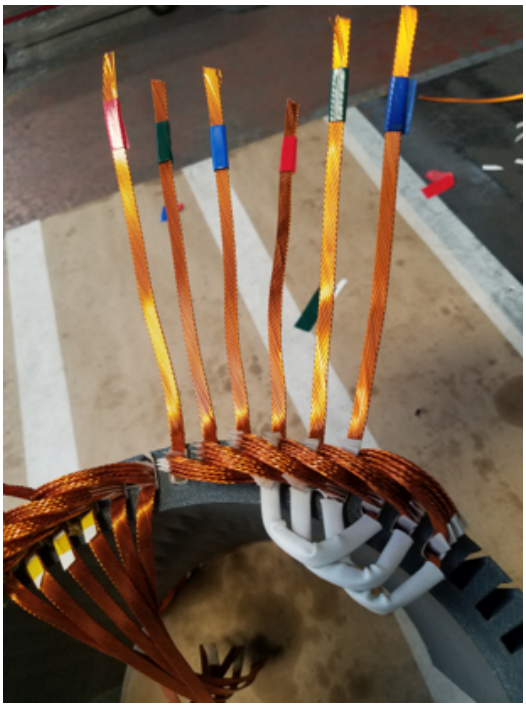

(c) PDR mockup jumpers.

Figure 5-17: PDR mockup photos provided courtesy of Mr. Marc Amato.

5.4.4 End Winding Geometry

Two measurements were made on the end turns to check against the analytic assumptions from Chapter 4. The first measurement, the axial extrusion, shown in Fig. 5-18a, was 24 mm. The diameter of the circular part of the turn, shown in Fig. 5-18b, was found to be 39 mm. These values were used for the end turn air cooling design.

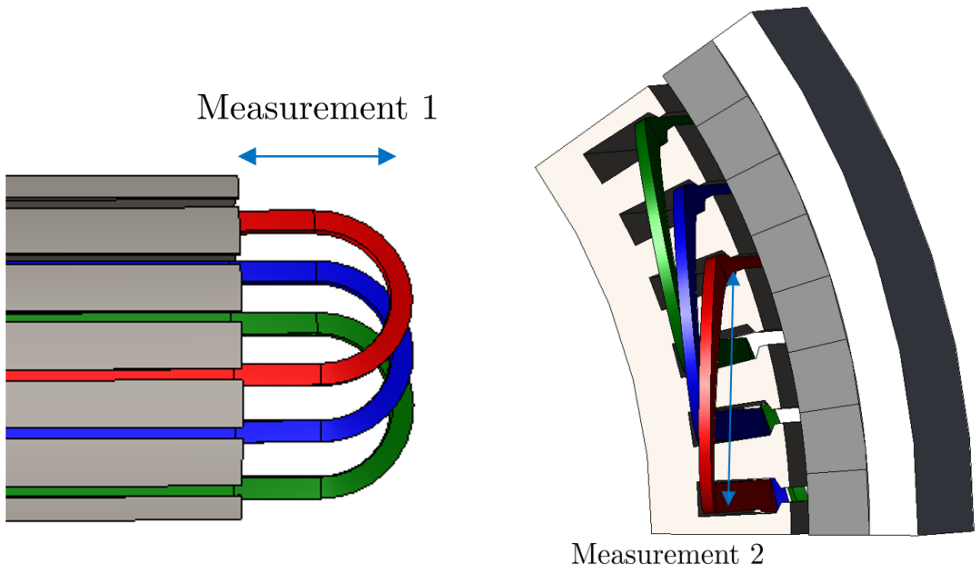

(a) First measurement for end turn geometry.

(b) Second measurement for end turn geometry is the distance between where the turn enters and exits the slot.

Figure 5-18: Two measurements were made on the end turn geometry.

5.4.5 Winding Loss

Due to the relatively large litz strand size compared to the skin depth from the high frequency power electronics current, a model based on 2D finite element analysis data from different designs was used in the co-optimizer in Chapter 4 to estimate eddy current and proximity effect losses in the litz strands. In addition, the model for the eddy current and proximity effect losses due to the fundamental assumed a particular flux density pattern throughout the slot that might not hold in practice. The losses for the PDR design iteration were found to be acceptable with regards to not forcing the winding hotspot temperature beyond its material limit. However, it was not clear that this model could be extrapolated to this particular demonstrator design. In this section, 2D finite element analysis is used to check these losses for the demonstrator design.

Fundamental Ohmic Loss

As shown in Section 5.2.6, the Ohmic loss due to the excitation current at fundamental frequency is the second largest component of the EM loss. This is calculated analytically via a simple $I_{\text{rms}}^2 R$ formulation. Although previously a slot copper fill factor was used in lieu of the detailed Litz geometry, the Litz bundles are now known and the Ohmic loss for the PDR EM design takes into account the bundle geometry explicitly.

Litz Eddy Current and Proximity Effect Loss

The losses in the Litz wire due to proximity and eddy current effects are first estimated analytically and then simulated in 2D finite element analysis. These losses occur due to both the fundamental and high frequency ripple currents. The cross sectional area of the pole, including the Litz bundles for 2D FEA, is shown in Fig. 5-19. Since the maximum allowable hotspot temperature of the windings is 180°C, the conductor resistivity is adjusted for 180°C.

The estimates between the physics based models and the 2D FEA, shown in Table 5.6, match to within 7%. The discrepancy for the fundamental losses can be explained by the fringing magnetic fields at the top of the slot.

Table 5.6: The analytic and FEA Litz loss estimates match to within 7%, with the total differing by just 0.7%.

Excitation Waveform	**Analytic Loss [W]**	**2D FEA Loss [W]**	**Percent Difference**
Fundamental	381	407	6.8
PWM Ripple	1172	1135	3.2
Total (Fundamental + PWM)	1553	1542	0.71

The difference between the analytic and 2D losses due to the fundamental due to fringing fields at the top of the slot. These fringe fields are visible at the top of the slot in the flux line plot in Fig. 5-20a.

For the slot geometry shown in Fig. 5-21, the flux density at the slot opening is

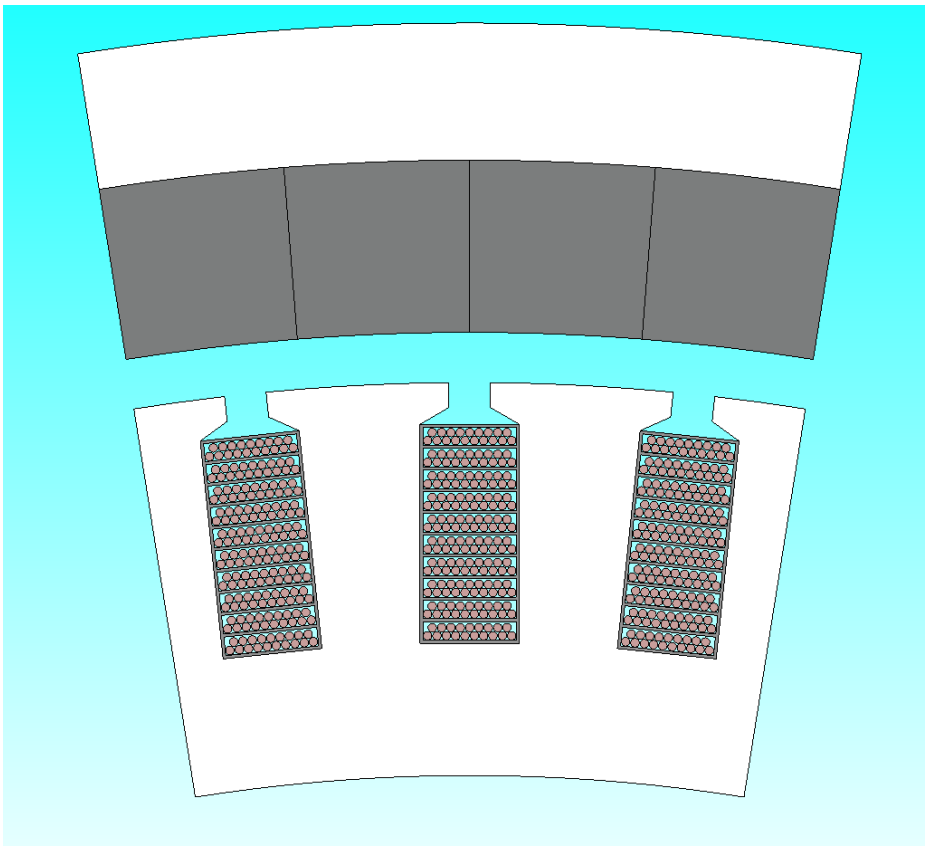

Figure 5-19: A 2D FEA is used to provide an additional estimate of the eddy current and proximity effect losses in the Litz bundles.

$$B_{\text{so}} = \mu_0 \frac{NI}{w_d} \tag{5.2}$$

Within the bundle regions, the flux density is

$$B_{\text{bundle}} = \mu_0 \left(\frac{NI}{w_s}\right)\left(\frac{y}{h_s}\right) \tag{5.3}$$

A comparison of the B-fields between the analytic and FEA values was created by probing different locations within the slot as shown in Fig. 5-22.

Table 5.7 shows the comparison between the analytic and 2D FEA B-field values. Therefore the difference in loss is due to the 13-25% difference in the B-field towards the top of the slot. To reduce this fringe field, the slot opening can be adjusted but this also changes the permanent magnet losses. In addition, the tooth tip height and its taper to the body of the slot can be adjusted, but this impacts either (1) the

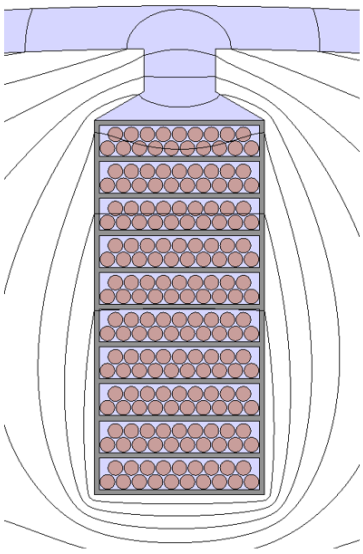

(a) Fields fringe above and below smaller slot openings, increasing loss at top of bundle.

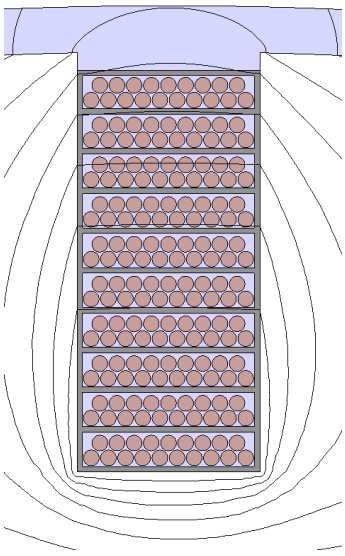

(b) Fields pass more horizontally across slot when opened, but increase PM loss.

Figure 5-20: Fringe fields at the slot opening lead to the difference between the analytic and finite element analysis loss estimates.

available space for the bundles, (2) the rotor back iron thickness, or (3) the rotor inner diameter. The results shown here are for the final slot after a parameter variation study on the tooth tip design.

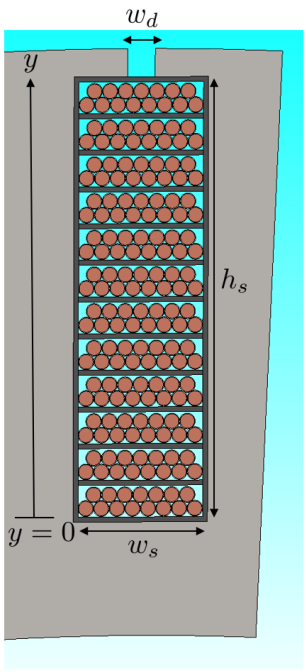

Figure 5-21: Slot geometry and variable definitions.

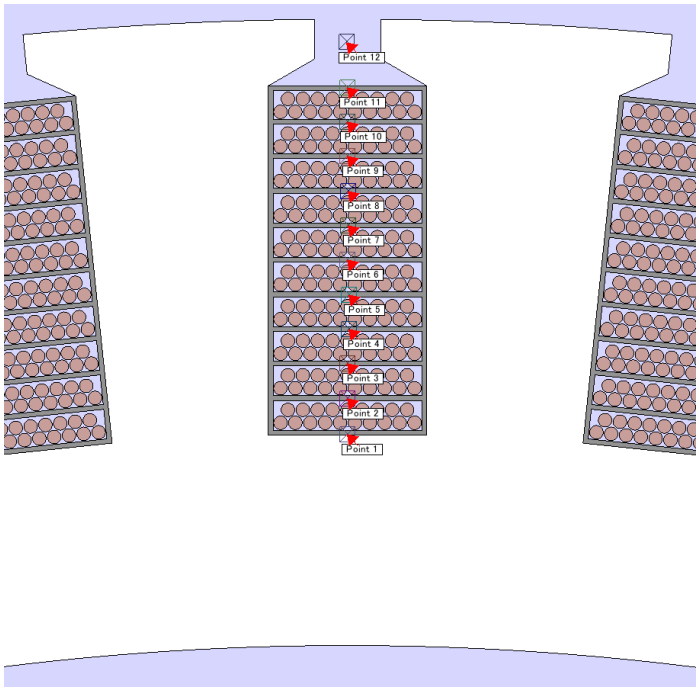

Figure 5-22: B-field probed in 2D FEA at 12 different locations for comparison with the analytic model.

Table 5.7: The analytic and FEA B-field values diverge towards the top of the slot due to fringe fields.

Point	**Analytic [T]**	**2D FEA [T]**	**Percent Difference**
12	0.515	0.402	24.8%
11	0.216	0.303	33.2%
10	0.195	0.223	13.3%
9	0.173	0.181	4.3%
8	0.152	0.153	1.3%
7	0.130	0.130	0.4%
6	0.108	0.108	0.2%
5	0.087	0.087	0.1%
4	0.065	0.065	0.1%
3	0.043	0.043	0.3%
2	0.022	0.022	0.2%
1	0	0	0%

5.5 Rotor Design Details

Once the winding design was finalized, both the rotor and stator designs proceeded in parallel. The high temperature samarium cobalt permanent magnets discussed in Chapter 4 are used in the final demonstrator. These magnets are expected to have a hotspot temperature of 76°C, so usually the 100°C performance is assumed in analysis as the closest available data. However, in anticipation that the eddy current losses could be greater, the performance at temperatures such as 200°C were also considered in the demagnetization analysis. The B-H and polarization, J, curves for 100°C, 150°C, and 200°C are shown in Fig. 5-23.

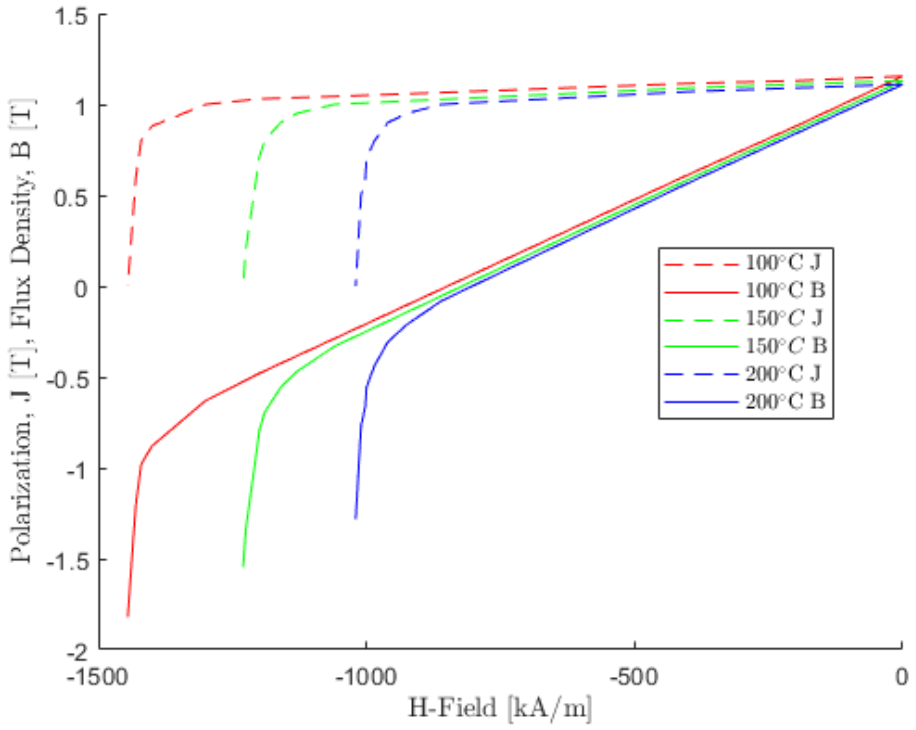

Figure 5-23: The 100°C B-H curve for AMT's RECOMA®35E is used in the electromagnetic analysis for the PDR EM design [5].

In this section, the following aspects of the rotor design are detailed:

1. the permanent magnet manufacturing and assembly,

2. magnetic forces and adhesive selection,

3. permanent magnet losses and segmentation,

4. demagnetization, and

5. Ti rim loss.

Item one describes the manufacturing and assembly process. Items two through five are used to mitigate the risk associated with the magnets.

5.5.1 Permanent Magnet Assembly

An adhesive is used to secure the magnets to the rotor. In addition, an adhesive is used to fill the gaps in between permanent magnets. This adhesive is non-conductive which insulates the magnets, preventing eddy current circulation. Lastly, glass beads are used for metering the space between magnets.

5.5.2 Magnetic Forces & Adhesive Selection

A magnet in a Halbach array may experience forces from adjacent magnets that attempt to dislodge the magnet from the Ti rim to which it is bonded. An analysis was conducted in 3D finite element analysis to estimate this force and compare it against the bonding strength of the adhesive. The 3D model for the finite element analysis is shown in Fig. 5-24. Spaces are left around the magnets in order to extract the force from the software.

The tangential and radial forces are shown in Fig. 5-25 and Fig. 5-26, respectively. In this simulation, the windings are excited with the rated currents to obtain an upper bound on the force the permanent magnet might see during operation, as well as to visualize the sensitivity to the rotor and stator alignment. The magnet numbers in these figures correspond to those in Fig. 5-24. The peak force in either direction from this analysis is 5 N. This force is similar even when the stator is turned off, so a similar stress is tested during the spin pit test.

The torsional force is the tangential force in Fig. 5-25 and is considered against the lap shear strength of the adhesive that is bonding the permanent magnets to the

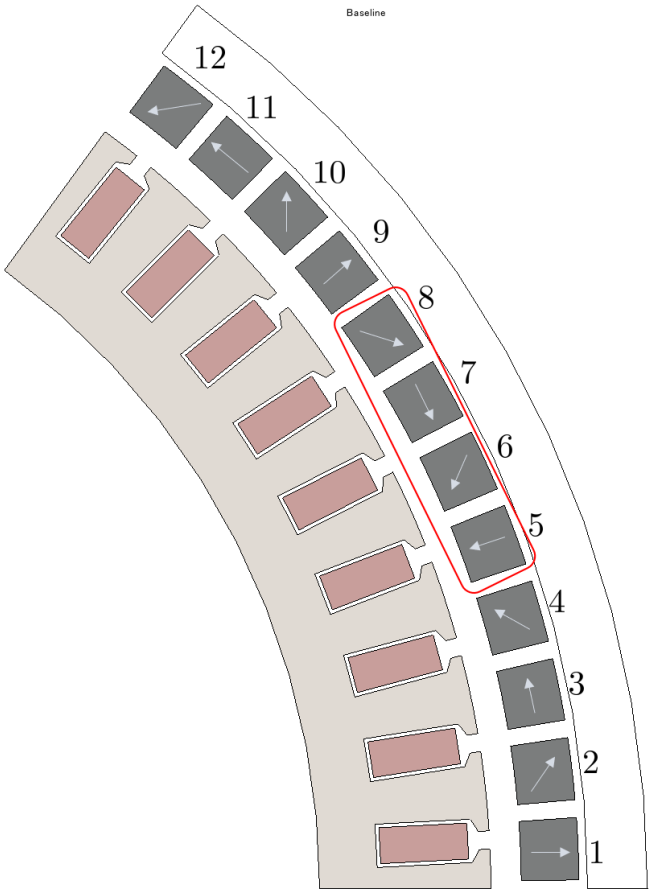

Figure 5-24: Labeled magnets for force analysis.

titanium rim. The face of the magnet flush against the rim is approximately 10 mm by 3.1 mm. Therefore, a force of 5 N results in a shear stress of approximately 161 kPa, which is two orders of magnitude lower than the lap shear strength of typical magnet adhesives [68]. Since the rim is made of titanium, experiments were conducted with titanium as well to verify a sufficient safety factor in using this adhesive for the test and final rotors. Ultimately, this will be confirmed via a spin pit test in which the rotor is operated to design speed with the magnets attached to the rim.

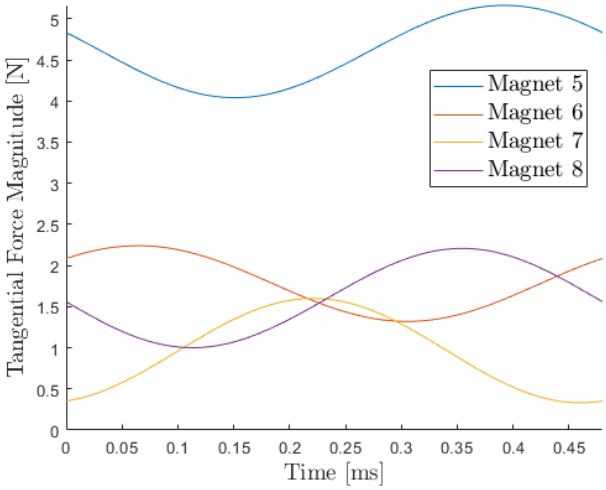

Figure 5-25: Tangential magnet force.

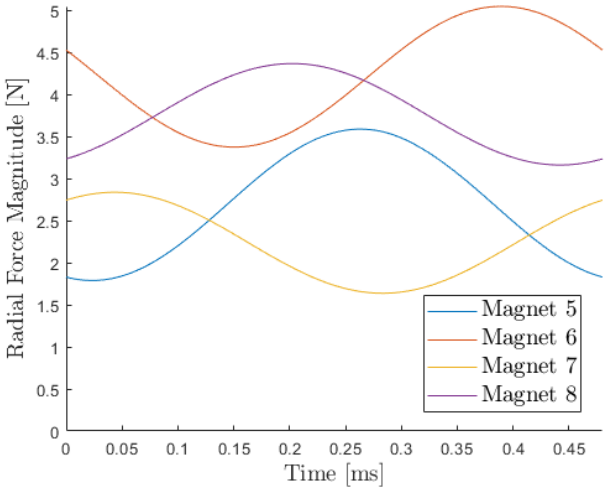

Figure 5-26: Radial magnet force.

5.5.3 Permanent Magnet Losses & Segmentation

The permanent magnets have a non-zero conductivity and are therefore subject to eddy current heating when exposed to the time-varying magnetic fields due to the stator. An additional source of loss that was not considered in Chapter 4 is the ripple current of the power electronics which will also generate eddy currents in the permanent magnets.

Although the permanent magnet (PM) loss due to eddy currents is not a large fraction of the total EM losses, the PM loss is critical because the heat generated is

local to the magnets and can increase their risk of demagnetization. To reduce the PM loss, the magnets can be segmented axially similar to stator laminations [69]. The permanent magnet loss assessment is coupled with a thermal analysis to check that the PM hotspot temperature does not significantly reduce the PM strength and ensures the PM is not at risk of demagnetizing.

Although Arnold Magnetic Technologies has the capability to segment magnets as thin as 0.5 mm, they recommend segmenting as little as necessary. Segmenting the magnets further adds cost and complexity since it requires installing more magnets. In addition, it introduces gaps between the magnet segments which reduces the volume of magnet and therefore reduces torque. To determine which amount of segmentation to use for the PDR design, a 3D FEA study was conducted in which the PM segmentation count was varied from 1 to 64 and the PM losses were calculated. These losses are used in the thermal analysis to estimate the PM hotspot temperature and ensure that it does not exceed the maximum allowable. While the RECOMA® 35E magnets can technically operate as high as 350°C, the manufacturer does not recommend designing them to operate above 200°C. The PM losses are simulated in 3D FEA considering both the fundamental excitation current and PE ripple current.

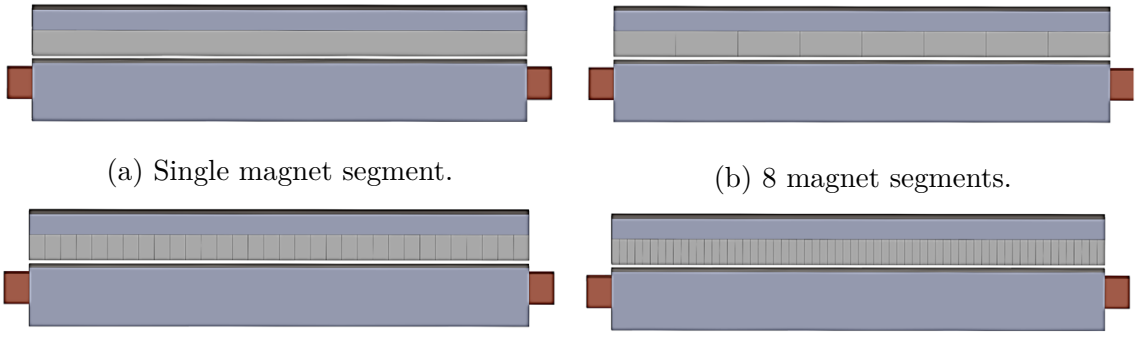

(a) Single magnet segment.

(b) 8 magnet segments.

(c) 32 magnet segments.

(d) 64 magnet segments.

Figure 5-27: Losses are compared for different levels of axial segmentation.

Table 5.8 shows that the PM losses decrease with increasing the number of permanent magnet segments. In particular, there is an approximately inverse relation with the number of magnet segments and the permanent magnet losses due to the fundamental frequency.

Table 5.8: The use of 64 PM segments theoretically reduces the PM eddy current losses by a factor of 2.5.

Number of Magnet Segments [-]	Segment Axial Length [mm]	Magnet Loss (Fundamental) [W]	Magnet Loss (Fundamental Plus Ripple) [W]
1	198	3850	4527
8	24.8	3323	4280
16	12.4	2766	3753
32	6.2	1803	2846
64	3.1	824	1835

In order to reach the assumed 200°C hotspot temperature, the eddy currents would need to generate 8000 W of loss. With the 64 segments, the PM loss estimate is 1800 W. Therefore, there is a safety factor of 4.4 on the loss estimate.

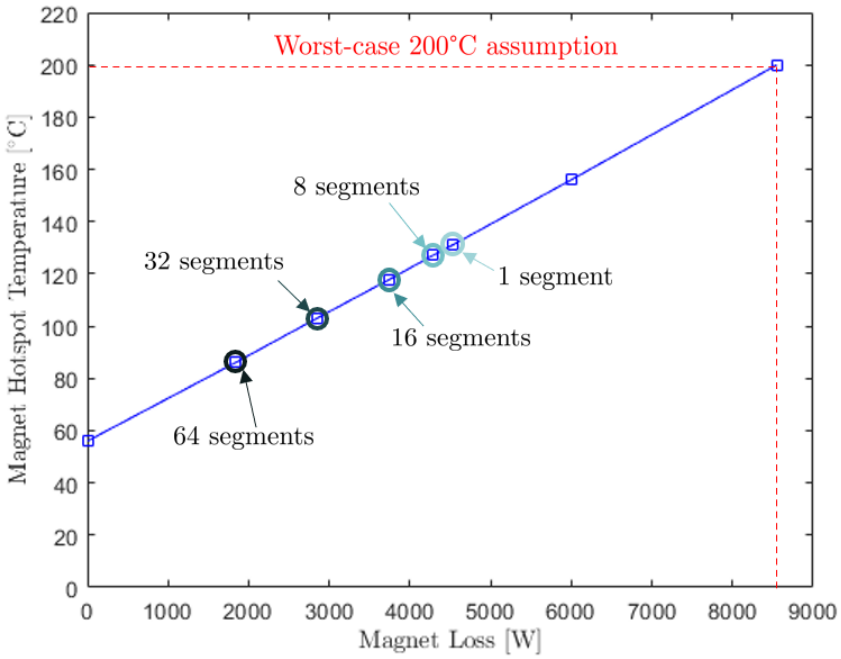

Figure 5-28: 8000 W of PM loss are required to approach to worst-case magnet hotspot temperature of 200°C.

When studying magnet segmentation, a dense mesh is required in the PMs to capture the 3D trajectories of the eddy currents. To reduce the mesh size and computation time for large amounts of segmentation, only one segment needs to be modeled

as shown in Fig. 5-29. Although only one segment is modeled, periodic boundary conditions are used to calculate the losses for the entire machine.

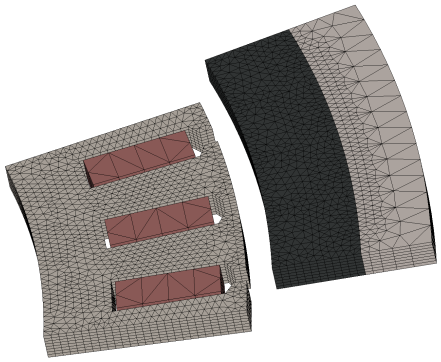

Figure 5-29: Mesh used to simulate eddy currents in permanent magnets.

The eddy current paths in the 3D FEA results match intuition. First, the eddy currents are generated in part from the magnetic flux density from the windings. Since the magnets and titanium rim behave magnetically similar to air, this flux density decays exponentially moving radially outward from the stator. Thus, the eddy currents should be greater towards the front of the magnet and weaker towards the back. The weaker current densities in the back of the magnet can be seen in Fig. 5-30. Second, since the flux density is radially outward, the eddy currents will circulate in the azimuthal and axial directions. This circulating eddy current pattern is shown in Fig. 5-31.

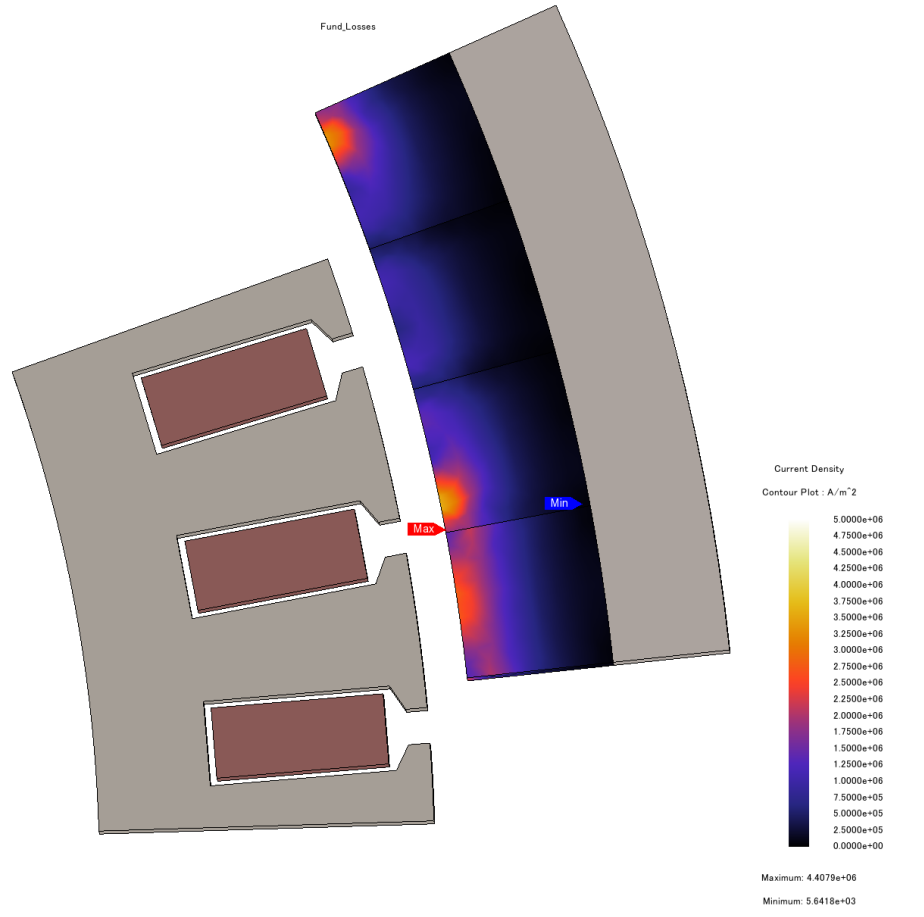

Figure 5-30: The current density decreases towards the back of the permanent magnet, as expected.

Figure 5-31: Circulating eddy currents as viewed from the airgap.

5.5.4 Demagnetization Study

Since the magnet hotspot temperature is estimated at 76°C, the demagnetization curve for RECOMA® 35E at 100°C was used in FEA as the closest approximation. This curve is shown in Fig. 5-32. In FEA, it is approximated with the straight blue lines. The recoil permeability is 1.08. The demagnetization study was also repeated at 200°C as a worst case analysis and the results did not change.

To compute the demagnetization analysis, the rotor is simulated in three condi-

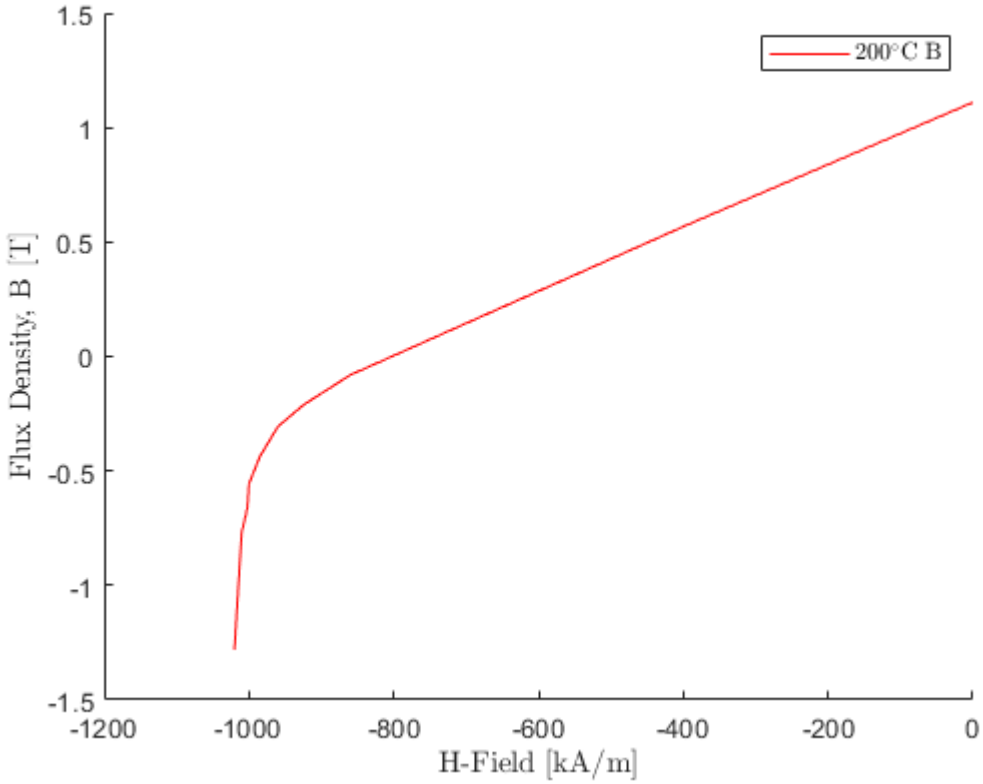

Figure 5-32: Demagnetization curve for Recoma 35e at 200°C.

tions for one electrical cycle each as shown in Fig. 5-33:

1. at no load to establish the baseline demagnetization for the magnets,
2. at rated conditions to determine the impact of the stator magnetic field on demagnetization, and
3. at no load again to determine if the rated currents demagnetized the magnets. If so, the B-H curve will now operate on a recoil line and a difference in torque and voltage will be observed.

The FEA software outputs the demagnetization ratio throughout the magnet based on (1)-(3) as shown in Fig. 5-34. The maximum demagnetization found is 0.2%, which has a negligble impact on the torque and voltage of the EM.

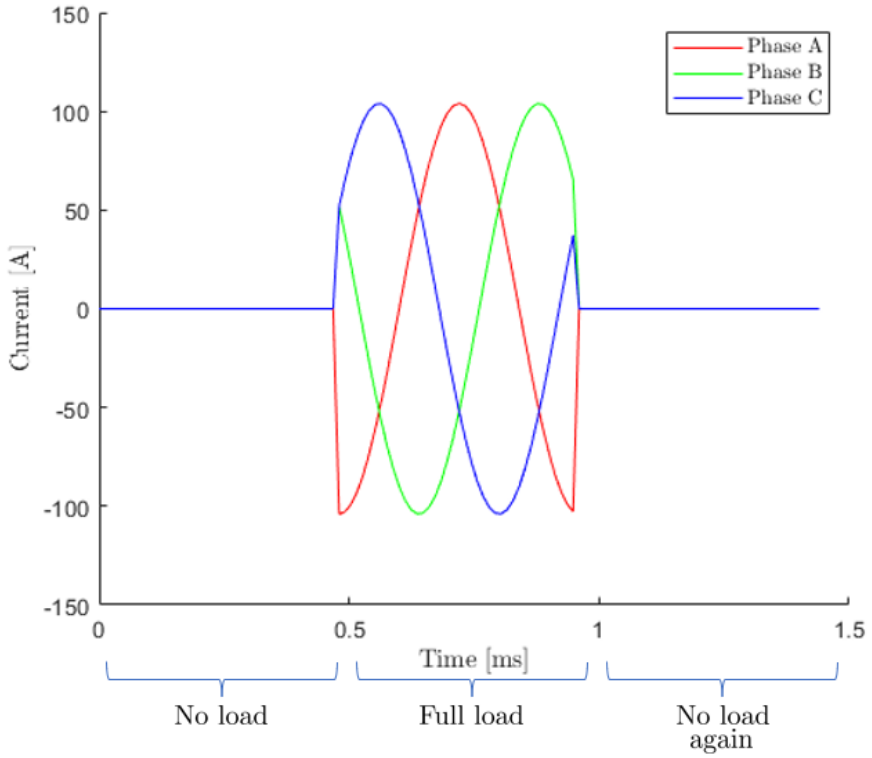

Figure 5-33: Excitation current used in demagnetization analysis.

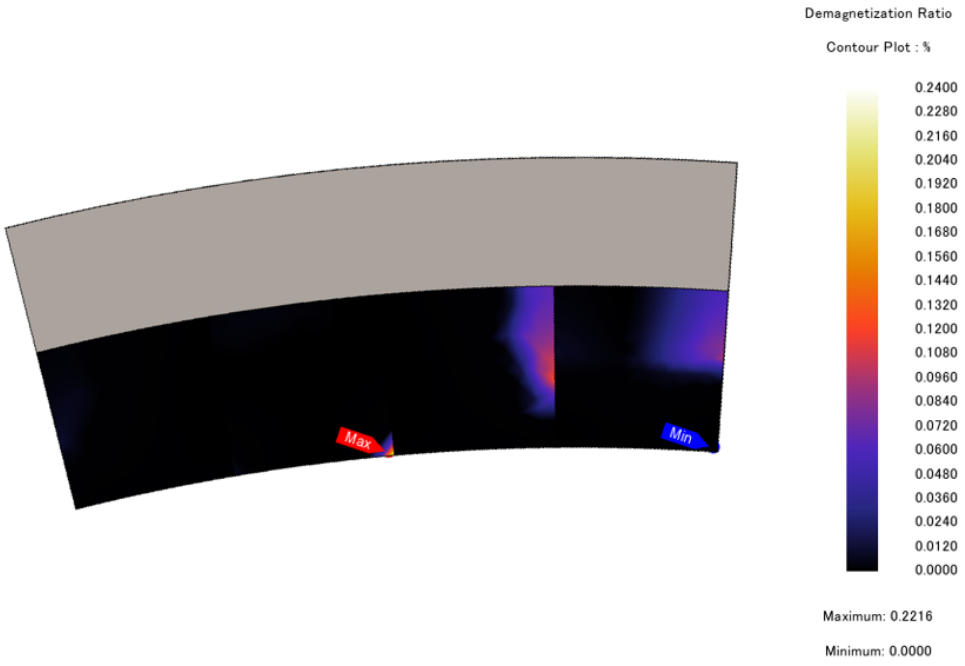

Figure 5-34: Isovalues of demagnetization ratio.

5.5.5 Ti Rim Losses

The titanium rim is modeled in FEA as a material having resistivity $1.78 \cdot 10^{-6} \Omega m$ and the permeability of free space. A 3D FEA is conducted to simulate the eddy currents in the titanium rim. The total loss in the Ti rim is estimated at 102 W. This includes losses due to both the fundamental excitation current (i.e., 2083 Hz) as well as the higher frequency ripple current (i.e., 160 kHz).

5.6 Stator Design Details

Iron-cobalt-vanadium (FeCoV) alloy is used for the stator in applications requiring the highest possible saturation magnetic flux density. Since the stator features are sized based on saturation flux density, cobalt alloy is suitable for the objective of minimizing electric machine mass. Since eddy current losses decrease with thinner lamination thicknesses, the thinnest available laminations of 4 mil (0.1016 mm) will be used for the stator laminations. The FeCoV alloys under trade names Hiperco® 50A (H50A) from manufacturer Carpenter Technology® and VACOFLUX® 48 from Vaccumschmelze® are under consideration for the stator steel since they offer the highest induction and lowest core losses compared to any alternatives.

In this section, the following aspects of the stator design are detailed:

1. stator material processing, and
2. core loss estimate via finite element analysis.

Item one describes the manufacturing and assembly process. Item two is used to mitigate the risk associated with the stator.

5.6.1 Stator Material Processing

Six different steps were identified for assembling the FeCoV alloy-based stator for the demonstrator:

1. obtain the unannealed FeCoV alloy,

2. cut the laminations,

3. anneal the FeCoV (either in sheet or lamination form),

4. insulating the laminations,

5. stack the laminations, and

6. mechanically clamping or bonding the stack.

These different steps are shown in Fig. 5-35. The annealing and cutting lamination steps are in the same row because their order is reversible depending on cutting technique.

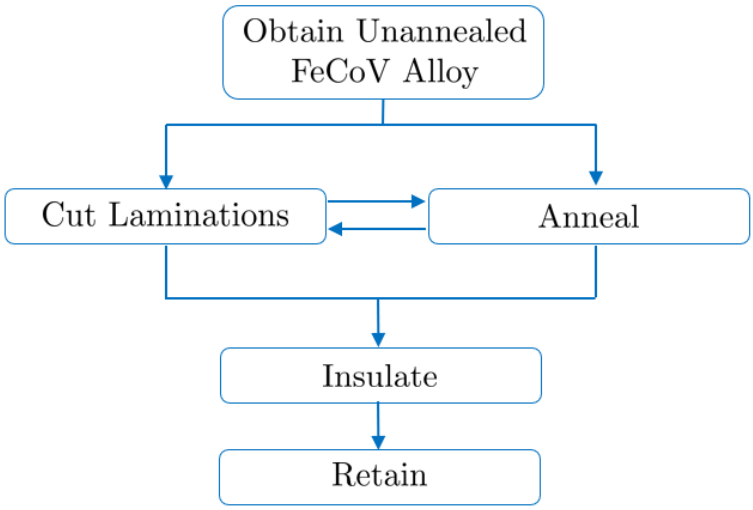

Figure 5-35: Flow diagram shows the various steps for manufacturing and processing a stator composed of FeCoV alloy.

Each of the steps above can be performed with various techniques. For example, the laminations can be cut via stamping, laser cutting, wire electrical discharge machining (EDM), or photochemical etching. The different processing paths considered for the demonstrator stator are summarized in Fig. 5-36 below. These options are not exhaustive, but capture the more common methods. The following subsections discuss the different options in more detail.

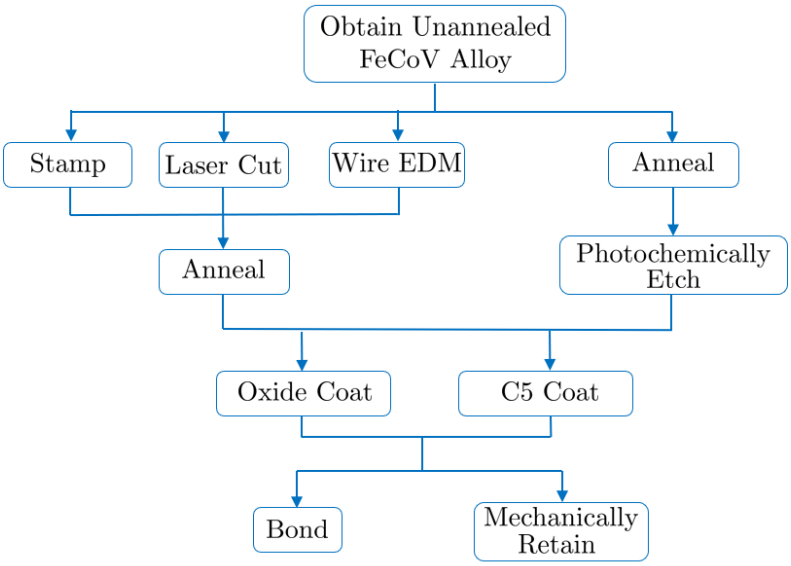

Figure 5-36: Different stator manufacturing processes are possible depending on the desired cut, insulation type, and retaining protocol.

Cutting Technique

Some common cutting techniques for stator laminations include stamping, laser cutting, wire EDM, and photochemical etching. Each manufacturing technique presents trade-offs between lead time, cost, and part tolerance. In addition, the cutting technique - stamping, laser cutting, etc. - can have varying affects on the magnetic performance of the FeCo alloy due to the stress imparted on the cut-edge of the FeCoV alloy [15]. A study from Ref. [16] showed that photocorrosion (i.e., photochemical etching) offers better performance to other cutting techniques such as laser cutting and stamping.

Photochemical etching was selected for the demonstrator since in theory it should minimize the cut-edge effects to the FeCoV laminations. In addition, the laminations can be annealed (i.e., heat treated) prior to etching, so no growth is induced in the laminations as would be the case with a post-cut anneal. This annealing is discussed in the next subsection.

Annealing

The FeCoV alloy must undergo a heat treatment to achieve the desired magnetic and mechanical properties. It is typical to heat treat after cutting out the laminations to relieve some of the stress at the cut-edge of the laminations. However, the annealing can also be performed before producing the laminations and still result in high magnetic performance for the photochemical etching process [16].

The annealing process grows the grains of the FeCoV alloy which improves the magnetic performance of the alloy. However, this growth also results in a permanent, 0.2% anisotropic length increase [14]. For the demonstrator design, this length increase is unacceptable since a tight tolerance needs to be maintained between the inner diameter of the stator and the outer diameter of the heat sink. Therefore, the annealing is performed before the cutting process. In addition, photochemical etching is selected due to the pre-etch anneal.

The manufacturer of Vacoflux 48 recommends the following annealing profile: the alloy is heated up to 880°C, held for 10 hours, and then decreased back to below 200°C at a rate of 100-200 K/h [14]. The annealing is performed in a pure dry hydrogen atmosphere because hydrogen is a reducing agent and helps remove impurities from the material.

Interlaminar Insulation

To prevent eddy currents from circulating between laminations and increasing core loss, each four mil lamination needs to be electrically insulated. Three insulation options were identified for use with the FeCoV laminations:

- oxide coating,
- C5 coating, and
- photoresist.

These insulation techniques differ in their application and impact on stacking factor. These are described briefly below.

The oxide coating is deposited after a stress relief anneal by heat treating the laminations in an oxidizing atmosphere from half an hour to three hours at 350°C to 450°C [14]. No public data was found that describes the relation between these baking parameters and the oxide coating thickness.

C5 coating is a standard industry technique for interlaminar insulation. The C5 coating is applied via a roller system. It is not conventionally used on thin laminations. From discussions with vendors, the C5 coating is expected to be 2.5 μm thick per lamination side.

The photoresist option was mentioned by the vendor who photochemically etched the stator laminations. The standard photoresist that the vendor uses leaves a 40 μm layer which is unacceptable for achieving a reasonable stacking factor. However, the vendor offers an alternative photoresist that only leaves a 5 μm layer on the lamination. This photoresist is dip coated on each sheet of material. This option was attractive because it is necessary to etch the laminations anyway, so no extra handling would be required. The thickness of the photoresist was measured using a stylus profilometer as shown in Fig. 5-37.

The stacking factor of the electric machine is the ratio of the ferromagnetic material volume, V_{FeCo}, to the total volume of the stator stack including insulation. As the stacking factor decreases, the available ferromagnetic material for guiding the magnetic flux decreases, which increases the B-fields in the stator. An increase in B-fields will increase the total core loss. Since the peak B-field is at 2.18 T, it is desirable to try to keep the stacking factor at 90% or greater to avoid deep saturation. If $V_{\text{insulation}}$ is the volume of the insulation, the stacking factor k_{stack} is defined as

$$k_{\text{stack}} = \frac{V_{\text{FeCo}}}{V_{\text{FeCo}} + V_{\text{insulation}}} \tag{5.4}$$

Figure 5-38 shows the stacking factor versus insulation thickness. The expected stacking factors for the photoresist (i.e., SC resist) and C5 coating are between 93-95%, which is acceptable. The oxide coating thickness is unknown.

In addition to stacking factor, another concern was whether or not the application

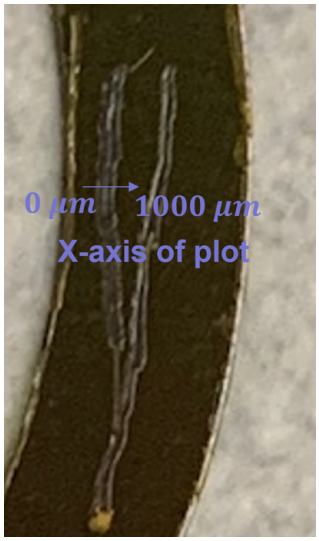

(a) Trajectory taken by profilometer

.

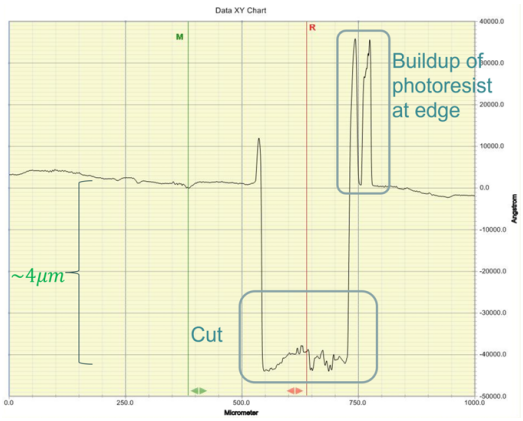

(b) Profile of photoresist

.

Figure 5-37: A profilometer was used to measure the depth of the photoresist layer.

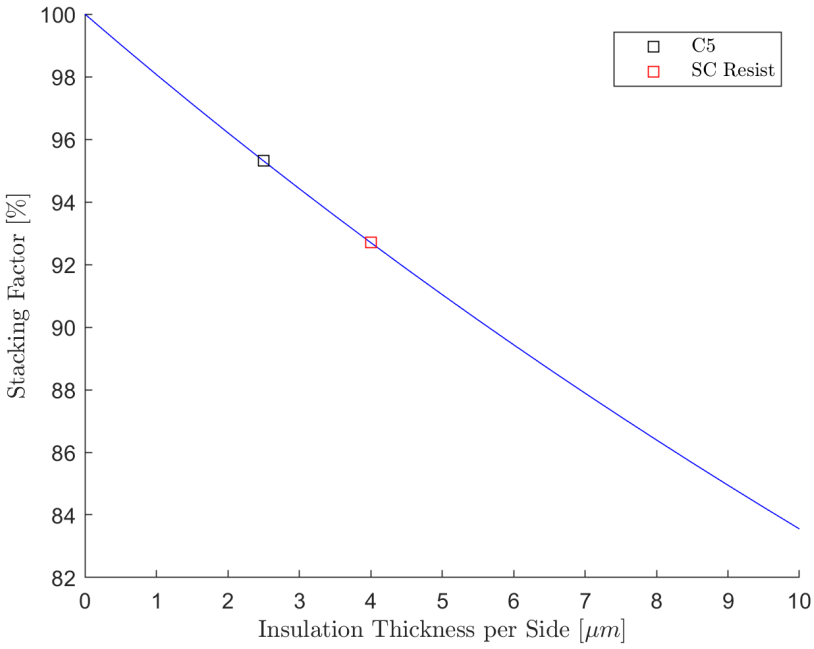

Figure 5-38: Difference found in stacking factor between C5 coating and SC resist.

of the insulation affects the performance of the Vacoflux 48. Three toroids were created - one with each coating. These coated toroids are shown in Fig. 5-39.

It was found that all three toroids had identical magnetic performance. The last constraint to differentiate the insulations was the maximum operating temperature. A maximum operating temperature for the photoresist could not be identified from datasheets or vendors. However, based on safety data sheets, it was suspected to be between 100°C and 200°C. C5 coating and oxide coating have much greater temperature rating in the hundreds of degrees celsius. Since the winding hotspot temperature is expected to be around 180°C, the photoresist option was eliminated.

The decision between C5 coating and oxide coating came down to the stacking factor. Due to the lack of data on the oxide coating, the C5 coating was selected for the demonstrator processing.

(a) Uncoated toroid.

(b) C5 coated toroid.

(c) Photoresist coated toroid.

Figure 5-39: A profilometer was used to measure the depth of the photoresist layer.

Stacking and Retention

Once the laminations have been cut, annealed, and insulated, the last step for the demonstrator build is to stack and retain them. A custom stacking fixture was created to stack, hold, and transport the laminations. With regards to retention, two options under consideration are bonding the laminations, or mechanically retaining the stack at the axial endpoints. The key consideration here is the compression from the retaining mechanism on the lamination stack. The core loss and induction of FeCoV alloy in particular is sensitive to compressive force via the magnetomechanical

effect.

5.6.2 Core Loss Estimate Via Finite Element Analysis

The core loss is estimated using the Steinmetz equation via two approaches:

1. a hand calculation assuming the entire stator is at 2.2 T, and
2. a refined estimate in FEA that accounts for the variation in flux density as well as the higher order harmonics.

In approach (1), the core loss per unit mass is modeled as

$$\frac{P_{\text{core}}}{m} = K_1 f B^2 + K_2 f^2 B^2 + K_3 f^{1.5} B^{1.5} \tag{5.5}$$

where f is the electrical frequency; B is the magnetic flux density; and K_1, K_2, and K_3 are obtained by a curve fit to measured loss data. To minimize EM mass, the stator features are as thin as possible without over-saturating the steel. Consequently, the flux density in most of the steel is close to 2.1 T. To be conservative, the maximum B-field is assumed to be 2.2 T when using Eqn. 5.5. A core loss of 4410 W is estimated with this approach. Based on anecdotal evidence, the core loss is doubled to try to account for other effects such as rotating magnetic fields which are not typically captured during the toroid loss measurements. Thus, the total core loss from approach (1) is 8820 W.

In approach (2), Eqn. 5.5 is still used, but with two key differences. First, the non-uniformity of the B-field is taken into account. Second, higher order harmonics are included in the calculation. Therefore, the coefficients K_1-K_3 vary with frequency.

Since the core loss data obtained from the manufacturer is limited to 4000 Hz, only the core loss due to the fundamental frequency is estimated via these two approaches. The high frequency core loss is estimated analytically. Figure 5-40 shows the core loss estimate from FEA. Since the steel is not heavily saturated and the Halbach array generates a relatively sinusoidal flux density, most of the loss is due to the fundamental. However, the higher order harmonics do contribute to the core loss as

well. Approach (2), with the same safety factor of two, provides a core loss estimate of 7260 W. The greater core loss estimate of 8820 W is used to provide additional safety margin.

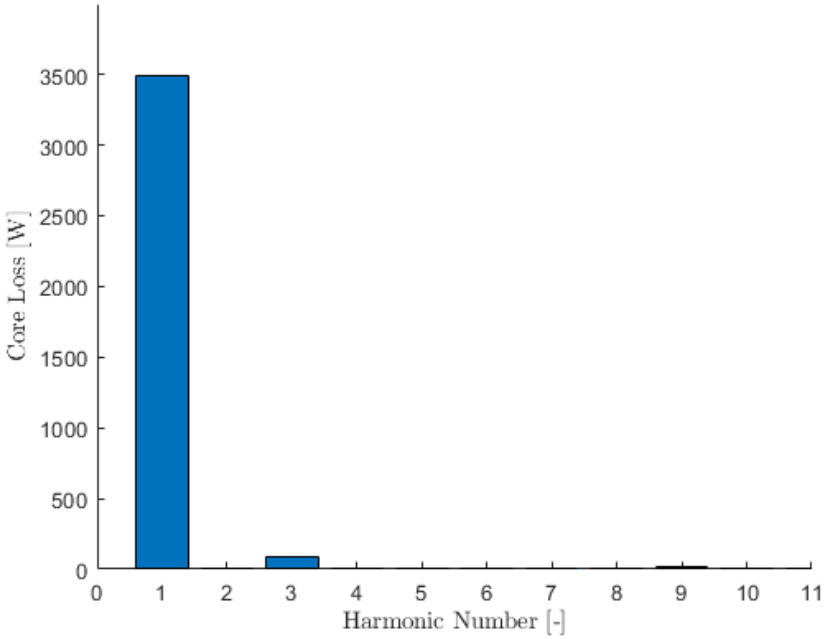

Figure 5-40: The core losses are primarily from the fundamental component.

5.7 Integrated Design Considerations

Since the electric machine, power electronics, and thermal management system are all tightly integrated, additional analysis was conducted on the electric machine to assist the design of other subsystems. These include

1. eddy current losses in the spindle, bearings, and heat sink;
2. stiffness estimates for the bearing design;
3. eddy current loss estimate in the spindle due to the pass through conductors;
4. stray fields for sensor placement; and
5. the axial force due to rotor compression during operation.

5.7.1 Eddy Current Losses

The permanent magnets and windings of the demonstrator may produce stray magnetic fields that can interact with nearby structure and sensors. In addition to the stray fields that may exist around the rotor and stator, the long electrical leads produce magnetic fields that may interact with any structures near their routing. The eddy currents in the structures can be problematic because they present another source of heat. Structures such as the bearings may require low temperatures to maintain functionality.

The objective of this eddy current loss section is to

1. evaluate the magnetic field strength of the stray fields, and

2. quantify the eddy current loss in the nearby structures. This loss will be used in thermal analysis to verify that components are operating at an acceptable temperature.

A combination of 2D and 3D magnetic finite element analysis is used to meet these objectives.

Spindle Losses

Grooves were added to the spindle to route the electrical leads from the electric machine to the power electronics. Figure 5-41 shows the support structure, spindle, and leads which pass through the groove and bend around the shoulder. In electromagnetic FEA, a cut plane was added for 2D analysis where the leads are surrounded on both the top and bottom by aluminum. This 2D analysis was used as a first pass to evaluate the magnitude of the losses. If significant, a 3D analysis would be used to obtain a higher fidelity estimate. The spindle and support structure are fabricated from Al 7075-t6 which has a resistivity of $5.15 \cdot 10^{-8} \Omega \cdot m$.

The 2D model of the spindle, superstructure, and leads is shown in Fig. 5-43. The spindle has 30 grooves. In each groove, a pair of leads passes through which belong to a single full bridge inverter.

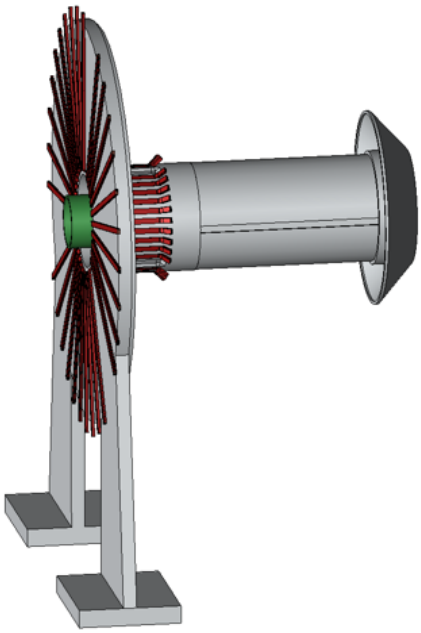

Figure 5-41: The leads pass through grooves in the spindle before routing up the elbow towards where the power electronics will be located.

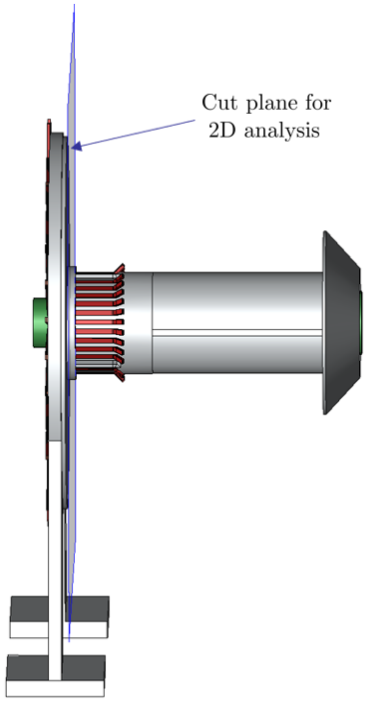

Figure 5-42: A cut plane is created in 2D analysis where the leads are completely surrounded by aluminum.

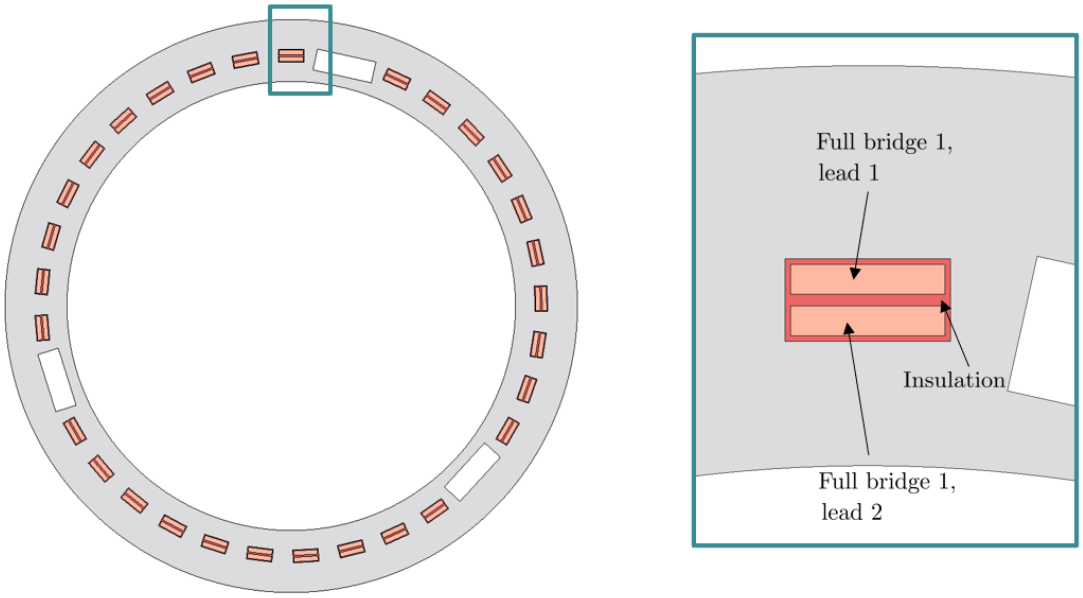

Figure 5-43: Cross-sectional view of the spindle shows the 60 electric machine leads that are routed through 30 slots. Each pair of leads in a slot corresponds to one full bridge inverter.

Since each slot has the leads for a single full bridge inverter, the currents carried on each lead in a slot travel in opposite directions. Figure 5-44 shows an assumed direction for the currents.

The total loss in the spindle was found to be 13 mW, which is considered negligible.

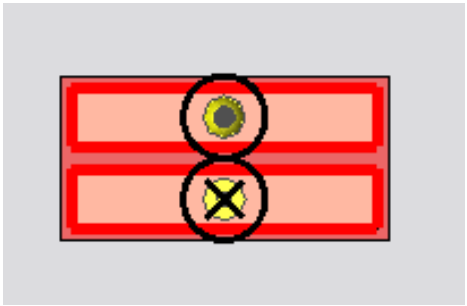

Figure 5-44: Since the currents in a spindle slot correspond to one full bridge circuit, they have opposite directions of current which cancels the external field.

Bearing Losses

The bearings will only be on the top side of the windings. Since the spindle surrounds both the top and bottom of the windings, an upper bound on the losses is obtained by switching the spindle material to that of the bearings. Specifically, the material property of the aluminum in Fig. 5-43 is changed to that of graphite. Therefore the resistivity is changed from $5.15 \cdot 10^{-8} \quad \Omega \cdot m$ to $6 \cdot 10^{-4} \quad \Omega \cdot m$. Similar to the spindle, the losses were found to be negligible at 1.6 mW.

Heat Sink Losses

The total heat sink losses due to stray magnetic fields is estimated at 4 mW. Due to this low magnitude, the heat sink losses are considered negligible. The current density isovalues due to these stray fields is shown in Fig. 5-45.

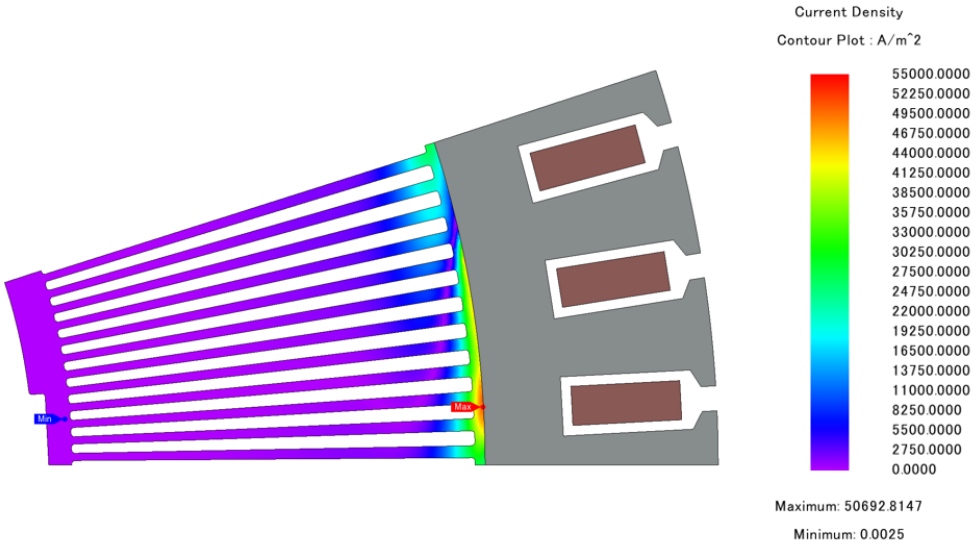

Figure 5-45: Current density isovalues of the heatsink.

5.7.2 Stiffness Estimates for Bearing Design

When selecting the bearings, the stiffness of the electric machine due to electromagnetic forces must be considered amongst the stiffnesses of other demonstrator structures such as the superstructure and shaft. To estimate this stiffness, the stator

is offset in the x-direction, and the x-directed and y-directed forces are extracted from finite element analysis. The bearing stiffness is estimated as

$$k_{\mathrm{xx}} = \frac{\Delta F_x}{\Delta x} \tag{5.6}$$

An initial 0mm offset is first simulated and confirmed that the net x- and y-directed forces are zero. Next, the stator is offset 1mm in the negative x direction as shown in Fig. 5-46.

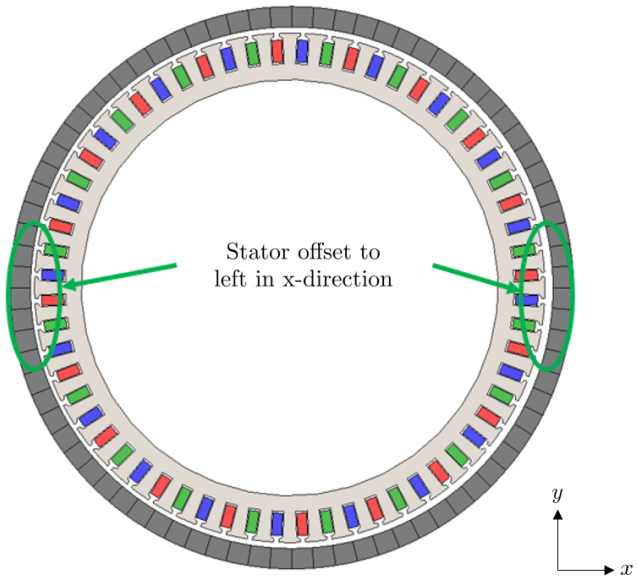

Figure 5-46: Stator with 1mm offset in -x direction.

The average x-directed force is 2,000 N in the direction of offset (i.e., to the left in this case) and the average y-directed force is 26.3 N. This same simulation was repeated for 0.5mm and it was found that the x-directed force was 1,000 N, which showed a linear relation. The relevant stiffness constant for the bearing design is therefore 1 kN/m.

5.7.3 Stray Fields Near Electric Machine

Stray fields are evaluated at the end of the electric machine axially and outside the titanium rotor rim which has the permeability of air. Figure 5-47 shows the area

where the stray fields are evaluated for a single pole section. These stray fields from the permanent magnet and stator windings can be seen in the side view in Fig. 5-48.

To evaluate the magnitude of the stray magnetic fields, ten probes are used as shown in Fig. 5-49a.

The B-field magnitude is found to decay exponentially, plateauing around 2 mT at 7 mm away as shown in Fig. 5-50. Since the end turns extrude approximately 24 mm away and sensors would be placed beyond the end turns, they are not expected to be affected by these stray fields.

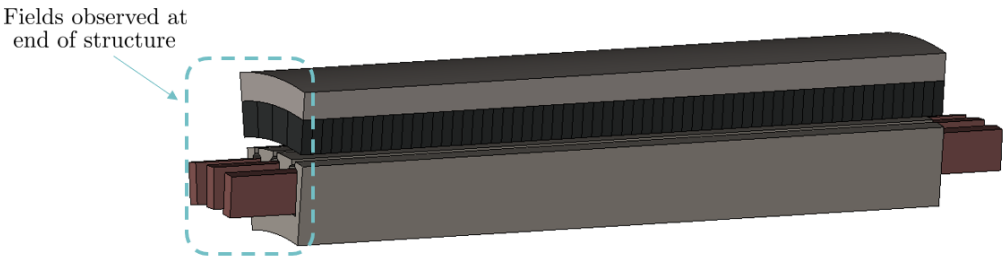

Figure 5-47: Side view of electric machine along axis of rotation shows fringe fields from magnet extend beyond machine boundary.

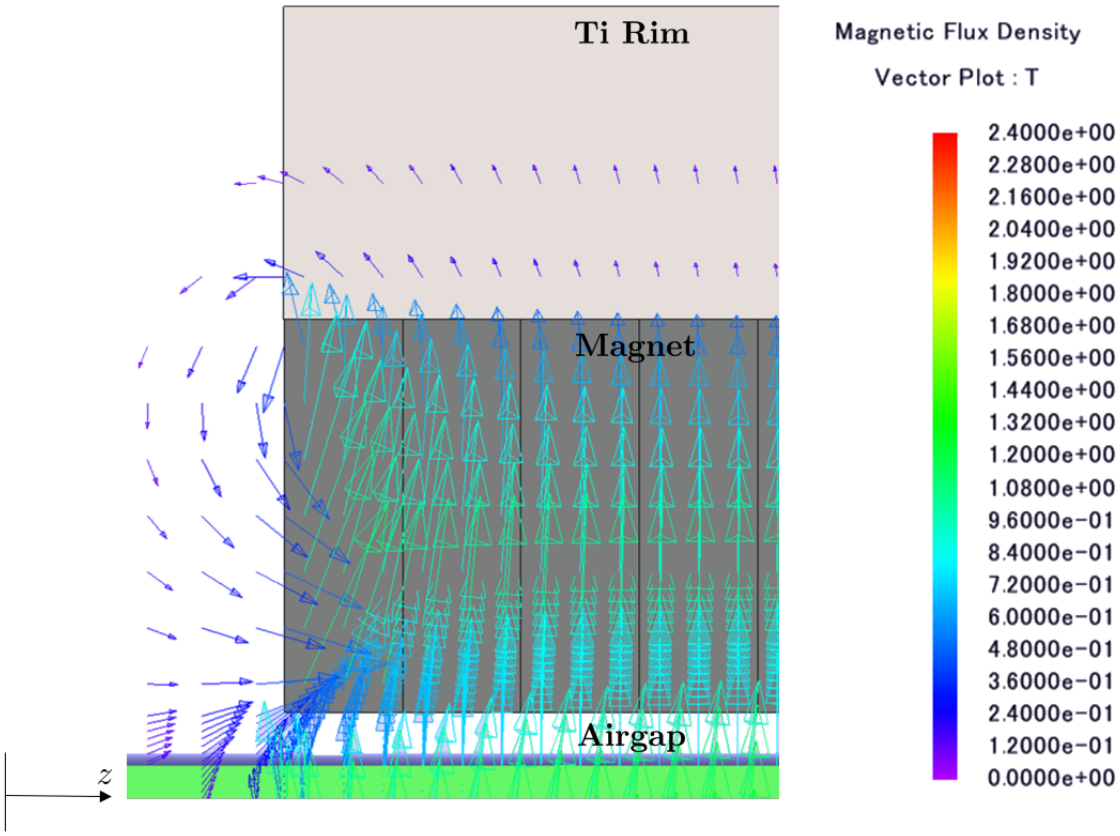

Figure 5-48: Vector plot of stray fields at axial end of machine.

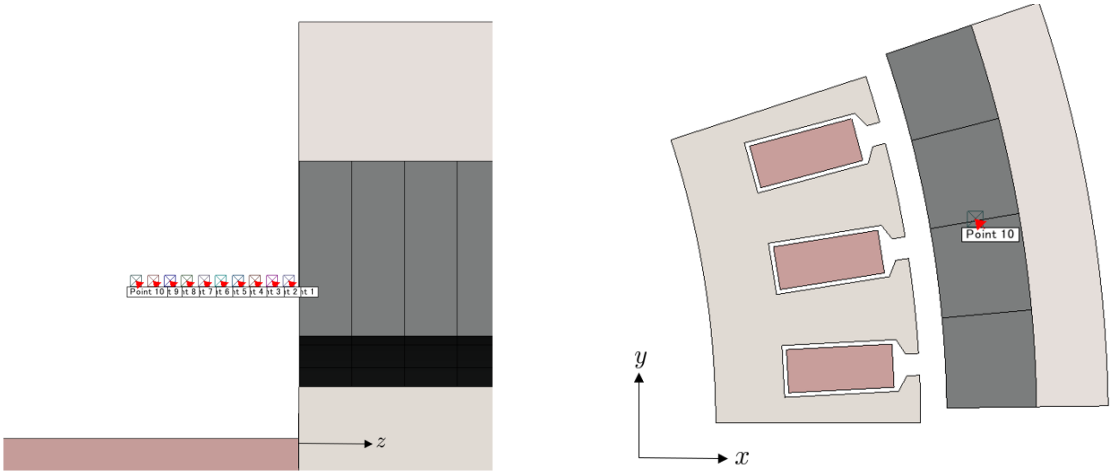

(a) Ten probes each placed 1 mm apart from edge of machine to extract B-fields.

(b) The probes are placed adjacent to the magnets (only one probe shown here).

Figure 5-49: Axial field probe locations.

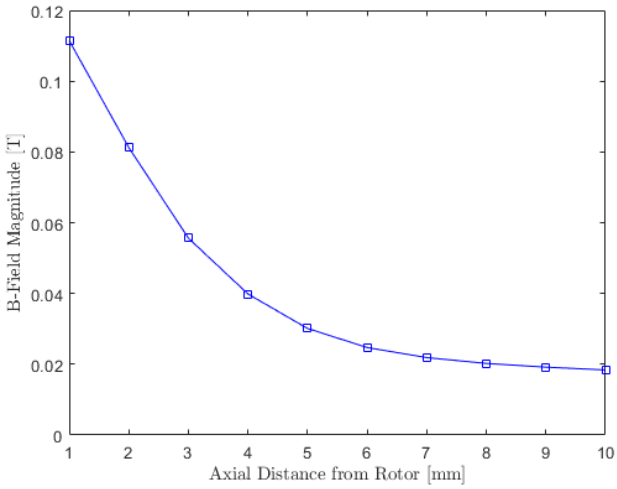

Figure 5-50: B-field values of axial field.

5.7.4 Axial Force due to Rotor Offset

Based on structural finite element analysis, the rotor is expected to be compressed in the axial direction up to 0.5 mm at the design speed of 12,500 rpm. This compression is due to the end bell expanding at design speed, which compresses the rotor drum towards the end bell. This axial rotor compression may impact the load on the bearings and therefore informs the final bearing selection. A force analysis was conducted in 3D finite element analysis to estimate the axial-directed force.

Figure 5-51 shows the initial 2mm offset of the rotor from the end of the stator. The offset is then decreased at 0.2mm increments to capture the change in axial force with displacement. The currents are assumed to be constant at balanced condition such that $I_a = I_{\text{pk}}$

The change in axial-directed force versus offset is summarized in Table 5.9. Around the 0.5mm of expected rotor compression, the force is found to be approximately 50 N. The force increases approximately linearly with offset. This magnitude of force is not considered significant from a bearing loading point-of-view.

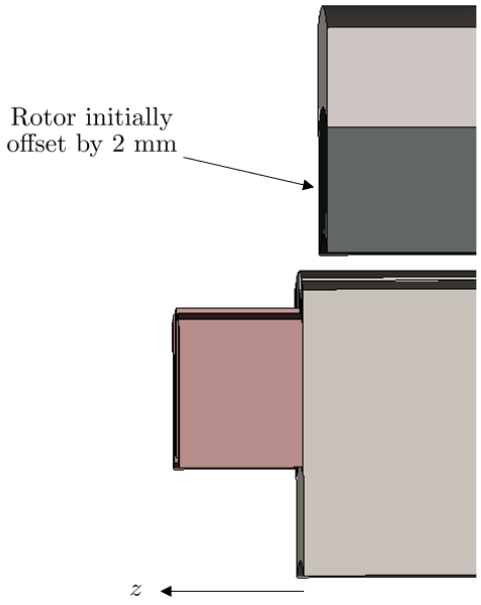

Figure 5-51: Rotor offset to analyze axial force.

Table 5.9: Z-directed force on the rotor versus its axial offset from the stator.

Offset [mm]	**Z-Directed Force [N]**
2	193
1.8	176
1.6	164
1.4	150
1.2	113
1.0	100
0.8	76
0.6	52
0.4	46
0.2	31
0	0

5.8 Outer Loop Control Design

The objective of the outer loop control is to slowly ramp the motor and generator up to design speed and design torque to produce one megawatt of power. Since the objective is simply to reach one megawatt of power, this ramp up can occur over a period of minutes.

The titanium rim is structurally designed for 12,500 rpm maximum with a safety

margin that will be quantified by the spin pit test. The objective of this preliminary controller design is to minimize the rotational speed overshoot to less than 10% of the rated operating speed. This requirement can be adjusted pending the spin pit test results. Similarly, the input currents to the motor and generator are limited to the rated current of 104 A because excessively high currents could lead to the winding hotspot temperature exceeding that of the insulation.

The outer loop control design is organized as follows: first, the system dynamics are described in Section 5.8.1. Next, these dynamics are cast in the state-space model formulation in Section 5.8.2. A linear quadratic-Gaussian control approach, such as that from Ref. [70], is then implemented to control the motor and generator speeds and torques. An overview of this approach is given in Section 5.8.3. Lastly, results of the preliminary control design are shown in Section 5.8.5. This controller design can be discretized for hardware implementation.

5.8.1 System Dynamics

For the demonstrator, the motor and generator are modeled as two moments of inertia connected via a spring that represents the shaft. The system is shown in Fig. 5-52 and the associated variables are explained below.

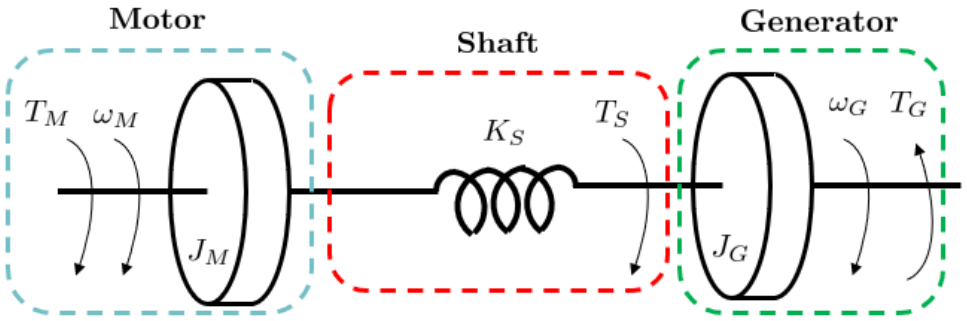

Figure 5-52: Back-to-back motor generator system is modeled as two inertias connected via a shaft.

The shaft torque, T_S, is proportional to the angular displacement between the motor and generator shafts via a shaft stiffness constant, K_S. If θ_G and θ_M are the shaft angles for the generator and rotor, respectively, then the shaft torque is

$$T_S = K_S\left(\theta_M - \theta_G\right) \tag{5.7}$$

Then, for the motor:

$$J_M \frac{d^2\theta_M}{dt^2} = T_M - T_s \tag{5.8}$$

and for the generator

$$J_G \frac{d^2\theta_G}{dt^2} = T_S - T_G \tag{5.9}$$

Lastly, the torques are related to the input currents via

$$T_M = \frac{3}{2} k_t^M i_q^M \tag{5.10}$$

and

$$T_G = \frac{3}{2} k_t^G i_q^G. \tag{5.11}$$

Since the motor and generator have identical designs, the torque constants and moments of inertia are assumed to be identical between the motor and generator. Therefore $J_M = J_G$ and $k_t^M = k_t^G$. Substituting Eqns. 5.7, 5.10, and 5.11 into Eqn. 5.8 and 5.9, the two differential equations describing the system are

$$\frac{d^2\theta_M}{dt^2} = \frac{1}{J}\left(1.5 k_t i_q^M - K_\theta \theta_M + K_\theta \theta_G\right) \tag{5.12}$$

$$\frac{d^2\theta_G}{dt^2} = \frac{1}{J}\left(-1.5 k_t i_q^M + K_\theta \theta_M - K_\theta \theta_G\right) \tag{5.13}$$

5.8.2 State-Space Model

The open-loop plant state-space representation of Eqn. 5.12 has the form

$$\begin{aligned} \dot{x} &= A_{\text{ol}} x + B_{\text{ol}} u + w \\ y &= C_{\text{ol}} x + v \end{aligned} \tag{5.14}$$

where

$$A_{\text{ol}} = \begin{bmatrix} 0 & 1 & 0 & 0 \\ -\frac{k_\theta}{J} & 0 & \frac{k_\theta}{J} & 0 \\ 0 & 0 & 0 & 1 \\ \frac{k_\theta}{J} & 0 & \frac{-k_\theta}{J} & 0 \end{bmatrix}, \quad B_{\text{ol}} = \begin{bmatrix} 0 & 0 \\ \frac{3}{2}\frac{k_t}{J} & 0 \\ 0 & 0 \\ 0 & -\frac{3}{2}\frac{k_t}{J} \end{bmatrix} \tag{5.15}$$

$$C_{\text{ol}} = \begin{bmatrix} 1 & 0 & 0 & 0 \\ 0 & 1 & 0 & 0 \\ 0 & 0 & 1 & 0 \\ 0 & 0 & 0 & 1 \end{bmatrix} \tag{5.16}$$

and $x = [\theta_m, \omega_m, \theta_g, \omega_g]^T$ and $u = \left[i_q^M, i_q^G\right]^T$. The process noise, w, and measurement noise, v, have been included in the state space model as is customary when designing LQG control systems.

5.8.3 Controller Design

As mentioned in the introduction of this section, a linear-quadratic-Gaussian (LQG) approach is used for the controller design of the outer control loop [70]. The LQG controller consists of a Kalman filter for state estimation and a linear-quadratic regular (LQR) for feedback control.

In this LQG approach, the LQR feedback control is modified to use a reference state, x_{ref} to implement a tracking solution [71], viz,

$$u = K\left(\hat{x} - x_{\text{ref}}\right) \tag{5.17}$$

where $\hat{x}$ is the state estimate from the Kalman filter and the control gain matrix $K = -R^{-1}B_{\text{ol}}P$. The matrix P is the solution to the control algebraic Ricatti equation

$$PA_{\text{ol}} + A_{\text{ol}}^T P + Q - PB_{\text{ol}}R^{-1}B_{\text{ol}}^T P = 0 \tag{5.18}$$

where Q and R are weighting matrices that are tuned for the controller design objec-

tives. The Kalman filter dynamics have the form

$$\begin{aligned} \dot{\hat{x}} &= A_{\text{ol}}\hat{x} + B_{\text{ol}}u + G\left(y - \hat{y}\right) \\ \hat{y} &= C_{\text{ol}}\hat{x} \\ G &= \Sigma C_{\text{ol}}^T V^{-1} \end{aligned} \tag{5.19}$$

where G is the Kalman filter gain. The error covariance matrix Σ is solved via the filter algebraic Ricatti equation

$$\Sigma A_{\text{ol}}^T + A_{\text{ol}}\Sigma + W - \Sigma C_{\text{ol}}^T V^{-1} C_{\text{ol}}\Sigma = 0 \tag{5.20}$$

where W is the process noise intensity matrix and V is the measurement noise intensity matrix.

Let $x_{\text{cl}} = [x_{\text{ol}}, \hat{x}]^T$ be the closed-loop system state vector. The closed-loop system dynamics are arrived at by combining Eqns. 5.14 and 5.19:

$$\begin{aligned} \dot{x}_{\text{cl}} &= A_{\text{cl}}x_{\text{cl}} + B_{\text{cl}}u \\ y_{\text{cl}} &= C_{\text{cl}}x_{\text{cl}} \end{aligned} \tag{5.21}$$

where

$$A_{\text{cl}} = \begin{bmatrix} A_{\text{ol}} & 0 \\ GC_{\text{ol}} & A_{\text{ol}} - GC_{\text{ol}} \end{bmatrix}, \quad B_{\text{cl}} = \begin{bmatrix} B_{\text{ol}} \\ B_{\text{ol}} \end{bmatrix} \tag{5.22}$$

$$C_{\text{cl}} = \begin{bmatrix} C_{\text{ol}} & 0 \end{bmatrix} \tag{5.23}$$

with the control, u, defined by Eqn. 5.17. Equation 5.21 is implemented with the fourth order Runge-Kutta method to simulate the controller design.

5.8.4 Design Parameters

The torque constant for the electric machine is the rated torque divided by the rated current, or $k_t = 7.36$ Nm/A. The moment of inertia for a single rotor was provided by Yuankang Chen [27] as 0.551 kg m^2.

The shaft stiffness is estimated as

$$K_\theta = \frac{T}{\theta} = \frac{GJ_{\text{shaft}}}{L} \tag{5.24}$$

where G is the modulus of rigidity, J_{shaft} is the shaft moment of inertia, and L is the shaft length. It is assumed that the shaft is a 20 mm thick, one meter long hollow shaft that has approximately the diameter of the electric machine at 200 mm. These numbers may be adjusted once the shaft design is complete. Under this assumption, the shaft stiffness is $K_\theta = 4 \cdot 10^7 Nm/rad$.

The weighting matrices Q and R are set to be the identity matrices. That is,

$$Q = \mathbb{I}_{4\times 4}, \quad R = \mathbb{I}_{2\times 2} \tag{5.25}$$

The noise intensity matrices, V and W, are selected as

$$V = \mathbb{I}_{4\times 4}, \quad W = 40000 \cdot \mathbb{I}_{4\times 4} \tag{5.26}$$

The noise intensities are viewed as design parameters, and are selected to obtain desired closed-loop system performance as opposed to optimal estimator response. These values may require tuning once the prototype hardware is available.

The state reference, x_{ref}, is selected to gradually increase the electric machines speed to design speed. The speed reference signals for the motor and generator have the form

$$\omega_{\text{ref}} = \omega_0 \left(1 - e^{-t/\tau}\right) \tag{5.27}$$

and the angular orientations are obtained by integrating Eqn. 5.27:

$$\theta_{\text{ref}} = \omega_0 \left(t - \tau \left(1 - e^{-t/\tau}\right)\right) \tag{5.28}$$

The state reference vector is then $x_{\text{ref}} = [\theta_{\text{ref}}, \omega_{\text{ref}}, \theta_{\text{ref}}, \omega_{\text{ref}}]^T$

5.8.5 Controller Results

The rotational speed of the motor converges to the 12,500 rpm target as shown in Fig. 5-54 without overshoot. The closed-loop speed reaches the 12,500 rpm target after approximately 20 seconds. Only the motor speed is shown in Fig. 5-54 because the generator speed control performance is identical. The time constant of the tracking signal, τ, can be adjusted depending on desirable ramp time. The controller designed for k_{theta} was found to control the speeds to their reference without overshoot even in the case where the actual k_{theta} is twice as high or 1,000 times as low. After the shaft and bearing designs are complete, the control design can be updated with a k_{theta} value representative of the final design.

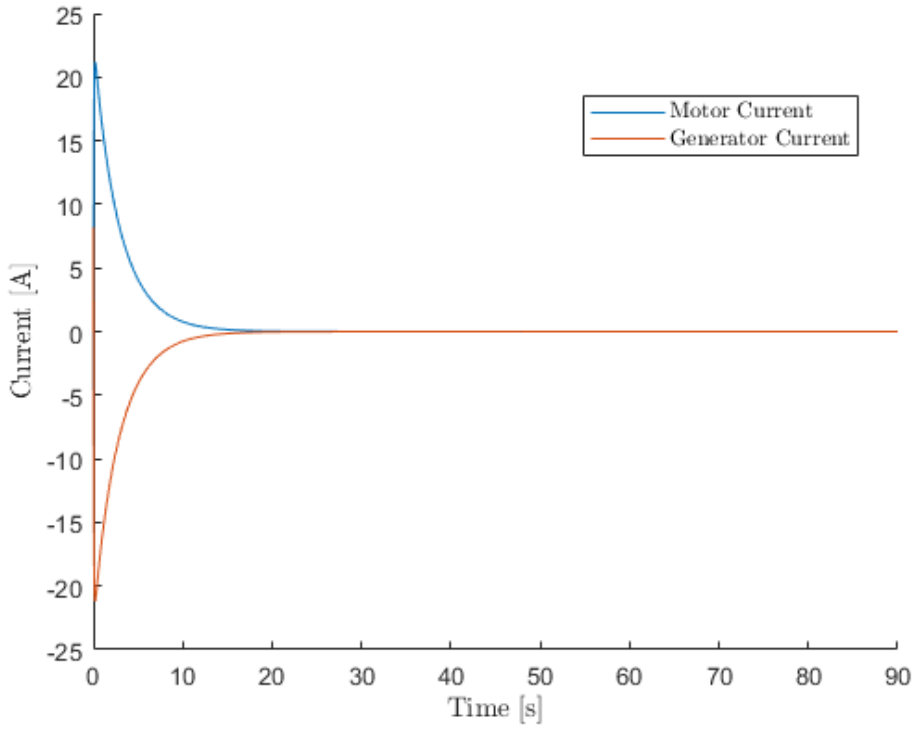

Figure 5-53: The generator and motor input currents do not exceed the 104 A maximum.

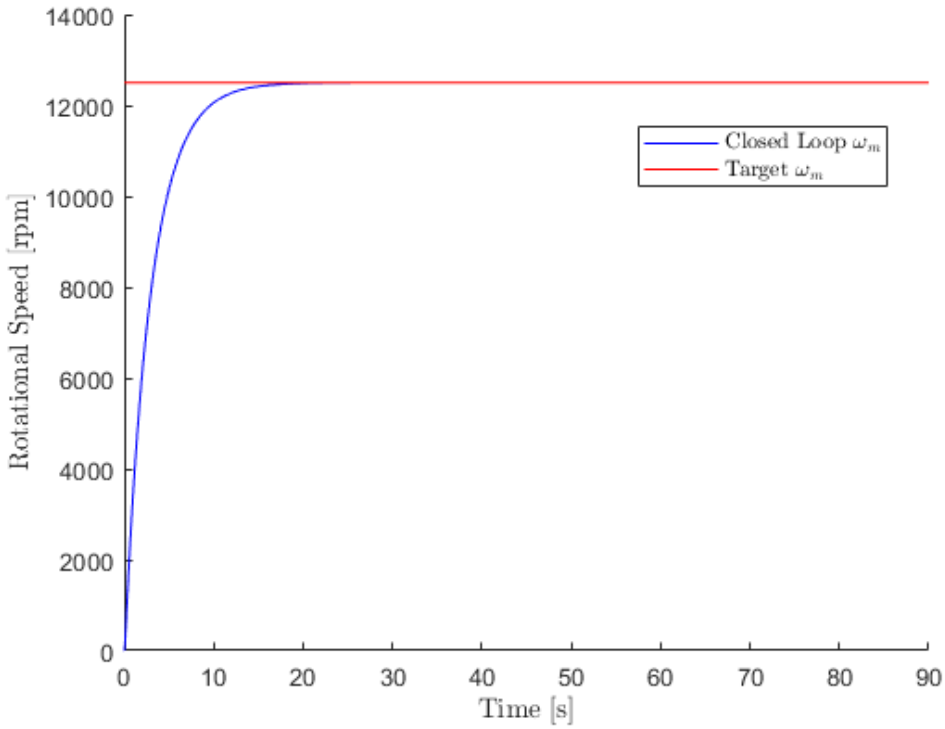

Figure 5-54: The closed loop motor and generator speed converge to the target 12,500 rpm without overshoot.

5.9 Summary of Results

In this chapter, a detailed design was conducted on the electric machine for the demonstrator. The manufacturing and assembly processes for each component were developed. 2D and 3D finite element analysis was used to obtain higher fidelity estimates of losses in the electric machine. This analysis informed:

- the loss quantities to use in the detailed hotspot temperature analysis,
- the selection of 64 axial permanent magnet segments,
- the tooth tip geometry of the stator, and
- the design and placement of other structures in the demonstrator.

Bench tests were performed early on to mitigate risk. For example, a 3D printed mockup was created to verify the feasibility of the conceptual winding pattern. Lastly,

a preliminary control design via the LQG approach was completed and the rotational speed slowly ramps up to the design speed with acceptable overshoot. The controller can be further tuned and optimized when experimental hardware is available. After the detailed design phase, the demonstrator is still anticipated to have a system specific power of 11 kW/kg..

Chapter 6

Summary and Conclusions

6.1 Summary

Turboelectric distributed propulsion (TeDP) systems may enable a reduction in the fuel consumption of commercial aircraft. This predicted fuel consumption reduction is due to boundary layer ingestion and distributed propulsion, both of which electrical transmission system facilitates. However, a key challenge in realizing turboelectric propulsion is the low specific powers of electric components available today. NASA has established target specific powers for the electric machines and power electronics in the years 2030 and 2035 which are necessary to realize the benefits of TeDP. The NASA target specific power of the standalone electric machine is 13 kW/kg and 16 kW/kg for 2030 and 2035, respectively.

A novel integrated prime mover (IPM) concept is proposed in this thesis to improve the overall specific power of turboelectric propulsion systems. In this concept, an electric machine is embedded within a turbomachine to utilize the turbomachine rim, to bleed air from the low pressure compressor for cooling purposes, and to share support structures. The conceptual design of the integrated prime mover is the outcome of three studies.

In the first study, covered in Chapter 2, candidate electric machine topologies for the IPM are surveyed. Coarse electric machine models and empirical ranges for design parameters are used at this stage. The outcome of this study is the selection of a

single electric machine topology for a more detailed analysis. Specifically, the radial flux, permanent magnet (PM) machine is selected for the IPM design. This electric machine topology was selected over the axial flux PM machine, coated solid rotor induction machines, and variable reluctance machines due to its promising predicted performance and medium risk with respect to heat flux.

More design detail was added to the radial flux permanent magnet machine in Chapter 3, in which various combinations of stator and rotor topologies are explored. In addition, both liquid-cooled and air-cooled electric machines are considered. Ultimately, it was found that the tooth-and-slot, Halbach array electric machine offers the greatest predicted specific power at one megawatt. At this power level, an air-cooled system is estimated to offer greater system specific power than a liquid-cooled one. The system specific power includes the mass and losses of both the electric machine and thermal management system.

In the last study at the end of Chapter 3, a conceptual IPM is designed. Specifically, an existing low fan pressure ratio engine is redesigned to integrate with a tooth-and-slot, Halbach array machine. In this conceptual design, the system specific power including both the engine and electric machine is maximized.

The identification of a concept IPM design motivated a technical demonstrator to further verify its feasibility. This technical demonstrator seeks to experimentally prove four key enabling technologies:

1. aggressive air-cooling of an integrated, high specific power electric machine;
2. structural integrity and rotordynamics of the turbomachine-integrated, high speed Halbach array rotor;
3. a low-loss tooth-and-slot stator via thin iron cobalt vanadium stator laminations; and
4. integrated, high specific power, power electronics.

The technical demonstration will be considered successful if the overall demonstrator meets its efficiency and specific power targets at one megawatt of rated power.

The design and learnings of this thesis are scalable to multi-megawatt machines that are necessary for realizing fuel reduction in turboelectric aviation.

The conceptual design of the one megawatt, tooth-and-slot Halbach array motor is iterated upon five times in Chapter 4 before identifying a design point to carry through to detailed design. Each design iteration incorporated additional learnings on manufacturability and component availability. Several measures of conservatism were assumed in the final design iteration which included doubling the manufacturer core loss, limiting the winding hotspot temperature to 180°C (or 20°C below the insulation rating), and constraining the maximum flux densities throughout the stator to the knee of the B-H curve.

Once the design point was frozen, the demonstrator was carried through a detailed design in Chapter 5. The electric machine is predicted to meet performance requirements via finite element analysis simulations and bench tests. A central theme throughout both the conceptual and detailed design phases of this electric machine is mitigating risk. A combination of sensitivity studies via parameter variation as well as bench tests is used throughout the design process for this purpose. The steps for manufacturing each electric machine component are outlined, and the electric machine manufacturing is currently in progress. This electric machine and thermal management system is expected to achieve a specific power of 19.7 kW/kg without the heat sink, or 16.5 kW/kg with the heat sink as shown in Fig. 6-1.

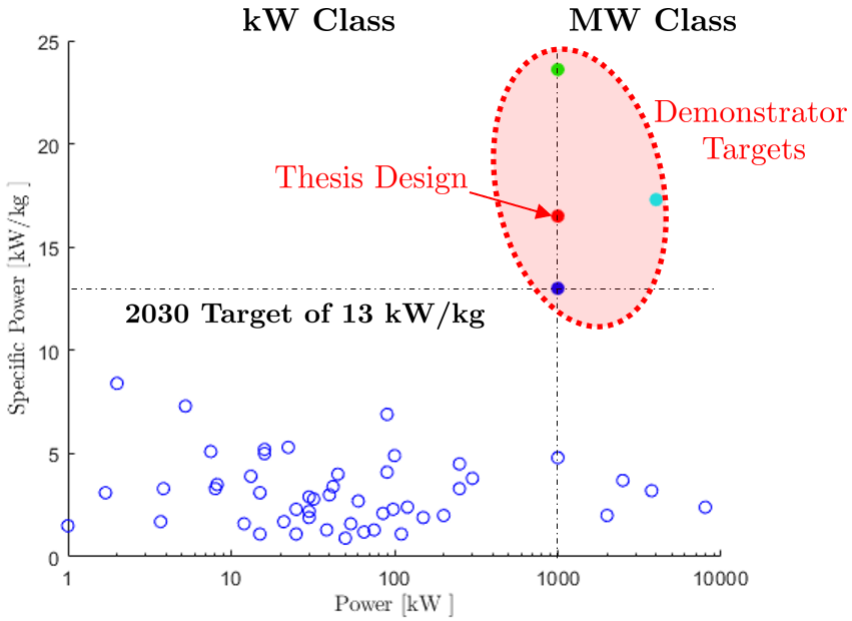

Figure 6-1: The electric machine plus heat sink in this thesis is expected to achieve a specific power of 16.5 kW/kg at one megawatt. This is shown in comparison to other demonstrators and the electric machines surveyed from Ref. [2].

6.2 Conclusions

The major findings of the studies in this thesis include:

1. An integrated prime mover is predicted to be feasible with the materials and technology available today. This IPM concept consists of an outer rotor, tooth-and-slot Halbach array machine integrated with the low pressure compressor of a re-optimized low fan pressure ratio engine. At the one megawatt output power level, this IPM is predicted to have a system specific power of 14.8 kW/kg which exceeds the 2030 target of 13 kW/kg.

2. An air-cooled, tooth-and-slot, Halbach array electric machine at one megawatt rated power is predicted to achieve a specific power of 19.7 kW/kg, which exceeds the NASA 2030 target. This electric machine is expected to have a specific power of 16.5 kW/kg if the heat sink is included.

3. Co-optimization of the electric machine, power electronics, thermal management system, and turbomachine rim results in a 38% greater system specific power

than optimizing for a standalone electric machine.

4. The core loss represents high risk to the electric machine due to the uncertainty in how the manufacturing process affects core loss. A 17% specific power improvement is predicted to be feasible if the nominal datasheet losses are realizable.

In addition, other conclusions drawn during this research are the following:

- With the materials and technology available today, and at the power levels examined in this thesis, tooth-and-slot electric machines offer superior specific power over slotless machines.

- Similarly, Halbach array rotors offer greater specific power to traditional surface permanent magnet rotors. This is due to the elimination of the rotor back iron.

- Air-cooling is estimated to offer superior system specific power over liquid-cooling at power levels of one megawatt or below. System specific power includes both the electric machine and thermal management sytem.

- Air-cooling the end turns is critical for obtaining a high demonstrator specific power.

- Rectangular litz bundles of US AWG 24 are state-of-the-art for maximizing slot copper fill factor in rectangular slot machines.

6.3 Recommendations for Future Work

Future work for this design includes the remaining electric machine manufacturing, the demonstrator experiments, and lastly improved modeling for future iterations of optimization. Each area is discussed in more detail in the following subsections.

6.3.1 Electric Machine Manufacturing

The windings for the demonstrator are already procured and have been tested in the 3D printed mockup. In addition, a test rotor (i.e., titanium rim plus the Halbach array of magnets) has been manufactured and successfully underwent a spin pit test in which it was spun up to design speed and beyond. The objective was to test, at design speed, the ability of (1) the titanium rim to withstand the hoop stress, and (2) the selected adhesive to hold the Halbach array magnets to the rim. Items (1) and (2) were both successfully conducted at room temperature. At higher temperature, the adhesive bond strength decreases and therefore the adhesive risks failing. The test rotor was spun at design speed at high temperature as well and the test rotor did not fail, but the results are still being processed. Once the results are processed and look acceptable, the build of the final rotors can begin. The other remaining component to be built is the electric machine stator.

Stator Manufacturing

FeCoV alloy has a relatively high magnetostriction and its performance is sensitive to the manufacturing process. As discussed in Section 5.6.1, each step of the manufacturing process (e.g., annealing or bonding) impacts the induction and potentially core losses of the FeCoV alloy. The impact of these processes on the FeCoV alloy is measurable via toroid tests. A caveat here is that the impact on the stator laminations could differ due to the different geometry and flux densities (hence the safety factor of two). Given the sensitivity of the winding hotspot temperature to core loss, it is important to minimize losses as much as possible.

At the time of writing, a suitable annealing protocol is still being identified. Toroids undergoing different protocols must be measured to select a viable annealing protocol for the final stator laminations. Next, the C5 coating process needs to be tested. Since the laminations are 4 mil thick, there is a risk that they could get caught in the roller system used for C5 coating. This can be confirmed with a few test laminations. Lastly, bonding the laminations will make the heat sink integration

easier. However, bonding involves compressing the laminations, which can increase core loss. This can be tested ahead of time with additional toroid tests.

6.3.2 Electric Machine Experiments

The torque, torque ripple, circuit parameters, and losses estimated from Chapter 5 should be verified with the experimental apparatus. The assumptions used in the design and modeling of the electric machine can be revisited for any observed differences between measured and predicted performance.

In Chapter 5, a nominal outer loop controller design was created and simulated based on the linear-quadratic-Gaussian approach. This design needs to be tested and tuned once the electric machine hardware is available. In addition, it needs to be implemented in digital hardware. A Monte-carlo simulation can be used to test the performance versus modeling uncertainties.

6.3.3 Improved Models for Co-Optimization

The co-optimization design iterations ended at the preliminary design review, at which point a design point[1] was selected and frozen to serve as the basis for the detailed design. This decision to freeze the design was necessary to move forward with the technical demonstrator. However, additional learnings during the detailed design phase can be incorporated into the co-optimization for future iterations on the demonstrator.

Permanent Magnet Segmentation Model

The permanent magnet axial segmentation was not considered during co-optimization. However, from Section 5.5.3, segmentation reduced the eddy current losses by a factor of two for the demonstrator. If this loss reduction is captured at the co-optimization stage, designs with smaller airgaps may be feasible that were discarded in this thesis. This air gap decrease increases torque if all else is held constant. Also, only the eddy

[1] A design point refers to a combination of a rotational speed, electromagnetic shear stress, air gap thickness, pole pair count, slot current density, and power electronics switching frequency.

current due to the fundamental frequency was considered in the permanent magnet loss model. However, the high frequency loss due to the power electronics ripple current could also be added for an improved loss estimate at the optimization stage. An axial segmentation model such as that derived in Ref. [69] might be sufficient.

Nonlinear B-H Curve Model

The Halbach array model used in Chapter 4 assumes infinitely permeable stator steel. This simplifies the electromagnetic analysis and it is also good design practice to keep the steel in the linear regime of the B-H curve to reduce harmonics and maximize torque. However, as discussed in Section 4.5.2, the machines outputted from the co-optimizer tended to have saturated teeth. A combination of parameter variation and finite element analysis was used to address the saturation. This process might be addressable at the co-optimizer level via implementation of more detailed tooth geometry and a nonlinear B-H curve model. One such example of this kind of a model is the flux tube approach in Ref. [58]. The downside to a nonlinear model is that it increases computation time and still may not mitigate the saturation issue for all stator geometries.

Appendix A

Chapter Two Electric Machine Models

This section summarizes the sizing and loss models used for the trade space analysis in Chapter 2. These models were developed jointly with colleague Yuankang Chen [27].

A.1 Sizing Models

A.1.1 Radial Flux Permanent Magnet Machine

The radial PM machine uses a tooth-and-slot configuration where the windings that form the electromagnet(s) of the machine are placed in slots and wrapped around ferromagnetic teeth. The components modeled for the radial PM machine are a rotor back iron, magnets, stator teeth, stator windings, and a stator back iron. The arrangement of these components is shown in Figure A-1.

The following subsections provide the theory used to determine the size of the various PM machine geometric variables shown in Figure A-2.

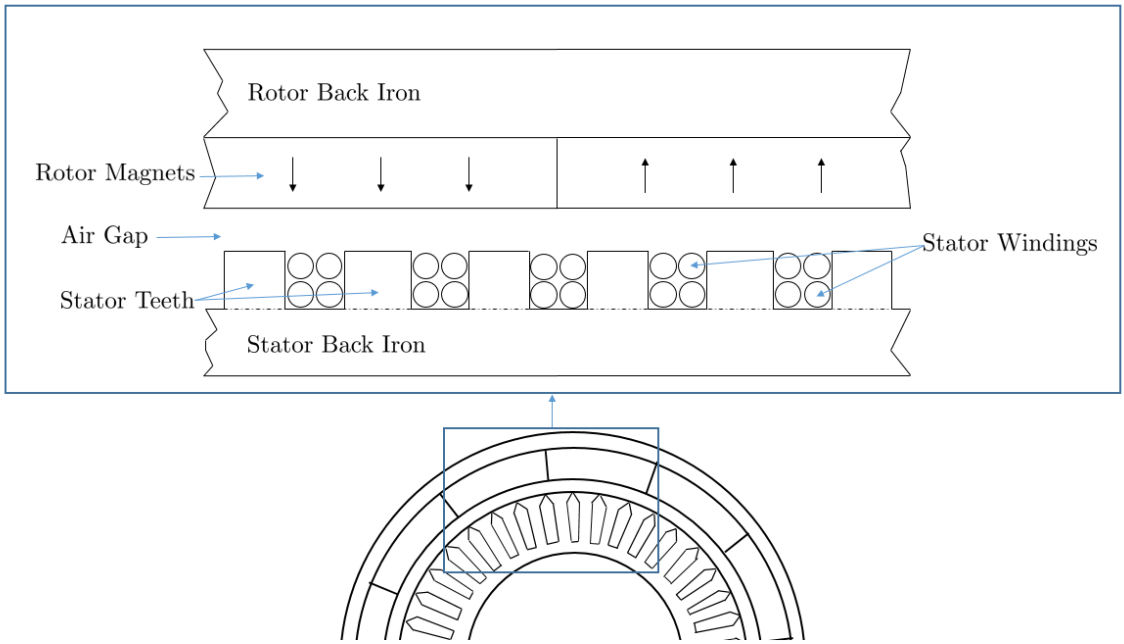

Figure A-1: Cross-section of the radial flux PM machine showing its components. The directions on the arrows on the magnets indicate directions of magnetic polarization.

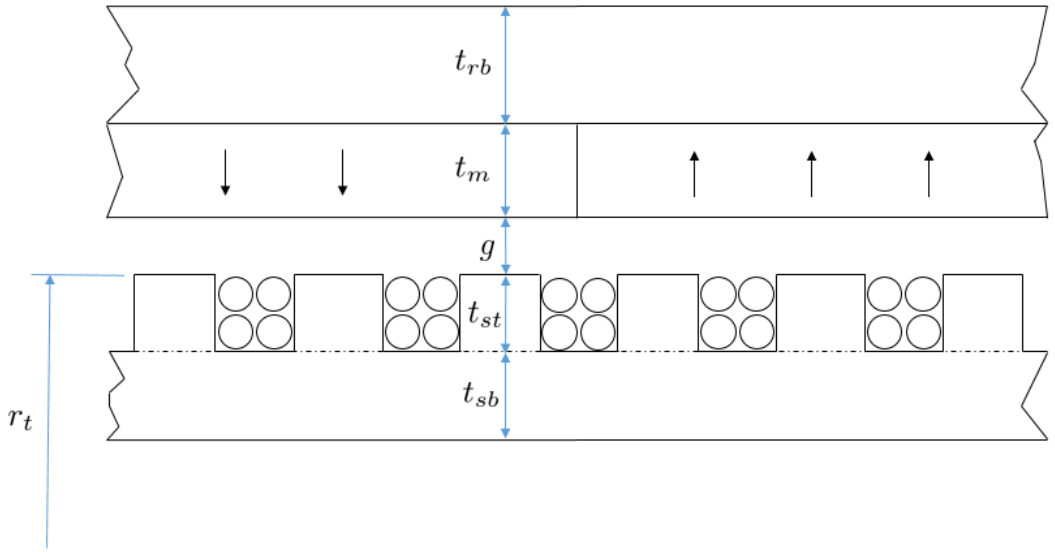

Figure A-2: Cross-section of the radial flux PM machine showing its geometric variable definitions.

Radial Flux PM: Stator and Rotor Back Iron

To minimize leakage flux, the stator and rotor back irons are sized such that their maximum flux density during operation is less than or equal to their saturation flux density – a material property. The stator and rotor back iron thicknesses, and hence mass, are *minimized* when their maximum flux densities are *equal to* their saturation flux density, and so it is assumed that the steel is saturated throughout this analysis.

To calculate the maximum flux density in either of the back irons during operation, first the air gap flux, ϕ_{ag}, is estimated. The total air gap flux is the product of the air gap flux density, B_{ag}, and the air gap surface area, A_{ag}. Using the circumference of the machine at the air gap ($2\pi r_t$),

$$\phi_{\text{ag}} = B_{\text{ag}} A_{\text{ag}} = B_{\text{ag}} 2\pi r_t \ell \tag{A.1}$$

For the stator back iron, the magnetic flux in the back iron, ϕ_{sb}, is the product of the steel saturation flux density, B_{sat}, and the cross section area of the stator back iron, A_{sbi}:

$$\phi_{\text{sbi}} = B_{\text{sat}} A_{\text{sbi}} = B_{\text{sat}} t_{\text{sb}} \ell \tag{A.2}$$

The maximum flux through the stator back iron is equal to that from half a rotor pole. Since there are N_p poles generating the air gap flux, this is equivalent to

$$\phi_{sb} = \frac{1}{2} \frac{\phi_g}{N_p} \tag{A.3}$$

Substituting Equations A.1 and A.2 into Equation A.3, the stator back iron thickness, t_{sb}, nondimensionalized by the tip radius, is

$$\frac{t_{\text{sb}}}{r_t} = \frac{B_{\text{ag}}}{B_{\text{sat}}} \frac{\pi}{N_p} \tag{A.4}$$

The derivation for the rotor back iron is the same, therefore the rotor back iron thickness, t_{rb}, nondimensionalized by the tip radius, is

$$\frac{t_{\text{rb}}}{r_t} = \frac{B_{\text{ag}}}{B_{\text{sat}}} \frac{\pi}{N_p} \tag{A.5}$$

Radial Flux PM: Stator Teeth, Windings, and Magnets

The stator teeth shorten the air gap to improve the air gap magnetic flux density. The tooth length is limited by geometrical constraints, tooth-tip saturation, and the magnetomotive force drop across the tooth. Since the electric machine has an outer rotor configuration, the stator tooth and stator back iron thicknesses must be less than or equal to the tip radius. That is,

$$t_{\text{sb}} + t_{\text{tooth}} \leq r_t \tag{A.6}$$

or

$$\frac{t_{\text{tooth}}}{r_t} \leq 1 - \frac{t_{\text{sb}}}{r_t} = 1 - \frac{B_{\text{ag}}}{B_{\text{sat}}} \frac{\pi}{N_p} \tag{A.7}$$

For poles with constant width, which keeps the radial flux passing through the tooth in a radial machine approximately constant, tooth area is the product of its length, t_{tooth}, and width, w_o. The nondimensional tooth width divided by pole pitch is

$$\frac{w_o}{2\pi r_t / n_{\text{slots}}} = \frac{(1 - f_{\text{tooth}})}{2} \frac{1 - (1 - \frac{t_{\text{tooth}}}{r_t})^2}{\frac{t_{\text{tooth}}}{r_t}} \tag{A.8}$$

When winding thickness, assumed equivalent to tooth thickness t_{tooth} approaches the limit of infinitely thin windings, Equation A.8 reduces to $\frac{w_o}{2\pi r_t / N_p} = 1 - f_{\text{tooth}}$. In this limit, tooth width is simply the tooth fraction of the pole pitch. From Equation A.8, the maximum possible value for the nondimensional winding thickness due to the tooth width is

$$\left.\frac{t_{\text{tooth}}}{r_t}\right|_{ttmax} = \frac{2\,(1 - f_{\text{tooth}})}{2 - f_{\text{tooth}}} \tag{A.9}$$

In the limits of Equation A.9, $\left.\frac{t_{\text{tooth}}}{r_t}\right|_{ttmax} = 1$ when $f_{\text{tooth}} = 1$ (no teeth), and

$\left.\frac{t_{\text{tooth}}}{r_t}\right|_{ttmax} = 0$ when $f_{\text{tooth}} = 0$ (no windings), which agrees with intuition. For the typical value of $f_{\text{tooth}} = 0.5$, maximum winding thickness is two thirds of tip radius.

Considering the constraints from Equation A.6 and Equation A.9, the maximum nondimensional stator winding thickness is the minimum of the two, or

$$\frac{t_{tooth,max}}{r_t} = \min\left(1 - \frac{B_{\text{ag}}}{B_{\text{sat}}}\frac{\pi f_{\text{tooth}}}{N_p} \ , \ \frac{2\left(1 - f_{\text{tooth}}\right)}{2 - f_{\text{tooth}}}\right) \tag{A.10}$$

The spatially limited surface current density for radial flux machines, $K_{s,sp}$ is then

$$K_{s,sp} = (1 - f_{\text{tooth}}) J_m r_t \frac{t_{\text{winding,max}}}{r_t} \tag{A.11}$$

which notably scales linearly with tip radius.

For tooth-and-slot stators, an additional constraint on the surface current density is saturation in the stator teeth. Although the teeth can saturate both in the tooth tips as well as the base of the tooth, the tooth tip saturation is considered here based on Ref. [41]. The flux density in the stator tooth tip is the vectorial sum of the radial magnetic flux from the permanent magnets as well as the azimuthal flux generated from the conductors in the slots [41]:

$$\left(\frac{B_{\text{ag}}}{f_{\text{tooth}}}\right)^2 + \left(\mu_0 J_m t_{\text{tooth}}\right)^2 \leq B_{\text{sat}}^2 \tag{A.12}$$

If the surface current density is approximated as the product of the slot current density and tooth thickness, $K_s = J_m t_{\text{tooth}}$, an upper bound on the surface current density due to saturation, $K_{s,sat}$, is derived by solving Equation A.12 with equality. This results in

$$K_{s,sat} = \frac{B_c\left(1 - f_{\text{tooth}}\right)}{\mu_0}\sqrt{1 - \left(\frac{B_{\text{ag}}}{f_{\text{tooth}} B_{\text{sat}}}\right)^2} \tag{A.13}$$

The current density is the minimum of the spatial limit and saturation limit, or

$$K_s = \min\left(K_{s,sp}, K_{s,sat}\right) \tag{A.14}$$

The permanent magnets are sized to provide sufficient usable magnetic flux density in the air gap, B_{ag}. The maximum flux density strength of a permanent magnet is also referred to as its remanent flux density, B_r. However, not all of this flux goes across the air gap. From Ampere's law and approximating the MMF drop across the back iron and teeth, the air gap flux density, $B_{\text{ag,nd}}$, which neglects magnet-to-magnet leakage flux, is

$$B_{ag,nd} = \frac{B_r t_m}{t_m + g} - \frac{\kappa}{\mu_{s,r}} B_{\text{sat}} \tag{A.15}$$

where t_m is the thickness of the permanent magnet, g is the air gap thickness, $\mu_{s,r}$ is the relative permeability of the stator and rotor magnetic core, and

$$\kappa = \left[\frac{2\frac{t_{\text{tooth}}}{r_t} + \frac{2\pi}{N_{\text{slots}}}\frac{r_{sb}}{r_t} + \frac{2\pi}{N_p}\frac{r_{rb}}{r_t}}{2(\frac{t_{rb}}{r_t} + \frac{g}{r_t})} \right] \tag{A.16}$$

represents the flux path through the magnetic core.

To capture the effect of magnet-to-magnet flux leakage due to large pole counts or air gap, the air gap flux density can be expressed based on Ref. [72] as

$$B_{\text{ag}} = B_{\text{ag,nd}} \left(1 - \frac{8N_p}{\pi^2} \frac{g}{r_t} \right). \tag{A.17}$$

A.1.2 Axial Flux PM Machine

Axial Flux PM: Stator and Rotor Back Iron

The axial flux PM machine stator and rotor back irons are sized in a similar manner to the radial PM machine. However, the expressions for the air gap and back iron fluxes differ due to the geometry of the axial PM machine:

$$\phi_{\text{ag}} = B_{\text{ag}} A_{\text{ag}} = B_{\text{ag}} \pi \left(r_t^2 - r_h^2 \right) \tag{A.18}$$

$$= f_{s,s} B_s \pi r_t^2 \left(1 - \chi_E^2 \right) \tag{A.19}$$

$$\phi_{sb} = B_{sb} A_{sb} = B_{\text{sat}} t_{sb} \left(r_t - r_h \right) \tag{A.20}$$

$$= B_{\text{sat}} t_{sb} r_t \left(1 - \chi_E \right) \tag{A.21}$$

where r_h is the inner radius of the axial machine. The maximum flux through the stator back iron is again equal to that from half a rotor pole, or

$$\phi_{sb} = \frac{1}{2}\frac{\phi_{\text{ag}}}{N_p}. \tag{A.22}$$

The stator back iron thickness, t_{sb}, nondimensionalized by the tip radius is

$$\frac{t_{sb}}{r_t} = \frac{B_{\text{ag}}}{B_{\text{sat}}}\frac{\pi\left(1-\chi_E\right)}{2N_p}. \tag{A.23}$$

Similarly, the rotor back iron thickness, t_{rb}, is

$$\frac{t_{rb}}{r_t} = \frac{B_{\text{ag}}}{B_{\text{sat}}}\frac{\pi\left(1-\chi_E\right)}{2N_p}. \tag{A.24}$$

Axial Flux PM: Stator Teeth, Windings, and Permanent Magnets

The axial PM machine stator teeth do not have the same geometrical constraints as those in the radial PM machine. Instead, a maximum stator tooth-to-tip radius ratio is imposed. That is,

$$\frac{t_{\text{tooth}}}{r_t} \leq \left(\frac{t_{\text{tooth}}}{r_t}\right)_{\max} \tag{A.25}$$

where $\left(\frac{t_{st}}{r_t}\right)_{\max}$ is a design input. This was chosen in anticipation of the integrating stage into a full architecture, where axial length will be limited.

For axial flux machines, the effective slot current density is lower than that of a comparable radial machine as the windings in axial flux machines travel radially from rotor hub to rotor tip, resulting in reduced winding area at the rotor hub for machines with a constant pole pitch which is assumed here. Slot current density reflects the difficulty in cooling the windings, so it is assumed the slot current density for the axial machine is maximum at rotor hub and decreases toward the tip. Thus, the effective slot current density for the axial machine is the average across the radial span of the machine, i.e.:

$$J_{m,effective} = \frac{1+\chi_E}{2} J_m \tag{A.26}$$

The spatially limited surface current density for axial flux machines is then simply

$$K_{s,sp} = (1 - f_{\text{tooth}}) J_{m,effective} r_t \frac{t_{sw,max}}{r_t} \tag{A.27}$$

The stator teeth have the same tooth tip saturation limit as the radial PM machine, or

$$\left(B_{\text{ag}}/f_{s,s}\right)^2 + \left(\mu_0 J_{m,eff} t_{\text{winding}}\right)^2 \leq B_{\text{sat}}^2 \tag{A.28}$$

which can be solved with equality to give the saturation surface current density of

$$K_{s,sat} = \frac{B_{\text{sat}}\left(1 - f_{\text{tooth}}\right)}{\mu_0} \sqrt{1 - \left(\frac{B_{\text{ag}}}{f_{\text{tooth}} B_{\text{sat}}}\right)^2}. \tag{A.29}$$

The surface current density $K_s = J_{m,eff} t_{\text{winding}}$ is again

$$K_s = \min\left(K_{s,sp}, K_{s,sat}\right). \tag{A.30}$$

The permanent magnets in an axial PM machine are sized using the same relations as those in a radial PM machine, given via Equations A.15-A.17.

A.1.3 Radial Flux Induction Machine

Similar to the radial flux PM machine, the radial flux induction machine uses a tooth-and-slot configuration on the stator. The magnets, however, are replaced with a layer of conductive material. The arrangement of the radial flux induction machine components is shown in Figure A-3. The following subsections provide the theory used to determine the size of the various induction machine geometric variables shown in Figure A-4. The radial induction machine is based approximately on the linear induction machine model from Ref. [73].

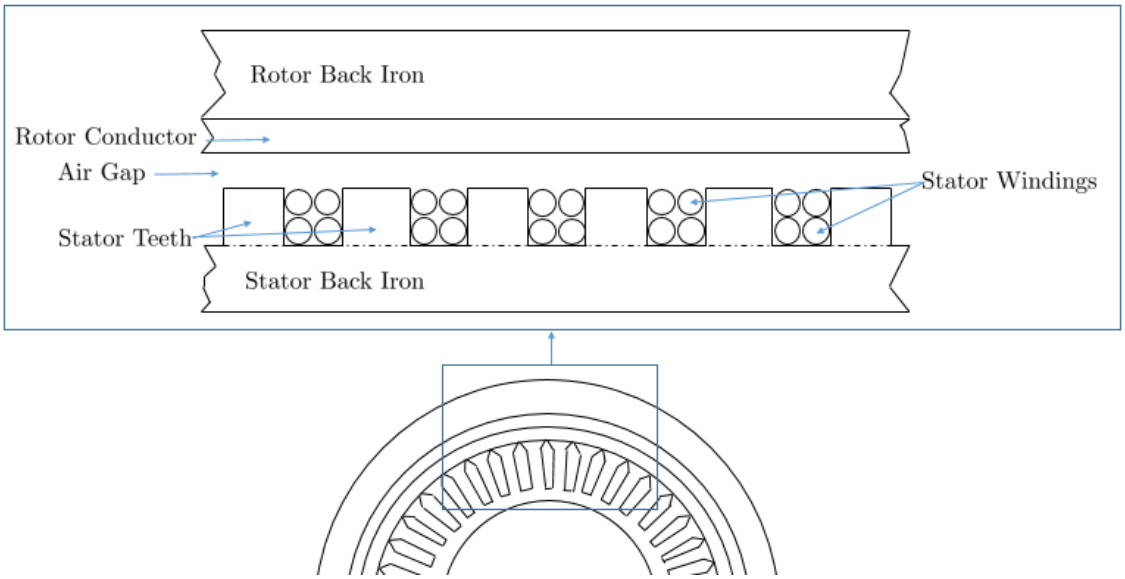

Figure A-3: Cross-section of the radial flux induction machine showing its components.

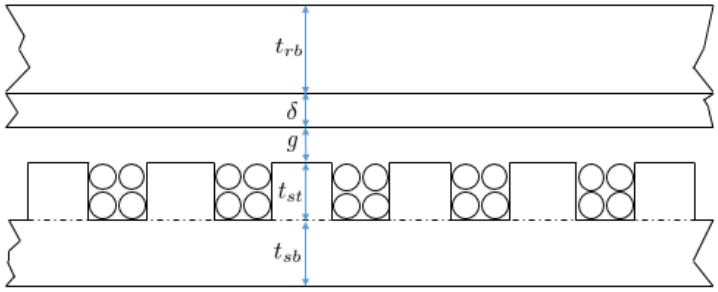

Figure A-4: Cross-section of the radial flux induction machine showing its geometric variable definitions.

Radial Flux Induction Machine: Stator and Rotor Back Iron

The radial induction machine back iron is sized the same as the radial PM machine. That is,

$$\frac{t_{sb}}{r_t} = \frac{B_{\text{ag}}}{B_{\text{sat}}} \frac{\pi}{N_p}. \tag{A.31}$$

Additionally, the stator back iron radius can be expressed as a function of tip radius, amongst other geometric variables:

$$\frac{r_{sb}}{r_t} = 1 - \frac{t_{t,s}}{r_t} - \frac{B_{\text{ag}}}{B_{\text{sat}}}\frac{\pi}{N_p}. \tag{A.32}$$

This radius is used in subsequent sections. Similarly, the rotor back iron thickness, t_{rb}, is

$$\frac{t_{rb}}{r_t} = \frac{B_{\text{ag}}}{B_{\text{sat}}}\frac{\pi}{N_p} \tag{A.33}$$

and the rotor back iron radius, nondimensionalized by the tip radius, can be expressed as

$$\frac{r_{rb}}{r_t} = 1 + \frac{t_{t,r}}{r_t} + \frac{B_{\text{ag}}}{B_{\text{sat}}}\frac{\pi}{N_p}. \tag{A.34}$$

Radial Flux Induction Machine: Stator Teeth, Windings, and Rotor Conductor

Similar to the radial PM machine, the radial induction machine has the same geometric constraint on the stator teeth (Equation A.9). The spatially limited surface current density, $K_{s,sp}$ is obtained from Equation A.11. In addition, the induction machine has the same tooth tip saturation constraint as the PM machine, with the magnetic field term from the PMs replaced with one for the rotor conductor:

$$B_{\text{sat}}^2 = \left(\frac{B_{\text{ag}}}{f_{\text{tooth}}}\right)^2 + \left(\frac{\mu_0 K_s}{1 - f_{\text{tooth}}}\right)^2 \tag{A.35}$$

To compute the air gap flux density, first the magnetic field generated by the current induced in the stator conductors is computed via

$$B_{\text{ag}} = \mu_0 K_s \, \frac{\mu_0 U_s \sigma_s}{k^2 g^2 + (\mu_0 U_s \sigma_s)^2} \tag{A.36}$$

where the wave number, $k = \frac{N_{p,s}}{2r_t}$, where $N_{p,s}$ is the number of stator poles, and r_t is the rotor tip radius. The rotor surface wave speed, $U_s = s\frac{\omega_s}{k} = \frac{s}{1-s}U_t$, where $U_t = r_t\Omega$ is the mechanical tip speed and s is the machine slip.

The rotor surface conductivity, σ_s is expressed as

$$\sigma_s = \frac{\delta(1 - f_{s,r})}{R_{s,rc}} = (1 - f_{s,r})\sqrt{\frac{2}{R_{s,rc}\omega_s\mu_w}} \tag{A.37}$$

where $f_{s,r}$ is the rotor tooth fraction, $R_{s,rc}$ is the resistivity of the rotor conductors, $\delta = \sqrt{\frac{2R_{s,rc}}{\omega_s\mu_{rc}}}$ is the skin depth, μ_{rc} is the magnetic permeability of the rotor conductors, and ω_s is the stator electrical frequency.

The induction machine rotor conductor thickness is assumed to be the skin depth, and slip is assumed to be independent of rotor geometry. The mechanical rotational speed Ω, rotor electrical frequency ω_r, and stator electrical frequency ω_s are related by the slip s via

$$\omega_r = s\omega_s \ , \ \omega_s = \frac{\frac{N_{p,s}}{2}\Omega}{1 - s} \ , \ s = 1 - \frac{\frac{N_{p,s}}{2}\Omega}{\omega_s} \tag{A.38}$$

The flux crossing the air gap B_s is calculated by considering the completed magnetic circuit (with the MMF drop across the back iron accounted for):

$$B_s = B_r \frac{\frac{\delta}{r_t}}{\frac{\delta}{r_t} + \frac{g}{r_t}} - \frac{\mu_0}{\mu_{steel}} B_c \kappa \tag{A.39}$$

where the geometric term κ that represents the flux path through the magnetic iron is

$$\kappa = \left[\frac{2\frac{t_{t,s}}{r_t} + \frac{2\pi}{N_{p,s}}\frac{r_{bs}}{r_t} + \frac{2\pi}{N_{p,r}}\frac{r_{br}}{r_t}}{2(\frac{\delta}{r_t} + \frac{g}{r_t})}\right] \tag{A.40}$$

where all of the lengths have been nondimensionalized with the tip radius r_t. Further making the definition

$$\alpha = \frac{\mu_0 U_s \sigma_s}{k^2 g^2 + (\mu_0 U_s \sigma_s)^2} \frac{\frac{\delta}{r_t}}{\frac{\delta}{r_t} + \frac{g}{r_t}} \tag{A.41}$$

the stator tooth tip saturation constraint is

$$B_c^2 = \left(\frac{\mu_0 K_s \alpha - \frac{\kappa}{\mu_{s,r}} B_c}{f_{s,s}}\right)^2 + \left(\frac{\mu_0 K_s}{1 - f_{s,s}}\right)^2 \tag{A.42}$$

Equation A.42 can be reorganized into a quadratic equation to solve for the saturation

constraint on the stator surface current density:

$$\mu_0^2\Big(\frac{1}{(1-f_{s,s})^2}+\frac{\alpha^2}{{f_{s,s}}^2}\Big)K_s^2-2\mu_0\frac{\kappa}{\mu_{s,r}f_{s,s}^2}\alpha B_c K_s+\Big(\frac{\kappa^2}{\mu_{s,r}^2 f_{s,s}^2}-1\Big)B_c^2=0 \qquad \text{(A.43)}$$

which has solution for the induction machine tooth saturation limit on surface current density

$$K_{s,sat}=\frac{B_c}{\mu_0}\gamma \ , \ \gamma=\left[\frac{\frac{\kappa}{\mu_{s,r}f_{s,s}^2}\pm\sqrt{\frac{\alpha^2\kappa^2}{\mu_{s,r}^2 f_{s,s}^4}+\Big(\frac{1}{(1-f_{s,s})^2}+\frac{\alpha^2}{{f_{s,s}}^2}\Big)\Big(1-\frac{\kappa^2}{\mu_{s,r}^2 f_{s,s}^2}\Big)}}{\Big(\frac{1}{(1-f_{s,s})^2}+\frac{\alpha^2}{{f_{s,s}}^2}\Big)}\right]. \qquad \text{(A.44)}$$

The surface current density, K_s, is the minimum of the spatially limited and saturation limited surface current densities.

A.1.4 Axial Flux Induction Machine

Axial Flux Induction Machine: Stator Back Iron

The axial induction machine stator back iron is sized the same as the axial PM machine. That is,

$$\frac{t_{sb}}{r_t}=\frac{B_{\text{ag}}}{B_{\text{sat}}}\frac{\pi\,(1-\chi_E)}{2N_p} \qquad \text{(A.45)}$$

The stator back iron radius, nondimensionalized by the tip radius, can be expressed as

$$\frac{r_{bs}}{r_t}=1+\frac{t_{ts}}{r_t}+\frac{B_{\text{ag}}}{B_{\text{sat}}}\frac{\pi\,(1-\chi_E)}{2N_p}. \qquad \text{(A.46)}$$

Similarly for the rotor back iron thickness, t_{rb},

$$\frac{t_{rb}}{r_t}=\frac{B_{\text{ag}}}{B_{\text{sat}}}\frac{\pi\,(1-\chi_E)}{2N_p} \qquad \text{(A.47)}$$

and the rotor back iron radius, nondimensionalized by the tip radius, is

$$\frac{r_{rb}}{r_t} = 1 + \frac{\delta}{r_t} + \frac{B_s}{B_c}\frac{\pi\left(1-\chi_E\right)}{2N_p}. \tag{A.48}$$

Axial Flux Induction Machine: Stator Teeth, Windings, and Rotor Conductor

Similar to the axial PM machine, the axial induction machine has a maximum stator tooth-to-tip radius, with the spatially limited surface current density for axial flux machines (Equation A.27) and the saturation limited surface current density is the same as that for the radial flux induction machine, given by Equation A.44.

Lastly, the usable air gap flux density from the stator is the same as that for the radial flux induction machine, given by Equation A.39.

A.2 Machine Mass

A.2.1 Magnetic Core

The magnetic core comprises the stator back iron, rotor back iron, stator teeth, and rotor teeth. The rotor and stator back irons are annular cylinders with volumes V_{rbi} and V_{sbi}, respectively. The total back iron volumes for radial flux machines are

$$\begin{aligned} V_{rbi} &= A_{rbi}\ell \\ &= \pi r_t^3 \frac{\ell}{r_{t,E}}\left[\left(\frac{r_{rb}}{r_t} + 0.5\frac{t_{rb}}{r_t}\right)^2 - \left(\frac{r_{rb}}{r_t} - 0.5\frac{t_{rb}}{r_t}\right)^2\right] \\ V_{sbi} &= A_{sbi}\ell \\ &= \pi r_t^3 \frac{\ell}{r_{t,E}}\left[\left(\frac{r_{sb}}{r_t} + 0.5\frac{t_{sb}}{r_t}\right)^2 - \left(\frac{r_{sb}}{r_t} - 0.5\frac{t_{sb}}{r_t}\right)^2\right] \end{aligned} \tag{A.49}$$

and for axial flux machines:

$$
\begin{aligned}
V_{rbi} &= (\pi r_t^2 - \pi(\chi_E r_t)^2)\ell_{rbi} \\
&= \pi r_t^3(1-\chi_E^2)\frac{t_{rb}}{r_t} \\
V_{sbi} &= (\pi r_t^2 - \pi(\chi_E r_t)^2)\ell_{sbi} \\
&= \pi r_t^3(1-\chi_E^2)\frac{t_{sb}}{r_t}
\end{aligned}
\tag{A.50}
$$

The total volume of the stator teeth, V_{st}, for radial flux, tooth-and-slot machines is

$$
V_{st} = \pi r_t^3 \frac{\ell}{r_{t,E}} f_{\text{tooth}} \left[1 - \left(1 - \frac{t_{st}}{r_t}\right)^2\right] \tag{A.51}
$$

and for axial flux, tooth-and-slot machines is

$$
V_{st} = \pi r_t^3 (1-\chi_E^2) f_{s,s} \frac{t_{st}}{r_t} \tag{A.52}
$$

The magnetic core mass is the product of the magnetic core mass density with the total volume of the magnetic core:

$$
M_{core} = \rho_{core}\Big(V_{sbi} + V_{rbi} + V_{st}\Big) \tag{A.53}
$$

A.2.2 Windings

The volume of the stator windings V_{sw} is the product of the total slot area $A_{tsw} = N_{p,s}A_{wind}$ and the sum of the slot and end winding lengths $(l_{slot} + l_{ew})$. For radial flux machines, this is

$$
\begin{aligned}
V_{sw} &= A_{tsw}\Big(l_{slot} + l_{ew}\Big) \\
&= \pi r_t^3(1-f_{s,s})\left[\frac{l}{r_{t,E}} + \frac{2\pi}{N_{p,s}}\left(1 - 0.5\frac{t_{sw}}{r_t}\right)\sqrt{1-(1-f_{s,s}^2)^2}\right]
\end{aligned}
\tag{A.54}
$$

and for axial flux machines it is

$$\begin{aligned} V_{sw} &= A_{tsw}\Big(l_{slot} + l_{ew}\Big) \\ &= 2\pi\chi_E r_t(1 - f_{s,s})\left[(1-\chi_E) + \frac{2\pi}{N_{p,s}}\frac{1+\chi_E}{2}\right] \end{aligned} \tag{A.55}$$

For the induction machine, the volume of the rotor windings V_{rw} is

$$V_{rw} = \pi r_t^3 \frac{l}{r_{t,E}}(1 - f_{s,r})\left[\left(1 + \frac{g}{r_t} + \frac{\delta}{r_t}\right)^2 - \left(1 + \frac{g}{r_t}\right)^2\right] \text{ (Radial Flux Machines)} \tag{A.56}$$

$$V_{rw} = \pi r_t^3 (1 - \chi_E^2)(1 - f_{s,r})\frac{\delta}{r_t} \text{ (Axial Flux Machines)} \tag{A.57}$$

The winding insulation is assumed massless, and the mass of the stator windings M_w is then

$$M_w = \rho_{sw} V_{sw} PF + \rho_{rc} V_{rw} \text{ (Induction Machines)} \tag{A.58}$$

$$M_w = \rho_{sw} V_{sw} PF \text{ (PM Machines)} \tag{A.59}$$

A.2.3 Magnets

For PM machines, the magnets are mounted on the air-gap facing surface of the rotor, with total mass M_m. For radial flux machines, this is

$$M_m = \rho_m V_m = \rho_m \pi r_t^3 \frac{l}{r_{t,E}}(1 - f_{s,r})\left[\left(1 + \frac{g}{r_t} + \frac{t_m}{r_t}\right)^2 - \left(1 + \frac{g}{r_t}\right)^2\right] \tag{A.60}$$

and for axial flux machines, this results in

$$M_m = \rho_m V_m = \rho_m \pi r_t^3 (1 - \chi_E^2)(1 - f_{s,r})\frac{t_m}{r_t} \tag{A.61}$$

A.3 Loss Model

Losses in the electric machine can be broken down into core loss due to hysteresis and eddy currents in the core, ohmic loss due to resistance in the windings, and windage loss produced by viscous torque on the electric machine rotor.

A.3.1 Core Loss

Core loss P_c is calculated as the product of core mass M_{core} and the core loss per unit mass P_{cm}, i.e.:

$$P_c = P_{cm} M_{core} \tag{A.62}$$

Core loss per unit mass is a material parameter with empirically derived correlations for electrical frequency f and magnetic flux density in the core B_{core}. The core loss per unit mass functions used for the Hiperco-50A material with 0.006 inch thick laminations were obtained from the manufacturer and fit to the following:

$$P_{cm}(W/kg) = k_1 f B^2 + k_2 f^2 B^2 + k_3 f^{1.5} B^{1.5} \tag{A.63}$$

The core is assumed to be fully saturated ($B = B_{\text{sat}}$), and the core loss per unit mass is then interpolated from Equation A.63 to the electrical frequency of the machine.

A.3.2 Ohmic Loss

Ohmic loss refers to the resistive losses in the electrically conductive elements of the electric machine (primarily the stator windings).

Permanent Magnet Machines

For PM machines, the only source of ohmic loss is the stator windings. The ohmic loss P_d is expressed as

$$P_d = {J_m}^2 R_{s,sw} \frac{V_w}{PF} \tag{A.64}$$

where the product of slot current density J_m squared and winding resistivity $R_{s,sw}$ can be thought of as an 'I^2R' loss per unit volume of the windings.

Induction Machines

In addition to the stator winding loss (Equation A.64), induction machines incur additional loss in the rotor conductors. This additional ohmic loss is a function of the machine mechanical power P and slip s:

$$P_{d,rotor} = P\frac{s}{1-s} \tag{A.65}$$

A.3.3 Windage Loss

The windage loss models for radial flux and axial flux electric machines were developed by colleague Yuankang Chen and details are available in Ref. [27]. These models consider the viscous torque on both the inner and outer surfaces of the rotor. For radial flux machines, the torque on the axial-facing surface is assumed to be negligible. Similarly, for the axial flux case, the torque on the radial-facing surfaces of the rotor is assumed to be negligible.

Appendix B

Chapter Three Electric Machine Models

B.0.1 Torque Production

Tooth-and-Slot Surface Permanent Magnet and Halbach Array

The average electromagnetic shear stress in the air gap, $\bar{\tau}$ is related to the linear surface current density from the windings, K_s, and magnetic flux density from the permanent magnets, B_s, via the Maxwell stress tensor [41]:

$$\bar{\tau} = \frac{B_s K_s}{2} \tag{B.1}$$

The geometry of the tooth-and-slot electric machine with labeled parameters is shown in Fig. B-1.

Surface Current Density A peak slot current density, J_m, and slot fraction, f_{ss}, are specified as inputs to the tooth-and-slot sizing algorithm. The total length of the windings, t_{sw}, is swept, and the total winding area, A_{wind}, is calculated as

$$A_{\text{wind}} = f_{\text{ss}} \frac{\pi \left(r_{\text{ag}}^2 - \left(r_{\text{ag}}^2 - \left(\frac{t_{\text{sw}}}{r_{\text{ag}}} \right) r_{\text{ag}} \right)^2 \right)}{n_{\text{ps}}} \tag{B.2}$$

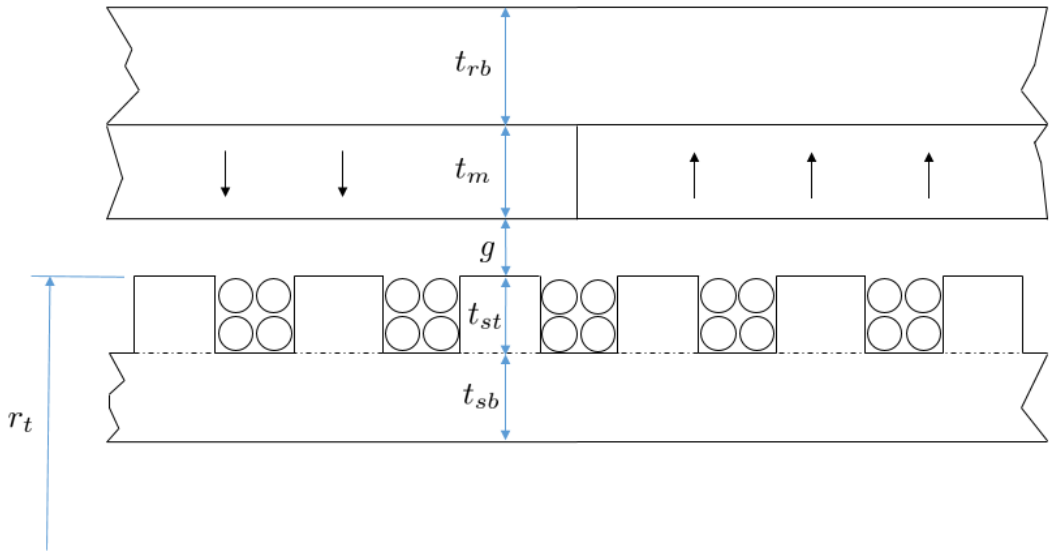

Figure B-1: Cross-sectional area of a tooth-and-slot SPM pole showing the labeled geometric parameters used for the sizing and performance analysis.

where n_{ps} is the total number of slots and r_{ag} is the air gap radius. The surface current density is computed as if all the slot conductors were at the air gap interface:

$$K_s = \frac{J_m A_{\text{wind}} n_{\text{ps}}}{2\pi r_{\text{ag}}} \tag{B.3}$$

Permanent Magnet Magnetic Flux Density The airgap magnetic flux density from the permanent magnets is approximated using Ampere's Law and conservation of magnetic flux. Let H_g, H_m, H_{st}, H_{rbi}, and H_{sbi} be the magnetic field strength in the airgap, magnet, stator teeth, rotor back iron, and stator back iron, respectively. The line integral about the Amperian contour shown in Fig. B-2 for no-load conditions is

$$\oint H \cdot d\ell = 2H_g g + 2H_m t_m + 2H_t t_{st} + H_{\text{rbi}} \frac{2\pi r_{\text{rbi}}}{n_{\text{pr}}} + H_{\text{sbi}} \frac{2\pi r_{\text{sbi}}}{n_{\text{pr}}} = 0 \tag{B.4}$$

where

$$B_m = \mu_0 \left(H_m + M\right) \tag{B.5}$$

$$B_g = \mu_0 H_g \tag{B.6}$$

$$B_t = \mu_t H_t \tag{B.7}$$

$$B_{\text{rbi}} = \mu_{\text{rbi}} H_{\text{rbi}} \tag{B.8}$$

$$B_{\text{sbi}} = \mu_{\text{sbi}} H_{\text{sbi}} \tag{B.9}$$

and $B_{(\cdot)}$ and $\mu_{(\cdot)}$ are the magnetic field density and permeability of each region, respectively, and $M = B_{\text{rem}}/\mu_0$. The radii r_{rbi} and r_{sbi} are the radii to the center of the rotor back iron and stator back iron, respectively.

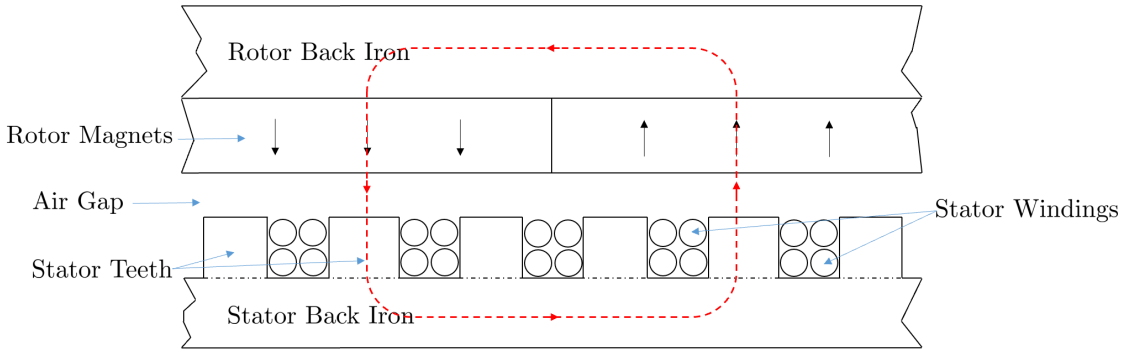

Figure B-2: Ampere's Law is used on the dashed red loop to estimate magnetic flux density.

From substituting Eqns. B.5-B.9 into Eqn. B.4, the magnitude of the gap flux density is solved as

$$B_g = \frac{\mu_0 M t_m}{t_m + g} - \frac{\mu_0}{\mu_t}\frac{B_{\text{st}} t_{\text{st}}}{t_m + t_g} - \frac{\mu_0}{\mu_{\text{rbi}}}\frac{\pi B_{\text{rbi}} r_{\text{rbi}}}{t_m + g} - \frac{\mu_0}{\mu_{\text{sbi}}}\frac{\pi B_{\text{sbi}} r_{\text{sbi}}}{t_m + g} \tag{B.10}$$

The remanent flux density of the permanent magnets decreases linearly with temperature and is accounted for during this sizing approach:

$$B_{\text{rem}} = B_{\text{rem},\,20^\circ\text{C}} \left(1 - \alpha_m \left(T_{\text{mag}} - 20^\circ C\right)/100\right) \tag{B.11}$$

where $B_{\text{rem},\,20°\text{C}}$ is the magnet remanent flux at 20°C (e.g., 1.2 T for NdFeB), T_{mag} is the magnet temperature, and α_m is the temperature coefficient of the magnet.

Since the magnets produce a square wave in the air gap, the fundamental component that interacts with the stator conductors, B_s, is

$$B_s = \frac{4}{\pi} B_g \tag{B.12}$$

For our design, we assume the teeth and back iron are driven into saturation such that $B_{\text{rbi}} = B_{\text{sbi}} = B_{\text{st}} = 2.36\,\text{T}$, and $\mu_{\text{rbi}} = \mu_{\text{sbi}} = \mu_{\text{st}} = 38\mu_0$.

From Eqns. B.3 and B.12, the electromagnetic shear stress produced by the machine, $\bar{\tau} = \frac{B_s K_s}{2}$, is estimated. If this matches the desired shear stress of the machine, the sizing algorithm is complete and the magnet thickness, t_m, and winding thickness, t_{ws}, are set.

Back Iron Sizing The magnetic flux from the airgap for half of a magnet pole is $\phi_{\text{gap,pole}} = \frac{B_{\text{gap}}(\pi r_{\text{ag}} \ell)}{n_{\text{pr}}}$. For the rotor back iron, the magnetic flux is $\phi_{\text{rbi}} = B_{\text{rbi}} t_{\text{rbi}} \ell$. Assuming the back iron is sized for saturation, and that all the magnetic flux from the magnet pole passes through it:

$$t_{\text{rbi}} = \frac{B_{\text{gap}}}{B_{\text{sat}}} \frac{\pi r_{\text{ag}}}{n_{\text{pr}}} \tag{B.13}$$

Similarly, for the stator back iron,

$$t_{\text{sbi}} = \frac{B_{\text{gap}}}{B_{\text{sat}}} \frac{\pi r_{\text{ag}}}{n_{\text{pr}}} \tag{B.14}$$

Conductor Sizing It is assumed that the generator is driving a load that can be modeled as an ideal, three-phase current source. The peak current is calculated based on the electric generator geometry, slot current density, and number of turns:

$$I = \frac{J_m A_{\text{slot}}}{N_{\text{turns}}} \tag{B.15}$$

The per-phase voltage is approximated as

$$V = P/I/3 \tag{B.16}$$

The voltage may be lower when the efficiency is accounted for. The area of a single turn (a bundle of Litz strands) is

$$A_{\text{wire}} = \frac{K_u A_{\text{slot}}}{N_{\text{turns}}} \tag{B.17}$$

and the radius of the turn is $r_{\text{wire}} = \sqrt{A_{\text{wire}}/\pi}$. Next, the number of Litz wire strands is calculated by assuming the smallest strand that can be used is US American Wire Gauge (AWG) 28, which has a radius of $r_{\text{str}} = 0.1605\,\text{mm}$. The corresponding diameter, $2r_{\text{str}}$, is used to set the slot width. A bundle packing factor of 0.91 is assumed, and the total number of strands is thus

$$n_{\text{str}} = 0.91\frac{A_{\text{wire}}}{\pi r_{\text{strand}}^2} \tag{B.18}$$

The necessary dielectric thickness for each Litz wire strand, t_{di}, is sized from the maximum electric field in a cylindrical dielectric:

$$t_{\text{di}} = r_{\text{str}}\left(e^{\left(\frac{V}{r_{\text{str}}E_{\text{max}}}\right)} - 1\right) \tag{B.19}$$

where E_{max} is the maximum dielectric strength – a material property. For Kapton MT 100 insulation, the dielectric strength is $2.16 \cdot 10^8\,\text{V/m}$. A safety factor of 10 is used such that the effective dielectric strength used in our calculations is $2.16 \cdot 10^7\,\text{V/m}$.

Tooth-and-Slot Halbach Array For the electric machine trade studies, the tooth-and-slot Halbach array electromagnetic model is the same as the tooth-and-slot surface permanent magnet model, but it is assumed that the rotor back iron is eliminated during the turbomachinery rim sizing and mass calculation. The basis for this assumption is that (1) for a fixed volume of magnets, the Halbach array will produce

at least as much magnetic flux in the airgap as an equivalent surface PM machine and (2) the azimuthal magnets cancel the flux on the outside of the electric machine, eliminating the need for the rotor back iron. In this project, finite element analysis is used to obtain a higher fidelity assessment of the output torque. A detailed 2-D analytic model is recommended for future work.

Slotless Surface PM and Halbach Array

The slotless surface PM and Halbach array electric machine performance is estimated using the model from Chapter 2 of Reference [17], which is not repeated here for brevity. To summarize, this model is a two-dimensional analysis of the magnetic flux distribution from both the radial-facing and azimuthal-facing permanent magnets. The torque is computed through integrating the product of the radial component of the total air gap flux density and the armature current density over the winding volume. Lastly, similar to the tooth-and-slot model, the winding thickness and magnet thickness are varied until the desired shear stress, $\bar{\tau} = T/\left(2\pi r_{\text{ag}}^2 \ell\right)$, is produced.

B.0.2 Mass Models

The mass of the rotor back iron, m_{rbi}, stator back iron, m_{sbi}, stator teeth, m_{st}, both the windings through the slot and end windings, m_{wind} and m_{endwind}, and magnets, m_{mag}, are determined from the various electric machine radii and thicknesses defined previously as

$$m_{\text{rbi}} = \rho_{\text{fem}} \pi \left(r_{\text{ro}}^2 - r_{\text{ri}}^2\right) \tag{B.20}$$

$$m_{\text{sbi}} = \rho_{\text{fem}} \pi \left((r_{\text{ag}} - t_{\text{st}})^2 - r_{\text{si}}^2\right) \tag{B.21}$$

$$m_{\text{st}} = \rho_{\text{fem}} \pi \left(1 - f_{\text{ss}}\right) \left(r_{\text{ag}}^2 - (r_{\text{ag}} - t_{\text{st}})^2\right) \tag{B.22}$$

$$m_{\text{wind}} = \rho_{\text{wind}} n_{\text{ps}} K_u A_{\text{wind}} \ell \tag{B.23}$$

$$m_{\text{endwind}} = m_{\text{wind}} \left(\frac{\ell_{\text{ew}}}{\ell}\right) \tag{B.24}$$

$$m_{\text{mag}} = \rho_{\text{mag}} \pi \left(r_{\text{ri}}^2 - (r_{\text{ag}} + g)^2\right) \tag{B.25}$$

where ρ_{fem} is the magnetic steel mass density, ρ_{wind} is the winding mass density, ρ_{mag} is the magnet mass density. For a tooth-and-slot machine, the end winding length, ℓ_{ew} is approximated as triangular loops exiting the slots [17]:

$$\frac{\ell_{\text{ew}}}{\ell} = \frac{2\pi}{n_{\text{ps}}} \frac{1 - 0.5\left(\frac{t_{\text{sw}}}{r_{\text{ag}}}\right)}{\sqrt{1 - (1 - f_{\text{ss}})^2}} / \left(\ell / r_{\text{ag}}\right) \tag{B.26}$$

For a slotless machine, the stator teeth are eliminated via $f_{ss} = 1$. In addition, the end-turns are approximated as circular arcs:

$$\frac{\ell_{\text{ew}}}{\ell} = \pi^2 \frac{\left(r_{\text{ag}} - \frac{t_{sw}}{2}\right)}{2 n_{\text{pr}} \ell} \tag{B.27}$$

Lastly, as a first approximation for the slotless design, the rotor and stator back iron was sized conservatively by assuming the gap flux density and armature reaction in the back iron sum to half the saturation flux density. It is anticipated that conducting a detailed design would enable reduction of the back iron thickness, and hence an increase in the slotless electric machine specific power.

B.0.3 Loss Models

Ohmic Losses

The total rms current through a slot is $I = K_{\text{u}} A_{\text{slot}} J_m$. Similarly, the total resistance of the windings in a slot is expressed as a function of machine specifications and geometry as

$$R = \rho \frac{\ell + \ell_{\text{et}}}{K_{\text{u}} A_{\text{slot}}} \tag{B.28}$$

where K_u is the slot fill factor. To account for the effect of temperature on winding resistivity, the resistivity, ρ, is adjusted from a baseline at $20°C$ via

$$\rho = \rho_{\,20°\text{C}} \left(1 + \alpha_\rho \left(T_{\text{wind}} - \ 20°\text{C}\right)\right) \tag{B.29}$$

where $\rho_{20^\circ\mathrm{C}}$ is the winding resistivity at 20°C, T_{wind} is the winding temperature, and α_ρ is the temperature coefficient for the winding material.

Considering that there are n_{ps} slots, the winding losses from the fundamental, P_{ohm}, are simplified to

$$P_{\mathrm{ohm}} = n_{\mathrm{ps}} A_{\mathrm{wind}} \ell \left(1 + \ell_{\mathrm{ew}}/\ell\right) \rho \frac{J_m^2}{K_u} \tag{B.30}$$

To account for proximity and eddy current effects, the approach from [74] is used in which the loss from the fundamental is modified by a factor F_r that is a function of Litz wire geometry. A key assumption in this analysis is that the loss factor corresponds to that of a conducting cylinder in a uniform magnetic field, and that the Litz wire strand diameter is small compared to the skin depth. The AC loss factor is [74]

$$F_r = 1 + \frac{\pi^2 \mu_0^2 N^2 n^2 \omega^2 d_c^2}{768 \rho^2 b^2} \tag{B.31}$$

where N is the number of Litz wire bundle turns, n is the number of Litz wire strands, ω is the electrical frequency of the current, d_c is the Litz strand diameter, ρ is resistivity, and b is the height of the slot.

Stator Core Losses

The stator eddy and hysteresis (core) losses per unit mass, $P_{\mathrm{core}}/m_{\mathrm{core}}$, are estimated using the classic Bertotti loss separation model [45]:

$$\frac{P_{\mathrm{core}}}{m_{\mathrm{core}}} = P_h + P_c + P_e \tag{B.32}$$

$$= K_h f B^\alpha + K_c f^2 B^2 + K_e f^{1.5} B^{1.5} \tag{B.33}$$

where P_h, P_c and P_e are hysteresis, classic eddy current, and additional current loss, respectively, and K_h, K_c, and K_e are their coefficients. For FeCoV alloy data [75],

the core losses per unit mass in W/kg are

$$\frac{P_{\text{core}}}{m_{\text{core}}} = \left(7.3726 \cdot 10^{-9}\right) f B^2 + \left(1.4187 \cdot 10^{-5}\right) f^2 B^2 + \left(2.5312 \cdot 10^{-4}\right) f^{1.5} B^{1.5} \quad \text{(B.34)}$$

where f is in Hz and B is in T.

Appendix C

Halbach Array Electromagnetic Analysis

The analysis for the Halbach array torque was provided by Professor James L. Kirtley in internal memos and is repeated here with his permission.

C.1 Approach

The general approach to analyzing the Halbach array is the following:

1. the permanent magnets are represented as either (1) fictitious 'Chu' surface magnetic charge densities [53], (2) Amperican currents, or (3) a combination of each;

2. the charge densities and Amperican currents are then represented by their Fourier series expansions for use as boundary conditions; and

3. the B- and H-fields are solved via a 2-D boundary problem.

First, the fields are solved in Cartesian coordinates. These field solutions are then converted to the polar coordinate system. Both solutions are reported here.

C.2 Cartesian Coordinates

For a Halbach array with N_{mc} magnet blocks per pole, each magnet segment has angular width $\Delta\theta = \frac{\pi}{N_{\text{mc}}}$. To express the boundary conditions, the magnet rotation angle is clockwise from the positive x-axis shown in Fig. C-1. The angle coordinate system is defined such that the downward facing magnet at 90° is itself when $\theta_k = 90°$.

The angle of direction of magnetization for each magnet segment, θ_k, where k is the block number, varies depending on whether an even or odd number of magnet segments per pole is used. The angle definitions as shown in Fig. C-1 come out to

$$\theta_k = k\Delta\theta, \quad k = 0 \ldots N_{\text{mc}} - 1, \quad N_{\text{mc}}even \tag{C.1}$$

$$\theta_k = (k + 1/2)\,\Delta\theta, \quad k = 0 \ldots N_{\text{mc}} - 1, \quad N_{\text{mc}}odd \tag{C.2}$$

With this coordinate system defined, the magnetization of each block can be represented as a combination of Amperian currents, K_z, and 'Chu' magnetic charge, M_y [53]. In this representation, the magnetic charges are used to express the y-directed magnetization component, whereas the Amperican currents are used to express the x-directed components. The Amperian component is

$$\mu_0 K_z = -B_{\text{rem}} \cos(\theta_k) \tag{C.3}$$

and the 'Chu' Magnetic charge component is

$$M_y = B_{\text{rem}} \sin(\theta_k) \tag{C.4}$$

Eqns. C.3 and C.4 are used to estimate the magnitude of K_z and M_y. Lastly, the Amperian currents and magnetic charges can be expressed as a sum of sinusoids via their Fourier series expansion. Since K_z and M_y are odd and antisymmetric, the Fourier series for M_y is

$$M_y = \sum_{n odd} M_n \sin(nkx) \tag{C.5}$$

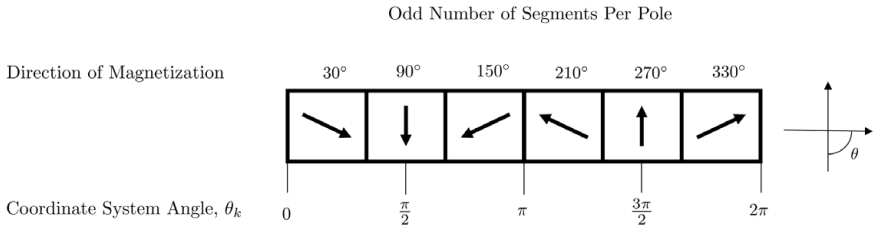

(a) Angles for odd number of Halbach array segments.

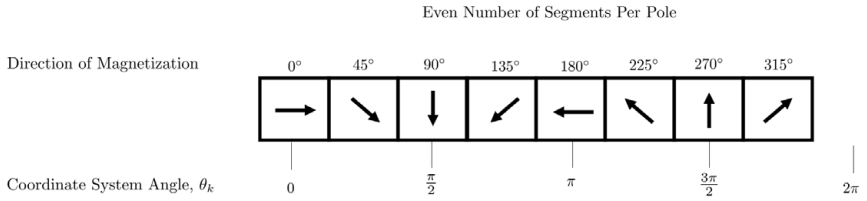

(b) Angles for even number of Halbach array segments.

Figure C-1: Definition of segment angles with odd number of Halbach array segments (top) versus even number of Halbach array segments (bottom).

where

$$M_n = \frac{2}{\pi}\int_{\pi/4}^{3\pi/4} M_0 \sin(nkx)\, d(kx) \tag{C.6}$$

$$= \frac{4}{n\pi}\sin\left(n\frac{\pi}{2}\right)\sin\left(n\frac{\pi}{4}\right) \tag{C.7}$$

and the Fourier series for K_z is

$$K_z = \sum_{nodd} K_n \cos(nkx) \tag{C.8}$$

where

$$K_n = \frac{2}{\pi}\int_{-\pi/4}^{\pi/4} -M_0 \cos(nkx)\, d(kx) \tag{C.9}$$

$$= -\frac{4}{n\pi}\sin\left(n\frac{\pi}{4}\right) \tag{C.10}$$

The 2-D magnetic field is solved using the magnetic scalar potential approach. In this approach, scalar potentials, ψ_i, are defined in each region i of the machine.

These scalar potentials satisfy Laplace's equation, $\nabla^2\psi_i = 0$. The magnetic field in the region is then $H_i = -\nabla\psi_i$. The ferromagnetic stator is assumed to be infinitely permeable such that ψ_i vanishes at its boundary.

Let region (a) be the airgap region between the stator and magnetic charge or Amperian current. Let region (b) be the air beyond the magnetic charge or Amperian current. Figure C-2 shows these regions if either the lower or upper boundary of the magnet is considered. Each boundary problem can be solved separately, and the solutions can be added via superposition.

The magnetic scalar potential in region (b) must decay as $y \to \infty$, so the scalar potential has an e^{-nky} component. The y-directed component of H_b is $H_\mathrm{b} = -\frac{\partial\psi_\mathrm{b}}{\partial y}$. This y-directed component must match the magnetic charge boundary condition of $M_\mathrm{y} = \sum M_n \sin(nkx)$, so the scalar potential must have a $\sin(nkx)$ term. Therefore, the form of ψ_b is

$$\psi^{(b)} = \sum_n B_n e^{-nky} \sin(nkx) \tag{C.11}$$

The H-field therefore has the form:

$$H_x^{(b)} = -\frac{\partial H}{\partial x} = -(nk) B_n e^{-nky} \cos(nkx) \tag{C.12}$$

$$H_y^{(b)} = -\frac{\partial H}{\partial y} = (nk) B e^{-nky} \sin(nkx) \tag{C.13}$$

For region (a), the magnetic scalar potential vanishes at the stator surface. Therefore, the scalar potential has a $\sinh(nky)$ component such that the scalar potential equals zero when $y = 0$ (i.e., at the stator surface). Similar to region (b), the y-directed component must match the magnetic charge boundary condition, so the scalar potential must have a $\sin(nkx)$ term. Therefore

$$\psi^{(a)} = \sum_n A_n \sinh(nky) \sin(nkx) \tag{C.14}$$

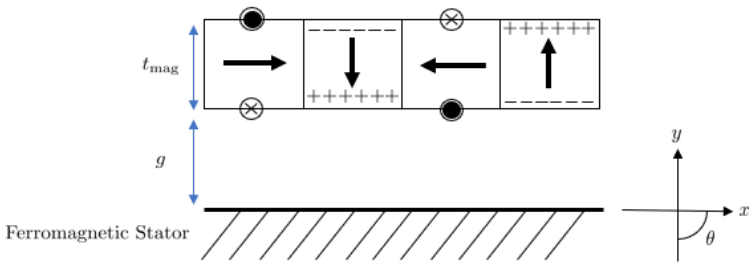

(a) General layout of boundary value problem.

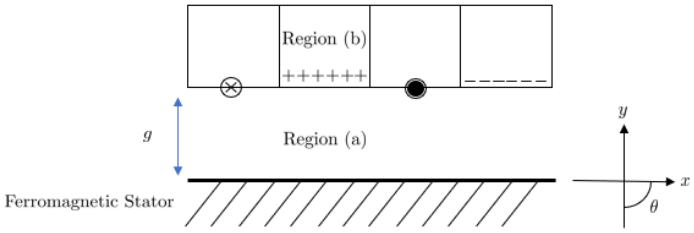

(b) Regions for lower boundary value problem.

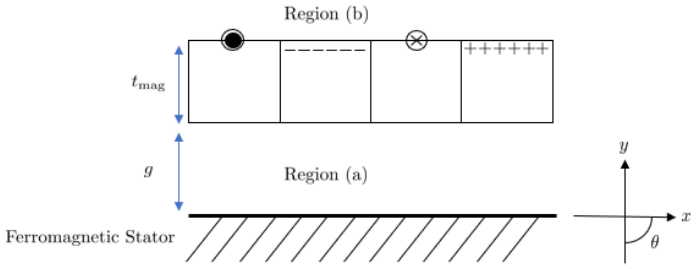

(c) Regions for upper boundary value problem.

Figure C-2: The Halbach array analysis is separated into two, 2-dimensional boundary value problems.

and the H-field has the form

$$H_x^{(a)} = -\frac{\partial H^{(a)}}{\partial x} = -\left(nk\right) A_n \sinh\left(nky\right) \cos\left(nkx\right) \tag{C.15}$$

$$H_y^{(a)} = -\frac{\partial H^{(a)}}{\partial x} = -\left(nk\right) A_n \cosh\left(nky\right) \sin\left(nkx\right) \tag{C.16}$$

At the lower magnet surface, $y = g$, the continuity condition for the magnetic charges

states

$$H_{\mathrm{y}}^{(b)} - H_{\mathrm{y}}^{(a)} = -M_n \sin(nkx) \tag{C.17}$$

$$(nk)\, B_n e^{-nkg} \sin(nkx) + (nk)\, A_n \cosh(nkg) \sin(nkx) = -M_n \sin(nkx) \tag{C.18}$$

$$(nk)\, B_n e^{-nkg} + (nk)\, A_n \cosh(nkg) = -M_n \tag{C.19}$$

for the Amperian currents,

$$H_{\mathrm{x}}^{(b)}(y = g) - H_{\mathrm{x}}^{(a)}(y = g) = K_z \cos(nkx) \tag{C.20}$$

$$-(nk)\, B_n e^{-nkg} \cos(nkx) + (nk)\, A_n \sinh(nkg) \cos(nkx) = K_n \cos(kx) \tag{C.21}$$

$$-(nk)\, B_n e^{-nkg} + (nk)\, A_n \sinh(nkg) = K_n \tag{C.22}$$

Combining these equations,

$$2(nk)\, A_n^{lower} (\sinh(nkg) + \cosh(nkg)) = K_n - M_n \tag{C.23}$$

$$2(nk)\, A_n^{lower} e^{nkg} = K_n - M_n \tag{C.24}$$

$$A_n^{lower} = \frac{(K_n - M_n)\, e^{-nkg}}{2nk} \tag{C.25}$$

At the top of the magnet (i.e., $y = g + t_{\mathrm{mag}}$), the solution has a similar form, but $g \to g + t_{\mathrm{mag}}$ and the solution is negated since the magnetic charge and Amperian current boundary conditions have the opposite form. Therefore,

$$A_n^{upper} = \frac{(-K_n + M_n)\, e^{-nk(g + t_{\mathrm{mag}})}}{2nk} \tag{C.26}$$

The total y-directed H-field in region (a) is therefore

$$H_y^{(a)} = -\sum_{\text{nodd}} (nk)\left(A_n^{upper} + A_n^{lower}\right)\cosh(nky)\sin(nkx) \tag{C.27}$$

$$= -\sum_{\text{nodd}} \left(A_n^{upper} + A_n^{lower}\right)\cosh(nky)\sin(nkx) \tag{C.28}$$

$$= -\sum_{\text{nodd}} \frac{(M_n - K_n)\left(e^{-nk(g+t_{\text{mag}})} - e^{-nkg}\right)}{2}\cosh(nky)\sin(nkx) \tag{C.29}$$

$$= \sum_{\text{nodd}} \frac{4}{n\pi}\sin\left(n\frac{\pi}{4}\right)\left(1+\sin\left(n\frac{\pi}{2}\right)\right)\left(e^{-nk(t_{\text{mag}}+g)} - e^{-nkg}\right)\cosh(nky)\sin(nkx) \tag{C.30}$$

The B-field is $B_y^{(a)} = \mu_0 H_y^{(a)}$. At the stator surface ($y = 0$), which is used to estimate voltage, the y-directed B-field solution is:

$$B_y(x) = -\sum_{\text{nodd}} B_0 \frac{4}{n\pi}\sin\left(n\frac{\pi}{4}\right)\left(1+\sin\left(n\frac{\pi}{2}\right)\right)\left(e^{-nkg} - e^{-nk(g+t_{\text{mag}})}\right)\sin(nkx) \tag{C.31}$$

where B_0 is the remanent flux density of the magnets and t_{mag} is the magnetic thickness.

C.3 Polar Coordinates

The boundary conditions in the polar coordinate case are the same as those in the Cartesian coordinate case, except with $r\theta$ substituted for x. Let the inner radius of the magnet array be R_{bi} and the outer radius be $R_{bo} = R_{bi} + t_{\text{mag}}$. The stator outer radius is $R_i = R_{bi} - g$. The magnetic fields are solved similar to the rectangular coordinates case. For $R_i < r < R_b$,

$$H_r = \left(-Ar^{p-1} + Br^{-p-1}\right)\sin(p\theta) \tag{C.32}$$

$$H_\theta = \left(Ar^{p-1} + Br^{-p-1}\right)\cos(p\theta) \tag{C.33}$$

For $r > R_b$,

$$H_r = Cr^{-p-1}\sin(p\theta) \tag{C.34}$$

$$H_\theta = Cr^{-p-1}\cos(p\theta) \tag{C.35}$$

Since the stator is ferromagnetic, the azimuthal fields at the airgap interface, R_i, are zero. Therefore,

$$H_\theta(R_i) = \left(AR_i^{p-1} + BR_i^{-p-1}\right)\cos(p\theta) = 0 \tag{C.36}$$

$$AR_i^{p-1} + BR_i^{-p-1} = 0 \tag{C.37}$$

$$B = -AR_i^{2p} \tag{C.38}$$

The two boundary conditions at R_b are therefore:

$$-A_nR_b^{np-1}\left(1 + \left(\frac{R_i}{R_b}\right)^{2np}\right) - C_nR_b^{-np-1} = -M_n \tag{C.39}$$

$$A_nR_b^{np-1}\left(1 - \left(\frac{R_i}{R_b}\right)^{2np}\right) - C_nR_b^{-np-1} = K_n \tag{C.40}$$

Therefore,

$$A_n = \frac{M_n + K_n}{2R_b^{np-1}} \tag{C.41}$$

$$B_r(r = R_i) = \sum B_{\text{rem}}\frac{4}{n\pi}\sin\left(\frac{n\pi}{4}\right)\left(1 + \sin\left(n\frac{\pi}{2}\right)\right)\left[\left(\frac{R_i}{R_{bi}}\right)^{np-1} - \left(\frac{R_i}{R_{bo}}\right)^{np-1}\right]\sin(np\theta) \tag{C.42}$$

C.4 Terminal Voltage

The voltage induced in the electric machine winding is the magnetic flux density, B, times the length of the winding, ℓ, times the rotational velocity, U. Therefore, for a winding with N_a turns,

$$V = 2N_a B_r \ell U \tag{C.43}$$

The factor of two accounts for the two active sides of the winding that spans the pole pair and links the magnetic flux density. The rotational velocity can be approximated as $U = r_{\text{ag}}\Omega$, so that

$$V = 2N_a B_r \ell r_{\text{ag}} U \tag{C.44}$$

C.5 Power and Torque

The power is defined since it is a requirement for the demonstrator. The required current to generate this power is therefore

$$I_{\text{req}} = \frac{P_{\text{req}}}{3N_c V_1} \tag{C.45}$$

where N_c is the number of parallel circuits and V_1 is the fundamental component of the electric machine internal voltage.

The torque is then estimated as

$$T = \frac{V_a I_a + V_b I_b + V_c I_c}{\Omega} \tag{C.46}$$

Bibliography

[1] J. Welstead, J. Felder, M. Guynn, B. Haller, M. Tong, S. Jones, I. Ordaz, J. Quinlan, and B. Mason, "Overview of the nasa starc-abl (rev. b) advanced concept," in *One Boeing NASA Electric Aircraft Workshop*, 2017.

[2] X. Zhang, C. Bowman, T. O'Connell, and K. Haran, "Large electric machines for aircraft electric propulsion," *IET Electric Power Applications*, vol. 12, no. 6, pp. 767–779, July 2017.

[3] E. Ganev, "Electric machines for electrical power generation systems," in *IEEE Electrification Magazine*, 2015.

[4] "Altair flux overview." [Online]. Available: https://altairhyperworks.com/product/flux

[5] Arnold Magnetic Technologies, "Recoma®35e," available at https://www.arnoldmagnetics.com/wp-content/uploads/2017/10/Arnold_DS_RECOMA35E_FINAL6-1.pdf.

[6] D. Gerada, A. Mebarki, N. L. Brown, C. Gerada, A. Cavagnino, and A. Boglietti, "High-speed electrical machines: Technologies, trends, and developments," *IEEE Transactions on Industrial Electronics*, vol. 61, no. 6, pp. 2946–2959, June 2014.

[7] M. Kruger, S. Byahut, A. Uranga, J. Gonzalez, D. Hall, and A. Dowdle, "Electrified aircraft trade-space exploration," in *Aviation Technology, Integration, & Operations Conference*, 2018.

[8] D. Hall, A. Dowdle, J. Gonzalez, L. Trollinger, and W. Thalheimer, "Assessment of a boundary layer ingesting turboelectric aircraft configuration using signomial programming," in *Aviation Technology, Integration, & Operations Conference*, 2018.

[9] E. The National Academies of Sciences and Medicine, "Commercial aircraft propulsion and energy systems research: Reducing global carbon emissions," The National Academies Press, Washington, DC, 2016.

[10] "Acs6000 brochure," ABB, 3 2015.

[11] R. Cramer and A. Engler, "Optimizing power electronics for the more electric aircraft," in *SAE 2014 Aerospace Systems and Technology Conference*, September 2014.

[12] D. Golovanov, D. Gerada, G. Sala, M. Degano, A. Trentin, P. Connor, Z. Xu, A. La Rocca, A. Galassini, L. Tarisciotti, C. Eastwick, S. Pickering, P. Wheeler, J. Clare, M. Filipenko, and C. Gerada, "4-mw class high-power-density generator for future hybrid-electric aircraft," *IEEE Transactions on Transportation Electrification*, vol. 7, no. 4, pp. 2952–2964, 2021.

[13] R. Jansen, C. Bowman, A. Jankovsky, R. Dyson, and J. Felder, "Overview of nasa electrified aircraft propulsion research for large subsonic transports," in *53rd AIAA/SAE/ASEE Joint Propulsion Conference, AIAA Propulsion and Energy Forum*, 2017. [Online]. Available: https://ntrs.nasa.gov/archive/nasa/casi.ntrs.nasa.gov/20170012222.pdf

[14] Vacuumschmelze®, Soft Magnetic Cobalt-Iron Alloys, 2013.

[15] T. D. Jayaram, "Effect of processing of hiperco®50 alloy laminates on their magnetic properties," *Journal of Electronic Materials*, vol. 44, no. 11, 2015.

[16] M. Emura, F. J. G. Landgraf, W. Ross, and J. R. Barreta, "The influence of cutting technique on the magnetic properties of electrical steels," *Journal of Magnetism and Magnetic Materials*, vol. 254-255, 2003.

[17] J. Ofori-Tenkorang, "Permanent-magnet synchronous motors and associated power electronics for direct-drive vehicle propulsion," Ph.D. dissertation, Massachusetts Institute of Technology, 1996.

[18] A. D. Anderson, Y. Wang, Y. Yu, and K. S. Haran, "Experimental validation of a high-power slotless stator," in *IEEE International Electric Machines & Drives Conference*, 2019.

[19] J. Swanke, D. Bobba, T. Jahns, and B. Sarlioglu, "Design of high-speed permanent magnet machine for aerospace propulsion," in *AIAA/IEEE Electric Aircraft Technologies Symposium (EATS)*, 2019.

[20] University of Nottingham - Institute for Aerospace Technology. LIFT Lightweight Innovative Generator For Future Air Transportation. Available at "https://www.nottingham.ac.uk/aerospace/projects/cleansky/lift-project.aspx.".

[21] Aviation Week article. (2017) GE Set For Key Electric Propulsion Technology Test. Available at "https://www.flightglobal.com/news/articles/ge-reveals-major-achievements-in-hybrid-electric-pro-440602/".

[22] R. M. Klaas and C. DellaCorte, "The quest for oil-free gas turbine engines," *SAE International*, November 2006.

[23] General Electric Co., "Blade tip electric machine," U.S. Patent 7 603 864B2, Oct. 20, 2009.

[24] General Electric Co., "Integrated turbine-generator," U.S. Patent US5 376 827A, Dec. 27, 1994.

[25] T. Balachandran, J. Reband, M. Lewis, and K. Haran, "Co-design of integrated propellor and inner rotor pmsm for electric aircraft application," in *International Electric Machines & Drives Conference (IEMDC)*, 2021.

[26] T. Balachandran, J. Reband, J. Xiao, S. Sirimmana, R. Dhilon, and K. Haran, "Co-design of an integrated direct-drive electric motor and ducted propellor for aircraft propulsion," in *AIAA Propulsion and Energy Forum*, 2020.

[27] Y. Chen, "Technology demonstration of a megawatt class integrated motor drive for aircraft propulsion," Ph.D. dissertation, Massachusetts Institute of Technology, 2022, unpublished thesis.

[28] M. Qasim, D. Otten, J. Lang, J. Kirtley, and D. Perreault, "Comparison of inverter topologies for high-speed motor drive applications," in *IEEE 22nd Workshop on Control and Modelling of Power Electronics*, November 2021.

[29] M. Qasim, "Design of High Speed, High Specific Power Motor Drives for Megawatt Aircraft Applications," Ph.D. dissertation, Massachusetts Institute of Technology, 2022, unpublished thesis.

[30] J. Swanke, D. Bobba, T. Jahns, and B. Sarlioglu, "Comparison of modular pm propulsion machines for high power density," in *IEEE Transportation Electrification Conference and Expo*, 2019.

[31] T. Balachandarn, S. Srimmana, A. Anderson, X. Yi, N. Renner, and K. Haran, "Assembly and qualification of a slotless stator assembly for a mw-class permanent magnet synchronous machine," in *AIAA/IEEE Electric Aircraft Technologies Symposium (EATS)*, August 2020.

[32] W. Zhao, X. Wang, C. Gerada, H. Zhang, C. Liu, and Y. Wang, "Multi-physics and multi-objective optimization of a high speed pmsm for high performance applications," *IEEE Transactions on Magnetics*, vol. 54, no. 11, 2018.

[33] A. Vannini, A. Marfoli, L. Papini, P. Bolognesi, and C. Gerada, "Materials for electric machines suited for high-temperature applications: a survey," in *IEEE Workshop on Electrical Machines Design, Control, and Diagnosis*, 2021, pp. 101–106.

[34] M. R. Institute, "Brushless dc motors," National Aeronautics and Space Administration, Washington, D.C., Tech. Rep. NASA CR-2506, May 1974.

[35] Y. Wang, S. Nuzzo, H. Zhang, and W. Z. and, "Challenges and opportunities for wound field synchronous generators in future more electric aircraft," *IEEE Transactions on Transportation Electrification*, vol. 6, no. 4, pp. 1466–1477, 2020.

[36] J. Nøland, M. Leandro, J. Suul, and M. Molinas, "High-power machines and starter-generator topologies for more electric aircraft: A technology outlook," *IEEEAccess*, vol. 8, pp. 130 104–130 123, 2020.

[37] E. Sayed, M. Abdalmagid, G. Pietrini, N. Sa/'adeh, A. Callegaro, C. Goldstein, and A. Emadi, "Review of electric machines in more-/hybrid-/turbo-electric aircraft," *IEEE Transactions on Transportation Electrification*, vol. 7, no. 4, pp. 2976–3005, 2021.

[38] N. Cumpsty and A. Heyes, *Jet Propulsion*. Cambridge University Press, 2015.

[39] F. C. A and E. Richter, "Detailed design of a 250-kw switched reluctance starter/generator for an aircraft engine," *SAE Transactions*, vol. 102, pp. 289–300, 1993.

[40] E. Richter, J. P. Lyons, C. Ferreira, A. V. Radun, and E. Ruckstadter, "Initial testing of a 250 kw starter/generator for aircraft applications," *SAE Technical Paper Series*, 1994.

[41] J. L. Smith, Jr., J. L. Kirtley, J. Gerstman, and F. C. Rumore, "Assessment of the technology of electric transmission subsystems," *Institute for Defense Analyses Paper IDA-P-1278*, September 1978.

[42] Y. Zhao, D. Li, T. Pei, and R. Qu, "Overview of the rectangular wire windings ac electrical machine," *CES Transactions on Electrical Machines and Systems*, vol. 3, no. 2, pp. 160–169, 2019.

[43] N. N. Farve, "Design of a low-mass high-torque brushless motor for application in quadruped robotics," Ph.D. dissertation, Massachusetts Institute of Technology, 2012.

[44] D. Trumper, M. Williams, and T. Nguyen, "Magnet arrays for synchronous machines," in *Proceedings of the IEEE IAS 28th Annual Meeting*, October 1993.

[45] F. Zhang and D. Guanghui, "Electromagnetic design and loss calculations of a 1.12-mw high-speed permanent-magnet motor for compressor applications," *IEEE Transactions on Energy Conversion*, vol. 31, pp. 132–140, 2016.

[46] E. D. L. R. Blanco, C. Hall, and D. Crichton, "Challenges in the silent aircraft engine design," in *45th AIAA Aerospace Sciences Meeting and Exhibit*, 2007.

[47] J. Pyrhonen, T. Jokinen, and V. Hrabovcova, *Design of Rotating Electrical Machines*. John Wiley & Sons, Ltd., 2014.

[48] "Aircraft Electric Power Characteristics," U.S. Department of Defense, Standard MIL-STD-704F, March 2004.

[49] J. Kurzke and I. Halliwell, *Propulsion and Power: An Exploration of Gas Turbine Performance Modeling*. Springer, Cham, 2018.

[50] D. K. Hall, E. M. Greitzer, and C. S. Tan, "Performance Limits of Axial Compressor Stages," in *Turbo Expo: Power for Land, Sea, and Air*, vol. 8: Turbomachinery, Parts A, B, and C, 07 2013, pp. 479–489. [Online]. Available: https://doi.org/10.1115/GT2012-69709

[51] S. F. Smith, "A simple correlation of turbine efficiency," *The Journal of the Royal Aeronautical Society*, vol. 69, no. 655, p. 467–470, 1965.

[52] J. Kerrebrock, *Aircraft Engines and Gas Turbines*. The MIT Press, 1992.

[53] R. Fano, L. J. Chu, and R. Adler, *Electromagnetic Fields, Energy and Forces*. Wiley, 1963.

[54] J. L. Kirtley Jr., "Class notes 6: Dc (commutator) and permanent magnet machines," 2005.

[55] X. Nan and C. Sullivan, "An improved calculation of proximity-effect loss in high-frequency windings of round conductors," in *34th Annual IEEE Power Electronics Specialists Conference*, June 2003.

[56] X. Nan and C. Sullivan, "Simplified high-accuracy calculation of eddy-current loss in round-wire windings," in *35th Annual IEEE Power Electronics Specialists Conference*, October 2004.

[57] J. L. Kirtley Jr. and E. C. Lovelace, "Drag loss in retaining rings of permanent magnet motors," in *IEEE International Electric Machines and Drives Conference*, vol. 2, March 2003.

[58] M. G. Angle, "Modeling, design and optimization of permanent magnet synchronous machines," Ph.D. dissertation, Massachusetts Institute of Technology, 2016.

[59] F. Liu, X. Wang, Z. Xing, A. Yu, and C. Li, "Reduction of cogging torque and electromagnetic vibration based on different combination of pole arc coefficient for interior permanent magnet synchronous machine," *CES Transactions on Electircal Machines and Systems*, vol. 5, no. 4, December 2021.

[60] J. L. Kirtley Jr., "Class notes 8: Analytic design evaluation of induction machines," 2009.

[61] DuPont™, Nomex®410, 2016.

[62] M. J. Carlin, "Design of a high-speed motor-alternator for flywheel energy storage systems," Ph.D. dissertation, Massachusetts Institute of Technology, 1997.

[63] Arnold Magnetic Technologies, "Sintered neodymium-iron-boron magnets," available at https://www.arnoldmagnetics.com/wp-content/uploads/2017/11/N38AH-151021.pdf.

[64] B. Tekgun, "Analysis, Measurement and Estimation of the Core Losses in Electrical Machines," Ph.D. dissertation, The University of Akron, 2016.

[65] NASA Glenn Research Center. University of Illinois Gallium Nitride Inverter. [Online]. Available: https://www1.grc.nasa.gov/aeronautics/eap/larger-aircraft/converters/university-of-illinois-gallium-nitride-inverter/

[66] "Jmag®," available at https://www.jmag-international.com/.

[67] New England Wire Technologies, "Shaped compacted litz wire: Type 8 litz wire construction," https://www.newenglandwire.com/product/shaped-compacted-litz-wire/.

[68] Loctite®, AA 331™ Technical Data Sheet, 2017.

[69] M. Mirzaei, A. Binder, B. Funieru, and M. Susic, "Analytical calculations of induced eddy currents losses in the magnets of surface mounted pm machines with consideration of circumferential and axial segmentation effects," *IEEE Transactions on Magnetics*, vol. 48, no. 12, pp. 4831–4841, 2012.

[70] M. Athans, "The role and use of the stochastic linear-quadratic-gaussian problem in control system design," *IEEE Transactions on Automatic Control*, vol. AC-16, no. 6, pp. 529–552, 1971.

[71] B. D. O. Anderson and J. B. Moore, *Optimal Control: Linear Quadratic Methods*. Dover Publications, 2007.

[72] R. Qu and T. Lipo, "Analysis and modeling of air-gap and zigzag leakage fluxes in a surface-mounted permanent-magnet machine," *IEEE Transactions on Industry Applications*, vol. 40, no. 1, pp. 121–127, Feb 2004.

[73] J. L. Kirtley Jr., "Class notes 1: Electromagnetic forces," 2003.

[74] C. R. Sullivan, "Optimal choice for number of strands in a litz-wire transformer winding," in *IEEE Power Electronics Specialist Conference*, 06 1997, pp. 28–35.

[75] "Carpenter 50a core loss formula for maxwell software." [Online]. Available: https://magweb.us/wp-content/uploads/2017/05/Hiperco-50A-0.006in-.xls